

Microporous Polymer Networks as Macroligands for the Immobilization of Metal-Organic Catalysts

vorgelegt von

Sarah Vogl

an der Fakultät II – Mathematik und Naturwissenschaften
der Technischen Universität Berlin
zur Erlangung des akademischen Grades

Doktor der Naturwissenschaften

- Dr. rer. nat. -

genehmigte Dissertation

Promotionsausschuss:

Vorsitzende: Prof. Dr. Maria Andrea Mroginski

1. Gutachter: Prof. Dr. Arne Thomas

2. Gutachter: Prof. Dr. Martin Oschatz

Tag der wissenschaftlichen Aussprache: 13. August 2021

Berlin 2021

Danksagung

Die Bedeutung der Wissenschaft ist uns wohl allen im vergangenen Jahr besonders deutlich geworden. Inmitten einer weltweiten Pandemie und dem fortschreitenden Klimawandel wird mir jeden Tag bewusster, welch ein Privileg es ist, wissenschaftlich zu arbeiten und die dafür notwendigen Werkzeuge während meines Studiums erlernt zu haben, um mich so in zahlreiche wissenschaftliche Themenfelder einarbeiten zu können.

Ein herzlicher Dank geht an Herr Prof. Dr. Arne Thomas, der mir die Möglichkeit gab, in seiner Arbeitsgruppe eine Promotion zu absolvieren. Ich bin sehr dankbar für seine Unterstützung in allen theoretischen und praktischen Fragen und insbesondere für sein Vertrauen in meine Arbeit, das mir die Freiheit gab auf diversen Themen zu forschen.

Ein weiterer Dank geht an Herr Prof. Dr. Martin Oschatz für die Übernahme des Zweitgutachtens und an Frau Prof. Dr. Maria Andrea Mroginski für die Übernahme des Prüfungsvorsitzes.

Ein ganz herzliches Dankeschön geht an alle aktuellen und ehemaligen Arbeitskolleg*innen des AK Thomas für die schöne Zeit und die tolle Arbeitsatmosphäre. Insbesondere meinen Schreibtischnachbar*innen, Michaela König, Nicolas Chaoui, Thomas Langenhahn und Esteban Gioria, möchte ich für den intensiven Wissensaustausch und ihre Unterstützung danken. Ihr habt mich so oft zum Lachen gebracht und für einen schönen Arbeitsalltag gesorgt. Hervorheben möchte ich auch die enge Zusammenarbeit mit Dr. Johannes Schmidt und Dr. Pradip Pachfule, die mir zu Rat und Tat beistanden und sehr zum Gelingen dieser Arbeit beigetragen haben. Außerdem möchte ich Anne Svilarov, Andrea Rahmel, Christina Eichenauer und Maria Unterweger für ihre stetigen Einsatz in allen organisatorischen und labortechnischen Angelegenheiten danken. Zudem danke ich Jonas Kube, dessen Bachelor- als auch Masterarbeit ich betreuen durfte, für seine Mitarbeit, die meine Thesis an Ergebnissen bereichert hat. Außerdem danke ich Dr. Matthias Trunk, der immer ein offenes Ohr für mich hatte und auch nach Verlassen des AKs bei vielen meiner wissenschaftlichen Fragen half, Dr. Rafael de Lima Oliveira für die Beantwortung aller meiner anorganischen Fragen und Durchführung der Hydrierungen, Amitave Acharjya und Jin Yang für die unzähligen photokatalytischen Messungen, und Dr. Shuang Li und Meng-Yang Ye für ihre Hilfe bei Fragen zur Elektrochemie. Ein weiteres Dankeschön geht auch an Dr. Jérôme Roeser, Dr. Miriam Klapproth, Dr. Xiaojia Zhao, Dr. Ha Vu Le, Dr. Suman Chandra, Julia Grüneberg, Vincent Weigelt, Daniel Hagemayer, Sophie Kücken, Leo Sagurna, Michael

Traxler, Yasmine Ziouani, Robert Sroka, Najmeh Bashiri und Hüseyin Küçükkeçeci. Viele von euch sind mir nicht nur als Kolleg*innen sondern auch privat ans Herz gewachsen. Daher bin ich sehr dankbar für die Zeit mit euch.

Für die Durchführungen der Analysen, danke ich Christina für die vielen BET und TGA Messungen, Harald Link für die ICP Messungen, Meng und Hüseyin für die SEM Analysen, Yasmine für die TEM Aufnahmen, Juana Krone und Barbara-Cornelia Fischer für die unzähligen FTIR Messungen, und zudem Jan-Dirk Epping für all die lehrreichen Tipps und Messungen am Festkörper NMR.

Ein besonderer Dank geht an meine Kollaborationspartner*innen in Peking, die Arbeitsgruppe von Herrn Prof. Dr. Bao-Hang Han, die mich mit großer Gastfreundschaft am National Center of Nanoscience and Technology empfangen haben. Während meines einmonatigen Aufenthalts in China habe ich sehr viele neue Eindrücke und Einblicke gesammelt, die ich nicht hätte missen wollen. Bei Tian-Xiong Wang möchte ich mich für seine Hilfe während meines Aufenthalts bedanken, da er mir bei allen Fragen und Problemen zur Seite stand, als auch die Stadt und Kultur zeigte. Außerdem danke ich Hai-Peng Liang für seine Zusammenarbeit während seines Aufenthalts an der TU Berlin.

Des Weiteren danke ich der Arbeitsgruppe von Herrn Prof. Dr. Grützmacher an der ETH Zürich. Insbesondere bei Dr. Monica Trincado möchte ich mich für die produktive und gute Teamarbeit bedanken. Weiterhin danke ich den Kollaborationspartnern Carolina Urban und Ariane Weber vom Arbeitskreis von Prof. Dr. Schomäcker, Dr. Bartholomäus Pieber und Cristian Cavedon vom Max-Planck-Institut für Kolloid- und Grenzflächenforschung in Potsdam, als auch Dr. Tianyi Wang vom Helmholtz-Zentrum Berlin für den intensiven wissenschaftlichen Austausch und die erfolgreiche Zusammenarbeit.

Ein großes Dankeschön geht an meine Eltern und meinen Bruder, die mir immer wieder Mut zugesprochen haben und mich dabei unterstützten meinen Weg zu gehen. Es ist ein Privileg so eine sorgenfreie und wunderschöne Studien- und Promotionszeit gehabt zu haben, die nur durch den bedingungslosen Zuspruch und Unterstützung meiner Eltern möglich war.

Zuallerletzt möchte ich Tobi für seine Unterstützung danken. Insbesondere im letzten Jahr während meiner Schreibphase und in Zeiten einer Pandemie, war es kein Leichtes die Ausdauer beizubehalten, jeden Tag zu Hause am Schreibtisch zu sitzen. Daher bin ich ihm sehr dankbar für all den motivierenden Zuspruch und Aufmunterungen in dieser Zeit.

Zusammenfassung

Diese Arbeit stellt neue carbazolhaltige poröse organische Polymere CPOPs^[1] vor, welche mittels oxidativer Polymerisation synthetisiert und im Bereich der heterogenen Katalyse und Wasserstoffspeicherung eingesetzt werden. Der Einbau chelatbildender Liganden in das Polymernetzwerk, die so genannten „poröse Makroliganden“^[2] bilden, eröffnet die Möglichkeit, Metallkomplexe im Material zu immobilisieren, um die Vorteile der homogenen und heterogenen Katalyse zu kombinieren. Realisiert wurde dies durch die Synthese des bipyridinhaltigen Materials **CPOP-30**, welches als Trägermaterial für $[\text{Re}(\text{bipy})(\text{CO})_3\text{Cl}]$, einem bekannten Katalysator für die selektive Photoreduktion von CO_2 zu CO , dient. Beim Einsatz von **CPOP-30-Re** in der photokatalytischen CO_2 Reduktion ergab sich eine CO Ausbeute von $623 \mu\text{mol g}^{-1} \text{h}^{-1}$ mit einer Chemoselektivität von 98%.^[3] Im Vergleich zum molekularen Katalysator, der sich während der Bestrahlung zersetzt, erwies sich der immobilisierte Re(I) -Katalysator als robust und recyclebar.

Durch die Kombination von Nickel- und Photoredoxkatalyse, werden edelmetallfreie Kreuzkupplungen unter milden Bedingungen möglich. **CPOP-30** kann auch als Makroligand zur Chelatisierung von Ni-Komplexen eingesetzt werden, um als Katalysator in der C–S Kreuzkupplung unter Bestrahlung von Licht im sichtbaren Bereich zu fungieren. **CPOP-30-Ni** verfügt über ein erweitertes, konjugiertes π -System, welches durch die Einstrahlung von blauem Licht (440 nm) direkt aktiviert wird und die Kreuzkupplung von 4-Iodobenzotrifluorid und p-Toluolsulfonat mit einer Ausbeute von 99% und Selektivität von 77% katalysiert.

Ein weiteres Ziel ist die Entwicklung eines Materials zur Wasserstoffspeicherung basierend auf *N*-Ethylcarbazol (NECz), welches durch seinen Einsatz in flüssigen organischen Wasserstoffspeichern bekannt sind.^[4] Dafür wurden Copolymere aus NECz (20-60 mol%) und 1,3,5-Tri(*N*-carbazolyl)benzol (TCB) hergestellt, deren BET Oberflächen sich zwischen 736 und $2054 \text{ m}^2 \text{g}^{-1}$ bewegen. Die Speicherkapazität der Copolymere durch Physisorption bei 77 K, ergab eine maximale Wasserstoffaufnahme von 1.98 Gew.% und Adsorptionenthalpien von bis zu 11.0 kJ mol^{-1} . Um das Copolymer **P_{0.5}**, bestehend aus 50 mol% NECz, als Festphasen-Wasserstoffspeicher einzusetzen, wurde das Material mit Hexachloroplatinsäure imprägniert und bei 150 °C unter 40 bar Wasserstoff gesetzt. Die Hydrierung des Polymergerüsts **P_{0.5}** wurde durch die *in situ* gebildeten Platin Nanopartikel katalysiert, wobei Platingehalte zwischen 0.2 und 6.0 Gew.% eingesetzt wurden. ^{13}C Festkörper NMR und FTIR Spektroskopiemessungen zeigen zusätzliche aliphatische Gruppen im

Polymergerüst, welche den hydrierten NECz Einheiten zu Grunde liegen und damit die erfolgreiche Hydrierung beweisen. Außerdem zeigen erste Dehydrierungsstudien, dass durch Einsatz eines ausbalancierten Verhältnisses zwischen passendem Hydrierungsgrad und Nanopartikelgröße die thermische Dehydrierung erreicht werden kann.

Der zweite Teil der Thesis befasst sich mit der Entwicklung einer Strategie zur Herstellung von stabilen, mikroporösen Triphenylphosphin(TPP)-Polymeren, welche mittels Yamamoto-Kreuzkupplungen hergestellt wurden. Die TPP-basierten Materialien **polyTPP** und das Copolymer **CopolyTPP**, welche als Makroliganden fungieren, wurden als Trägermaterial für den Hydrosilylierungs-Katalysator $[\text{Rh}(\text{trop}_2\text{NH})](\text{OTf})$ eingesetzt. Nach der Immobilisierung des Rh(I)-Komplexes wurden jeweils 8.0 und 6.6 Gew.% Rh-Beladung für **Rh-polyTPP** und **Rh-CopolyTPP** gemessen. Der Einsatz der beiden Materialien erzielte in der Hydrosilylierung von NO_2 Umsätze zwischen 96 und 98%. Außerdem wurde der Präkursor $[\text{Rh}(\text{CO})_2(\text{acac})]$ auf die Trägermaterialien **polyTPP** und **CopolyTPP-2**, in welchem die Konzentration an TPP Koordinationsstellen verdünnt wurde, immobilisiert um neue Hydroformylierungs-Katalysatoren herzustellen. Bei Anwendung des **Rh-CopolyTPP-2** in der Hydroformylierung von 1-Octen wurde eine Ausbeute von 99% mit einem Verhältnis von 40:60 n-Nonanal zu iso-Aldehyd erhalten. Der Vergleich der Katalysatoren zeigt, dass durch hohe Oberflächen eine geringere Metallbeladung nötig ist, um höhere Umsätze zu erreichen.

Carbazol-Monomere können nicht nur zu Pulvern, sondern auch zu Polymerfilmen umgesetzt werden, welche auf leitenden Oberflächen mittels Elektropolymerisation, abgeschieden werden können. Die Dicke der Filme kann über die Anzahl der Zyklen in der Cyclovoltammetrie (CV) gesteuert werden. Die phosphinhaltigen Filme **polyCzTPP** besitzen eine Oberfläche von $355 \text{ m}^2 \text{ g}^{-1}$, und stellen einen ersten Ansatz zur Entwicklung einer „Wittig-Elektrode“ dar. Darüber hinaus wurden dünne bipyridinhaltige Filme mittels CV auf FTO hergestellt und auf ihre optischen und elektronischen Eigenschaften untersucht. Basierend auf UV-Vis und UPS Messungen konnte sowohl die Bandlücke von 3.03 eV als auch die Position des Leitungs- und Valenzbandes festgestellt werden, die sich für die OER- und HER-Reaktion eignen. Die 600 nm dicken **polyCzbipy** Filme wurden mit Ni(II)- und Co(II)-Komplexen funktionalisiert und bezüglich ihrer Aktivität in Elektro- und Photoelektrokatalyse getestet. Bei kurzen Bestrahlungsintervallen mit steigendem Potential weist der *p*-Typ Halbleiter **polyCzbipy** eine hohe Photosensibilität auf, dass sich in einer Stromdichte von bis zu $3.0 \mu\text{A cm}^{-1}$ zeigt. Desweiteren wurde **polyCzbipy** auf dem *p*-Typ Halbleiter CuBi_2O_4 abgeschieden. Die Kombination der zwei *p*-Typ Materialien **$\text{CuBi}_2\text{O}_4/\text{polyCzbipy-Ni}$** und **$\text{CuBi}_2\text{O}_4/\text{polyCzbipy}$** ergaben Photostromdichten von jeweils 60 und $47 \mu\text{A cm}^{-2}$.

Abstract

This work presents new tailor-made carbazole-based porous organic polymers CPOPs,^[1] which were synthesized *via* oxidative polymerization, targeting their applications for heterogeneous catalysis and hydrogen storage. Introducing chelating ligands into the polymer network, so-called ‘porous macroligands’,^[2] gives the opportunity to immobilize metal-complexes within the materials, combining the advantages of homo- and heterogeneous catalysis. This approach was realized by synthesizing bipyridine-containing material **CPOP-30**, which was applied as support for the molecular compound [Re(bipy)(CO)₃Cl], a well-known catalyst for the selective photoreduction of CO₂ to CO. The photocatalytic CO₂ reduction using **CPOP-30-Re** gave maximal values of 623 $\mu\text{mol g}^{-1} \text{h}^{-1}$ for CO production with a chemoselectivity of 98%. In comparison to the molecular catalyst, which suffers from photodecomposition under irradiation, the immobilized Re(I) catalyst proved to be robust and recyclable.^[3]

By combining visible-light photoredox- and Ni-catalysis, noble metal-free cross-coupling reactions under mild conditions become feasible. The polymer **CPOP-30** is also applicable as chelating macroligand for Ni-complexes as sulfonylation catalyst under irradiation of visible-light. **CPOP-30-Ni** provides an extended conjugated π -system, which is directly activated by blue light (440 nm), to catalyze the coupling of 4-iodobenzotrifluoride and p-toluenesulfinate with a conversion rate of 99% and a selectivity of 77%.

Furthermore, the design of hydrogen storage materials based on *N*-ethylcarbazole (NECz), which is known as liquid organic hydrogen carrier (LOHC), was targeted.^[4] For that purpose, copolymers synthesized from NECz (20-60 mol%) and 1,3,5-tri(*N*-carbazolyl)benzene (TCB) were prepared, possessing BET surface areas ranging from 736 to 2054 $\text{m}^2 \text{g}^{-1}$. The copolymers were tested for their hydrogen uptake capacities by physisorption at 77 K, presenting maximum hydrogen uptake of 1.98 wt% and isosteric heat of adsorption up to 11.0 kJ mol^{-1} . To apply copolymer **P_{0.5}**, prepared from 50 mol% NECz, as solid-state hydrogen carrier, the material was impregnated with chloroplatinic acid and treated with 40 bar of hydrogen gas at 150 °C. Due to the *in situ* formed Pt nanoparticles, hydrogenation of the polymeric backbone of **P_{0.5}** was catalyzed. Solid-state ¹³C NMR and FTIR spectroscopy analysis proved the additional aliphatic moieties within the polymer backbone, deriving from hydrogenation of the NECz units. Successful hydrogenation of **P_{0.5}** was performed by adjusting the platinum content between 0.2 and 6.0 wt%. Besides, first

dehydrogenation studies were conducted, showing that a balance between the right hydrogenation level and nanoparticle size must be found to achieve thermal dehydrogenation.

In the second part of the thesis, a strategy was developed to manufacture stable microporous triphenylphosphine (TPP) polymers *via* Yamamoto cross-coupling reaction. The TPP-based materials **polyTPP** and copolymer **CopolyTPP** functioning as macroligand, were applied as supporting materials for the hydrosilylation catalyst [Rh(trop₂NH)](OTf). After immobilization of Rh(I) complex, 8.0 and 6.6 wt% of Rh loading were detected for the materials, respectively. For both polymers **Rh-polyTPP** and **Rh-CopolyTPP**, yields between 96 and 98% were reached during hydrosilylation of nitrous oxide to form non-hazardous nitrogen by transferring oxygen into the silane bonds. Furthermore, precursor [Rh(CO)₂(acac)] was immobilized on **polyTPP** as well as on a copolymer **CopolyTPP-2**, exhibiting a diluted concentration of TPP coordination sites, to design new hydroformylation catalysts. In the hydroformylation of 1-octene, for **Rh-CopolyTPP-2**, a conversion up to 99% was obtained in a ratio of 40:60 n-nonanal to iso-aldehyde. The comparison of the catalysts showed that higher surface areas require less metal loading and lead to higher conversion rates within less time.

Besides powdery bulk materials, taking the advantage of possible electropolymerization of carbazole monomers on conductive glass surfaces such as ITO and FTO, polymer films were also prepared. The thickness of these films was controllable by applying different number of scans during the cyclic voltammetry (CV). The design of phosphine-containing **polyCzTPP** film, exhibiting a surface area of 355 m² g⁻¹, was a first attempt to implement phosphine coated ITO electrodes as ‘Wittig electrode’. Moreover, bipyridine-containing thin films were synthesized *via* CV on FTO and analyzed regarding their optical and electronical properties. Based on UV-Vis and UPS measurements, the band gap was determined to be 3.03 eV and the position of conduction and valence band found to be suitable for OER and HER reaction. The 600 nm thick **polyCzbipy** films were coordinated with Ni(II) and Co(II) complexes as a co-catalyst to test their electro- and photoelectrocatalytic performances. In chopped LSV studies, the *p*-type material **polyCzbipy** showed a sharp photo-response and a maximum current density of 3.0 μA cm⁻¹. In a further study, also *p*-type semiconductor CuBi₂O₄ was coated with **polyCzbipy**. The combination of two *p*-type materials, **CuBi₂O₄/polyCzbipy-Ni** and **CuBi₂O₄/polyCzbipy** gave photocurrent densities of 60 and 47 μA cm⁻², respectively.

Index

1	Introduction	1
2	Theory	3
2.1	Microporosity	3
2.1.1	Determination of Surface Area	4
2.1.2	Pore Size Distribution	7
2.1.3	Microporous Materials.....	7
2.2	Bridging Homogeneous and Heterogeneous Catalysis	11
3	Scope of the Thesis	13
4	Microporous Carbazole-based Polymer Networks	15
4.1	Theoretical Background	15
4.1.1	Carbazole-containing Polymers	15
4.1.2	Porous Carbazole-containing Polymer Networks.....	17
4.1.3	Photocatalytic Carbon Dioxide Reduction.....	18
4.1.4	Dual Transition Metal/Photoredoxcatalysis.....	20
4.1.5	Hydrogen Storage	21
4.2	Objective.....	23
4.3	Results and Discussion	24
4.3.1	Carbazole-based Polymer Networks for Photocatalysis	24
4.3.2	Carbazole-based Polymer Networks Applied in Nickel-catalyzed Cross-coupling under Visible-light Irradiation.....	29
4.3.3	Carbazole-based Copolymers for Hydrogen Storage	32
4.3.4	Carbazole-based Homopolymers for Hydrogen Storage	45
4.4	Conclusion and Outlook	49
5	Microporous Phosphine-based Polymer Networks	53
5.1	Theoretical Background	53
5.1.1	Wittig Reaction	53
5.1.2	Phosphine as Ligand in Catalysis	53
5.1.3	Hydrogenation and Hydrosilylation of Nitrous Oxide.....	54
5.1.4	Protection Method for Phosphines.....	55
5.1.5	Phosphine-based Polymers	56
5.2	Objective.....	59

5.3	Results and Discussion	60
5.3.1	Material Synthesis and Characterization of Phosphine-based Polymers	60
5.3.2	Applications of Phosphine-based Polymers.....	73
5.4	Conclusion and Outlook	77
6	Microporous Polymer Films.....	79
6.1	Theoretical Background	79
6.1.1	Electrochemical Oxidation of Carbazole	79
6.1.2	Carbazole-based Films.....	80
6.1.3	Electrocatalytic Water Splitting.....	82
6.1.4	Photoelectrochemical Water Splitting	82
6.2	Objective.....	85
6.3	Results and Discussion	86
6.3.1	Phosphine-containing Films.....	86
6.3.2	Bipyridine-containing Films	89
6.4	Conclusion and Outlook	104
7	Summary	107
8	Experimental Section	109
8.1	Materials	109
8.2	Characterization Methods and Sample Preparation.....	112
8.2.1	Nuclear Magnetic Resonance Spectroscopy (NMR)	112
8.2.2	Gas Sorption Measurements	112
8.2.3	Fourier Transform Infrared Spectroscopy (FTIR)	112
8.2.4	Ultraviolet-Visible Spectroscopy (UV-Vis)	113
8.2.5	Thermogravimetric Analysis (TGA).....	113
8.2.6	Thermal Gravimetric Mass Spectroscopy (TG-MS).....	113
8.2.7	Flash Chromatography	113
8.2.8	Inductively Coupled Plasma Optical Emission Spectrometry (ICP-OES).....	113
8.2.9	Ultraviolet Photoelectron Spectroscopy (UPS)	113
8.2.10	Scanning Electron Microscopy (SEM)	114
8.2.11	Transmission Electron Microscopy (TEM)	114
8.2.12	X-Ray Photoelectron Spectroscopy (XPS)	114
8.3	Synthesis of the Monomers	115
8.4	Synthesis of the Polymers.....	121
8.4.1	Carbazole-based Polymers.....	121

8.4.2	Phosphine-based Polymers	124
8.4.3	Microporous Polymer Films	129
8.5	Catalysis.....	131
8.5.1	Photocatalytic CO ₂ Reduction	131
8.5.2	Visible-Light-Mediated Nickel Catalysis	131
8.5.3	Hydrogenation.....	132
8.5.4	Hydrosilylation	132
8.5.5	Hydroformylation	132
8.5.6	Electrocatalytic Oxygen Evolution Reaction (OER)	132
8.5.7	Photoelectrochemical (PEC) Measurements.....	133
9	Appendix	134
9.1	Spectra and Characterization Methods	134
9.1.1	Carbazole-based Polymers.....	134
9.1.2	Phosphine-based Polymers	137
9.1.3	Microporous Polymer Films	139
9.2	References	141

List of Abbreviations

abbreviation	meaning
2D	two-dimensional
3D	three-dimensional
BET	Brunauer-Emmett-Teller (theory)
CA	chronoamperometry
CB	conduction band
CMP	conjugated microporous polymer
COD	1,5-cyclooctadiene
COF	covalent organic framework
CPOP	carbazole-based porous organic polymer
CTF	covalent triazine-based framework
CV	cyclic voltammetry
Czbipy	5,5'-di(9 <i>H</i> -carbazol-9-yl)-2,2'-bipyridine
DCM	dichloromethane
DMF	dimethylformamide
E _g	band gap
eq	equivalents
FTO	fluorine doped tin oxide
HER	hydrogen evolution reaction
HOMO	highest occupied molecular orbital
ICP-OES	inductively coupled plasma optical emission spectroscopy
IR	infrared
ITO	indium tin oxide
IUPAC	International Union of Pure and Applied Chemistry
J	coupling constant
LOHC	liquid organic hydrogen carrier
LSV	linear sweep voltammetry
LUMO	lowest unoccupied molecular orbital
MOF	metal-organic framework
MPN	microporous polymer network

MS	mass spectrometry
NECz	<i>N</i> -ethylcarbazole
NMR	nuclear magnetic resonance
OER	oxygen evolution reaction
PAF	porous aromatic framework
PIM	polymers of intrinsic microporosity
PMO	periodic mesoporous organosilane
ppm	parts per million
PPN	porous polymer network
rt	room temperature
S_{BET}	BET surface area
SEM	scanning electron microscopy
SET	single electron transfer
TEM	transmission electron microscopy
TCB	1,3,5-tri(<i>N</i> -carbazolyl)benzene
TGA	thermogravimetric analysis
THF	tetrahydrofuran
TOF	turnover frequency
TPP	triphenylphosphine
VB	valence band
wt%	weight percent
XPS	X-ray photoelectron spectroscopy

1 Introduction

The world's growing population and further rising demand of high-standard technologies lead to increasing energy consumption largely complied by fossil energy resources.^[5] Over the last decades, burning fossil fuels caused a drastic rise in the quantity of carbon dioxide and other greenhouse gases in our atmosphere. Hence, society is facing climate change which needs to be decelerated by developing new strategies to bring down the emission of greenhouse gases. In near future, the dependence on fossil fuels needs to be resolved rapidly to achieve the targets set by Paris Agreement to hold the elevation in global temperatures well below 2 °C. Therefore, replacements especially for coal and oil need to be targeted to create sustainable energy supply.^[5]

Commonly used combustibles such as gasoline or diesel show high volumetric energy densities in comparison to alternative energy carriers such as methanol, hydrogen or lithium-ion batteries as an energy storage media (Figure 1). But if the mentioned combustibles are compared based on their gravimetric energy density, a different picture emerges that ranks hydrogen based techniques first with values of 33.3 kWh kg⁻¹ followed by much lower gravimetric energy densities for gasoline and diesel fuels with 11 kWh kg⁻¹.^[6]

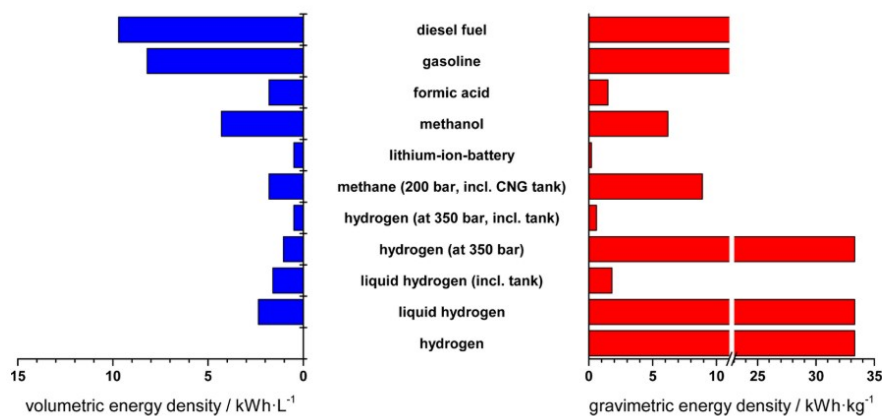


Figure 1: Combustibles and their volumetric (left) and gravimetric (right) energy densities in comparison.^[6]

The high gravimetric energy density is just one of the advantages why hydrogen is designated as promising energy carrier for the future. Furthermore, hydrogen used in fuel cells is desirable as its only by-product is water. However, hydrogen must be generated from alternative energy sources to assure a sustainable pathway for cleaner combustibles, to replace

the existing technologies such as steam reforming, partial oxidation, and autothermal reforming.^[6]

Besides the efforts to replace fossil fuels, an essential goal is to decrease energy consumption in general. Especially in industry a high energy demand is registered. That is why catalysis plays a key role in reducing energy costs and consumption of resources to produce chemicals and combustibles. More than 90% of all chemical processes are performed in presence of catalysts.^[7] By enhancement of the reactivity and selectivity of catalysts the energy input is diminished, and multiple reaction steps and competing side reactions could be avoided. The design of more efficient catalytic processes has a major impact on global greenhouse gas (GHG) emission and energy consumption considering that the synthesis of the 18 most important chemicals, including olefins, ammonia, BXT aromatics (benzene, xylene, toluene) and methanol among others, account for 75% of global GHG emission as well as 80% of the energy need in the chemical industry.^[7] Nowadays catalysis in industry is mainly based on heterogeneous catalysis and only in a few cases homogeneous catalysis is applied. This is attributed to better recyclability of solid catalysts making the industrial process more economic in contrast to their molecular equivalents.^[8] Nevertheless, homogeneous catalysis often benefits from well-understood structure-activity relationships which leads to higher controllability of reactions. A new concept to design catalysts with higher activity as well as selectivity, is to bridge the gap between homogeneous and heterogeneous catalysts to profit from both advantages, which could be achieved by heterogenization of homogeneous catalysts.^[9,10]

This work focuses on the development of solid catalysts for heterogeneous catalysis by incorporation of common organic ligands into porous structures, so-called macroligands,^[2] to immobilize molecular catalysts. Microporous polymer networks are applied functioning as support for well-defined catalysts to combine the economic advantage of good reusability and better controllability. Especially, catalytic transformation of greenhouse gases into harmless chemicals are targeted ranging from photocatalytic carbon dioxide reduction to reducing nitrous oxide by hydrosilylation. Furthermore, a new approach to design solid hydrogen carriers is introduced by applying carbazole-based polymers, which can be hydrogenated to store hydrogen chemically.

2 Theory

2.1 Microporosity

To understand porosity, often a sponge is taken as exemplary object to explain how surface area plays a key role in soaking up high amounts of liquid. Comparable to the interconnected channels and pores of sponges, microporous materials possess similar structures but on much smaller scale. In 1985, porous materials were classified regarding their pore size into macroporous (> 50 nm), mesoporous (2-50 nm) and microporous (< 2 nm) solids by the International Union of Pure and Applied Chemistry (IUPAC).^[11] The size of micropores range on molecular scale, which means that molecular interactions between pore walls and gas molecules need to be considered.^[12] The adsorption on the porous surface depends on intermolecular forces such as polarity of the interacting pore walls and guest species.^[11,13] Its strength is determined by the isosteric heat of adsorption (Q_{st}), which is often calculated in kJ mol^{-1} and describes how much energy is set free during the adsorption process regarding one adsorbed molecule.^[14] The Q_{st} is determined based on the Clausius–Clapeyron equation employing gas adsorption isotherms measured at different temperatures.^[15] The Clausius–Clapeyron equation provides a correlation between the pressure and temperature during the gas uptake. The slope of the plot of $\ln p$ vs. $1/T$ gives access to the isosteric heat of adsorption:^[16]

$$(\ln p)_V = -\frac{Q_{st}}{R} \frac{1}{T} + D \quad (1)$$

where R presents the ideal gas constant and D a further constant.

In general, decreasing pore size yields enlarging surface area, which is valid up to the point that pores get too small to be infiltrated by guest molecules. The higher the accessible internal surface area is, the more guest molecules can be absorbed on the pore walls (Figure 2).

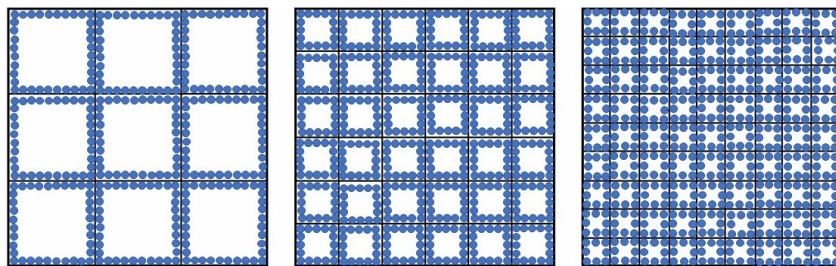


Figure 2: 2D lattice (black line) represented in a schematic way to show how various sized pores are occupied with a monolayer of guest molecules (blue).

Introducing porosity is one way to gain functionality from a material. By maximizing the surface area, the accessibility is enhanced and therefore porous solids are potential candidates for applications in which interactions on solid surfaces are crucial such as catalysis, sorption, separation and purification, gas storage and sensors.^[17]

Macro- and mesoporous materials are synthesized by templating of solids, micelles from surfactants or amphiphilic block copolymers.^[17,18] After the desired solid is formed, the structure-given templates are removed to yield the porous material, for example ordered mesoporous silica (OMS).^[17,19] The preparation of microporous materials is highly diverse and ranges from hydrothermal synthesis to form zeolites over carbonization methods or activated carbons.^[20,21] Besides, microporous polymers are most commonly synthesized from bottom-up synthesis methods meaning that stiff building blocks are connected piece by piece to construct molecular scaffolds.^[22] The structure-directing knots or tectons exhibiting two- or three-dimensional geometry so that the architecture of the networks can in principle be fine-tuned depending on the applied monomers.^[17,23]

2.1.1 Determination of Surface Area

Physisorption measurements, i.e. low-temperature gas adsorptions, are used in order to determine the pore size and surface area. The host material and adsorbate should not be affected by adhesive interactions and the pore volume needs to be entirely emptied before physisorption takes place, which is achieved by the sample activation at reduced pressure and elevated temperatures. Once the material is activated, a suitable probe gas is applied to infiltrate the pores. The amount of absorbed gas is monitored as a function of pressure changes in the measuring cell, the relative pressure p/p_0 . By means of the empirical method, differently shaped adsorption curves are detected, which are contingent on size and geometry of the pores. If the total volume of the measuring cell is saturated by the probe gas, the gradual decrease of pressure gives the desorption isotherm. In case adsorption and desorption curves do not concur, a so-called hysteresis is observed.^[11,13]

The obtained adsorption-desorption isotherms were classified into six types and their corresponding hysteresis types by IUPAC (Figure 3).^[11] The reversible type I isotherm typically occurring for microporous solids shows a pronounced increase at low pressures ($< 0.1 p/p_0$) and merges into a near-flat plateau over the given pressure range. Due to the relatively small external surfaces of microporous materials, the uptake of gas is limited to accessible pore volume rather than by the internal surface.^[11] Meaning that after a monolayer of adsorbate is generated, no multilayer formation can take place due to the restricted micropore volume.

Type II isotherms are characteristic for non-porous or macroporous adsorbents. The referred point 'B' marks the initiation of an almost linear curve section at which the formation of a monolayer is accomplished, and multilayers of adsorbed gas start growing.

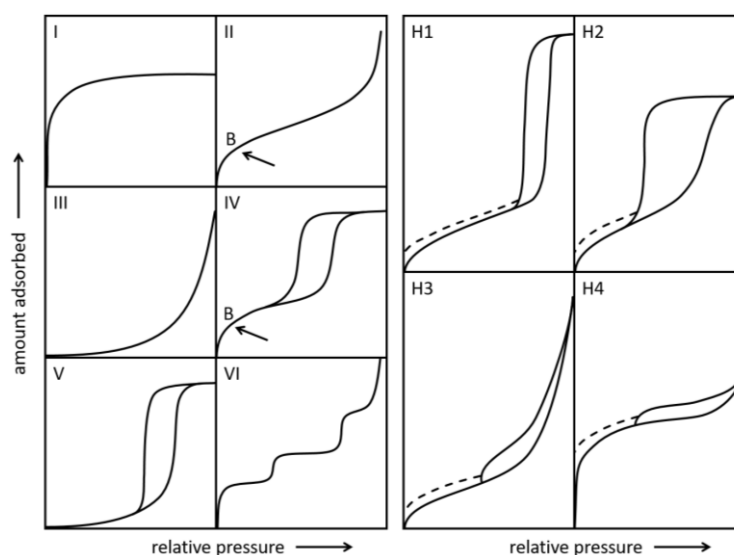


Figure 3: Classes of isotherm and hysteresis types determined by IUPAC.^[11,13]

Type III isotherms, which are convex to the x-axis are less common and the absence of point 'B' indicates that monolayer formation is excluded, but the clusters of guest species occur due to weak adsorbent-adsorbate interactions. Mesoporous materials are typically represented by type IV isotherms, which distinguish from reversible isotherms due to their hysteresis loop. The occurrence of a hysteresis is based on capillary condensation of probe gas in the mesopores. As describe for type II isotherms, point 'B' determines the stage on which monolayer coverage is completed and multilayer formation is initiated. At high relative pressures the uptake of gas is limited and consequently a plateau in the curve shape is observed. Similar to type III, type V isotherms show a flat increase at low relative pressures that could be attributed to comparatively weak adsorbent-adsorbate interactions. Moreover, this type is irreversible and shows a hysteresis loop. For reversible isotherm type VI, several steps in the curve shape are notable, which suggests the unrestricted growth of layer by layer. Each step presents the generation of a new monolayer. This phenomenon occurs on uniform non-porous surfaces.^[11,13]

Besides different classes of isotherms, four hysteresis types were identified by IUPAC.^[11] The hysteresis loops are located in the multilayer range of physisorption isotherms, which are linked to capillary condensation. Hysteresis types H1 and H4 (Figure 3, right panel) outline two extreme cases whereas type H2 and H3 feature the intermediate between H1 and H4. The nearly vertical desorption branch of H1 is provoked by desorption at a defined value of p/p_0 , that can be ascribed to materials possessing a narrow pore size distribution. In contrast, type H2 is associated to samples with less uniform pore geometries and sizes, hence a more

complex pore architecture. A H3-like hysteresis is characteristic for non-rigid aggregates and plate-shaped particles. The adsorption branch of type H4 combines type I and II isotherms and thus a high uptake at low relative pressures, which is attributed to micropores. Hysteresis type H4 is often affiliated with narrow slit-shaped pores. Especially for materials containing micropores, low pressure hysteresis (marked as dashed lines in Figure 3) occur due to the ‘soft’, non-rigid structures which are swelling during the uptake of probe gas. If swelling of pores impedes the closure of desorption and adsorption branch, the physisorption of gas is irreversible and may only be removed at elevated temperatures.^[11,13]

The results obtained by physisorption measurements are evaluated *via* a method developed by Brunauer, Emmett and Teller (BET method) to calculate the specific surface area of a given material.^[24] The BET method is an extended concept of Langmuir’s adsorption theory, in whose model it is assumed that only a monolayer of gas molecules is absorbed on a homogeneous, perfectly flat and energetically equivalent surface.^[25] Further assumptions were added by BET theory, most important the extension to multilayer formation making the validation of the method more realistic. Additionally, it is supposed that the probe gas is adsorbed as infinite layers on the material surface, there are no specific interactions between layers and each layer is treated as a monolayer suggested by Langmuir’s theory, like the ‘ideal localized monolayer’.^[24,26] Considering the previous assumptions, it results in the equation

$$\frac{p}{n^a(p_0 - p)} = \frac{C - 1}{n_m^a C} \cdot \frac{p}{p_0} + \frac{1}{n_m^a C} \quad (2)$$

$$y = S \cdot x + I$$

where n^a describes the molecular amount of adsorbed gas and n_m^a the molecular amount of adsorbate forming the first monolayer, p is the pressure and p_0 stands for the saturation pressure. The linear formulation of the equation is presented below the BET equation in which S gives the slope and I the y-intercept.

The BET constant C is defined as follows

$$C = \exp\left(\frac{E_1 - E_L}{RT}\right) \quad (3)$$

in which E_1 and E_L represent the enthalpy of adsorption for a single layer and second or higher adsorbed layers, respectively. BET constant C is exponentially growing with the energy of monolayer adsorption meaning strong adsorbent-adsorbate interactions are taking place if parameter C reaches high values. C and the monolayer capacity n_m^a can be calculated by means of the linear BET equation using following equation:

$$C = 1 + \left(\frac{S}{I}\right) \quad \text{and} \quad n_m^a = \frac{1}{S + I} \quad (4)$$

The total surface area SA_{total} is determined by n_m^a , which gives the value of how much moles of gas are adsorbed on a completely covered surface, the Avogadro's constant N_A and the area occupied by one adsorbate molecule a_m . To compare materials, total surface area SA_{total} is divided by factor of weight m to give the specific surface area SA in units of $m^2 g^{-1}$ according to the following equations

$$SA_{total} = n_m^a \cdot N_A \cdot a_m \quad \text{and} \quad SA = \frac{SA_{total}}{m} \quad (5)$$

The linearity of the BET graph is just given in case specific points of the isotherm are chosen. In most instances relative pressures p/p_0 ranging from 0.05 to 0.30 result in a linear graph which is valid for isotherm type II and IV.^[11,13] In the presence of micropores further criteria need to be taken into consideration to achieve a consistent evaluation. Rouquerol *et al.* suggest that the selected pressure range should continuously increase with $n^a(p_0 - p)$ as a function of p/p_0 as well as a positive value for the y-intercept meaning a parameter C becomes greater than zero.^[27]

2.1.2 Pore Size Distribution

Besides the surface area, the pore size distribution is an important parameter to classify the porous material. For the analysis of mesopores, the pore radius is determined by Kelvin equation, providing a correlation between pore size and pore condensation pressure.^[12] The BJH method, named by E. Barret, L. Joyner and P. Halenda, is a classic macroscopic model based on the Kelvin equation, applying computational procedure to calculate the pore size distribution from nitrogen isotherms for mesoporous materials.^[28] However, it appeared that the BJH method deriving from a model based on cylindrical pores is inaccurate for narrow mesopores or micropores, as pore diameters <10 nm are underestimated by the BJH method.^[13,29] Especially for micropores further adsorbate-adsorbate interactions have to be considered, to obtain a more precise description of the adsorbed phase in the narrow pores. The density functional theory (DFT) presents a more reliable microscopic method to determine the pore size distribution by offering a more realistic description of the pore shapes and behavior of fluids on the surface of the confined pores.^[13]

2.1.3 Microporous Materials

A significant representative of inorganic microporous materials are the naturally occurring zeolites, which are crystalline compounds consisting of aluminosilicate as primarily investigated by Cronstedt in 1756.^[30] The first synthetic zeolites were produced by Barrer *et*

al.^[31] in 1946 and his pioneering work was continued by Milton and Breck.^[32] In principle zeolites are built up from tetrahedral silicon oxide and aluminum oxide building blocks that are connected by the oxygens of each tetrahedra. The intrinsic skeleton charges originating from negatively charged aluminate building units are balanced by cations sitting within the porous structure. This characteristic leads to easily exchangeable cations and made the minerals popular as ion exchangers in waste water purification and for catalysis.^[33,34]

In the early 20th century, activated carbon was one of the first well-explored microporous materials. Its permanent porosity is introduced by carbonization of purely organic material in combination with metal halides. At elevated temperatures the mixture partially oxidized in presence of carbon dioxide or steam to produce activated carbon. In the early 70s, the American Oil Company developed activated carbons possessing BET surface areas with values higher than 3000 m² g⁻¹ produced from aromatic precursors under activation with potassium hydroxide.^[20] Activated carbons are mostly applicable in industrial processes for removing impurities from gases and liquids and for domestic usages in water purification. Nowadays, these amorphous materials are produced in such a controlled fashion that activated carbons are used in more complex applications, for instance electrocatalysis, energy storage in supercapacitors, lithium ion batteries and hydrogen storage.^[35]

In 1974, ‘macronet isoporous gels’ copolymerized from cross-linked polystyrene chains and divinylbenzene were introduced by Davankov and coworkers (Figure 4).^[36] The surface area of the polymer derives from a high degree of cross-linkage and allows the uptake of gasses and solvents due to its swelling behavior. The following emerging class of materials was therefore called hyper-crosslinked polymers (HCPs).

The class of ‘scaffold-like materials’ was introduced by Hoskins and Robson in 1990.^[37] The coordination of tetrakis(4-cyanophenyl)methane by copper(I) salts yielded in a crystalline hybrid material consisting of organic linkers and inorganic nodes. Later, this new type of materials were designated as porous coordination polymers (PCPs), and were further investigated by other groups.^[38–40] In 1995, Yaghi *et al.* established the subclass of metal-organic frameworks (MOFs),^[41,42] which are formed by metal ions or clusters, the so-called ‘secondary building unit’ (SBU) with multifunctional organic molecules, yielding porous and crystalline materials. Their crystallinity originate from reversible bond formations by thermodynamic control of the reaction to create long-range ordered structures and uniform pore size distributions.^[43] One of the most noted representative of this class is MOF-5^[44] (Figure 4) consisting of Zn₄O clusters linked over six chelating 1,4-benzenedicarboxylates (BDC) to give a cubic framework with a calculated SA_{BET} of 2320 m² g⁻¹.^[45] The fact that this way of

constructing scaffolds gives the opportunity to introduce multiple functionalities by simply exchanging the organic linker or metal salt, gained tremendous attention in the field of porous materials. Due to their great chemical variety, MOFs have been applied in the field of catalysis, gas storage, separation and drug delivery.^[46–48]

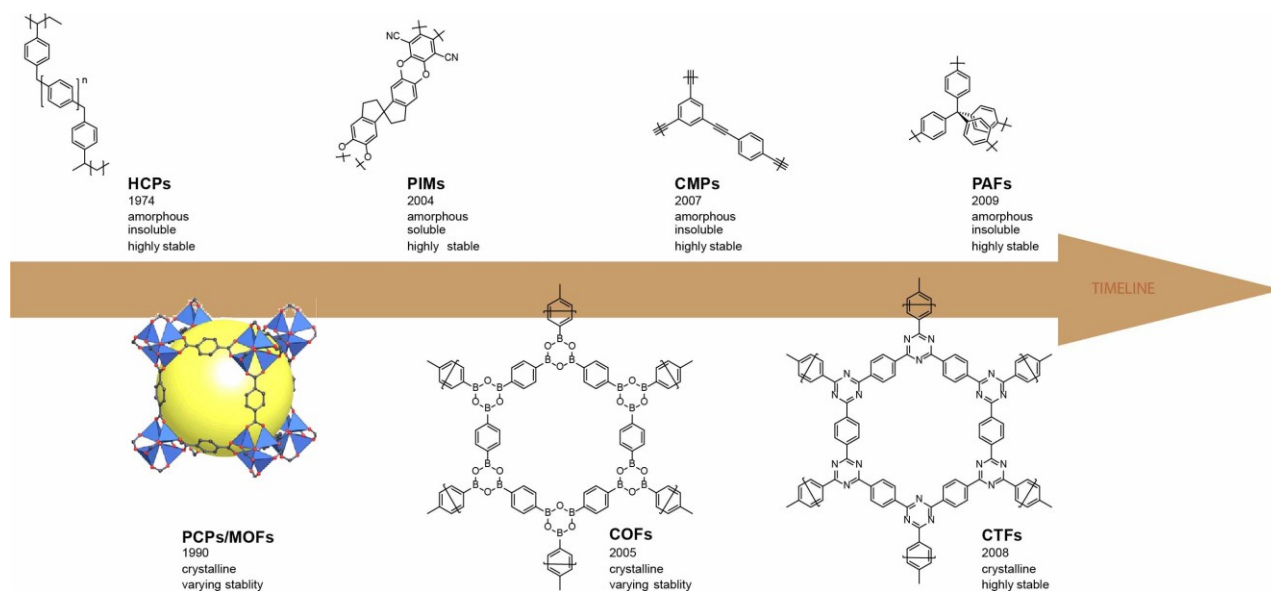


Figure 4: Timeline of important classes of microporous materials. The ‘macronet isoporous gel’ by Davankov, MOF-5, PIM-1, COF-1, CMP-1, CTF-1 and PAF-1 are depicted. ^[36,43,44,49–52]

Nonetheless, the choice of organic linker is limited to functional groups, which do not interfere with the coordination reaction to form the SBU, thus incompatible functionalities need to be introduced post-synthetically. While many MOFs possess permanent porosity, it must be considered that structural modifications can also lead to a loss in stability and porosity since the networks collapse due to solvent evacuation sometimes.^[53]

In 2004, the class of polymer of intrinsic microporosities (PIMs) were presented by Budd and McKeown.^[52] In contrast to previously discussed materials, PIMs are one-dimensional polymers consisting of rigid ring spacers such as spirocyclic functionalities, which lead to kinks within the linear chains. The porosity of PIMs derives from inefficient space-filling packing of the highly contorted and non-crosslinked polymer chains. Due to their solubility, PIMs have, in contrast to other microporous materials, the advantage to be solution processable, for instance to form membranes that can be applied in gas separation.^[54,55] PIM-1,^[52] synthesized from spirobisindane-based monomer attached to two catechol functionalities and fluorinated dicyanobenzene *via* a dibenzodioxane formation, represents the first of its kind (Figure 4). The calculated SA_{BET} of PIM-1 was found to be as high as $850 \text{ m}^2 \text{ g}^{-1}$.

Since the MOFs as inorganic-organic hybrids gained such great attention, it was not unforeseen that 10 years later purely organic and crystalline equivalents were designed. In 2005, Yaghi *et al.* published the discovery of covalent organic frameworks (COFs) in which the

inorganic nodes were replaced by organic molecules, thus the materials contain only light elements such as H, B, C, N and O.^[49] Dependent on the geometry of the organic nodes either 2D or 3D porous scaffolds are formed. The bond formation for COFs is based on the same concept as MOFs, by applying reaction condition allowing the reversible bond formation, it results in a highly crystalline material. Significant representatives are COF-1 (Figure 4) and COF-5 which are formed from self-condensation of 1,4-phenylenediboronic acid *via* cyclotrimerization and co-condensation reaction of diboronic acid and hexahydroxy triphenylene, respectively.^[49] Beside boron-oxide bonds that are sensitive towards hydrolysis and therefore rather unstable, more stable COFs based on imine (COF-300)^[56] and hydrazone linkages (COF-42, COF-43)^[57] were developed. Even though the first designed COFs were known to be comparably labile in acidic, basic or aqueous solutions, nowadays highly stable COFs have been designed,^[58] the same applies to MOFs.^[59] In addition, the subclass of covalent triazine-based frameworks (CTFs) was established by Thomas and coworkers in 2008 by applying ionothermal synthesis using molting salts.^[43] For example, CTF-1^[43] was synthesized by trimerization of 1,4-dicyanobenzene in presence of molten zinc chloride at 400 °C (Figure 4). CTFs are not only known for their chemical robustness, but also because of high nitrogen content which is useful for applications in energy storage, photocatalysis, *etc.*^[60,61]

The introduction of microporous polymer networks (MPNs), which are organic, amorphous and 3D-crosslinked polymers with high surface areas, demonstrated that crystallinity is not a compulsive requirement to generate porosity.^[62] Due to irreversible reactions in the synthesis of amorphous frameworks the polymer skeletons possess, compared to crystalline networks, a statistical and unordered pore structure with broader pore size distributions.^[63] By applying stiff building block, the rigidity of the monomers ensures permanent porosity, which does not collapse upon solvent removal. Mostly the fixed geometry of the units is derived from aromatic monomers, which are directly coupled or linked by further inflexible groups such as alkenes or alkynes.^[22] The synthesis of networks is based on C-C bond formation, for instance cross-coupling reactions like Palladium-catalyzed Suzuki^[64] and Sonogashira-Hagihara^[65] or Nickel-mediated Yamamoto^[66] reaction. Typically, MPNs show type I isotherms and a hysteresis loop, which is not attributed to mesopores but to the swelling of the relatively 'soft' network during the uptake of gas.^[13] One of the first representatives of MPNs are conjugated microporous polymers (CMPs), which were first published by Cooper *et al.* in 2007.^[50] CMP-1 (Figure 4) was synthesized from 1,3,5-triethynylbenzene and halide substituted benzene *via* Sonogashira-Hagihara cross-coupling reaction. These π -conjugated systems with permanent porosity presented a new group of potential candidates for heterogeneous catalysis as well as energy storage.^[63] The development of CMPs was followed by the well-known porous aromatic framework

(PAFs) PAF-1^[51] in 2009, attracting great attention due to its high SA_{BET} of 5600 m² g⁻¹ (Figure 4). The material was homopolymerized from tetrakis(4-bromophenyl)methane *via* Yamamoto reaction at 80 °C. Further, nickel-mediated Yamamoto polymer reactions were first introduced by Schmidt and coworkers.^[66] Compared to metal-catalyzed cross-coupling reactions, a nickel(I) complex was applied in stoichiometric amounts leading to high degrees of cross-linkage and abstraction of non-converted end groups.^[67] In 2011, Lu *et al.* replaced the rather harsh reaction conditions for synthesis of PAF-1 by a milder synthesis to produce the structural analogue PPN-6^[68] applying atmospheric conditions. Under the optimized conditions a variety of more temperature-sensitive molecules could be applied in the polymer synthesis.

2.2 Bridging Homogeneous and Heterogeneous Catalysis

The key role of catalysis becomes clear by contemplating the process-related energy data: In Europe the energy consumption in chemical industry was decreased by 53.4% from 1990 to 2010 by achieving catalytic process advances.^[7] Nowadays, more than 90% of all synthetic products in industry are produced by means of catalysis. These energy saving processes are crucial for reducing carbon dioxide emissions to slow down the climate change and shift towards a sustainable circular energy economy. Accordingly, research is focusing on the development of efficient and recyclable catalysts. The optimization processes include improvement of catalyst performances regarding their activity, selectivity and costs.^[69] Homogeneous catalysis, especially using molecular metal-organic catalysts that are structurally defined on molecular level, benefits from well-understood structure-activity relationships. However, the highly accessible single-site catalysts suffer from difficult recyclability leading to expensive and complex purification steps and complicated separation from produced products.^[8,70] In contrast to that, heterogeneous catalysis is less restricted in recovering the solid phase catalysts and thus favorable concerning sustainability.^[70] Despite this advantage, it needs to be considered that for bulk materials it is challenging to specify and control the active centers and tailor the activity as desired.^[69,70] To bridge the gap between homogeneous and heterogeneous catalysis, combining the benefits of the structural understanding of molecular catalysts and advantageous properties of robust solid-state materials, heterogenization of molecular catalyst is targeted.^[8]

For the heterogenization of homogeneous molecular catalysts, the surface structure of the support needs to be precisely controlled and separation of catalytic metal sites should be maintained to achieve high activity and selectivity.^[71] High surface area supports are potential

candidates for such purposes and in many cases polymers or porous silicas are applied.^[8,9] In comparison to porous polymers, silicas possess limitations regarding their chemical modification since the surface is defined by oxygen-based coordination.^[72] To make sure that no further interactions between the surrounding support and the grafted molecular catalyst occur, an effective strategy is to eliminate the support itself and create a self-supported molecular catalyst.^[2] This is realizable by designing a ‘macroligand’^[2], which is built exclusively from repeating units consisting of the desired ligand that coordinates the selected molecular catalyst. Especially, porous polymers are tunable in their composition and various functionalities can be introduced functioning as ligands. Microporous polymer networks (MPNs) present such defined host matrixes, which are ideal candidates to function as porous macroligands to coordinate catalysts.^[2] Achieving defined coordination sites within the structure lead to homogeneous distribution of immobilized catalysts and hence single-site catalysis.^[8,9] By the encapsulation of the active centers in the scaffold, stability of the catalyst could be improved and therefore reusability can be accomplished.

Nevertheless, there are still limiting factors for the anchored catalysts being applied in industry. For instance, the fact that synthesis of immobilized catalysts requires multiple step reactions, which makes the final catalyst more expensive, whereby slightly higher production rates and reusability are relativized.^[73] If, however the support effects the catalysis properties itself, the benefits of immobilized catalysts could outweigh their production costs, for instance: (i) by applying light-harvesting polymer networks for photocatalysis, (ii) employing supports effecting an increased stability, for instance due to their highly hydrophobic character shielding the sensitive active species, or (iii) by using the electron-donating or -withdrawing properties of the polymeric backbone leading to a stabilization of the heterogenized catalyst.^[2,3,10]

Furthermore, the declination in activity of heterogenized catalysts in comparison to their homogeneous analogues, which are caused by hindered accessibility of active sites, is still a problem in some cases, which has to be solved.^[9,71] Engineering pore transportation helps to enhance transportation kinetics, for example introduction of hierarchical pore systems.^[9]

The field of immobilized metal-organic complexes on porous polymer networks received great attention due to its high potential for designing more efficient heterogeneous catalysts.^[9,10] Consequently, this research field is growing rapidly and although it faces the challenges to outperform homogeneous catalysts and find its way into industrial catalysis.

3 Scope of the Thesis

Microporous polymer networks (MPNs) are an emerging class of functional materials, which have the great potential of being applied in new technologies to create a more sustainable and energy-saving environment. Due to their purely organic composition, large surface areas and robustness, MPNs are used in a broad range of applications including gas storage, heterogeneous catalysis and energy storage devices.^[23] The incorporation of specific functional groups can help to tailor the pores, the polarity as well as the optical and electronic properties of the network. The aim of the thesis is to demonstrate the applicability of carbazole- and phosphine-containing MPNs in catalysis and gas storage.

The first part presents microporous carbazole-based polymer networks synthesized *via* oxidative polymerization. Synthetic methods for homo- as well as copolymerizations will be demonstrated. By introducing bipyridine moieties heterogeneous immobilization of various photocatalysts was realized. Besides, MPNs incorporating *N*-ethylcarbazole were applied in physical and chemical storage of hydrogen.

In the second part, the focus lies on designing phosphine-based MPNs and a strategy to protect the oxygen sensitive phosphines. As this functionality is widely applied as ligand in diverse catalysts, the feasibility of introducing metal-complexes into the porous materials was employed to produce heterogeneous hydrosilylation and hydroformylation catalysts.

The third part outlines the manufacturing of carbazole-based polymer films *via* electropolymerization. The deposition of thin films opened up the applicability of phosphine- and bipyridine-containing films for electrode materials for electrocatalysis and photoelectrocatalytic water splitting.

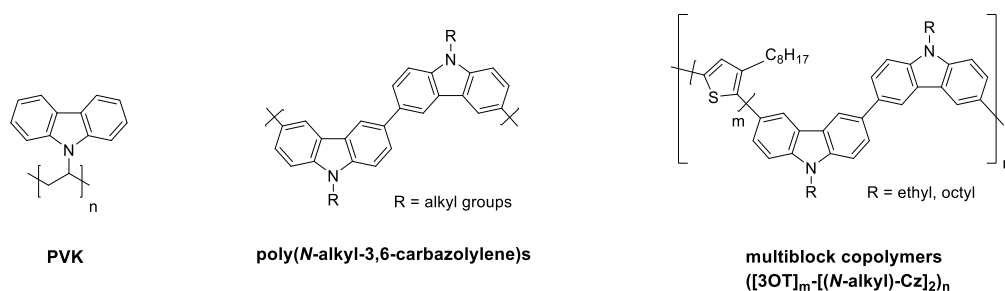
In summary, the thesis gives an overview about synthesis and application of various amorphous microporous polymer systems, especially carbazole- and phosphine-containing MPNs. Each chapter begins with a short introduction into the most important theoretical background, followed by a detailed discussion about the synthesis methods, suitable applications followed by a conclusion including an outlook for the respective topic.

4 Microporous Carbazole-based Polymer Networks

4.1 Theoretical Background

4.1.1 Carbazole-containing Polymers

Since 1965, carbazole-based polymers gained great interest, when Hoegl *et al.* discovered the photoconductivity in poly(*N*-vinylcarbazole) (PVK) synthesized from *N*-vinylcarbazole *via* radical or cationic polymerization.^[74] Apart from PVK consisting of a linear polyethylene chain equipped with pendant carbazole units, polymers with carbazole-containing backbones were developed (Scheme 1). The first π -conjugated poly(*N*-alkyl-3,6-carbazolylene)s were synthesized from bromo- or iodo-equipped carbazole derivatives *via* nickel-mediated Yamamoto reaction or palladium catalyzed cross-coupling reaction.^[75–78] Due to their conjugated π -electron systems, carbazole-containing polymers became promising candidates for optoelectronic applications such as organic photoconductors and polymeric light emitting diodes.^[76] Besides exhibiting high charge carrier mobility, carbazole gained popularity as a cheap and abundant starting material for MPNs with high thermal and photochemical stability. Moreover, carbazole units are easily substituted at the nitrogen position upon which various carbazole derivatives were obtained to tailor the properties of carbazole-based materials.^[79]

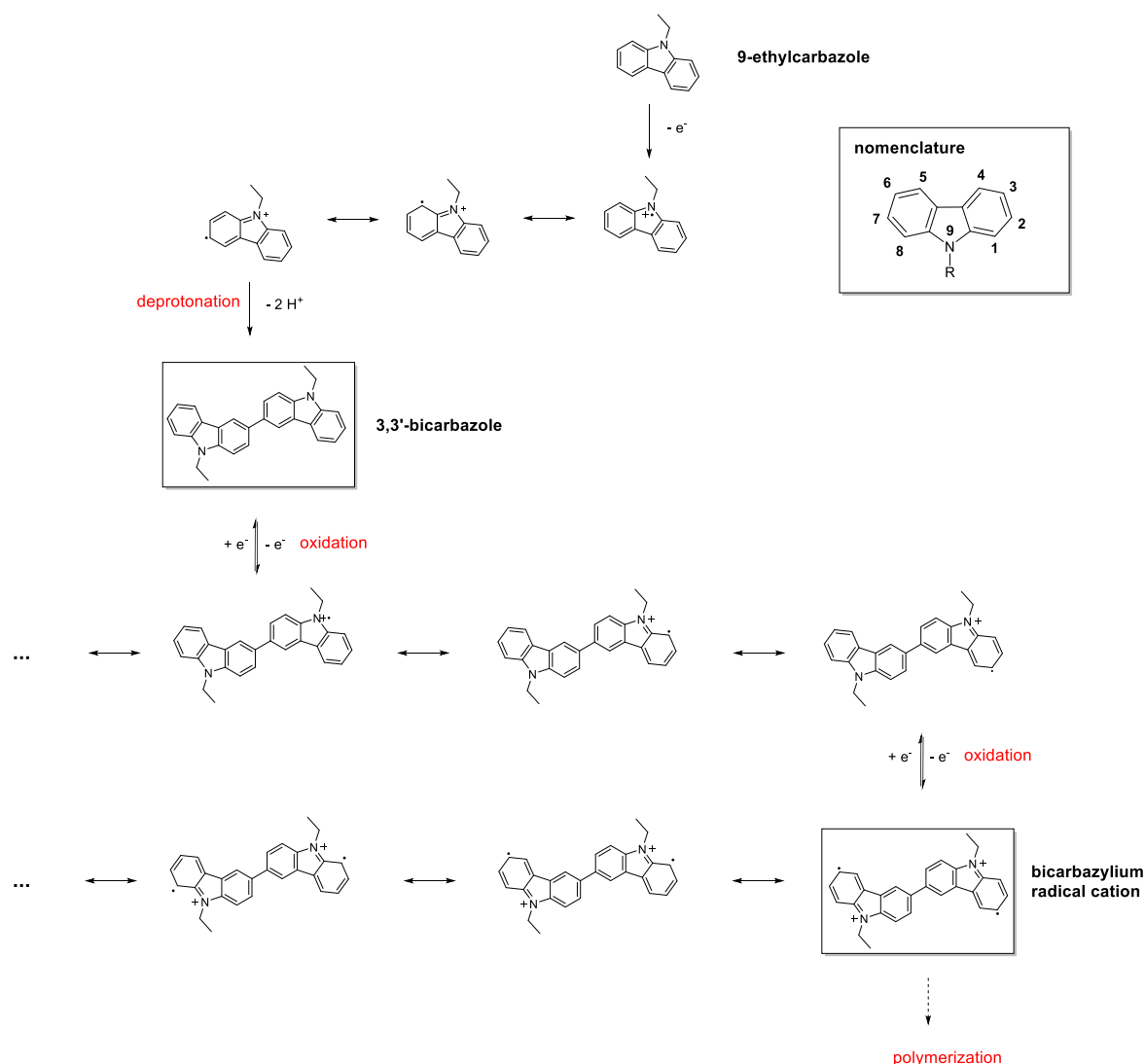


Scheme 1: Structure of poly(*N*-vinylcarbazole), poly(*N*-alkyl-3,6-carbazolylene)s and multiblock copolymers of bis-(*N*-alkyl carbazolylene) and 3-octylthiophene.^[76]

By applying iron(III) chloride as an oxidative agent to polymerize *N*-substituted carbazoles, dimers instead of polymer chains were formed.^[79] Siove and coworkers achieved the generation of polymer chains by addition of 3-octylthiophene as a second monomer to produce multiblock copolymers of bis-(*N*-alkyl carbazolylene) and 3-octylthiophene (Scheme 1) *via* oxidative polymerization with iron(III) chloride in chloroform.^[80] The soluble copolymer

was purified from remaining carbazole dimers and homopolymerized thiophene chains were subsequently characterized by nuclear magnetic resonance (NMR) spectroscopy to prove the successful incorporation of bicarbazyl blocks.

The mechanism of 3,3'-coupling of *N*-alkyl substituted carbazoles has been extensively discussed over the past decades.^[79,81,82] Under oxidative conditions highly reactive radicals are formed which predominantly couple to give 3,3'-bicarbazoles after deprotonation (Scheme 2). Since the dimer cation radical is more stable due to delocalization of the unpaired electron over two carbazole units than the monomer cation, it is likely that under most reaction conditions the follow-up coupling of 3,3'-bicarbazoles does not take place and only dimers are produced.^[79]



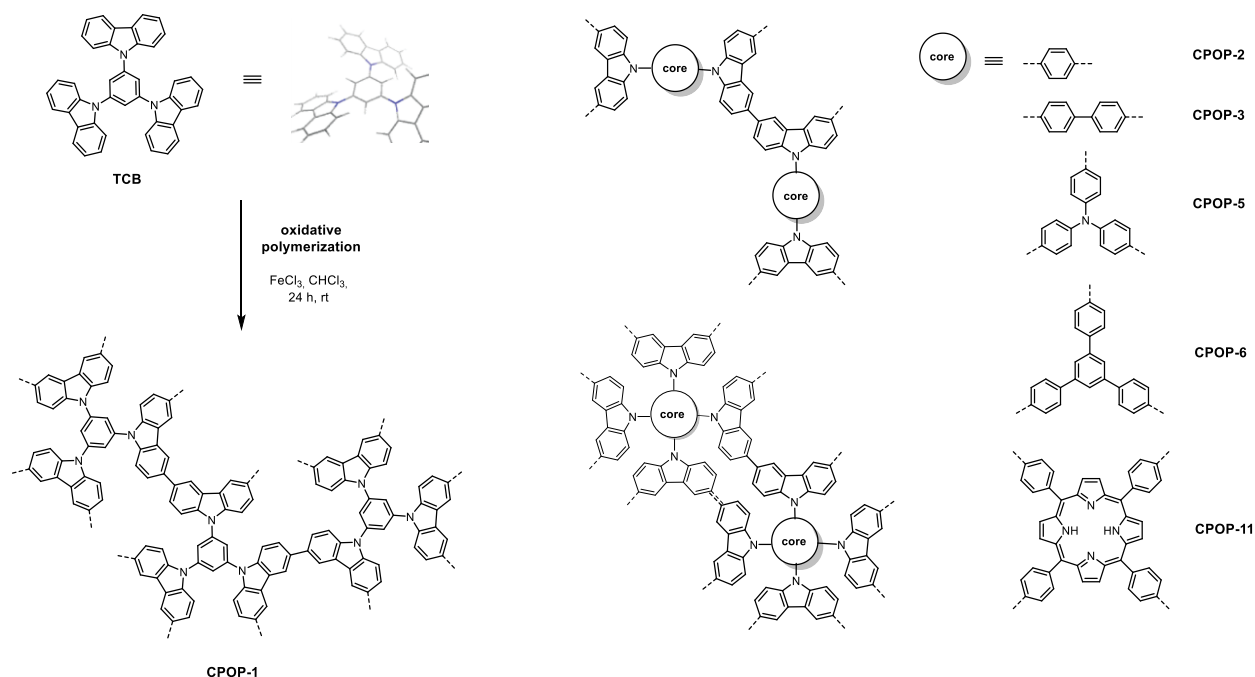
Scheme 2: Mechanism for the formation of dimers and bicarbazylum radical cations.

Nevertheless, Siove *et al.* showed that stable *N*-alkyl substituted 3,3'-bicarbazolylum diradicals were incorporated into copolymers by addition of more reactive comonomer species such as thiophenes to form polymers with bicarbazolyl units.^[80]

4.1.2 Porous Carbazole-containing Polymer Networks

In 2012, Han's group presented the so-called CPOP-1^[1] (Scheme 3), which was the first of its class and stands for carbazole-based porous organic polymers (CPOPs) synthesized *via* oxidative polymerization. The oxidative coupling of 1,3,5-tri(*N*-carbazolyl)benzene (TCB) was mediated by anhydrous iron(III) chloride at room temperature to give a highly microporous polymer network possessing a BET surface area of 2200 m² g⁻¹. The synthesis method is beneficial due to the cheap oxidative reagent, ambient reaction conditions and high yields. CPOP-1 attracted attention on account of its high surface area and gas uptake capacities. At 1 bar, 2.8 wt% of hydrogen (77 K) and 21.2 wt% of carbon dioxide (273 K) were physisorbed within the microporous structure.^[1]

Over the years, many different CPOPs were synthesized *via* oxidative polymerization from various carbazole-based monomers containing different functionalities (Scheme 3). By changing the monomer core, the networks were functionalized with triphenylamine, porphyrins or metal complexes such as tris(phenylpyridine)iridium(III).^[83–86] The materials were tested for a broad range of applications, for instance in (photo)catalysis, gas storage or as electrochemical capacitor.^[3,85–88]



Scheme 3: Overview of carbazole-based porous organic polymer networks (CPOPs) polymerized *via* oxidative polymerization with iron(III) chloride.^[1,83,84]

To tailor the polymer structures for a certain application, different functional groups are required. For that purpose, Luo *et al.*^[89] studied copolymerizations of electron donor-acceptor carbazole-based porous organic frameworks (POFs) by oxidative polymerization to tailor the band gaps for visible-light photocatalysis. In addition to oxidative polymerizations, Liao *et al.*

synthesized porous carbazole-based copolymers *via* Yamamoto reaction from 3,6-dibromo-9-(4-bromophenyl)carbazole and different basic comonomers.^[90] These copolymer networks showed high carbon dioxide and hydrogen uptakes as well as isosteric heat of hydrogen adsorption up to 10.3 kJ mol⁻¹.

4.1.3 Photocatalytic Carbon Dioxide Reduction

With rising levels of carbon dioxide in the atmosphere, humankind is challenged to reduce the emission of the greenhouse gases, which rapidly elevated since the start of the industrial revolution during the 18th century. Instead of burning fossil fuels, greener alternatives in the form of renewables, such as sunlight and wind energy are targeted. Mimicking natural photocatalysis systems producing bioenergy and carbohydrates from water and carbon dioxide by utilizing solar radiation is a major challenge of our time.^[91] Typically, products such as carbon monoxide, formate or methanol are formed during the photocatalytic reduction, depending on how efficiently multi-electron transfer processes are assisted by the photocatalyst.^[92]

Since 1983, rhenium(I) tricarbonyl complexes *fac*-[Re^I(N[^]N)(CO)₃L]ⁿ⁺ (N[^]N = e.g. bipyridine, L = monodentate ligand) have been utilized as photocatalysts due to their high selectivity and efficiency to reduce carbon dioxide to carbon monoxide.^[93,94] However, rhenium photocatalysts only absorb light in higher energy regions of visible-light.^[95] Therefore, photocatalytic systems were designed consisting of photocatalysts as well as photosensitizer in order to enhance the visible light absorption.^[94] Thus, light-harvesting complexes such as tris(bipyridine)ruthenium(II) complexes ([Ru(bipy)₃]²⁺) absorbing visible-light in a wide-range have been utilized to achieve photo-induced charge separation by elevating electrons to an excited state. Due to the long lifetime of the excited state, electrons can be transferred to the photocatalyst before charge recombination occurs and consequently reduction of carbon dioxide by rhenium(I) catalysts take place.^[93,96] Since the molecular catalyst is oxidized during this process, the excited state needs to be reductively quenched by an electron donor. Use of water as a reductant is targeted but electron capture from water is mostly insufficient, hence sacrificial agents such as triethanolamine (TEOA) are applied.^[97,98] The advantage of homogeneous catalysts is that the structure-activity relationship is well-understood, nevertheless homogeneous systems are vulnerable for photochemical decomposition and suffer from poor recyclability.^[99] One example for such homogeneous catalytic systems, are supramolecular catalysts, which combine photosensitizer and -catalyst by a covalent bond (Figure 5).^[95,100]

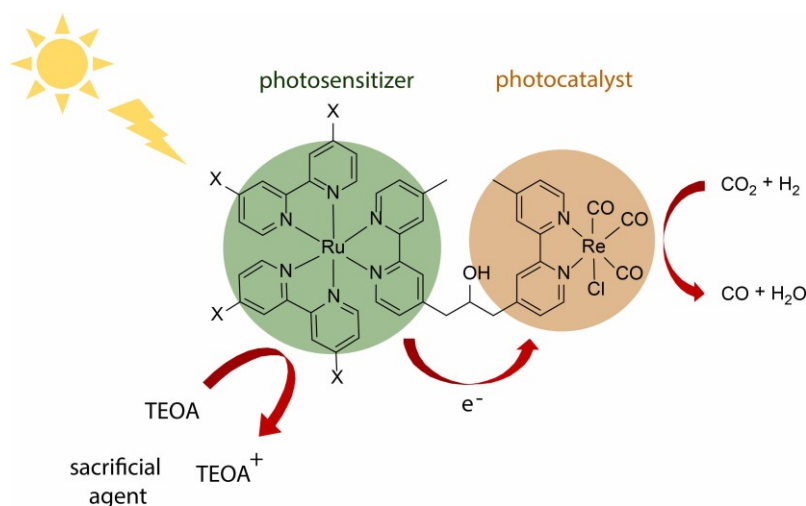


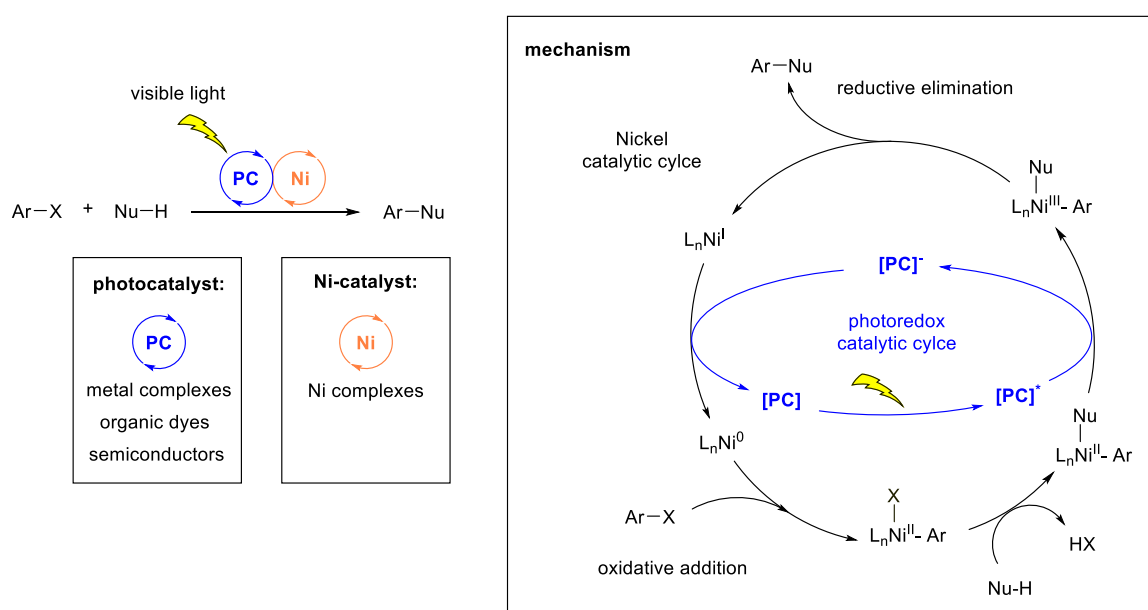
Figure 5: Supramolecular photocatalyst consisting of ruthenium-rhenium binuclear complexes^[100] for carbon dioxide reduction.

In case of heterogeneous photocatalysis, semiconductors are often used. By applying photons with equal or greater energy than the band gap (E_g) of the semiconductor, electrons are excited from the valence band into the conduction band. Consequently, photogenerated charge separation is achieved and the electrons and holes migrate to the surface of the catalyst, where the electrons react with carbon dioxide.^[92,101] However, this approach exhibits several drawbacks, for instance, mismatching of the available light spectrum with the band gap energy, unsuitable band gap positions leading to competing side reactions or poor charge carrier separation efficiencies.^[92]

In comparison to classic semiconductors, MPNs benefit from simple tuneability of their photophysical properties by introducing a broad variety of functionalities into the polymer network.^[102,103] The band gaps can be engineered by doping materials with co-monomers in different ratios or introducing diverse combinations of donor-acceptor systems.^[23,104,105] Besides, it was shown that materials with high accessible surface areas are promising candidates for combining the benefits of homo- and heterogeneous catalysis.^[8,9] Porous systems such as periodic mesoporous organosilicas^[106], MOFs^[107], COFs^[108] or CMPs^[109] were applied as supports for rhenium complexes, which were immobilized by coordination within the pores. In contrast to supramolecular catalysts, these materials have the advantage to possess isolated active centers grafted on the pore walls in a specific way. By anchoring the active species to a robust surface it is likely to improve photostability and recyclability of the photocatalytic system.^[110]

4.1.4 Dual Transition Metal/Photoredoxcatalysis

The usage of photocatalysis in combination with another catalytic reaction is called a dual catalytic process.^[111] Applying transition metal complexes, such as nickel, along with a photocatalyst opened up new synthetic paths for carbon-carbon and carbon-heteroatom bond formations as an alternative for palladium-catalyzed cross-coupling reactions.^[112] For this purpose, photoactive complexes, for instance Ru(II) or Ir(III) polypyridyl complexes, organic dyes or heterogeneous semiconductors are commonly used as photocatalysts.^[111,113] In dual nickel-/photoredoxcatalysis, also called metallaphotoredox catalysis, single electron transfer (SET) or energy transfer (EnT) play a crucial role between nickel and the photoredox catalyst. The proposed mechanism for the dual catalytic cycle is initiated by an oxidative addition of an aryl halide to the Ni(0) complex to form a Ni(II) species and a subsequent ligand exchange with an eligible nucleophile (Nu) (Scheme 4). At the same time, the photocatalyst (PC) gets excited upon irradiation with visible light leading to the oxidative intermediate (PC*), which accepts an electron of the Ni(II) complex to enable the reductive elimination of the product. In a final step, both catalytic cycles are closed and the Ni(0) complex and ground-state of the photocatalyst get regenerated *via* a SET event between Ni(I) and the photocatalyst (PC⁻).^[111]



Scheme 4: Mechanism of Nickel-catalyzed dual photoredox catalysis for cross-coupling reactions.^[111]

Besides homogenous dual catalytic reaction systems, bifunctional materials such as MOFs^[114,115] or organic polymers^[116] incorporating Ni(II) and Ir(III) polypyridyl complexes were also applied for heterogeneous catalysis. By embedding organic ligands into the polymeric backbone of MPNs, the possibility opens to immobilize photo- and Ni-catalysts into MPNs for applying the heterogenized systems in metallaphotoredox catalysis.

4.1.5 Hydrogen Storage

Besides catalysis, porous materials turned out to be suitable for gas storage, especially their ability in storing carbon dioxide and hydrogen has been intensely investigated over the last years.^[117–119] As hydrogen is designated as an alternative energy carrier, the motivation is to replace fossil fuels by a hydrogen-based technologies. However, one important challenge is to store hydrogen safely and economically to realize hydrogen on-board applications.^[120]

Several approaches have been developed to store hydrogen, one technique is physisorption on highly porous materials operating at 77 K and 0.1–0.5 MPa.^[121] The advantages of porous materials are the storage under moderate pressures as well as the rapid uptake and release of hydrogen due to weaker binding strength compared to chemically bonded hydrogen.^[120] Especially microporous polymer networks (MPNs) show high potential to be used in solid-state hydrogen storage due to their purely organic nature, thus light-weight character and their high accessible surface area.^[6,120,122] By means of pore sizes below 2 nm or even <1 nm, MPNs are capable of achieving high adsorption capacities.^[121,122] For instance, CPOP-1^[1] shows a hydrogen uptake of 2.8 wt% at 1 bar and 77 K.

In general, hydrogen storage technologies are divided into physical and chemical storage techniques. Physical storage of hydrogen is not based on covalent bonding but on physical adsorption of hydrogen molecules to a host material. Besides physisorption on porous materials, other technologies such as compressed gaseous hydrogen storage running at room temperature at 35–70 MPa as well as liquid hydrogen tanks, possessing an operating temperature at -253 °C and 0.1–1 MPa, are applied.^[121] Running storage facilities under the mentioned conditions leads to a high energy expenditure, which is uneconomic and causes safety issues.^[120,123]

The significant difference between physical and chemical storage is the deviating adsorption enthalpies, which are in such a low range for physisorption that low temperatures or rather high pressure are needed to store hydrogen.^[124] On average, physisorption on high-surface-area materials is characterized by adsorption enthalpies between 2 and 5 kJ per hydrogen molecule, which is in comparison to chemisorption, a relatively weak interaction between gas and host material.^[121,125] In the field of chemical hydrogen storage techniques, metal hydrides or liquid organic hydrogen carriers (LOHCs) have received considerable attention. Metal hydrides are, due to their high gravimetric storage capacity and ability to store hydrogen under ambient conditions, promising candidates for H₂ storage.^[126] Nevertheless, considering the limited gravimetric density (< 2 wt% H₂) of conventional intermetallic hydrides (e.g. LaNi₅H₆, TiFeH₂, ZrMn₂), the focus shifted towards light-weight metals, such as lithium,



In 2014, dibenzyltoluene (DBT) was introduced as an alternative LOHCs system to NECz.^[131] In this case, dibenzyltoluene is hydrogenated reversibly to perhydro-dibenzyltoluene (H18-DBT) and exhibits a hydrogen storage capacity of 6.2 wt%.^[6,131] In comparison to NECz, platinum instead of ruthenium is applied as dehydrogenation catalyst, and higher dehydrogenation temperatures, above 250 °C, are needed.^[6,131]

In summary, techniques for hydrogen storage need to fulfill the requirement of appropriate volumetric and gravimetric energy densities.^[6] Nevertheless, the suitability of an on-board hydrogen application does not only depend on the weight and volume of containers, but also on reversibility, kinetics and operating temperatures.^[120]

4.2 Objective

The class of carbazole-based porous polymers, so-called CPOPs^[1] emerged quickly over the last decade. Especially, due to their high porosity and chemical stability they attracted attention as potential materials for catalysis, gas storage or as electrochemical capacitor.^[3,85–88] The following chapter focusses on the synthesis of homopolymeric networks as well as different copolymers for various applications. One approach is the design of tailor-made materials for heterogeneous photocatalysis, for which light-harvesting porous polymers are supposed to function as macroligands for molecular catalysts. For this purpose, the synthesis of polymers bearing chelating groups to coordinate various metals was targeted to embed metal-organic catalysts within the porous structure. Ligands, such as bipyridine should be introduced into the carbazole-based network as bipyridines are known for efficient complexation of molecular complexes for carbon dioxide photoreduction, or nickel salts for photoredox sulfonylation upon visible-light irradiation.

A second study on the incorporation of *N*-ethylcarbazole (NECz) into a porous carbazole network is targeted, taking advantage of the affinity of NECz towards hydrogen. The statistical copolymers are synthesized with various comonomer proportions *via* well-established oxidative polymerization with iron(III) chloride. The distribution of monomers within the polymeric backbone must be studied to understand the chemical nature of the copolymer. The aim is to apply NECz-equipped materials for physical and chemical storage of hydrogen. To that end, hydrogen physisorption at 77 K as well as hydrogenation of the polymer network to create a solid-state hydrogen carrier, must be studied. Especially the chemical storage of hydrogen is targeted as the carbazole-based polymers are purely organic and would fulfill the requirement of good gravimetric energy densities. By decoration with low percentages of platinum nanoparticles, the hydrogenation process on the polymer backbone is theoretically feasible. The applicability of copolymers as solid-state hydrogen carriers will be compared to suitable homopolymers which contain high amounts of NECz moieties.

4.3 Results and Discussion

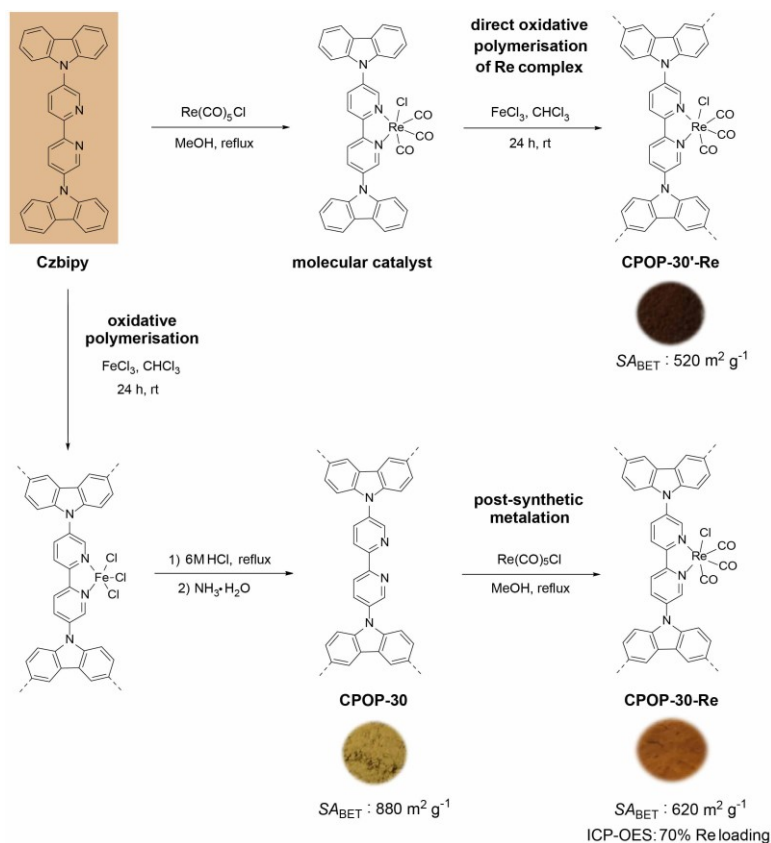
4.3.1 Carbazole-based Polymer Networks for Photocatalysis

When designing microporous polymer networks regarding their applicability in photocatalysis, an accessible high surface area, chemical robustness and tunable functionality are important. For this purpose, polymers bearing chelating groups to coordinate metal complexes were synthesized to embed photocatalysts within the porous structure. Carbazole-based materials containing bipyridine functionalities are applied as supports for the immobilization of a rhenium catalyst for photoinduced carbon dioxide reduction.^[3] For applying these materials as supports, it is of great importance to tailor the polymeric scaffold to obtain a suitable band position for the desired reaction, for instance carbon dioxide reduction. Besides, it is essential to isolate active centers within the pores to ensure single-site catalysis.^[8,109]

4.3.1.1 Synthesis and Characterization of Carbazole-based Polymer Networks

The following materials were synthesized in close collaboration with Haipeng Liang from National Center of Nanoscience and Technology in Beijing.^[3] My contribution in this project was mainly the polymer synthesis as well as characterization of the materials.

To embed a rhenium (I) catalyst into carbazole-base polymer networks, two approaches were applied (Scheme 6). First, the molecular catalyst $[\text{Re}(\text{Czbipy})(\text{CO})_3\text{Cl}]$, which was synthesized from 5,5'-di(9*H*-carbazol-9-yl)-2,2'-bipyridine (Czbipy) and pentacarbonylchlororhenium ($\text{Re}(\text{CO})_5\text{Cl}$), was oxidatively polymerized to form a homopolymer (**CPOP-30'-Re**). Second, homopolymerization of Czbipy was conducted and the resulting polymer was post-synthetically modified by metalating the purely organic structure with pentacarbonylchlororhenium (**CPOP-30-Re**).^[3] When applying the rhenium complex as monomer, a dark brown polymer with a BET surface area (S_{BET}) of $520 \text{ m}^2 \text{ g}^{-1}$ was obtained. In the second approach, a yellow carbazole-based homopolymer **CPOP-30** was synthesized with a resulting S_{BET} of $880 \text{ m}^2 \text{ g}^{-1}$ after removal of remaining iron residues. The further metalated **CPOP-30-Re** was obtained as a dark orange polymer which possess a S_{BET} of $620 \text{ m}^2 \text{ g}^{-1}$. By means of inductively coupled plasma-optical emission spectroscopy (ICP-OES) rhenium loading was determined to 17.3 wt% and 16.6 wt% for **CPOP-30'-Re** and **CPOP-30-Re**, respectively. This means that 73% and 70% of the available bipyridine units were coordinated by rhenium(I) for **CPOP-30'-Re** and **CPOP-30-Re**.



Scheme 6: Polymerization strategies to yield Re(I) immobilized photocatalysts CPOP-30-Re and CPOP-30-Re'.^[3]

In theory, both approaches are supposed to result in the same materials. To verify this, the elemental composition of the materials was examined by X-ray photoelectron spectroscopy (XPS) (Figure 6). The high-resolution Re 4f core-level spectrum of the molecular catalyst $[\text{Re}(\text{Czbipy})(\text{CO})_3\text{Cl}]$ shows two peaks at 43.6 and 41.2 eV, which were assigned to $4f_{5/2}$ and $4f_{7/2}$, respectively.^[132] The spectrum of **CPOP-30-Re** shows a coinciding doublet with signals at 43.7 and 41.3 eV, whereas Re 4f core-level spectrum of **CPOP-30'-Re** gives a broad distribution of peaks shifting towards higher binding energies indicating higher valence states of rhenium. Three species were detected at 45.1, 42.3 and 41.2 eV, which were ascribed to $4f_{7/2}$ peaks of rhenium(VII), rhenium(IV) and rhenium(I) species^[133,134], respectively, proving oxidation of rhenium(I) species during the oxidative polymerization. Based on these findings, **CPOP-30-Re** was preferred over **CPOP-30'-Re** for further studies due to the existence of pure rhenium(I) catalyst, which was chosen for its high activity for photocatalytic carbon dioxide reduction.^[94]

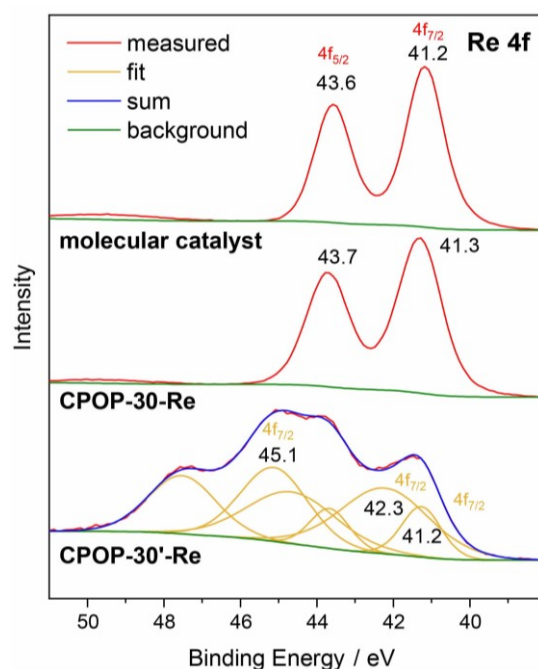


Figure 6: Re 4f XPS spectra of the molecular catalyst, CPOP-30-Re and CPOP-30'-Re.

The structure of **CPOP-30** and **CPOP-30-Re** was further confirmed by ^{13}C CPMAS NMR spectroscopy (Figure 7, a)). For **CPOP-30** the signals between 130 and 152 ppm verify the existence of bipyridine moieties within the structure. The resonance peak at 152 ppm is assigned to carbons in vicinity to nitrogen and connecting both pyridine moieties. Additionally, at 137 ppm a signal corresponding to carbons in vicinity to carbazoyl nitrogen $\text{C}_{\text{Ar-N}}$ was detected. Signals between 106 and 121 ppm were monitored and ascribed to unsubstituted aromatic groups $\text{C}_{\text{Ar-H}}$ and substituted aromatic carbons $\text{C}_{\text{Ar-C}_{\text{Ar}}}$ of the carbazoyl moieties. After metalation, the spectrum for **CPOP-30-Re** shows a shift of the signals at around 130 ppm towards low-field occurring due to the coordination of rhenium(I) to bipyridinic nitrogen. According to that, the broad resonance peak at 135 ppm is ascribed to carbons of the bipyridine unit.

Furthermore, Fourier transform infrared (FTIR) spectroscopy shows the successful immobilization of rhenium(I) catalyst (Figure 7, b)). By comparing **CPOP-30-Re** with **CPOP-30** and the molecular catalyst, vibration bands at 2050 and 1900 cm^{-1} , which are assigned to carbonyl ligands of the metal-organic complex were detected for **CPOP-30-Re** as well as the molecular catalyst $[\text{Re}(\text{Czbipy})(\text{CO})_3\text{Cl}]$.

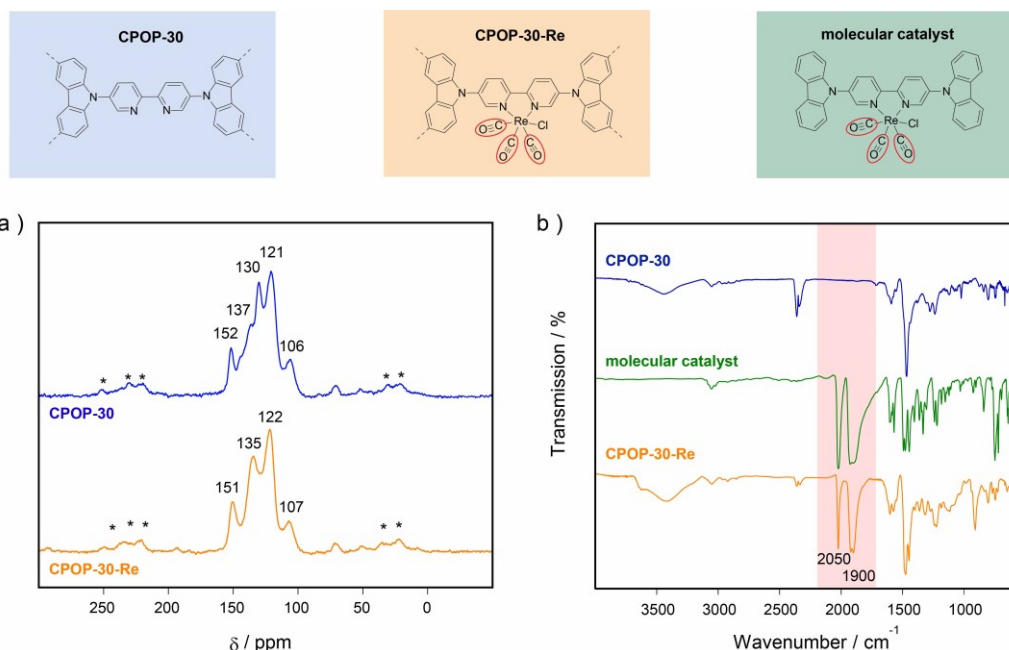


Figure 7: a) ^{13}C CPMAS NMR spectroscopy and b) FTIR spectroscopy of CPOP-30 and CPOP-30-Re in comparison with the molecular catalyst.

Ultraviolet–visible (UV-Vis) absorption spectroscopy was carried out to determine the suitability of the obtained materials for carbon dioxide photoreduction (Figure 8, a)). The absorption edges were detected at 450 and 528 nm for **CPOP-30** and **CPOP-30-Re**, respectively. The red shift is ascribed to the metal-to-ligand charge transfer (MLCT) and the extended delocalization due to metalation. By applying the Tauc plot the band gap energies (E_g) for **CPOP-30** and **CPOP-30-Re** were calculated to be 2.97 and 2.53 eV, respectively (Figure 8, b)).

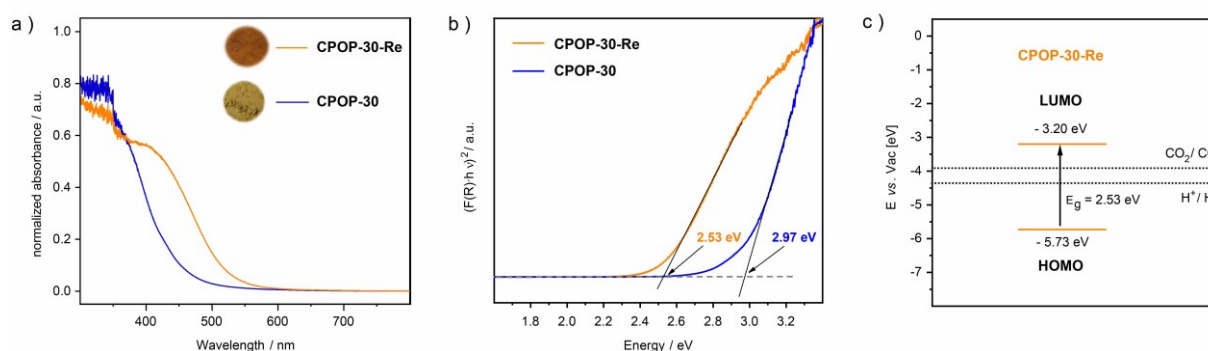


Figure 8: a) UV-Vis spectrum and b) Tauc plot of CPOP-30 and CPOP-30-Re, c) band diagram of CPOP-30-Re.

Additionally, the LUMO position of **CPOP-30-Re** was determined by Mott-Schottky measurements (appendix Figure A 1) and calculated to be at -3.20 eV vs. vacuum.^[3] As the energy levels of HOMO and LUMO of **CPOP-30-Re** (Figure 8, c)) straddle the standard redox energy of CO_2/CO , which is set at -3.91 eV vs. vacuum, the Re(I)-immobilized material emerges as principally suitable photocatalyst for carbon dioxide reduction.^[135]

4.3.1.2 Carbazole-based Polymer Networks Applied in Photocatalytic Carbon Dioxide Reduction

Photocatalytic carbon dioxide reduction tests (Table 1) were carried out by Amitava Acharjya. For applying the polymers in photocatalysis, the materials were dispersed in solvent (dimethylformamide or acetonitrile) along with a sacrificial agent (triethanolamine). The mixture was placed in a photoreactor and saturated with carbon dioxide before irradiating the solution (395 nm). In the first step, metal-free **CPOP-30** was applied in a photocatalytic test. Low amounts of carbon monoxide (1.9 μmol) were detected after 4 h as well as hydrogen (0.2 μmol), which originates from the competing proton reduction.

Table 1: Photoreduction of carbon dioxide catalyzed by CPOP-30 and CPOP-30-Re.^[3]

catalysts	solvent	V% TEOA	CO [μmol]	H ₂ [μmol]	reaction time [h]
CPOP-30	DMF	20	1.9	0.2	4
CPOP-30-Re	DMF	20	7.4	0.3	4
CPOP-30-Re	ACN	20	15.8	0.5	4
CPOP-30-Re	ACN	10	17.2	0.4	4
CPOP-30-Re	ACN	10	62.3	1.3	10
CPOP-30-Re	ACN	10	173.0	17.7	40

Standard conditions for CO₂ photoreduction: photocatalyst (10 mg), CO₂-saturated solvent (10 mL, different solvent: TEOA ratios), 300 W Xe lamp with cut-off filter of 390 nm.

Carbon monoxide production was increased by almost 4 times when using rhenium(I)-containing **CPOP-30-Re** (7.4 μmol) instead of **CPOP-30**. By varying the conditions, for instance changing the solvent from dimethylformamide to acetonitrile and using less sacrificial agent, the amount of carbon monoxide was elevated to 17.2 μmol within 4 h of reaction time (Table 1). Finally, under optimized reaction conditions, 62.3 μmol carbon monoxide were produced after 10 h, which makes an average production rate of 623 $\mu\text{mol g}^{-1} \text{h}^{-1}$ for carbon monoxide. Considering the additional 1.3 μmol of hydrogen, which was produced, the selectivity of **CPOP-30-Re** to reduce carbon dioxide to monoxide is calculated to be 98%.

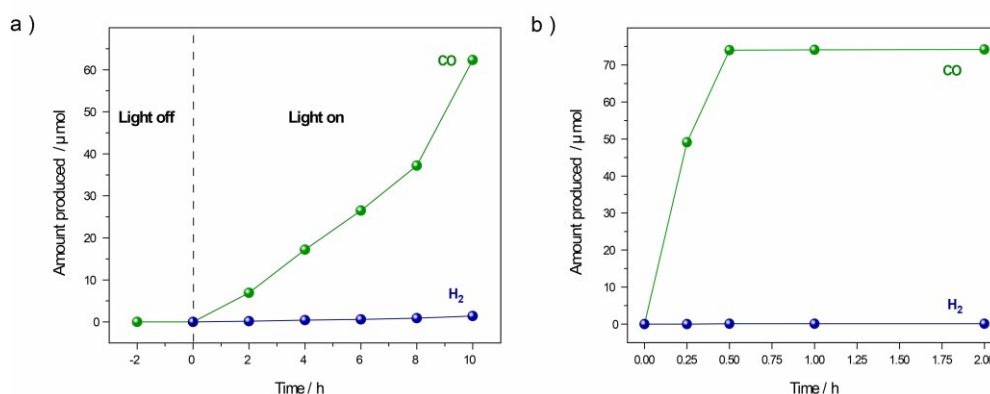


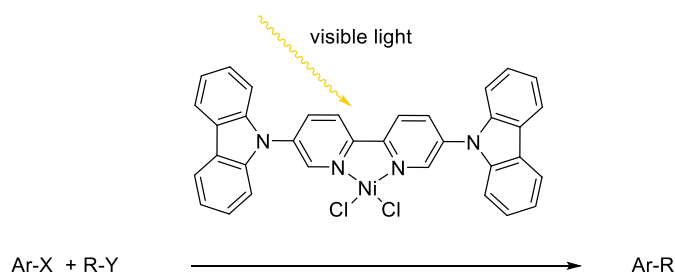
Figure 9: Carbon monoxide and hydrogen evolution as a function of time for a) CPOP-30-Re and b) molecular catalyst [Re(Czbipy)(CO)₃Cl] applied in photocatalytic carbon dioxide reduction.^[3]

The production of carbon monoxide for **CPOP-30-Re** is increasing constantly over time, whereas the molecular catalyst [Re(Czbipy)(CO)₃Cl] showed a rapid increase in productivity and a maximum value of 74 μmol of carbon monoxide within the first 30 min (Figure 9). However, for the homogeneous analogue the carbon monoxide evolution stagnates after 30 min, meaning its photoactivity stopped. According to these observations, it is assumed that the molecular catalyst decomposes under irradiation and ends in formation of inactive dimers.^[136,137] Assuming that immobilized catalyst exhibits much higher stability in comparison to its homogeneous analogues and by extending the reaction time to 40 h, the supported catalyst **CPOP-30-Re** outperforms the molecular catalyst (Table 1). Additionally, **CPOP-30-Re** is easily recyclable by filtration and retains 83% of its activity after four cycles.^[3]

4.3.2 Carbazole-based Polymer Networks Applied in Nickel-catalyzed Cross-coupling under Visible-light Irradiation

The material **CPOP-30**^[3] was not only applied as support for Re(I) photocatalyst but also for visible-light-mediated nickel catalysis. By combining visible-light photoredox- and Ni-catalysis, cross-coupling reactions can be applied under mild conditions presenting an approach to replace expensive palladium catalysts.^[113] In general, Ni-catalyzed dual photoredox catalysis (see 4.1.4) is performed by using nickel complexes along with a photocatalyst, though the more elegant way would be to modify the Ni-complex so that it would be directly activated by visible-light.^[113,138] Shields *et al.* presented a bipyridine-equipped Ni-catalyst, which performed C-O couplings without an additional photocatalyst.^[138] It is suspected that by extending the conjugated π -system of the ligand, the Ni-complexes would have the ability to harvest light under visible-light irradiation in absence of an exogenous photocatalyst.

The previously presented monomer 5,5'-di(9*H*-carbazol-9-yl)-2,2'-bipyridine (Czbipy)



It was shown that monomer Czbipy can be applied as ligand for Ni-catalyzed sulfonylation (cross-coupling C-S) under illumination.^[139] The coordination of Czbipy with Ni(II) leads to an efficient homogeneous catalyst to cross-couple 4-iodobenzotrifluoride and p-toluenesulfinate under irradiation of visible-light (Table 2, entry 1). In order to optimize the solvent, Ni source and the lamp power were systematically varied, and it was shown that ideally 5 mol% of NiCl₂·glyme in dimethylacetamide (DMAc) and two blue LED light lamps (440 nm) were applied. After 22 h of reaction time, conversions higher than 99% were obtained in 92% selectivity of the desired sulfone **1**.

entry	ligand	conversion [%] ^b	1 [%] ^c
1	homogeneous Czbipy	>99	92
2	CPOP-30 ^[3]	>99	77

30

Czbipy proved to be an efficient ligand for photocatalyst-free, Ni-catalyzed C-S coupling as activation of Ni-complex was achieved under irradiation of visible-light instead of UV-light, which is attributed to the extension of the ligand's π -system.^[140,141]

In a next step, bipyridine-containing **CPOP-30**^[3] was applied as solid macroligand for the Ni-complex and tested for heterogeneous visible-light-mediated nickel catalysis. Therefore, Ni(II)-complex was immobilized on **CPOP-30** and the porosity of **CPOP-30-Ni** investigated by means of N₂ sorption isotherms, from which the BET surface area was determined to be 470 m² g⁻¹ (Figure A 2). The nickel content within the material was measured by ICP-OES and calculated to be 3.7 wt% equating to a metal loading of around 40% of all possible bipyridine coordination sites.

Scanning electron microscopy (SEM) images of **CPOP-30-Ni** show the morphology of the amorphous polymeric particles analyzed by elemental mapping. The images depict a homogeneous distribution of nickel and chlorine within the material (Figure 10).

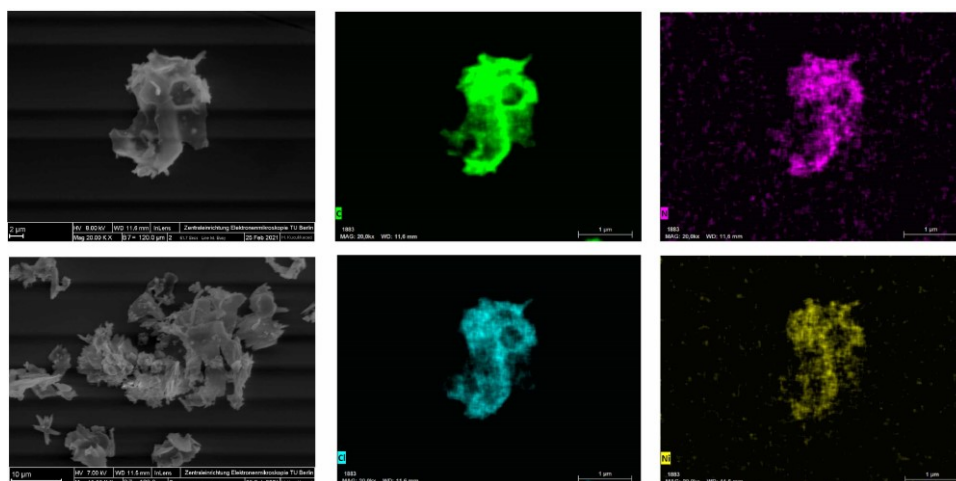


Figure 10: Scanning electron microscopy and elemental mapping of CPOP-30-Ni. Elemental mapping of carbon (green), nitrogen (pink), chlorine (blue) and nickel (yellow).

The chemical structure of **CPOP-30-Ni** was characterized by XPS spectroscopy (Figure 11) showing successful immobilization of Ni(II) species. The N 1s core spectrum contains three species of nitrogen: (i) an intense peak at 400.4 eV corresponding to polymerized carbazole moieties, (ii) a signal at 399.7 eV, which is assigned to N-Ni coordination of the Ni(II)-complex, and (iii) a low-intensity peak at 400.2 eV deriving from bipyridine nitrogen species, which are not coordinated to metal.^[142,143] The elemental composition was further investigated by Ni 2p core-level measurements (Figure 11, b). The Ni 2p spectrum of **CPOP-30-Ni** shows a doublet and its corresponding satellites, the peaks are located at 855.6 eV and 873.3 eV, which are assigned to 2p_{3/2} and 2p_{1/2} signals for Ni(II) species, respectively.^[144]

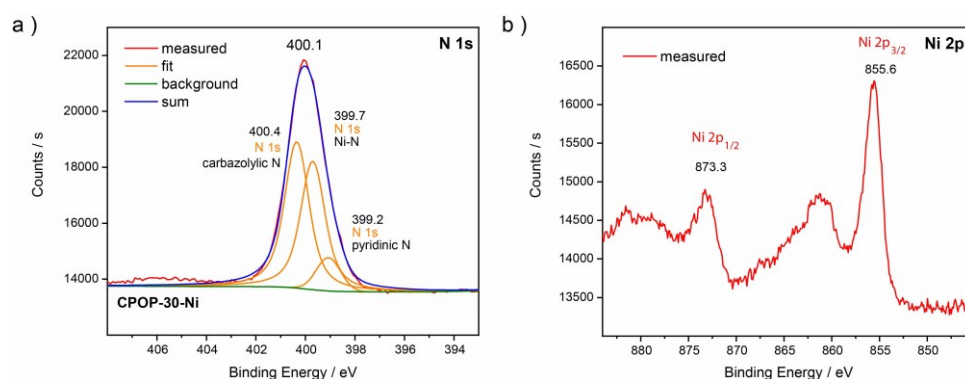


Figure 11: a) N 1s and b) Ni 2p XPS spectra CPOP-30-Ni.

When the material **CPOP-30-Ni**, instead of Czbipy, was applied as ligand under the previously optimized conditions, conversions higher than 99% with 77% selectivity were achieved during the first catalytic tests (Table 2, entry 2).^[139]

The preliminary work using polymer network **CPOP-30-Ni** shows the potential of applying heterogeneous visible-light-mediated Ni-catalysts without requiring an exogenous photocatalyst and perform sulfonylations under mild conditions. With further studies, the reaction can be optimized and **CPOP-30-Ni** is likely to be applicable to other cross-coupling reactions. Due to easy recovery of heterogenized systems, **CPOP-30-Ni** will open the possibility for new recyclable solid catalysts for noble-metal free cross-coupling reactions.

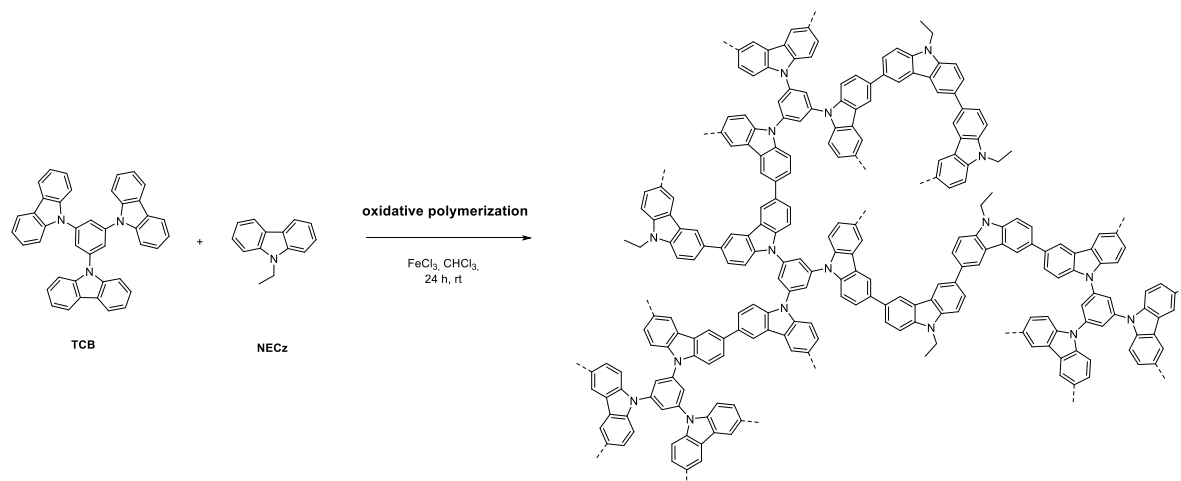
4.3.3 Carbazole-based Copolymers for Hydrogen Storage

Several research groups reported successful copolymerization of carbazole-based copolymers to fine-tune the functionality of the materials by additional monomers within the structure.^[89,90,145] However, the challenging part is to control the composition and distribution of monomers within the networks. Either the monomer units can be arranged in an alternating or statistical manner but also block copolymers or even separate homopolymers are conceivable.^[89] The following chapter describes the design of copolymers prepared by oxidative polymerization with special focus on incorporation of *N*-ethylcarbazole (NECz) moieties into the polymeric structure and their exploitation as hydrogen carriers.

4.3.3.1 Synthesis and Characterization of Carbazole-based Copolymers

Carbazole-based copolymerizations were attempted *via* oxidative polymerization by applying different amounts of *N*-ethylcarbazole (NECz) units (Scheme 8), which are known for their capacity to bind hydrogen chemically for reversible hydrogen storage (see chapter 4.1.5).^[146] Furthermore, comonomer NECz possesses the advantage of being equipped with an ethyl group, which helps to differentiate from purely aromatic moieties and to determine the

incorporation of NECz within the polymer structure by NMR and FTIR spectroscopy.



Scheme 8: Copolymerization from TCB and NECz via oxidative polymerization according to a procedure of Chen *et al.*^[1]

The synthesis of copolymers with different percentages of NECz and 1,3,5-tri(*N*-carbazolyl)benzene (TCB) were carried out in close collaboration with Jonas Kube who did his Bachelor project under my supervision.

The oxidative polymerization was carried out according to the synthesis of CPOP-1.^[1] In general 18 eq. of iron(III) chloride were used and the reaction was stirred for 24 h at room temperature. For the copolymerizations, proportions of 20, 50 and 60 mol% of NECz were applied, respectively. In addition, a TCB homopolymer was prepared as a reference in comparison to the copolymers. The additional indices of the polymer nomenclature refer to the molar equivalents of NECz building units applied to form the copolymer networks.

The porosity of the copolymers **P_{0.2}**, **P_{0.5}** and **P_{0.6}** as well as homopolymer **P₀** were evaluated by nitrogen sorption measurements (Figure 12). The materials reveal a pronounced increase at low relative pressures which is characteristic for microporous polymers.

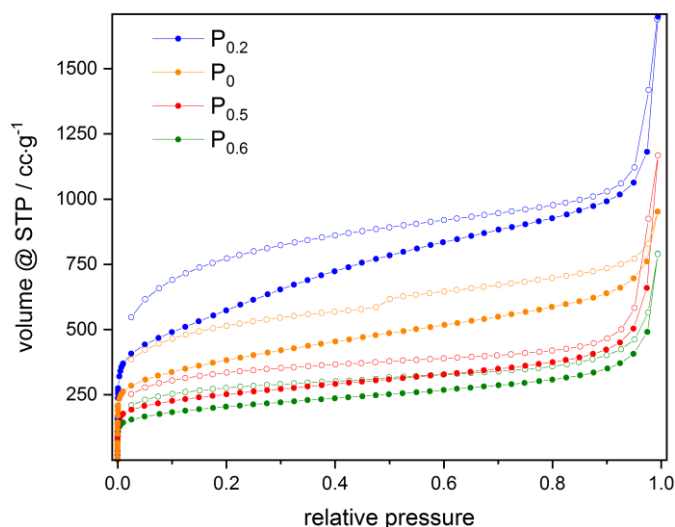
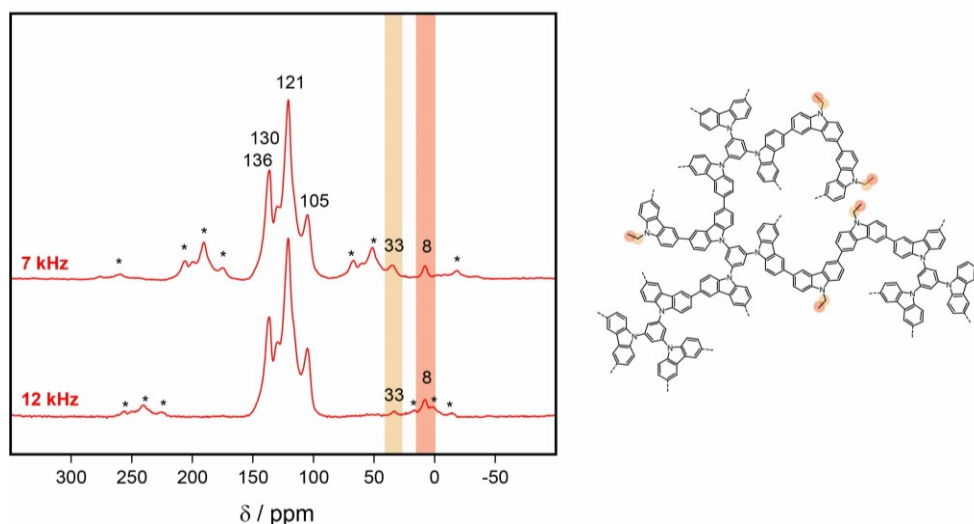


Figure 12: N₂ isotherms of P₀, P_{0.2}, P_{0.5} and P_{0.6}.

Table 3: S_{BET} of the polymers for different incorporation ratios of NECz.

polymer	yield [%]	S_{BET} [$\text{m}^2 \text{g}^{-1}$]
P₀	99	1342
P_{0.2}	100	2054
P_{0.5}	90	911
P_{0.6}	93	736

Applying the BET model results in surface areas ranging from 736 (**P_{0.6}**) to 2054 $\text{m}^2 \text{g}^{-1}$ (**P_{0.2}**) (Table 3). With increasing amount of NECz within the polymer, the surface areas decreased significantly. However, the surface area of copolymer **P_{0.2}** reached a maximum of 2054 $\text{m}^2 \text{g}^{-1}$ and drops again to 1342 $\text{m}^2 \text{g}^{-1}$ for homopolymer **P₀**. By rising percentages of NECz the yields of the polymers decreased and therefore no exact ratios of TCB and NECz can be determined from the initial monomer concentration. This is especially the case for **P_{0.5}** and **P_{0.6}**.

**Figure 13:** ^{13}C CPMAS NMR spectra of **P_{0.5}** at different spinning rates measured at 7 kHz (top) and 12 kHz (bottom).

In the following, the material **P_{0.5}** was chosen as an example for NECz containing copolymers and was characterized by NMR and FTIR spectroscopy. The chemical structure of **P_{0.5}** was confirmed by ^{13}C CPMAS NMR spectroscopy (Figure 13). Different spinning rates were applied to detect the aliphatic groups without having an overlap with spinning sidebands. At spinning rates of 7 kHz and 12 kHz, signals at 8 and 33 ppm were monitored, respectively. The signal at 8 ppm is assigned to the methyl group $-\text{CH}_3$ and the second signal at 33 ppm corresponds to methylene group $-\text{CH}_2-$ of the NECz. The signals between 106 to 121 ppm are ascribed to unsubstituted aromatic groups $\text{C}_{\text{Ar}}-\text{H}$ and substituted aromatic carbons $\text{C}_{\text{Ar}}-\text{C}_{\text{Ar}}$ of the carbazoyl moieties. The resonance peaks between 130 and 137 ppm correspond to carbons in the vicinity of carbazoyl nitrogen $\text{C}_{\text{Ar}}-\text{N}$.^[1]

In addition, FTIR spectroscopy (Figure 14 and Figure A 3) shows further proof for the incorporation of NECz moieties in the polymer scaffold. The vibration bands at 2974, 2933 and 2875 cm^{-1} were assigned to $-\text{CH}_3$ asymmetric, $-\text{CH}_2-$ asymmetric and symmetric stretching bands, respectively (Figure 14).^[147] These vibrations originating from aliphatic groups were ascribed to the ethyl groups of NECz. The vibration band at 3058 cm^{-1} is ascribed to aromatic C-H stretching bands.

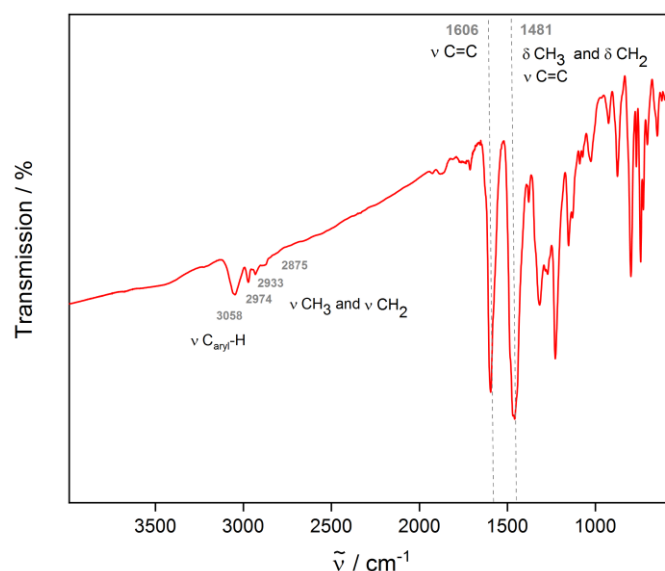


Figure 14: FTIR spectrum of P_{0.5}.

Since neither NMR, nor FTIR spectroscopy provide evidence on the distribution of the two molecules in the copolymer, a kinetic study of the formation of the copolymer was performed. For this purpose, samples of the reaction solution were analyzed at different reaction times to determine remaining soluble compounds, meaning the non-incorporated mono- and oligomers, by ^1H NMR spectroscopy (Figure 15).

A reaction mixture of the comonomers TCB and NECz in 1:1 ratio was used for this study. The ^1H NMR spectra show that NECz (blue) was completely converted after 15 s as the characteristic signals at 8.12, 7.43 and 7.25 ppm were not detected anymore, whereas the significant signals for TCB at 8.16, 7.96, 7.66 and 7.33 ppm (Figure 15, highlighted in yellow) are still detected up to 1 min after the reaction started. Additionally to the monomer resonance peaks, the intensities of the signals at 8.41, 8.19, and 7.83 ppm (Figure 15, highlighted in green) increase over time, which are assigned to the dimer *N,N'*-diethyl-3,3'-bicarbazole.^[148] After 24 h, only dimer signals of low intensity remained in the spectrum. These results show that NECz is immediately converted into the dimer form, which does not further polymerize with itself, but with TCB moieties to yield a copolymer with incorporated NECz dimers.

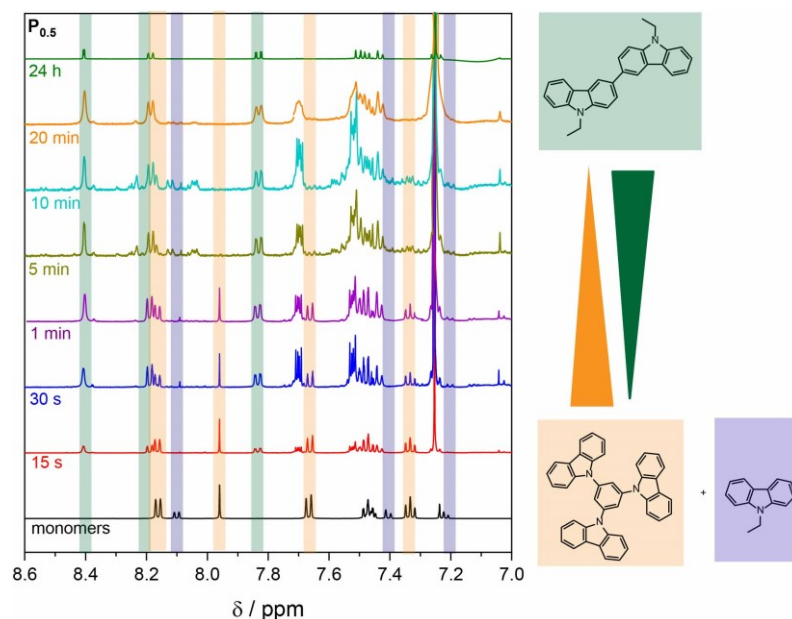


Figure 15: ^1H NMR spectra during the copolymerization of $\text{P}_{0.5}$. Signals for TCB and the NECz dimer are highlighted in yellow (TCB) and green (dimer).

Consequently, several assumptions concerning the formation of copolymers can be stated. First, considering the kinetic study, NECz moieties are always present in form of incorporated dimers. NECz chains consisting of more than two NECz units are not formed by applying oxidative polymerizations with iron(III) chloride. These observations correspond to previous reports in literature claiming that bicarbazylum radical cations, which are formed during the reaction, are well stabilized and therefore unlikely to polymerize with themselves whereby only dimers are generated.^[79,149] In general, poly(*N*-ethylcarbazoles) are synthesized by Nickel-mediated Yamamoto coupling^[77], Palladium-catalyzed cross-coupling^[78] or photoinduced polymerizations^[150]. Besides, these findings explain why yields of the copolymers $\text{P}_{0.5}$ and $\text{P}_{0.6}$ are decreasing. The bicarbazylum radical cations do not polymerize with each other to form a NECz polymer chain, but with TCB, which is probably due to their higher reactivity in comparison to dimeric NECz radical cations. This phenomenon was already reported in 1995 by Siove *et al.*, who showed that bis-(*N*-alkyl carbazolyene) reacted by addition of comonomer 3-octylthiophene to yield a copolymer (see 4.1.1).^[80]

4.3.3.2 Carbazole-based Copolymers as Hydrogen Carriers

NECz is known for its applicability as liquid organic hydrogen carrier (LOHC) storing hydrogen reversibly by hydrogenation and dehydrogenation.^[146] As the synthesized copolymers consist of NECz units, the materials were studied in their usability as solid-state hydrogen carriers. For that purpose, their physisorption properties as well as their ability to store hydrogen chemically within the polymer backbone by hydrogenation were investigated. This approach should elucidate if solid-state hydrogen carriers can be realized based on the concept of LOHCs.

Hydrogen Storage by Physisorption

The copolymers consisting of different monomer ratios were tested for their H₂ uptake capacities at 77 K, respectively (Table 4). The values for the H₂ storage capacity enhances with increasing surface area and can reach up to 1.98 wt% for copolymer **P_{0.2}**, which is higher than previous reported microporous carbazole-based polymer networks.^[83,90] For the copolymers synthesized by oxidative polymerization, isosteric heat of adsorptions up to 11.0 kJ mol⁻¹ were obtained, which is comparably high as reported values for carbazole-containing materials just range between 5.0-8.0 kJ mol⁻¹.^[83,90] The homopolymer **P₀** exhibits the lowest value with 8.8 kJ mol⁻¹. It should be noted that with elevating units of NECz an enhancement of the isosteric heats of H₂ adsorption is achieved.

Table 4: Summary of the hydrogen adsorption properties.

polymer	S_{BET} [m ² g ⁻¹]	H ₂ uptake [wt%] ^a	$Q_{\text{st, hydrogen}}$ [kJ mol ⁻¹] ^b
P₀	1342	1.51	8.8
P_{0.2}	2054	1.98	10.2
P_{0.5}	911	1.21	11.0
P_{0.6}	736	1.02	9.5

^a H₂ sorption experiments were carried out at 77 K and 1 bar. ^b Isosteric heat of adsorption Q_{st} for H₂ was calculated from H₂ sorption isotherms at 77 K and 87 K up to 1 bar.

Hydrogen Storage by Hydrogenation

A favorable organic material for the chemical storage of hydrogen ideally possesses a high percentage of units, which can be hydrogenated and which are fully accessible due to a high surface area. Therefore **P_{0.5}** was chosen for the first hydrogenation test. The BET surface area of **P_{0.5}** was determined to be 911 m² g⁻¹. In order to hydrogenate the polymer network, the copolymer was impregnated with chloroplatinic acid (H₂PtCl₆) to form platinum nanoparticles under H₂ pressure, which are well known as hydrogenation catalysts.^[151] The impregnated copolymer was placed in a hydrogenation reactor and 40 bar of hydrogen at 150 °C were applied over 3 d.

Different weight percentages of chloroplatinic acid were used for the impregnation of copolymers. The amount of platinum within the copolymers ranges from 5.8 to 0.2 wt%, determined by inductively coupled plasma optical emission spectroscopy (ICP-OES). In the following the hydrogenated materials are named **hP_{0.5}-Pt_{5.8}**, **hP_{0.5}-Pt_{2.7}**, **hP_{0.5}-Pt_{1.1}** and

hP_{0.5}-Pt_{0.2} whereby ‘h’ stands for hydrogenated and ‘Pt_x’ indicates the platinum content in weight percentage (x).

After the formation of platinum nanoparticles and the hydrogenation procedure, ¹³C CPMAS NMR spectra at 7 kHz (Figure 16) show additional signals in the aliphatic area. Due to extra resonance peaks at 19, 26 and 28 ppm it is assumed that NECz moieties within the copolymer were partly hydrogenated to yield 9-ethyl-tetrahydrocarbazole (4H-NECz), 9-ethyl-octahydrocarbazole (8H-NECz) and 9-ethyl-perhydrocarbazole (12H-NECz) units.^[152,153] In some of the spectra at 12 kHz a broad signal at 62 ppm was observed (Figure A 4), which is identical to the chemical shift of the aliphatic carbon in vicinity to nitrogen C_{aliph}-N of 12H-NECz.^[153] Furthermore, slight changes in the aromatic area can be monitored due to transformation of fully aromatic rings to 4H-NECz and 8H-NECz derivatives within the structure. The higher the degree of hydrogenation, the more intense is the signal at 136 ppm, whereas the signal at 131 ppm decreases, which is assumably due to hydrogenated carbon bonds in vicinity to carbazoyl nitrogen C_{Ar}-N.^[1] In the aliphatic area the methyl groups -CH₃ of NECz shifts from 9 to 10-11 ppm.

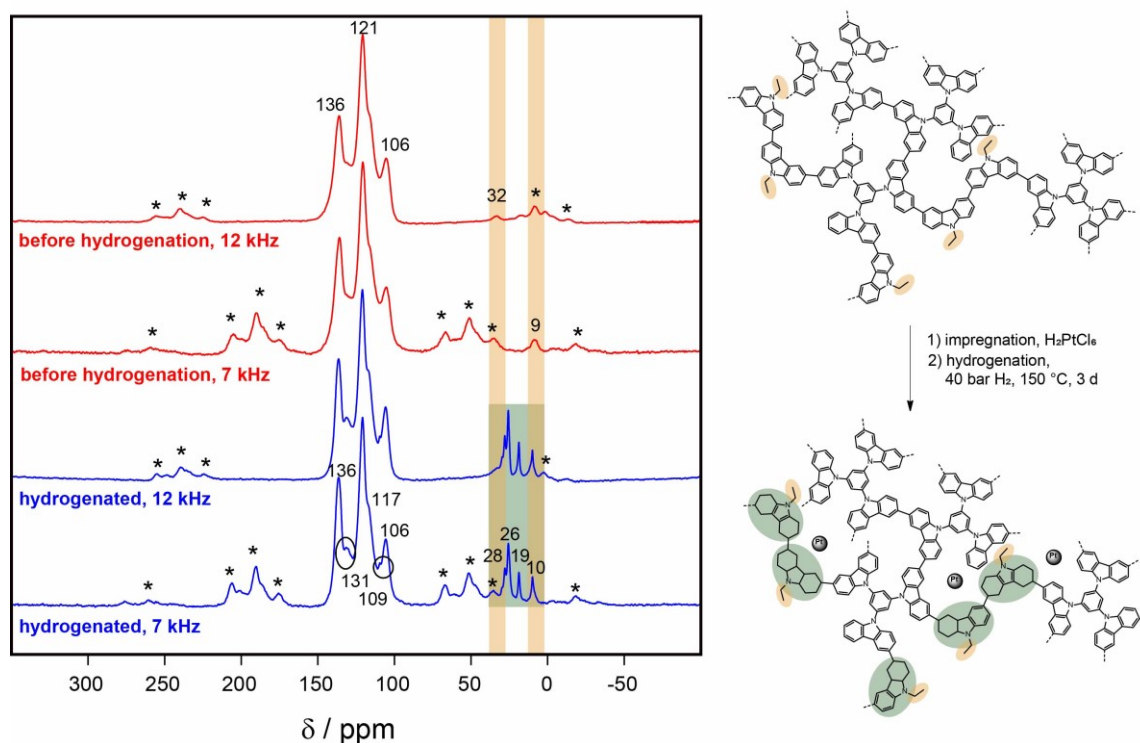


Figure 16: ¹³C CPMAS NMR spectra of P_{0.5} (red) and the hydrogenated copolymer hP_{0.5}-Pt_{0.2} (blue) at different spinning rates measured at 7 kHz and 12 kHz.

Furthermore, the hydrogenation of the copolymers was confirmed by FTIR spectroscopy. It reveals the successful formation of aliphatic groups after exposing the material to high hydrogen pressure. The signals at 2955, 2922 and 2851 cm⁻¹ increase significantly after hydrogenation and can be assigned to -CH₃ asymmetric, -CH₂- asymmetric and symmetric

stretching bands, respectively.^[147] The vibration bands at 1460 and 3057 cm^{-1} are assigned to $-\text{CH}_2-$ deformation bands and aromatic $\text{C}_{\text{aryl}}\text{-H}$ symmetric stretching bands, respectively.

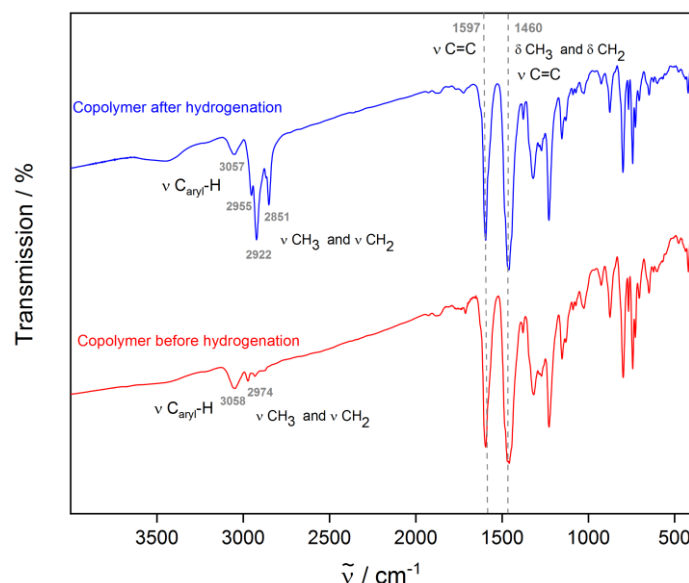


Figure 17: FTIR spectra of $\text{P}_{0.5}$ (red) and $\text{hP}_{0.5}\text{-Pt}_{0.2}$ (blue).

In Figure 18, the ^{13}C CPMAS NMR spectra at 7 kHz and FTIR spectra of the hydrogenated copolymers $\text{hP}_{0.5}\text{-Pt}_{5.8}$, $\text{hP}_{0.5}\text{-Pt}_{2.7}$, $\text{hP}_{0.5}\text{-Pt}_{1.1}$ and $\text{hP}_{0.5}\text{-Pt}_{0.2}$ are presented. $\text{hP}_{0.5}\text{-Pt}_{2.7}$ possesses intense signals in the aliphatic region in its NMR spectrum as well as pronounced $-\text{CH}_3$ and $-\text{CH}_2-$ stretching vibration bands in its FTIR spectrum indicating a significantly higher hydrogenation level in comparison to the other copolymers. It must be noted that $\text{hP}_{0.5}\text{-Pt}_{5.8}$, even though it contains of the highest percentage of platinum, shows the lowest hydrogenation degree.

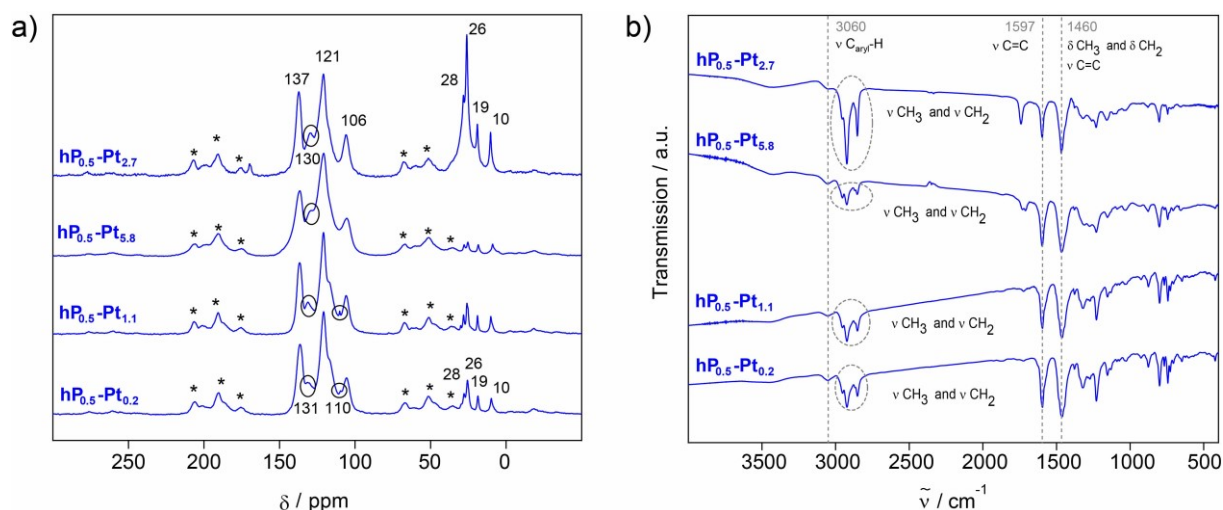


Figure 18: a) ^{13}C CPMAS NMR spectra at 7 kHz and b) FTIR spectra of hydrogenated copolymers $\text{hP}_{0.5}\text{-Pt}_{5.8}$, $\text{hP}_{0.5}\text{-Pt}_{2.7}$, $\text{hP}_{0.5}\text{-Pt}_{1.1}$ and $\text{hP}_{0.5}\text{-Pt}_{0.2}$.

The platinum nanoparticles were formed *in situ* during the hydrogenation process at 150 $^{\circ}\text{C}$ under 40 bar of hydrogen over a period of 3 days. By transmission electron microscopy

(TEM) it was shown that highly hydrogenated samples such as **hP_{0.5}-Pt_{2.7}**, exhibit homogeneous particle sizes at around 2 nm (Figure 19, b). Whereas less hydrogenated materials, for instance **hP_{0.5}-Pt_{5.8}**, show agglomerated nanoparticles ranging from 5 to 60 nm in size. Therefore the size of platinum nanoparticles is probably more important than the amount of platinum loading.^[151] Besides, it is assumed that higher amounts of platinum nanoparticles are more likely to agglomerate.

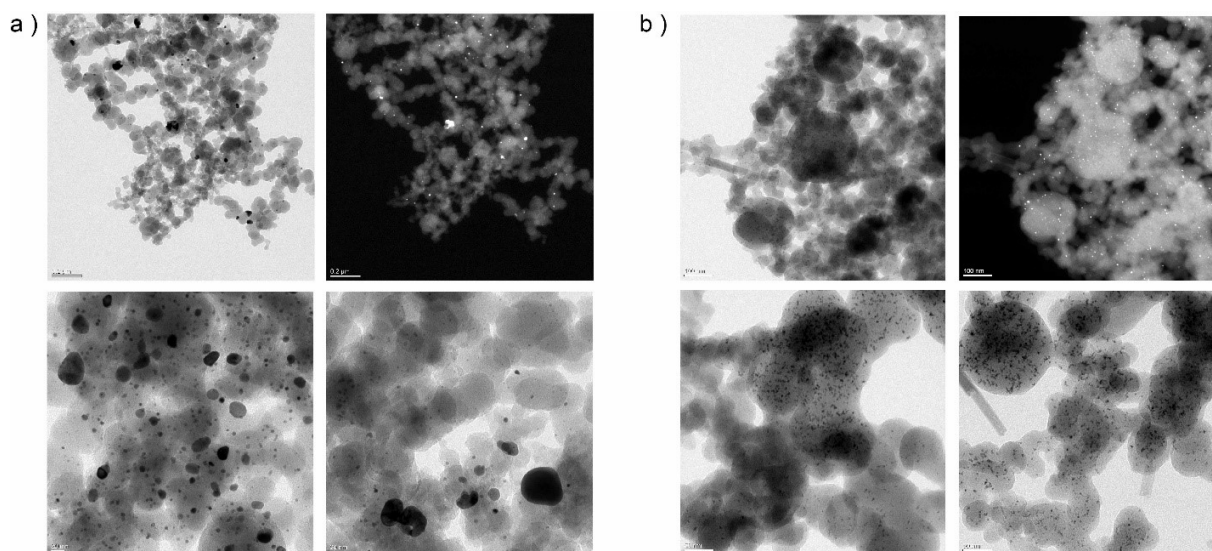


Figure 19: Transmission electron microscopy images in bright and dark field mode of a) hP_{0.5}-Pt_{5.8} and b) hP_{0.5}-Pt_{2.7}.

To confirm the indications for hydrogenation detected by solid-state NMR spectroscopy and FTIR, the material **P_{0.5}** decorated with platinum nanoparticles was characterized before the hydrogenation process. For this purpose, **P_{0.5}** was impregnated with chloroplatinic acid and exposed to hydrogen gas under mild conditions, whereby platinum nanoparticles were formed but no hydrogenation was initiated. In the following, the non-hydrogenated material is named **P_{0.5}-Pt**. The ¹³C CPMAS NMR as well as FTIR spectroscopy show results similar to spectra of untreated **P_{0.5}**. For **P_{0.5}-Pt** no signals in the aliphatic area between 10 and 60 ppm or any changes of the vibration bands between 2955 to 2851 cm⁻¹ were observed after the treatment at 1 bar H₂ (Figure A 5).

To identify which parts of the copolymer were hydrogenated, also purely TCB-containing homopolymer **P₀** was applied in a hydrogenation test. For that purpose, **P₀** was impregnated with chloroplatinic acid, accordingly to the other copolymers. ICP-OES measurements revealed a platinum loading of 6.0 wt% for **hP₀-Pt_{6.0}**.

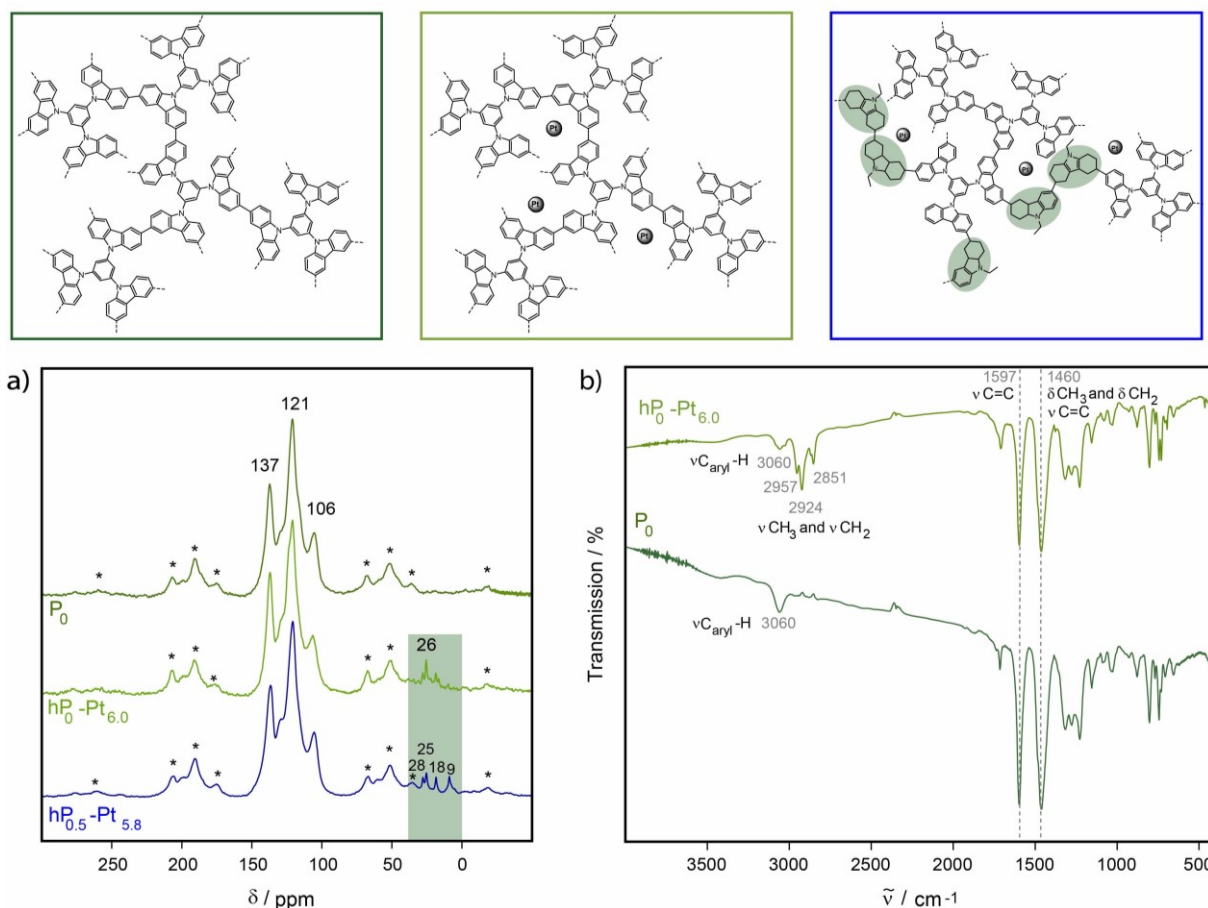


Figure 20: a) ^{13}C CPMAS NMR spectra of P_0 (dark green) and the hydrogenated polymer $\text{hP}_0\text{-Pt}_{6.0}$ (light green) and $\text{hP}_{0.5}\text{-Pt}_{5.8}$ (blue) measured at 7 kHz. b) FTIR spectra of P_0 (dark green) and $\text{hP}_0\text{-Pt}_{6.0}$ (light green).

The structure of P_0 and $\text{hP}_0\text{-Pt}_{6.0}$ was characterized by ^{13}C CPMAS NMR spectroscopy (Figure 20, a). The NMR spectrum of P_0 shows the typical signals at 137, 121 and 108 ppm as reported in literature.^[1] Resonance peaks at 108 and 121 ppm are ascribed to unsubstituted aromatic groups $\text{C}_{\text{Ar}}\text{-H}$ and substituted aromatic carbons $\text{C}_{\text{Ar}}\text{-C}_{\text{Ar}}$ of the carbazoyl moieties, respectively. The third signal at 137 ppm corresponds to carbons in the vicinity of carbazoyl nitrogen $\text{C}_{\text{Ar}}\text{-N}$. The spectrum of $\text{hP}_0\text{-Pt}_{6.0}$ shows slight differences in the aliphatic area. Comparable to $\text{hP}_{0.5}\text{-Pt}_{5.8}$, low intense signals at 28, 26 and 19 ppm were observed which indicate low rates of hydrogenation. Similar indications were found in the FTIR spectrum of $\text{hP}_0\text{-Pt}_{6.0}$ (Figure 20, b) showing extra vibration bands in the range between 2957 and 2851 cm^{-1} , stating the existence of aliphatic groups ($-\text{CH}_3$, $-\text{CH}_2-$) as described earlier for the hydrogenated copolymers (see Figure 17). These hints lead to the conclusion that even pure TCB homopolymers can be hydrogenated by the developed process. Nevertheless, the level of hydrogenation is low compared to copolymers containing NECz moieties. In conclusion, NECz units are needed to enhance the uptake of hydrogen and to build up a sufficient hydrogen carrier.

Dehydrogenation

In the previous section, it was shown that carbazole-based copolymers were successfully hydrogenated but for designing an efficient hydrogen carrier, the challenge is to find the balance between hydrogenation/dehydrogenation under close-to-ambient conditions. Ideally, neither high pressures nor very high or low temperatures are needed, as is the case for most known hydrogen transport techniques.^[121,154] For LOHCs (chapter 4.1.5), which are based on NECz, the liberation of hydrogen, hence the dehydrogenation process is performed under elevated temperatures up to 200 °C and in presence of a ruthenium catalyst.^[130] According to the dehydrogenation of LOHCs, the earlier discussed copolymers were studied regarding their behavior under elevated temperatures.

One technique of following the process of dehydrogenation is thermal gravimetric mass spectrometry (TG-MS), which detects the release of gases over time while slowly raising the temperature. Generally, the thermogravimetric device was heated up to 300 °C over 130 min, then the temperature was kept for 70 min at 300 °C. During that process, the decrease of mass is detected as well as the evolution of oxygen, carbon dioxide, nitrogen, hydrogen and water gas as a function of temperature. The low-level hydrogenated material **hP_{0.5}-Pt_{5.8}** exhibits a mass change of 13.0% as well as a constant output of the different gases (Figure 21). At around 95 and 135 °C two irregular peaks in the hydrogen mass curve were observed. The increasing evolution of hydrogen is assumed to origin from dehydrogenation of the polymer scaffold.

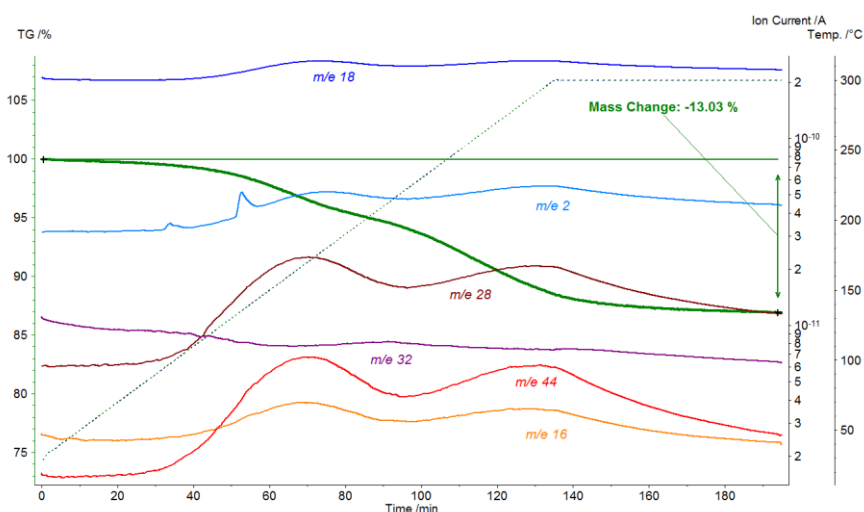


Figure 21: TG-MS measurements for hP_{0.5}-Pt_{5.8}.

In comparison to **hP_{0.5}-Pt_{5.8}**, highly hydrogenated material **hP_{0.5}-Pt_{2.7}** possess a decrease of mass of 30.5% over 300 min (Figure 22). The MS spectra of the gases show congruent swings but no deviation of hydrogen evolution. At 250 °C an increasing amount of hydrogen, carbon dioxide and oxygen were detected and consequently a significant mass loss. Due to the

high temperature and simultaneous increasing gas formation, presumably decomposition of the polymer network instead of dehydrogenation takes place. It is already reported, that the thermal stability of NECz is limited to around 270 °C, if it is applied as LOHC under the presence of ruthenium dehydrogenation catalysts as dealkylation of NECz is conceivable.^[131] Based on these observations, it can be assumed that higher hydrogenated polymer scaffolds become more unstable with increasing aliphatic character and rising temperatures, hence the structure decomposes before dehydrogenation temperatures are reached. Besides, the role of nanoparticle size and ratio within the polymer should be considered.^[155] Copolymer **hP_{0.5}-Pt_{2.7}** shows clearly greater differences in nanoparticle size as well as doubled platinum loading in comparison to **hP_{0.5}-Pt_{2.7}**.

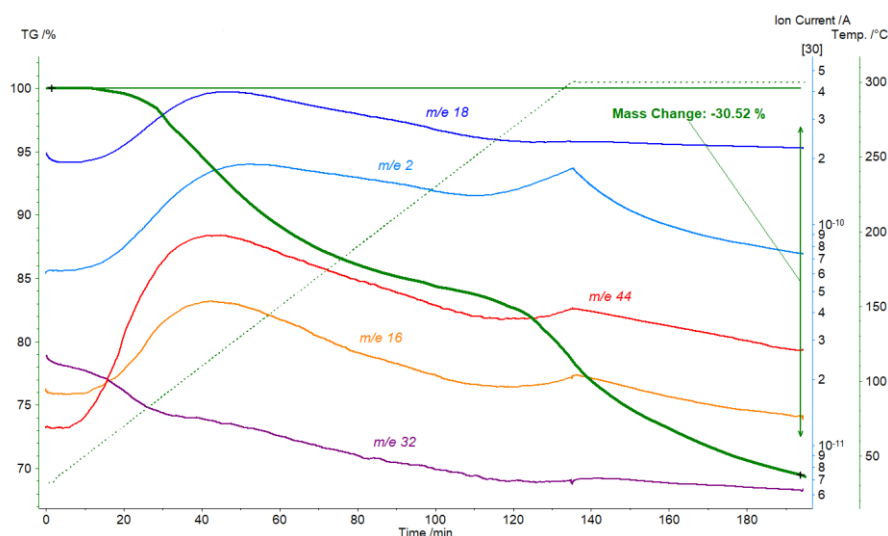


Figure 22: TG-MS measurements for **hP_{0.5}-Pt_{2.7}**.

To substantiate the hypothesis, thermogravimetric analysis (TGA) measurements were carried out to compare the stability of **P_{0.5}**, **hP_{0.5}-Pt_{2.7}** and **hP_{0.5}-Pt_{5.8}** under nitrogen and air (Figure 23).

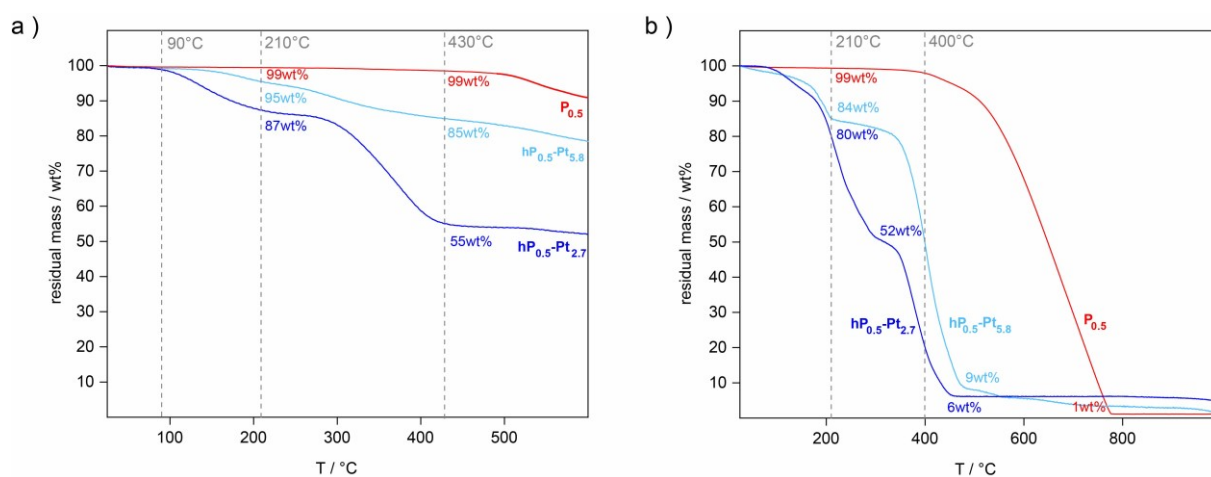


Figure 23: TGA measurements of **P_{0.5}**, **hP_{0.5}-Pt_{2.7}** and **hP_{0.5}-Pt_{5.8}** under a) nitrogen and b) air.

Measurements under nitrogen show that **P_{0.5}** is stable up to 500 °C, whereas for **hP_{0.5}-Pt_{2.7}** and **hP_{0.5}-Pt_{5.8}** a weight loss was observed starting at 90 °C. According to TG-MS, a loss of H₂, CO₂ and H₂O was observed. The much higher hydrogenated **hP_{0.5}-Pt_{2.7}** retains 87 wt% compared to **hP_{0.5}-Pt_{5.8}**, which retains 95 wt% at 210 °C. At 430 °C, the difference in weight loss increased especially for **hP_{0.5}-Pt_{2.7}**, for which a remaining mass of 55 wt% is detected compared to **hP_{0.5}-Pt_{5.8}** with 85 wt%. By comparing the numbers, there is a definite trend towards mass loss for materials with higher ratios of aliphatic moieties. Similar tendencies are noticed for TGA measurements under air. **P_{0.5}** is stable up to 400 °C in contrast to **hP_{0.5}-Pt_{2.7}** and **hP_{0.5}-Pt_{5.8}**, which start losing mass at around 100 °C and at 210 °C, were 84 and 80 wt% remained, respectively. Between 90 and 450 °C a steady lost in weight is detected for **hP_{0.5}-Pt_{2.7}** which stops at 450 °C, and 6 wt% remaining material was left over. For **hP_{0.5}-Pt_{5.8}** the rapid weight loss starts at 330 °C.

In addition, TG-MS measurement for non-hydrogenated copolymer **P_{0.5}-Pt** was carried out to monitor if any hydrogen release is detected for the aromatic system (Figure A 6). After 200 min and rising temperature up to 300 °C, a mass change of 12.8% was observed. As expected, no hydrogen evolution was observed in MS, only carbon dioxide was released, which is common for carbazole-containing materials due to their high isosteric heat of adsorptions for carbon dioxide.^[1]

Since the TCB-containing homopolymer also exhibits low levels of hydrogenated areas (**hP₀-Pt_{6.0}**), TG-MS measurement was performed (Figure 24). A mass loss of 20.7% was monitored and similar to **hP_{0.5}-Pt_{2.7}**, carbon dioxide, oxygen, hydrogen and water were liberated slowly as a function of temperature but no exceptional release of hydrogen independent from other gases was noticed.

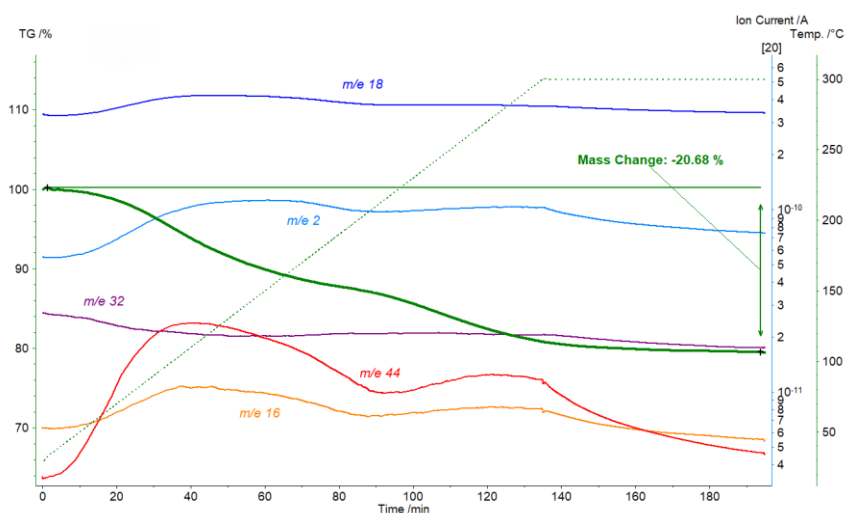


Figure 24: TG-MS measurements for **hP₀-Pt_{6.0}**.

Considering all data, it is concluded, that for successful dehydrogenation NECz units within the structure are needed to ensure the hydrogenation process is reversible. The hydrogenation level must be chosen carefully to not destabilize the scaffold, that decomposition takes place before dehydrogenation. For the TCB-containing homopolymer **hP₀-Pt_{6.0}** no reversibility of hydrogenation is observed but the polymer remains stable, thus it can be concluded that TCB units in copolymers help to stabilize the hydrogenated units. After all, TG-MS results of **hP_{0.5}-Pt_{5.8}** show clearly that it is possible to release hydrogen, if a balance between stability of the scaffold as well as enough hydrogenated NECz units are maintained.

4.3.4 Carbazole-based Homopolymers for Hydrogen Storage

4.3.4.1 Synthesis and Characterization of Carbazole-based Homopolymers

As the incorporation of NECz moieties within copolymers is difficult to control and determine, homopolymers instead of copolymers would give exact ratios of NECz units within the scaffold. For this purpose, a homopolymer **polyTNECzB** synthesized from 1,3,5-tris(*N*-ethyl-9H-carbazol-3-yl)benzene (TNECzB) was designed. The monomer TNECzB was specifically chosen since it possesses similar propeller-like geometry such as TCB (Figure 25). Furthermore, during oxidative polymerization of TNECzB the typical NECz 3,3'-dimers are formed, which were found in the copolymers **P_{0.2}-P_{0.6}**. Hence, **polyTNECzB** contains NECz dimers connected by benzene moieties.

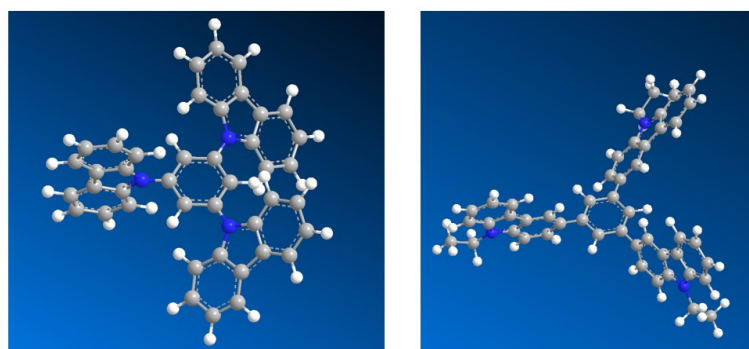
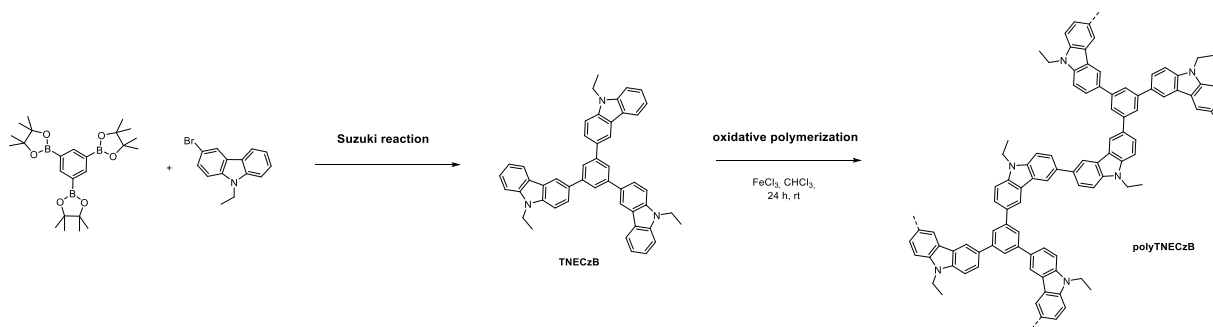


Figure 25: Geometry from Chem3D for TCB (left) and TNECzB (right).

The monomer TNECzB was synthesized from 1,3,5-Tris(4,4,5,5-tetramethyl-1,3,2-dioxaborolan-2-yl)benzene and 3-bromo-9-ethylcarbazole *via* Suzuki cross-coupling reaction.^[156] For comparison, homopolymer **polyTNECzB** was produced according to previous copolymers by applying 18 eq iron(III) chloride per mol of the monomer in a solution of chloroform (Scheme 9).^[1] The resulting yellow powder was obtained in a yield of 97%.



Scheme 9: Homopolymerization of TNECzB via oxidative polymerization according to a procedure by Chen *et al.*^[1]

Based on nitrogen sorption measurements the SA_{BET} of **polyTNECzB** was calculated to be $627 \text{ m}^2 \text{ g}^{-1}$ (Figure A 7). The chemical structure of **polyTNECzB** was confirmed by ^{13}C CPMAS NMR spectroscopy (Figure 26, a). The measurement at 7 kHz shows the characteristic signals at 37 and 12 ppm, which are assigned to methylene group $-\text{CH}_2-$ and methyl group $-\text{CH}_3$ of the NECz moieties, respectively. The aliphatic signals are proportionally higher in comparison to the aliphatic signals of **P0.5**, due to a higher ratio of NECz units within the structure of **polyTNECzB**. The resonance peaks in the aromatic region between 108 and 139 ppm derive from unsubstituted aromatic groups $\text{C}_{\text{Ar}}-\text{H}$, substituted aromatic carbons $\text{C}_{\text{Ar}}-\text{C}_{\text{Ar}}$ and carbazoyl nitrogen $\text{C}_{\text{Ar}}-\text{N}$.^[1]

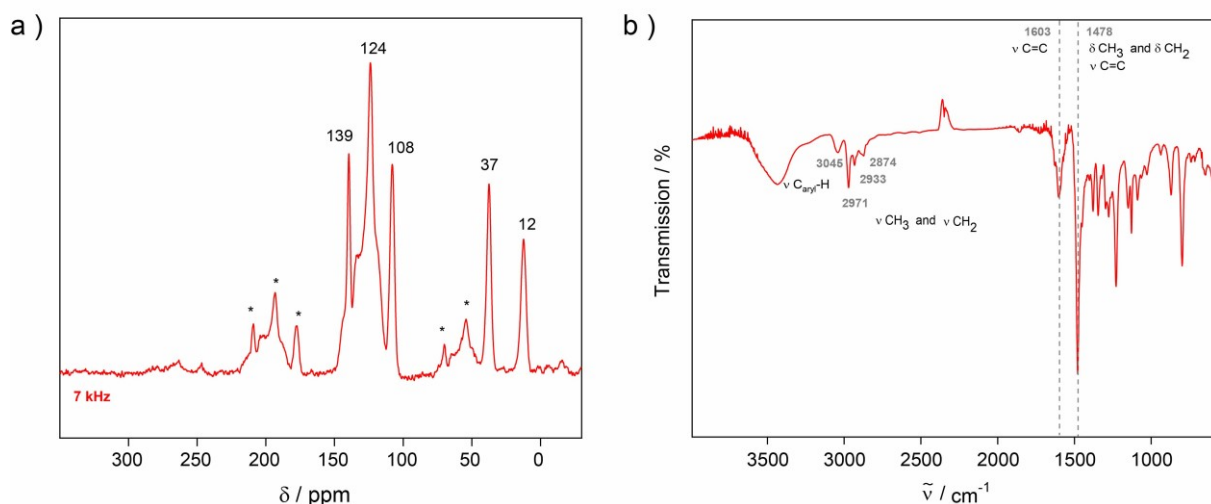
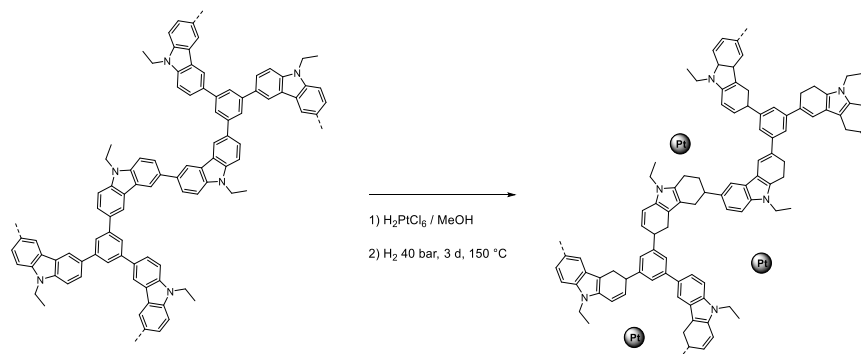


Figure 26: a) ^{13}C CPMAS NMR spectrum at 7 kHz and b) FTIR spectrum of polyTNECzB.

The analysis of **polyTNECzB** by FTIR spectroscopy shows the typical vibration bands for aliphatic groups deriving from the ethyl groups of NECz units. The bands at 2971, 2933 and 2874 cm^{-1} were assigned to $-\text{CH}_3$ asymmetric, $-\text{CH}_2-$ asymmetric and symmetric stretching bands, respectively (Figure 26, b).

4.3.4.2 Carbazole-based Homopolymers as Hydrogen Carriers

As the material **polyTNECzB** consists of proportional high amounts of NEC units, it is a promising candidate to function as a solid-state hydrogen carrier. Therefore, hydrogenation studies were performed to examine if the polymer backbone of **polyTNECzB** can be hydrogenated under the same conditions as **P_{0.5}** (chapter 4.3.3.2). After impregnation with chloroplatinic acid, the hydrogenation was carried out in a reactor with 70 mg of **polyTNECzB** which was heated up to 150 °C under 40 bar of hydrogen for 3 days.



Scheme 10: Impregnation and hydrogenation of polyTNECzB to yield in hpolyTNECzB-Pt_{1.1}.

The platinum content was determined to be 1.1 wt% by ICP-OES. Accordingly, the hydrogenated material is called **hpolyTNECzB-Pt_{1.1}** in the following text.

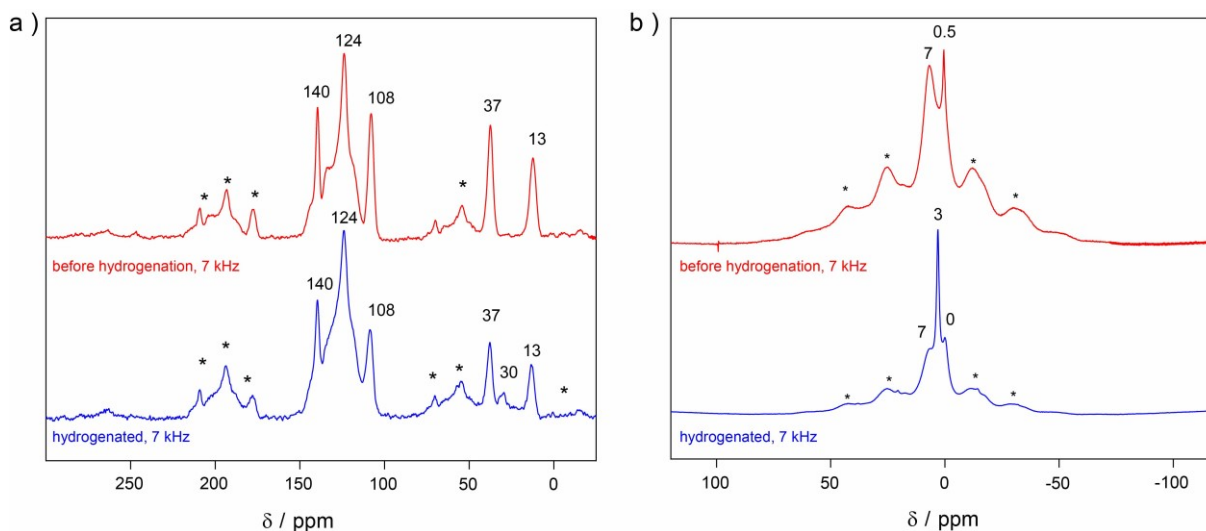


Figure 27: a) ^{13}C CPMAS NMR spectra of polyTNECzB (red) and the hydrogenated polymer hpolyTNECzB-Pt_{1.1} (blue) measured at 7 kHz. b) ^1H MAS NMR spectra of polyTNECzB (red) and the hydrogenated polymer hpolyTNECzB-Pt_{1.1} (blue) measured at 7 kHz.

The structure of **hpolyTNECzB-Pt_{1.1}** was characterized by ^{13}C CPMAS NMR spectroscopy (Figure 27, a). As is the case for **polyTNECzB**, signals with chemical resonances between 108 to 140 ppm were observed for the hydrogenated material deriving from the remaining aromatic backbone of **hpolyTNECzB-Pt_{1.1}**. The aliphatic signals at 37 and 13 ppm

were ascribed to ethyl groups ($-\text{CH}_2-$ and $-\text{CH}_3$) of NECz moieties. In addition to that, a third peak at 30 ppm was monitored, which assumingly stems from hydrogenated areas within the polymeric backbone. By including the results of ^1H MAS NMR spectroscopy further indications for partial hydrogenation were collected (Figure 27, b). Before hydrogenation, the material mainly exhibits signals in the aromatic area at 7 ppm and a sharp signal at 0.5 ppm, which is assigned to methyl groups $-\text{CH}_3$ of NECz. After hydrogenation, the intensity of the peak at 7 ppm decreased and the main signal at 3 ppm formed a shoulder, which is assumed to origin from aliphatic moieties in the scaffold due to hydrogenation.

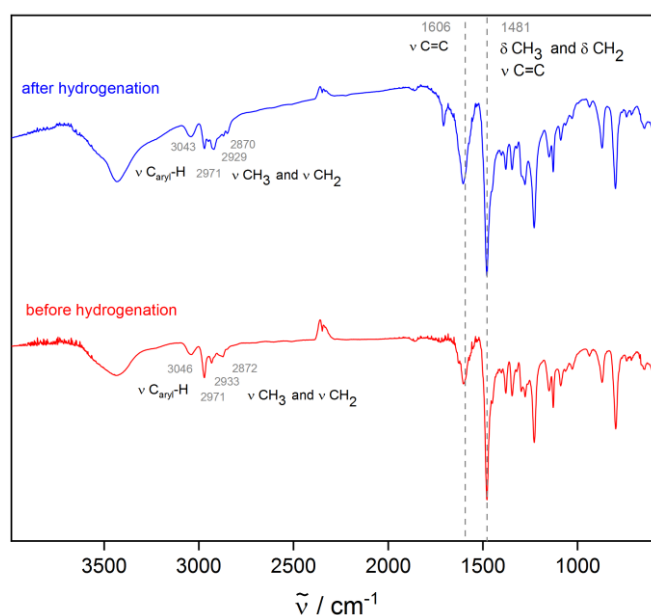


Figure 28: FTIR spectrum of polyTNECzB (red) and polyTNECzB-Pt_{1.1} (blue).

The FTIR spectrum of **hpolyTNECzB-Pt_{1.1}** shows that in comparison with **polyTNECzB** (Figure 28), the intensity of vibration stretching bands at 2929 and 2870 cm^{-1} increased pointing to an elevated amount of methylene $-\text{CH}_2-$ groups within the polymeric backbone.

The collected data for **hpolyTNECzB-Pt_{1.1}** give indications that hydrogenation on the polymer scaffold of **polyTNECzB** is possible. However, the hydrogenation degree seems lower in comparison to copolymer **hP_{0.5}-Pt_{2.7}**.

4.4 Conclusion and Outlook

The first part of the chapter demonstrates the applicability of bipyridine-containing CPOPs for photocatalysis. For that purpose, **CPOP-30** was synthesized from CzbiPy by oxidative homopolymerization. The BET surface area was determined to be $880 \text{ m}^2 \text{ g}^{-1}$ and UV-Vis spectroscopy indicated its suitability for light-harvesting purposes. For photocatalytic CO_2 reduction, successful postmodification with Re(I) complex was confirmed by XPS measurements. The metalated polymer **CPOP-30-Re** exhibits a BET surface area of $620 \text{ m}^2 \text{ g}^{-1}$ and consists of 16.6 wt% of rhenium, meaning 70% of all bipyridine units within the material were occupied by metal complexes. The direct synthesis of rhenium-containing monomers appeared to be an inappropriate method to form a Re(I)-complexed polymer network as the metal oxidizes during the polymerization in the presence of iron(III) chloride. First photocatalytic tests showed that metal-free **CPOP-30** acts as a photosensitizer and produces already small amounts of CO deriving from CO_2 reduction. For $[\text{Re}(\text{CzbiPy})(\text{CO})_3\text{Cl}]$ containing **CPOP-30-Re** maximal values of $623 \mu\text{mol g}^{-1} \text{ h}^{-1}$ CO production were achieved with a chemoselectivity of 98%. The catalyst possesses precisely defined active sites, which are comparable to its molecular equivalent $[\text{Re}(\text{CzbiPy})(\text{CO})_3\text{Cl}]$. In contrast to **CPOP-30-Re**, the molecular catalyst produces significantly higher amounts of CO within 30 minutes, however it decomposed immediately after that and formed inactive dimeric species under irradiation. Considering the short lifetime of the molecular equivalent, the immobilization of Re(I) catalyst on **CPOP-30** led to a more sustainable and stable catalyst in which the metal complex was protected from deactivation under illumination. In addition, **CPOP-30-Re** is easily recycled by filtration and used in further catalytic cycles. After four cycles of CO_2 reduction, 83% of its original activity was remained.

Furthermore, preliminary tests were performed to study **CPOP-30** as support for Ni-catalyzed sulfonylation under irradiation with visible-light. By coordination of Ni(II) salts with **CPOP-30**, 4-iodobenzotrifluoride and p-toluenesulfinate were cross-coupled with a conversion rate of 99% and a selectivity of 77%. The direct activation by blue light (440 nm) was achieved as the chelating macroligand of the Ni(II)-complex possesses an extended conjugated π -system. Therefore, CzbiPy-containing materials, such as **CPOP-30-Ni**, are promising candidates for noble metal-free systems to catalyze cross-couplings under mild conditions.

The third project of this chapter presents different carbazole-based polymers applied in physical and chemical storage of hydrogen. One approach was to synthesize copolymers by use of *N*-ethylcarbazole (NECz) as comonomer, which is already known for its hydrogen storage

capacity as liquid organic hydrogen carrier (LOHC).^[146] By addition of trigonal comonomer TCB, successful incorporation of NECz into a porous polymer network was achieved. Besides, NMR copolymerization studies gave evidence that the copolymers contained NECz dimer units, which were further cross-linked by TCB to give statistically distributed copolymers. Materials with percentages between 20 to 60 mol% of NECz were successfully produced and their BET surface areas ranged between 2054 and 736 m² g⁻¹. The copolymers as well as the TCB homopolymer, also known as CPOP-1^[1], were tested for their hydrogen uptake capacities by physisorption at 77 K. For **P_{0.2}**, the copolymer with 20 mol% of NECz, a maximum of 1.98 wt% hydrogen uptake was achieved. The highest value for the isosteric heat of adsorption was calculated for **P_{0.5}** with 11.0 kJ mol⁻¹, which is higher than previously reported values for carbazole-containing polymers ranging from 5.0-8.0 kJ mol⁻¹.^[83,90] Therefore, it is assumed that high percentages of NECz within the copolymer lead to higher affinity to hydrogen. For that reason, **P_{0.5}**, which consists 50:50 of NECz and TCB, was applied for further studies as solid-state hydrogen carrier. **P_{0.5}** exhibits a surface area of 911 m² g⁻¹ and was impregnated with chloroplatinic acid to form *in situ* Pt nanoparticles under hydrogen pressure. Different values between 6.0 to 0.2 wt% of platinum were applied to decorate the polymers with nanoparticles. For chemical storage of hydrogen within the polymeric scaffold, the impregnated materials were placed into the pressure reactor and were treated with 40 bar of hydrogen gas at 150 °C over 3 days. For all materials, ¹³C CPMAS NMR spectra after hydrogenation showed additional signals in the aliphatic area, pointing towards successful hydrogenation of the polymer backbone. It is assumed that NECz units were not fully converted into 12H-NECz moieties but also into partial hydrogenated derivatives such as 4H- and 8H-NECz. As the generation of nanoparticles happened *in situ* during the hydrogenation at 40 bar, the process of formation was not precisely controlled. TEM images reveal that agglomerated nanoparticles with diameters up to 60 nm led to low hydrogenation levels within the material. This was especially detected for **hP_{0.5}-Pt_{5.8}**, whereas TEM images for **hP_{0.5}-Pt_{2.7}** present homogeneously distributed nanoparticles around 2 nm and consequently a significantly higher proportion of hydrogenated moieties. Even with platinum loadings of 0.2 wt% successful hydrogenation of the polymer backbone took place. For future studies, the nanoparticle formation and their influence on the hydrogenation level, must be studied in more detail. For instance, controlled formation processes before the final hydrogenation are more favorable to vary the nanoparticle sizes. Another important aspect is the dehydrogenation of the solid-state hydrogen carriers. Preliminary tests applying TG-MS show that **hP_{0.5}-Pt_{5.8}** containing larger nanoparticles and yielding a rather low hydrogenation level, released small amounts of hydrogen at temperatures

between 95 and 135 °C, in contrast to **hP_{0.5}-Pt_{2.7}**, which is highly hydrogenated and seemingly decompose at 250 °C. It can be concluded that a balance between the right hydrogenation level and nanoparticle size must be found to prevent thermal decomposition before hydrogen is released in a controlled fashion. Another attempt to incorporate higher percentages of NECz units, was to design a homopolymer by use of 1,3,5-tris(*N*-ethyl-9H-carbazol-3-yl)benzene (TNECzB). The same hydrogenation procedure was applied to **polyTNECzB** and rather low hydrogenation levels were observed in comparison to previously discussed copolymers. The assumption consolidates that for reversible hydrogenation and dehydrogenation, a stable fundament, which is not hydrogenated, is needed to help in retaining the porous aromatic structure. For that purpose, high amounts of NECz are probably not favorable as the basic structure is irreversibly deformed. The hydrogenated material **hP_{0.5}-Pt_{5.8}** gives reason to assume that the concept of solid-state hydrogen carriers is feasible if the right conditions are found.

5 Microporous Phosphine-based Polymer Networks

5.1 Theoretical Background

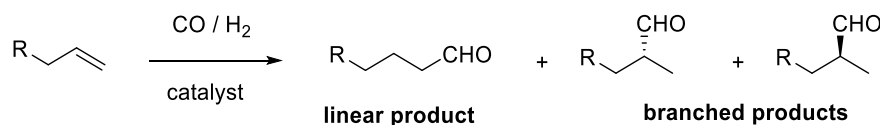
5.1.1 Wittig Reaction

When in 1952 the Wittig reaction was developed, it became of great relevance for opening up new possibilities in industrial preparation of vitamin A and carotenoids.^[157,158] To this day, the Wittig reaction plays a major role in industrial organic synthesis and production of fine chemicals, for which purpose tons of phosphorous reagents are applied.^[159] The Wittig reaction describes the formation of olefins from carbonyl compounds and stoichiometric amounts of triphenylphosphonium ylides. Triphenylphosphine and alkyl halides are applied as reactants to give different phosphonium salts which are further deprotonated by a strong base to yield phosphorus ylides. After [2+2] cycloaddition to generate an oxaphosphetane as an intermediate from ylide and carbonyl compound, it finally results in the desired olefin and triphenylphosphine oxide as a waste product.^[160,161] Further reactions such as Staudinger^[162], Appel^[163] or Mitsunobo^[164] reactions are also well-known for stoichiometric phosphine-promoted synthesis routes. For industry it is a huge drawback that the Wittig reaction is a stoichiometric process producing tons of by-product, which has no industrial application. For that reason, cheap ways to reduce triphenylphosphine oxides to triphenylphosphines are needed to target a catalytic protocol with an efficient recycling step.^[161,165] By re-entering reduced phosphine into the catalytic cycle sustainable processes are developed.^[166]

5.1.2 Phosphine as Ligand in Catalysis

In 1937, olefin hydroformylation, also known as oxo synthesis, was discovered by Otto Roelen of Ruhrchemie.^[167] During the process, alkenes are transformed into aldehydes in presence of hydrogen and carbon monoxide driven by cobalt catalysts under elevated temperatures and pressures.^[168] Nowadays, hydroformylation is one of the large-scale industrial processes for producing more than 10 million tons of aldehydes and other oxo compounds per year, which are further converted into alcohols, carboxylic acids, esters and amines.^[169,170] The

hydroformylation reaction is among the largest homogeneously catalyzed processes in industry usually based on cobalt or rhodium complexes (Scheme 11).^[169]



Scheme 11: Hydroformylation of olefins and its possible products depending on the regio- and stereo-selectivity of the catalyst.^[170]

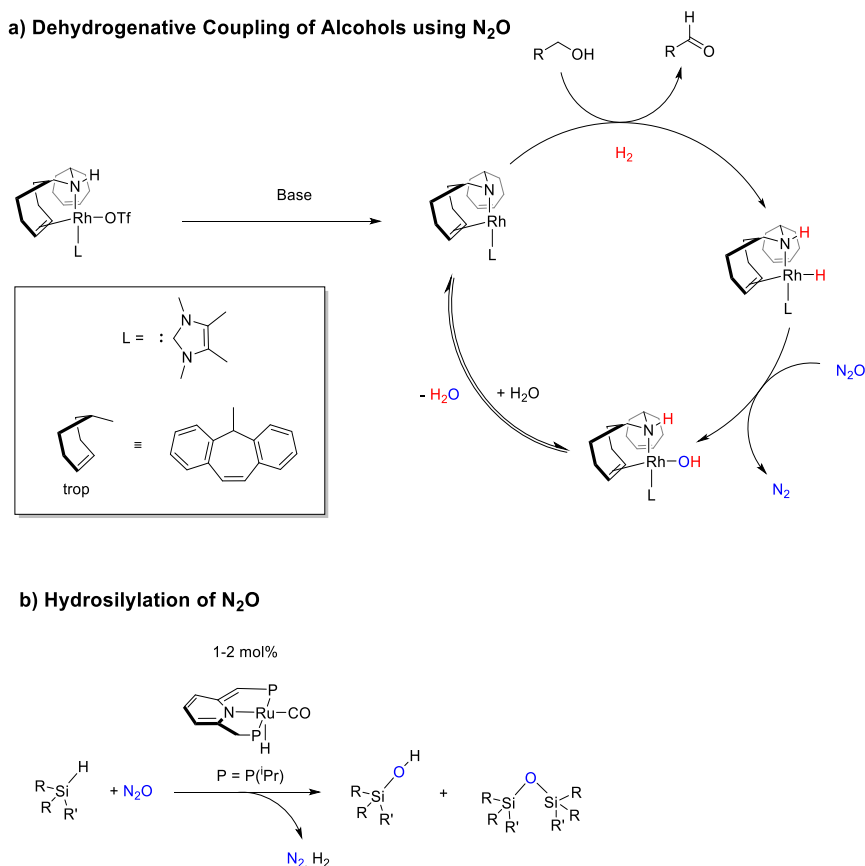
Cobalt catalysts require higher temperatures and pressures in comparison to rhodium-based catalysts, which are leading to higher selectivity and activity under milder reaction conditions.^[170] One of the first rhodium-based complexes was the Wilkinson-type catalyst^[171,172] ($\text{RhCl(PPh}_3)_3$), which was further developed by modifying the ligands, especially phosphorous-containing ones, to enhance regio- and stereoselectivity.^[169,170]

Since the 1980s, when triphenylphosphine was introduced as a ligand for the palladium-catalyzed Suzuki-Miyaura coupling reaction, phosphines have become an important class of ligands in catalysis of carbon-carbon cross coupling reactions. The Suzuki-Miyaura reaction links aryl halides and aryl boronic acids by means of tetrakis(triphenylphosphine)palladium(0) ($\text{Pd(PPh}_3)_4$).^[173]

As for most homogeneously catalyzed processes, phosphine-containing complexes are affected by poor catalyst recovery, high expenses for noble metals and impurities in generated products caused by remaining metal residues. Heterogenization of these catalysts is a possible strategy to solve the problem.^[170] Attempts to link triphenylphosphine moieties to different porous silica supports and following coordination of the catalyst increased the activity in contrast to their soluble counterparts.^[174,175] Furthermore, organic materials based on phosphine moieties are considered to be promising supports for rhodium catalysts (see chapter 5.1.5).^[72,176]

5.1.3 Hydrogenation and Hydrosilylation of Nitrous Oxide

Not just chlorofluorocarbons (CFCs) but also the greenhouse gas nitrous oxide (N_2O) is known to contribute to ozone-depleting processes.^[177] Consequently, it is of enormous relevance to develop ways of directly transforming nitrous oxide into harmless or even useful chemicals.^[178] Two ways of reducing nitrous oxide to molecular nitrogen are currently under consideration. On the one hand, hydrogenation of nitrous oxide releases nitrogen and water, and on the other hand hydrosilylation by which the oxygen atom of nitrous oxide is transferred into silane to form silicon-oxygen bonds and release nitrogen gas.^[178]



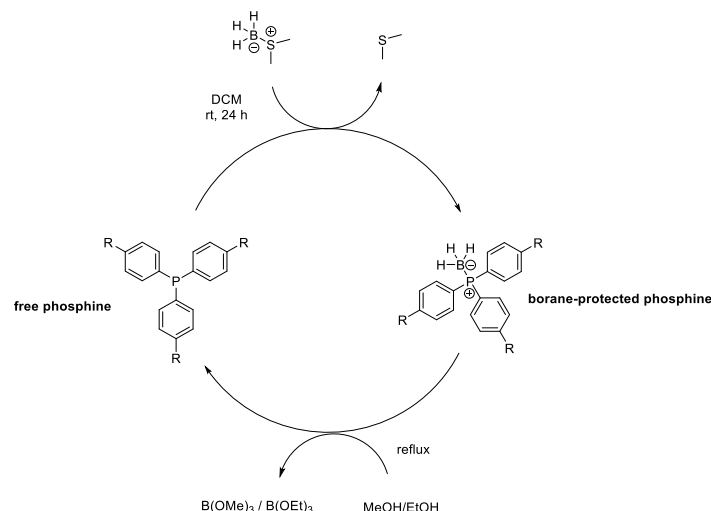
Scheme 12: a) Dehydrogenative coupling of alcohols in presence of nitrous oxide by applying rhodium(I) amido bis(olefin) catalyst.^[179] b) Hydrosilylation of nitrous oxide by pincer ruthenium complex.^[178]

In 2016, Gianetti *et al.* showed that rhodium(I) amido bis(olefin) complexes, which are already well-known as efficient transfer hydrogenation catalysts could be applied also in dehydrogenative coupling of alcohols utilize nitrous oxide as hydrogen acceptor (Scheme 12, a).^[179,180] During the catalytic cycle, the amido carbene rhodium complex promotes the hydrogenation of nitrous oxide to water.^[179] Zeng and coworkers published the first ruthenium pincer catalyst, which oxidizes tertiary silanes to silanols and siloxanes, known as catalytic hydrosilylation of nitrous oxide (Scheme 12, b). However, the process needs to be further optimized due to low turnover numbers (TON) and frequencies (TOF) and release of hydrogen as by-product of the hydrosilylation.^[178]

5.1.4 Protection Method for Phosphines

One disadvantage of handling phosphines is their sensitivity towards oxygen. Even if the formation of phosphine oxides is prevented during the synthesis, the purification and storage under inert conditions must be assured to exclude the possibility of oxidation.^[181,182] A possibility to prevent oxidation of trivalent phosphorous compounds is to form air-stable

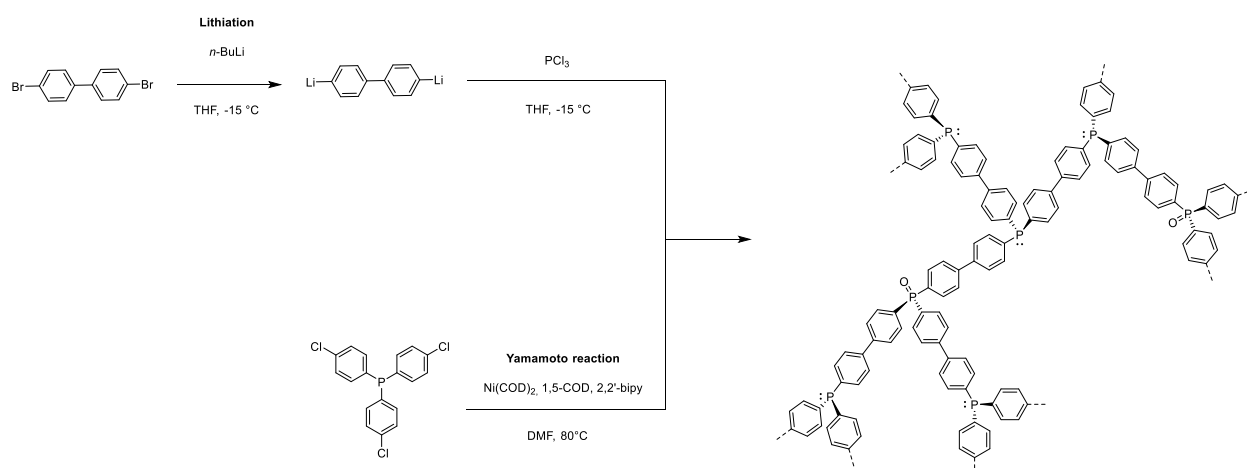
phosphine-borane adducts.^[183] This method of temporary protection is achieved by addition of commercial available adducts such as borane dimethylsulfide ($\text{BH}_3\text{-SMe}_2$) or borane tetrahydrofuran complexes to yield stable phosphine-borane analogues.^[182,184] Nevertheless, deprotection is easily accomplished through cleavage of phosphorous-borane bonds by alcoholysis (Scheme 13). Refluxing the adducts in methanol or ethanol leads to formation of volatile boranes, trimethyl and triethyl borate, respectively, which are efficiently removed by evaporation without further purification.^[181]



Scheme 13: Protection of triphenylphosphine by formation of phosphine-borane adducts.^[181]

5.1.5 Phosphine-based Polymers

In 2013, the first microporous phosphine-based polymer networks were reported by Fritsch^[176] and Zhang^[185] (Scheme 14). So-called EOF-17 (element organic framework) was synthesized from 4,4'-dibromobiphenyl and phosphorus chloride *via* lithiation and possesses a S_{ABET} of $458 \text{ m}^2 \text{ g}^{-1}$. The material was impregnated with different percentages of palladium(II) chloride and 5 mol% of Wilkinson's catalyst ($\text{RhCl}(\text{PPh}_3)_3$) for heterogeneously catalyzed transfer hydrogenation of cyclohexanone.^[176] Another approach of synthesizing triphenylphosphine networks was to apply nickel-mediated Yamamoto cross-coupling reaction to form a polymer from tris(4-chlorophenyl)phosphine exhibiting a S_{ABET} of $1284 \text{ m}^2 \text{ g}^{-1}$. Zhang and coworkers immobilized palladium nanoparticles within the structure by impregnation with tetrakis(triphenylphosphine)palladium(0) ($\text{Pd}(\text{PPh}_3)_4$) solution to catalyze Suzuki cross-coupling reactions of aryl halides with phenylboronic acids.^[185] However, for both synthesis strategies ^{31}P MAS NMR spectra show partially oxidized triphenylphosphine units within the structures due to air sensitivity of triphenylphosphine. Phosphine and phosphine oxide moieties were detected at around -8 ppm and 25-29 ppm, respectively.^[176,185]



Scheme 14: Synthesis methods for poly(triphenylphosphine) networks.^[176,185]

Over time, more synthesis approaches to incorporate triphenylphosphine moieties within polymeric scaffolds were developed and investigated for diverse applications (Figure 29). Porous organic ligands, POL-PPh₃, were introduced by Sun *et al.* who applied vinyl-functionalized triphenylphosphines in a solvothermal polymerization initiated by azobisisobutyronitrile (AIBN).^[72] The porous phosphine-support was impregnated with (acetylacetonato)dicarbonylrhodium(I) (Rh(CO)₂(acac)) and the resulting immobilized rhodium catalyst showed higher selectivity and stability in the hydroformylation of 1-octene in contrast to its molecular counterpart.^[72] In 2016 Yang and coworkers introduced the mesoporous poly(triphenylphosphine), poly(PPh₃)-azo, produced *via* oxidative polymerization from phosphine-based aromatic amines. Poly(PPh₃)-azo was coordinated by ruthenium and silver cations for catalyzing carbon dioxide transformation, such as carboxylative cyclization of propargylic alcohols.^[186]

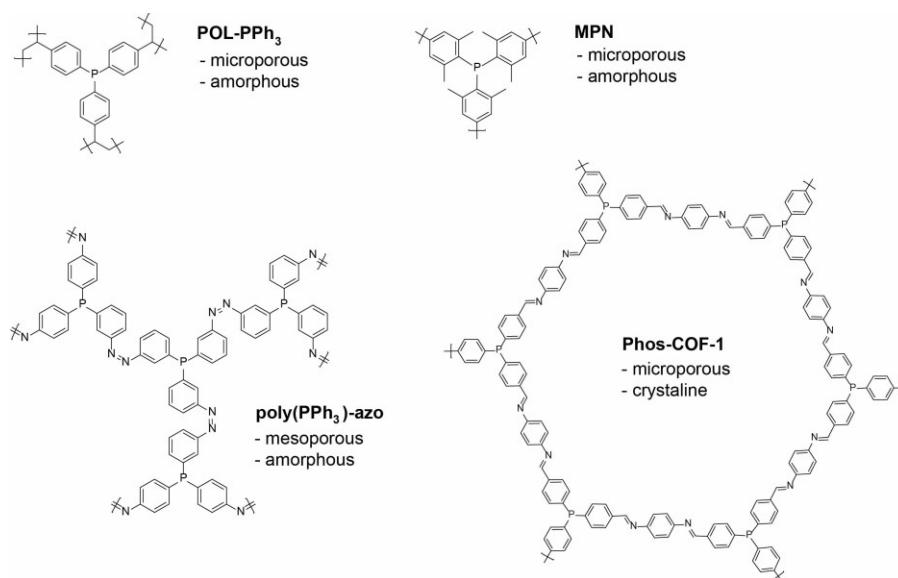


Figure 29: Different triphenylphosphine-containing polymer structures.^[72,186–188]

A strategy to lower the sensitivity of triphenylphosphine polymers towards air is to incorporate steric moieties to shield phosphorus from oxidation. Microporous polymer networks were synthesized from tris(4-bromo-2,6-dimethylphenyl)phosphine by Yamamoto cross-coupling reaction (Figure 29).^[187] By following impregnation of the polymer with a Lewis acid, an embedded frustrated Lewis pair within in a microporous material is obtained enabling hydrogen activation at room temperature.^[187] Recently, Tao and coworkers managed to obtain the first phosphine-based covalent organic framework, Phos-COF-1, which was manufactured *via* co-condensation of phosphine-containing trialdehyde and diamine. After introducing various metal nanoparticles, the heterogeneous catalyst was applied in Suzuki-Miyaura coupling reaction.^[188] Shortly after, Liu *et al.* published similar phosphine-based COFs called P-COF-1 and P-COF-2, which were applied as support for a Rh(I) catalyst for hydroformylation.^[189] For the hydroformylation of 1-octene, conversion rates of up to 92% with a regioselectivity of 1.1 molar ratio linear/branched aldehydes was achieved.

5.2 Objective

Over the years, phosphines and other phosphorous-based compounds became an important class of ligands in homogeneous catalysis. This includes catalytic processes such as hydroformylation, carbon-carbon cross coupling reactions, hydrogenation, hydrosilylation as well as the Wittig reaction.^[161,169,173,179] In order to bridge the gap between homogeneous and heterogeneous catalysis, an approach is to embed the phosphine-based metal-organic complexes on microporous polymer networks (MPNs) to enhance stability and recyclability of the catalysts.^[9] Considering the high sensitivity of phosphine towards air, a strategy needs to be developed, which ensures that oxidation to phosphine oxide is prevented. This is necessary to provide a high number of accessible coordination sites to obtain well-distributed metal species on the support.

For this purpose, borane-protected phosphines are applied as monomers in Yamamoto cross-coupling reactions to yield a phosphine-containing polymer, which can be deprotected on demand, and thus further postmodified. The phosphine network shall be used as porous macroligand for immobilization of rhodium(I) catalyst for hydrosilylation as well as hydroformylation. Additionally, statistical copolymers shall be designed, which lead to dilution of phosphine proportion in the polymeric backbone. One goal is to study the activity of copolymers in comparison with homopolymeric triphenylphosphine polymers for the different catalytic processes and the influence of coordinated amount of rhodium within the porous material.

5.3 Results and Discussion

5.3.1 Material Synthesis and Characterization of Phosphine-based Polymers

5.3.1.1 Phosphine-based Polymers for Hydrosilylation

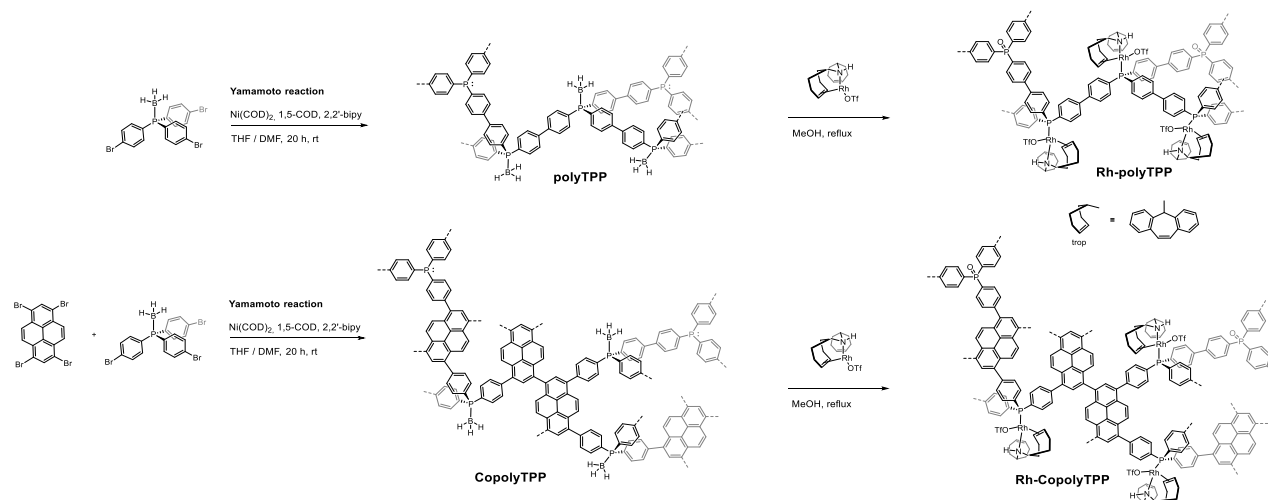
As already mentioned (chapter 5.1.2), the conversion of nitrous oxide into non-harmful chemicals is a crucial research field to fight global warming.^[177,179] The Grützmacher group from ETH Zürich is specialized in organometallic chemistry and works on development of rhodium-based catalysts for hydrogenation and hydrosilylation of nitrous oxide.^[179,190] In close collaboration with Monica Trincado from the Grützmacher group, the design of a heterogenized rhodium catalyst for hydrosilylation was targeted to enhance selectivity and stability of the catalyst. Therefore, the rhodium(I) amido bis(olefin) complex $[\text{Rh}(\text{trop}_2\text{NH})(\text{PPh}_3)](\text{OTf})$ ($\text{trop}_2\text{N} = \text{bis}(5\text{-H-dibenzo-[a,d]cyclohepten-5-yl)amide}$), which is already well-studied for its application in transfer hydrogenation, was provided by Trincado and coworkers.^[180] The design and synthesis of supporting materials for the metal-organic complex, as well as the characterization of solid phase catalyst was my contribution to this project and is described in the following chapter.

In order to provide a support for $[\text{Rh}(\text{trop}_2\text{NH})](\text{OTf})$ units to catalytically convert nitrous oxide, the polymeric system needs to function as an anchor point. A tailor-made microporous poly(triphenylphosphine) network would supply coordination sites in the polymer backbone and therefore it can ensure single-site catalysis. Due to the high sensitivity of triphenylphosphine (TPP) towards air, the polymerization of tris(4-bromophenyl)phosphine *via* Yamamoto^[191] reaction would lead to oxidized triphenylphosphine oxide moieties within the network.^[182] Hence, the protection of triphenylphosphine by boranes is needed to prevent the phosphine units from oxidation before coordination to the desired catalyst (chapter 5.1.4).^[181] For that purpose, the polymer was synthesized from borane coordinated tris(4-bromophenyl)phosphine *via* Yamamoto cross-coupling to yield a microporous network (**polyTPP**), which possesses accessible triphenylphosphine anchor points for single site catalysis (Scheme 15). In this approach, each repeating unit of the polymer can function as a coordination site.

To reduce the concentration of phosphine and therefore the amount of immobilized catalyst, it is possible to introduce a comonomer, such as tetrabromopyrene. The copolymerization is carried out similarly to the purely triphenylphosphine-containing polymer **polyTPP**. 1,3,6,8-Tetrabromopyrene and tris(4-bromophenyl)phosphine borane were applied

in a ratio of 3:4 and yielded a statistically distributed copolymer **CopolyTPP** (Scheme 15). Since, the yield was calculated to be 90%, it is not guaranteed that the ratio of incorporated comonomers is exactly 3:4.

For coordination of $[\text{Rh}(\text{trop}_2\text{NH})](\text{OTf})$, each material was refluxed in methanol to remove the borane protection group and exchange boranes by Rh(I) catalyst (**Rh-polyTPP** and **Rh-CopolyTPP**, Scheme 15).



Scheme 15: Synthesis of $[\text{Rh}(\text{trop}_2\text{NH})(\text{OTf})]$ immobilized microporous triphenylphosphine-containing polymer networks produced from tris(4-bromophenyl)phosphine borane (Rh-polyTPP**) and pyrene (**Rh-CopolyTPP**) derivatives, which were polymerized *via* Yamamoto cross-coupling reaction.**

The porosity was investigated by low-pressure N_2 sorption studies showing that the materials, before and after coordination to Rh(I), exhibit high N_2 uptake at low pressures, which is characteristic for microporous systems.^[11] By means of the BET model, the surface areas of borane-protected poly(triphenylphosphine) networks were determined to be $989 \text{ m}^2 \text{ g}^{-1}$ for **polyTPP** and $797 \text{ m}^2 \text{ g}^{-1}$ for **CopolyTPP**, whereas the Rh(I) coordinated polymers were calculated to be $31 \text{ m}^2 \text{ g}^{-1}$ and $290 \text{ m}^2 \text{ g}^{-1}$ for **Rh-polyTPP** and **Rh-CopolyTPP**, respectively (Figure 30). The strong decrease in S_{BET} for **Rh-polyTPP** was attributed to an increase of molecular weight due to immobilization of the rhodium catalyst as well as partial oxidation of non-coordinated phosphine units. In comparison to **Rh-polyTPP**, **Rh-CopolyTPP** shows a lower decrease in S_{BET} due to a lower loading of Rh(I) catalyst. This assumption was also confirmed by ICP-OES showing that **Rh-polyTPP** and **Rh-CopolyTPP** contain 8.0 wt% and 6.6 wt% of rhodium, respectively. In comparison to theoretical rhodium values, 71% of the available phosphine units in **Rh-polyTPP** were coordinated by Rh(I). If it is assumed that the ratio of incorporated comonomers in **Rh-CopolyTPP** corresponds to 3:4, 68% of the coordination sites were occupied by Rh(I) complex.

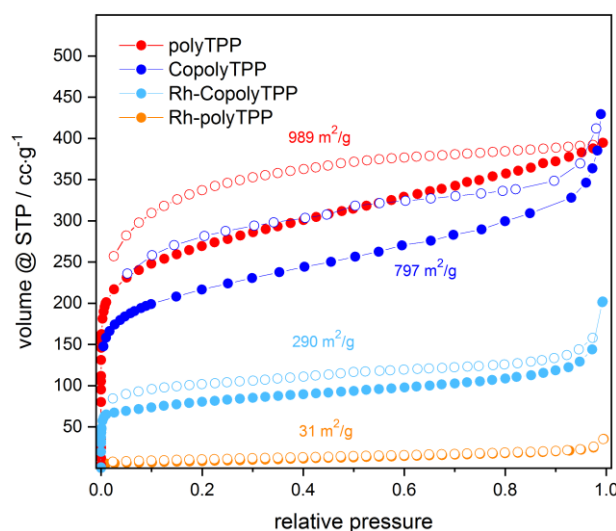


Figure 30: Nitrogen isotherms of polyTPP, Rh-polyTPP, CopolyTPP and Rh-CopolyTPP, respectively.

The chemical structure for **polyTPP** (Figure 31) and **CopolyTPP** (appendix, Figure A 8) were confirmed by ^{31}P , ^{11}B and ^{13}C solid-state NMR spectroscopy. In ^{31}P MAS NMR spectra the high-intensity signals at 22 ppm were assigned to phosphorus coordinated by boranes P-B and the second signal at -8 ppm corresponds to free triphenylphosphine units. The borane coordination was confirmed by ^{11}B MAS NMR spectroscopy showing a single signal at -42 ppm. In the ^{13}C CPMAS NMR spectrum, signals between 127 to 133 ppm were monitored and assigned to aromatic groups $\text{C}_{\text{Ar-H}}$. The signal at 142 ppm is shifted to low-field due to the coordination of aromatic carbons to phosphorus $\text{C}_{\text{Ar-P}}$.

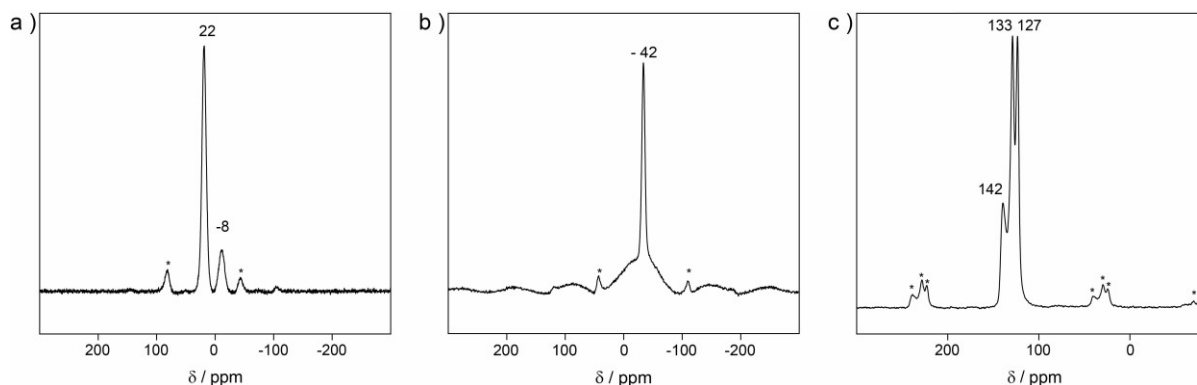


Figure 31: a) ^{31}P MAS, b) ^{11}B MAS and c) ^{13}C CPMAS NMR spectra of polyTPP.

After immobilization of Rh(I) catalyst on **polyTPP** and **CopolyTPP**, the catalyst decorated materials **Rh-polyTPP** and **Rh-CopolyTPP** were characterized by ^{31}P MAS NMR spectroscopy (Figure 32, a)). The spectrum of **Rh-polyTPP** shows an intense and broad signal at 40 ppm with two shoulders at 26 and 12 ppm. The main signal at 40 ppm corresponds to phosphorus coordinated to rhodium P-Rh. It is assumed, that the second low-intensity shoulder at 12 ppm is part of the doublet resulting from P-Rh coupling, due to the NMR active nuclei ^{31}P .

and ^{103}Rh .^[190] The findings accord with the solid-state NMR spectrum of the molecular catalyst showing a doublet with an intense signal at 34 ppm and a low-intensity signal at 14 ppm. For the Rh-coordinated materials, these signals are slightly shifted compared to the molecular catalyst, due to immobilization in the microporous polymer. For **Rh-polyTPP** as well as for **Rh-CopolyTPP**, a second signal between 26 and 29 ppm was detected, respectively, indicating oxidized phosphorus species $\text{P}=\text{O}$. Non-coordinated phosphine sites were probably oxidized after exposing the material to air. Nevertheless, the signal between 40 and 41 ppm confirms the successful coordination of Rh(I) catalyst on the porous supports.

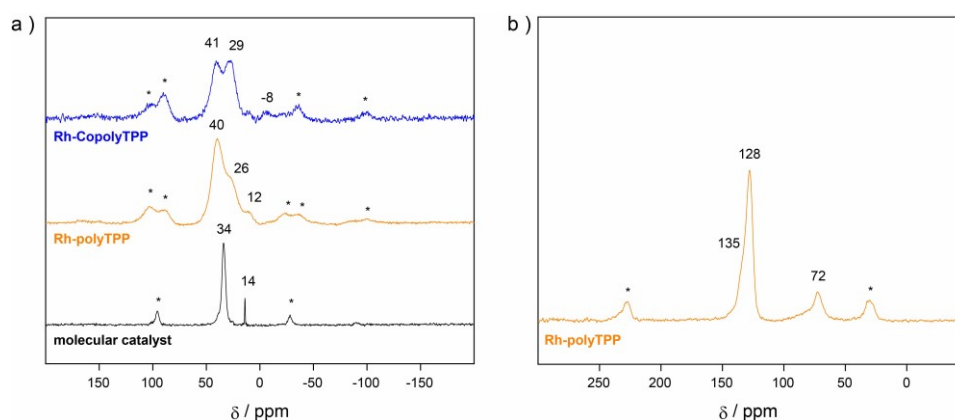


Figure 32: a) ^{31}P MAS NMR spectra of molecular catalyst, Rh-polyTPP and Rh-CopolyTPP, b) ^{13}C CPMAS NMR spectrum of Rh-polyTPP.

The material **Rh-polyTPP** was additionally analyzed by ^{13}C CPMAS NMR spectroscopy (Figure 32, b)). The spectrum presents a broad signal at 128 ppm corresponding to the chemical resonance peaks of **polyTPP** (Figure 31) and the aromatic carbons of the molecular catalyst. The low-intensity signal at 72 ppm derives from olefinic carbons of the ligands coordinated to Rh(I) catalyst and gives further indication for the successful immobilization of the rhodium complex.^[190]

Moreover, the immobilization of Rh(I) catalyst was confirmed by XPS (Figure 33). Rh 3d core-level spectra of **Rh-polyTPP** and **Rh-CopolyTPP** show a single doublet with signals at 307.9 (3 $d_{5/2}$) and 312.6 eV (3 $d_{3/2}$), which are consistent with the typical Rh(I)-doublet for molecular catalyst $[\text{Rh}(\text{trop}_2\text{NH})(\text{PPh}_3)]\text{OTf}$. Furthermore, the P 2p spectra of the Rh-coordinated polymers present a broad signal, respectively, occurring due to two phosphorous species within the materials. The doublet at 131.4 eV (2 $p_{3/2}$) and 132.4 eV (2 $p_{1/2}$) corresponds to phosphines coordinated by rhodium P-Rh, according to the P 2p signal of the molecular catalyst at 131.5 eV, and the second doublet at 132.4 (2 $p_{3/2}$) and 133.4 eV (2 $p_{1/2}$) appeared as a result of oxidized phosphorus $\text{P}=\text{O}$. This observation coincides with the previous stated assumption, that free phosphine moieties tend to oxidize, if they are not coordinated. The metal free polymers **polyTPP** and **CopolyTPP** show doublets with signals at 131.8 (2 $p_{3/2}$) and

132.9 eV ($2p_{1/2}$), which were assigned to phosphorus binding to borane P-B. Additionally, **polyTPP** shows a second doublet at 130.7 eV ($2p_{3/2}$) indicating free phosphine moieties, suggesting that some phosphine moieties within the polymers were shielded from oxidation.

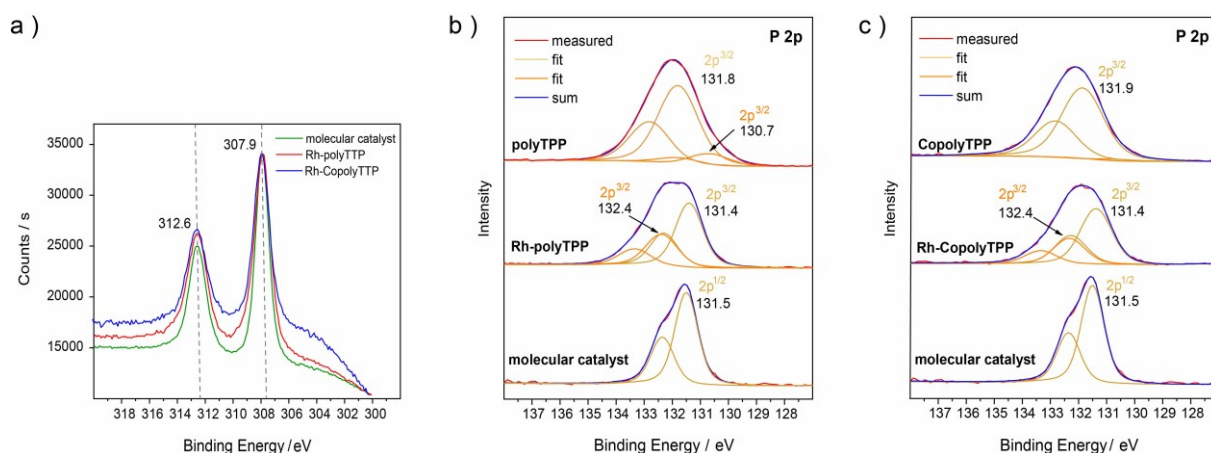


Figure 33: Rh 3d and P 2p XPS spectra. a) Rh 3d XPS spectra of Rh-polyTPP (red) and Rh-CopolyTPP (blue) in comparison to molecular catalyst [Rh(trop₂NH)(PPh₃)]OTf (green). b) P 2p XPS spectra of Rh-polyTPP, polyTPP and molecular catalyst. c) P 2p XPS spectra of Rh-CopolyTPP, CopolyTPP and molecular catalyst.

The morphology of the Rh-containing polymers was investigated by SEM and shows granular particles (Figure 34). Moreover, homogeneous distribution of phosphorus, rhodium and carbon was monitored by elemental mapping within **Rh-polyTPP** and **Rh-CopolyTPP**.

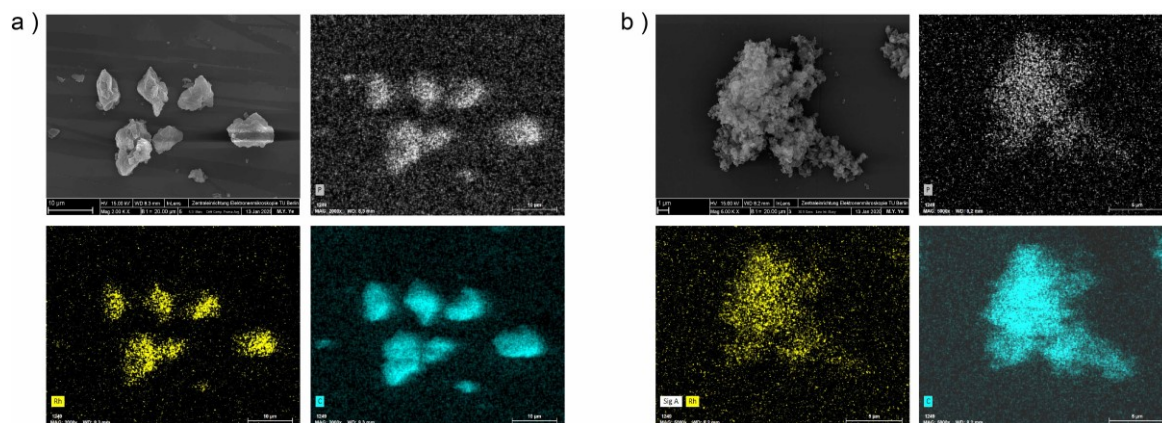
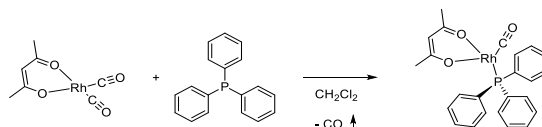


Figure 34: Scanning electron microscopy and elemental mapping of a) Rh-polyTPP and b) Rh-CopolyTPP. Grey belongs to phosphorus, yellow belongs to rhodium, blue belongs to carbon.

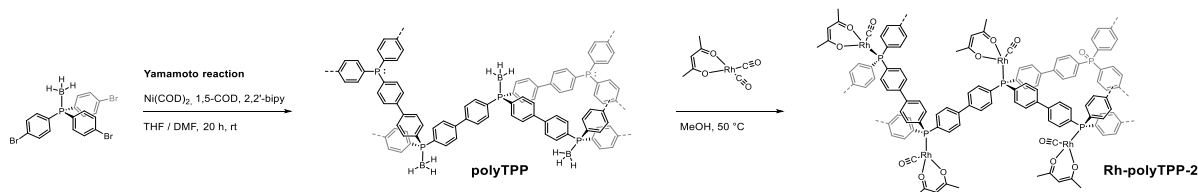
5.3.1.2 Phosphine-based Polymers for Hydroformylation

The previously described triphenylphosphine-based polymer **polyTTP** (chapter 5.3.1.1), was not only applied as support for the rhodium(I) amido bis(olefin) complex, but also for a hydroformylation rhodium catalyst. In presence of stoichiometric amounts of triphenylphosphine, the typical precursor rhodium(I) dicarbonyl acetylacetonate $[\text{Rh}(\text{CO})_2(\text{acac})]$ yields the hydroformylation catalyst rhodium(triphenylphosphine)-carbonylacetylacetonate $[\text{Rh}(\text{CO})(\text{acac})(\text{PPh}_3)]$ (Scheme 16).



Scheme 16: Synthesis of the molecular catalyst for hydroformylation from triphenylphosphine and $[\text{Rh}(\text{CO})_2(\text{acac})]$.

For the heterogenization of the molecular catalyst, similar conditions were applied to obtain rhodium(I) supported on **polyTTP**, so-called **Rh-polyTTP-2** (Scheme 17). Under inert atmosphere, the borane-protected phosphine polymer was refluxed in methanol to yield free phosphine units coordinated by $[\text{Rh}(\text{CO})_2(\text{acac})]$. The Rh(I) precursor was added in a slight excess of 1.1 equivalents regarding the possible coordination sites within **polyTTP**.



Scheme 17: Synthesis of $[\text{Rh}(\text{CO})_2(\text{acac})]$ immobilization on microporous triphenylphosphine-containing polymer network **polyTTP produced from tris(4-bromophenyl)phosphine borane via Yamamoto cross-coupling reaction.**

The chemical structure of **Rh-polyTTP-2** was analyzed by ^{31}P MAS NMR spectroscopy (Figure 35, a). The spectrum shows a broad signal at 31 ppm and a small shoulder at 47 ppm, which was assigned to Rh(I) catalyst coordinated by phosphine. The spectrum of the molecular catalyst $[\text{Rh}(\text{CO})(\text{acac})(\text{PPh}_3)]$ possesses a doublet at 27 and 47 ppm occurring due to the coupling of ^{103}Rh and ^{31}P nuclei. For the spectra of **Rh-polyTTP-2** and the molecular catalyst, comparable chemical shifts were observed, hence successful coordination of Rh(I) complex was assumed. For **Rh-polyTTP-2** an additional signal at -8 ppm was monitored, pointing towards small amounts of free phosphines as detected for metal-free polymer **polyTTP**. Nevertheless, oxidation of phosphine moieties cannot be excluded as oxidized species $\text{P}=\text{O}$ appear between 26 to 29 ppm, which can be overlapped by the broad signal at 31 ppm.

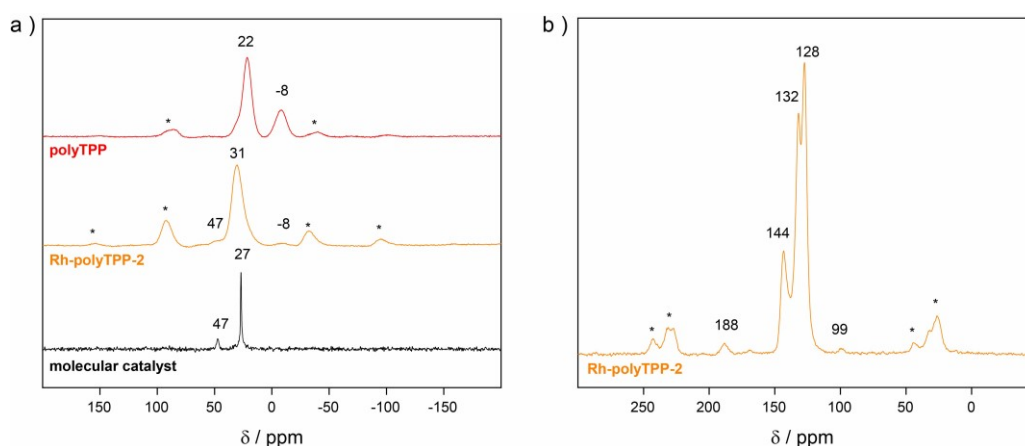


Figure 35: a) ^{31}P MAS NMR spectra of molecular catalyst, Rh-polyTPP-2 and polyTPP, b) ^{13}C CPMAS NMR spectrum of Rh-polyTPP-2.

Furthermore, ^{13}C CPMAS NMR measurements were conducted (Figure 35, b) to determine the chemical structure of **Rh-polyTPP-2**. The spectrum of **Rh-polyTPP-2** shows signals at 144, 132 and 128 ppm deriving from aromatic carbons of the triphenylphosphine backbone of metal-free support **polyTPP**. The characteristic chemical resonance at 188 ppm was assigned to carbonyl carbons coordinated to rhodium (Rh-C=O).^[192] Additionally, a signal at 99 ppm was detected corresponding to the sp^2 carbon of the acetylacetonato ligand. Further signals of the ligands should be detected at around 27 ppm, which probably overlap with the spinning sidebands. The observed signals are identical with the chemical resonances in liquid ^{13}C NMR spectra of the molecular catalyst $[\text{Rh}(\text{CO})(\text{acac})(\text{PPh}_3)]$ (experimental section 8.3).

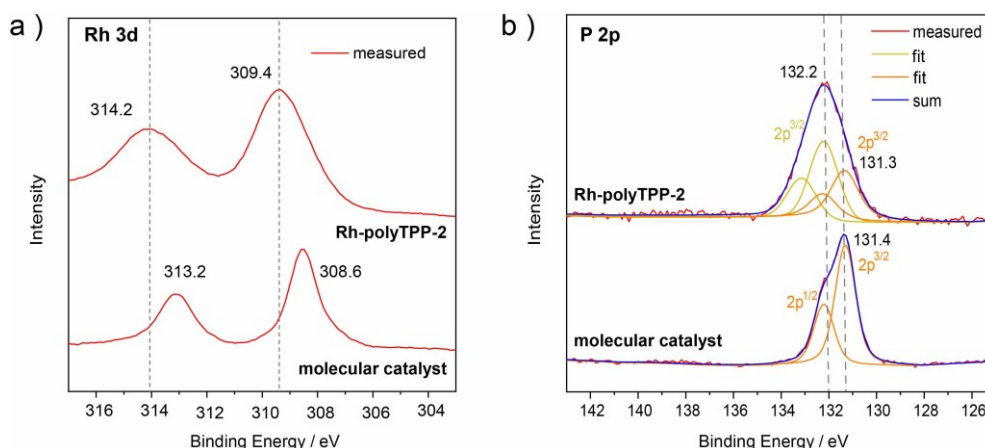


Figure 36: Rh 3d and P 2p XPS spectra. a) Rh 3d XPS spectra of Rh-polyTPP-2 in comparison to molecular catalyst $[\text{Rh}(\text{CO})(\text{acac})(\text{PPh}_3)]$. b) P 2p XPS spectra of Rh-polyTPP-2 and molecular catalyst.

The Rh 3d core-level XPS measurement of **Rh-polyTPP-2** confirmed successful immobilization of Rh(I) catalyst (Figure 36), showing the characteristic Rh(I) doublet signals at 309.4 ($3\text{d}_{5/2}$) and 314.2 eV ($3\text{d}_{3/2}$).^[193] In comparison to the molecular catalyst $[\text{Rh}(\text{CO})(\text{acac})(\text{PPh}_3)]$, the doublet is shifted by 0.8 eV towards higher binding energies. If the molecular complex is compared with **Rh-polyTPP-2**, it must be considered, that **polyTPP**

exhibits pores consisting of several TPP coordination sites. This means that the Rh(I) species are possibly coordinated by multiple TPPs instead of just one phosphorus ligand. As the amorphous character of **polyTPP-2** involves a broad pore size distribution, it results in different environments for coordination. This phenomenon was already observed by Sun *et al.*^[72], who reported coordination of three TPP ligands due to high concentration of phosphorus ligands in the surrounding of Rh(I) catalyst.^[170] They detected a doublet signal at 309.1 and 313.9 eV in the Rh 3d core level spectrum, coinciding with the values reported in this thesis. The shift of binding energy, which is observed in comparison to [Rh(CO)(acac)(PPh₃)], can be explained by the exchange of ligands and thus the environment of Rh(I). The coordination of an additional phosphine in the sphere of Rh(I), can add up to 0.5 eV towards the overall binding energy.^[194]

In the P 2p spectrum of the molecular catalyst, a single phosphorous species was detected. The doublet was monitored at 131.4 and 132.2 eV and assigned to phosphines coordinated by rhodium P-Rh. For polymer **Rh-polyTPP-2**, two phosphine species were found, the first doublet was observed at 131.3 (2 p_{3/2}) and 132.2 eV (2 p_{1/2}) corresponding the signals of the molecular catalyst. The additional doublet at 132.2 (2 p_{3/2}) and 133.2 eV (2 p_{1/2}) was ascribed to oxidized phosphorus P=O, occurring after deprotection of the phosphine units and treatment with the rhodium precursor. As observed for **Rh-polyTPP** and **Rh-CopolyTPP** (see 5.3.1.1), it is assumed that non-coordinated phosphine moieties would oxidize, if the polymer was exposed to air. Considering that XPS is a surface technique, the ratio of monitored phosphine oxides compared to Rh-coordinated phosphines measured might be higher in comparison to the overall ratio within the network.

With respect to all collected solid-state NMR and XPS measurements, it is assumed that the presence of different coordination environments within the polymer backbone led to Rh coordinated by multiple TPPs as well as a single TPP. This assumption also explains why the Rh 3d core-level spectra show broadened signals in comparison to the Rh immobilized polymer **Rh-polyTPP** from previous chapter 5.3.1.1.

ICP-OES confirms that **Rh-polyTPP-2** contains 21.5 wt% rhodium. In case of an ideal network, thus coordination of one phosphine unit by one rhodium complex, around 21.0 wt% of rhodium would be expected.

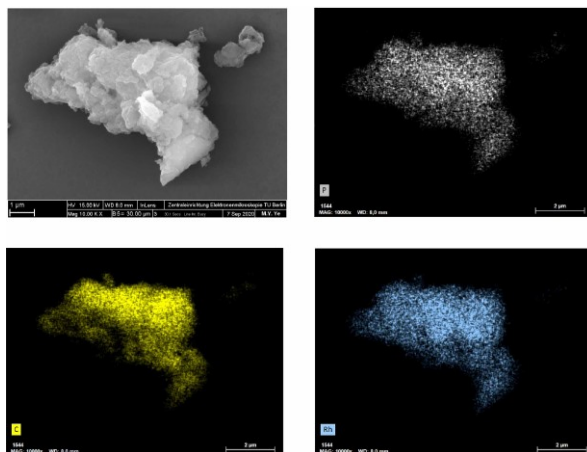


Figure 37: Scanning electron microscopy and elemental mapping of Rh-polyTPP-2. Grey belongs to phosphorus, yellow belongs to carbon, blue belongs to rhodium.

The morphology of the Rh-containing polymer **Rh-polyTPP-2** was investigated by SEM and show granular particles (Figure 37). Moreover, homogeneous distribution of phosphorus, rhodium and carbon was monitored within the polymer by elemental mapping.

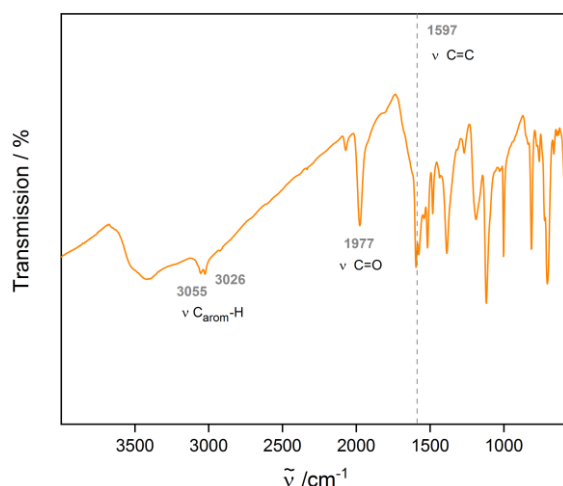


Figure 38: FTIR spectrum of Rh-polyTPP-2.

The FTIR spectrum confirms the incorporation of Rh(I) within the pores of **Rh-polyTPP-2**, displaying the vibration band at 1977 cm^{-1} , which was assigned to coordinated carbonyl C=O ligands of the metal-organic complex (Figure 38).^[193] Furthermore, typical vibration bands at 1597 , 3026 and 3055 cm^{-1} were detected, corresponding to aromatic C-C bond and aromatic C-H vibrations, respectively.

Nitrogen sorption measurements were performed to investigate the porosity of the materials (Figure 39). The type I shaped isotherms possess a pronounced increase at low relative pressures, which is characteristic for microporous polymers.^[11] The BET surface area of **Rh-polyTPP-2**, based on the N₂ isotherm, was determined to be $421\text{ m}^2\text{ g}^{-1}$, whereas the borane-protected **polyTPP** possesses a S_{BET} of $989\text{ m}^2\text{ g}^{-1}$. Thus, a decline by half, deriving from high weight percentages of Rh(I) complexes anchored to the pore walls, was observed.

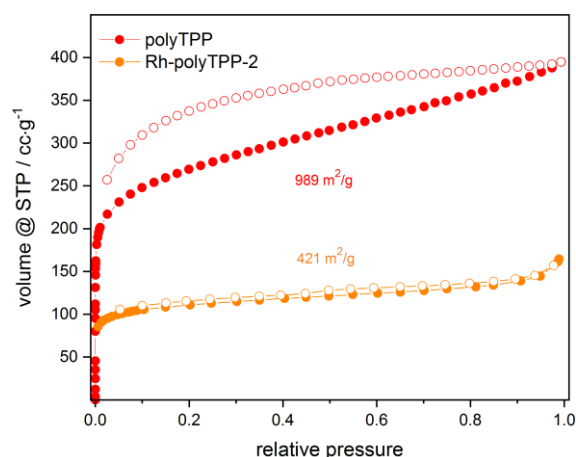
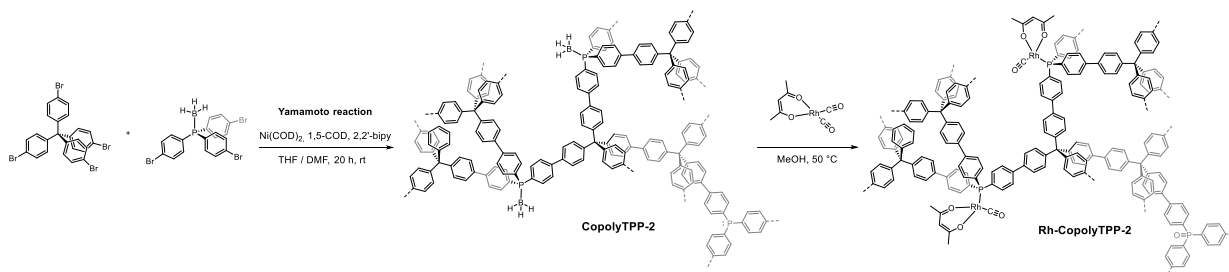


Figure 39: Nitrogen isotherms of polyTPP and Rh-polyTPP-2, respectively.

During the synthesis and characterization of **Rh-polyTPP-2** several challenges arose. On the one hand, the coordination process of Rh(I) catalyst onto **polyTPP** was not fully controllable, due to multiple TPP units within the coordination sphere. And on the other hand, the high loading of rhodium in **Rh-polyTPP-2** led to a significant decrease in surface area, whereby pores can be blocked, thus not all active sites would be accessible. Consequently, a copolymer was designed, possessing less TPP moieties within the polymeric backbone. In this way, the Rh(I) complexes are more separated from each other and coordination by multiple TPP becomes more unlikely. For that reason, the Yamamoto copolymer **CopolyTPP-2** was synthesized from tetrakis(4-bromophenyl)methane and tris(4-bromophenyl)phosphine-borane applied in a ratio of 4:1 equivalents (Scheme 18). As **CopolyTPP-2** is a statistical copolymer, it is not excluded that TPP moieties were incorporated in vicinity to each other. Nevertheless, the dilution of TPP units reduces the probability of clustered TPP coordination sites within the pores and promotes the formation of more defined catalytic centers.

The immobilization of Rh(I) catalyst was carried out according to the same procedure applied for **Rh-polyTPP-2**. After deprotection in methanol, an excess of catalyst precursor $[\text{Rh}(\text{CO})_2(\text{acac})]$ was added to yield **Rh-CopolyTPP-2**.



Scheme 18: Synthesis route of $[\text{Rh}(\text{CO})_2(\text{acac})]$ immobilization on microporous triphenylphosphine-containing polymer network CopolyTPP-2 produced from tris(4-bromophenyl)phosphine borane and tetrakis(4-bromophenyl)methane via Yamamoto cross-coupling reaction.

ICP-OES confirms that **Rh-CopolyTPP-2** contains 8 wt% of rhodium. For the theoretical network, in which Rh(I) is only coordinated by a single TPP, 6 wt% of rhodium would be expected.

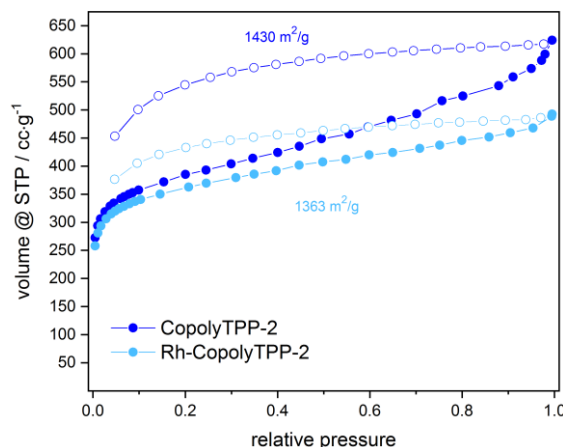


Figure 40: Nitrogen isotherms of CopolyTPP-2 and Rh-CopolyTPP-2, respectively.

The BET surface areas were calculated from nitrogen sorption isotherms of **CopolyTPP-2** and **Rh-CopolyTPP-2** and determined to be 1430 and 1363 m² g⁻¹ (Figure 40), respectively. It is assumed, that the addition of tetrahedral comonomer tetraphenylmethane led to a higher cross-linkage degree thus higher surface area. The nitrogen sorption isotherm of **CopolyTPP-2** exhibits a pronounced hysteresis loop indicating a flexible polymer scaffold, which can swell and enhance the accessibility of the pores.^[11] After immobilization of the Rh(I) catalyst, **Rh-CopolyTPP-2** shows a diminution of the hysteresis in contrast to **Rh-polyTPP-2**.

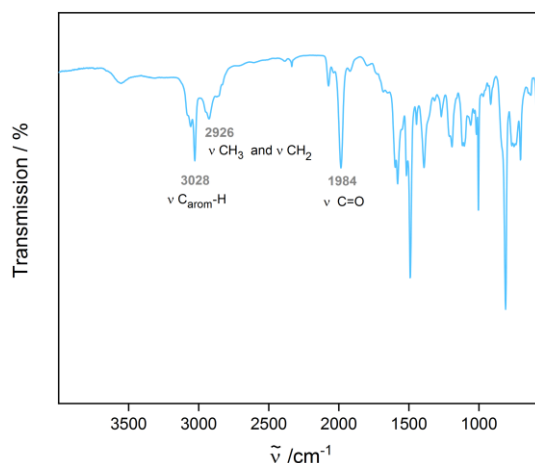


Figure 41: FTIR spectrum of Rh-CopolyTPP-2.

The structure of **Rh-CopolyTPP-2** was investigated by FTIR spectroscopy (Figure 41). The spectrum shows a clear stretching vibration at 1984 cm⁻¹, which is assigned to coordinated carbonyl C=O ligands of the metal-organic complex.^[193] The intense vibration band at 3028 cm⁻¹ corresponds to aromatic C-H vibrations occurring due to the high percentage of benzene units within in the polymer backbone. It is assumed, that the aliphatic C-H vibration at

2926 cm^{-1} derives from acetylacetonato ligands of the Rh(I) complex.

The chemical structure of **CopolyTPP-2** and **Rh-CopolyTPP-2** was further analyzed by solid-state NMR spectroscopy. The ^{11}B MAS NMR spectrum of **CopolyTPP-2** shows the typical signal at -43 ppm originating from phosphines coordinated by borane, and a second broad signal at 14 ppm indicating that some phosphine moieties were already deprotected (Figure 42, a). For **CopolyTPP-2**, the main signal in the ^{31}P MAS NMR spectrum was monitored at 23 ppm, which is slightly shifted towards low-field compared to **polyTPP-2**, due to overlapping of protected P-BH_3 and oxidized P=O phosphine signals (Figure 42, b). The second chemical resonance peak at -8 ppm was assigned to free TPP species in the polymer, which were shielded from oxidation. After rhodium immobilization, signals at 47 and 25 ppm were detected corresponding to the doublet for metal-phosphine coordination Rh-P , as observed for molecular catalyst $[\text{Rh}(\text{CO})(\text{acac})(\text{PPh}_3)]$. It is assumed, that additional signals due to partial oxidized P=O species, overlap with the doublet.

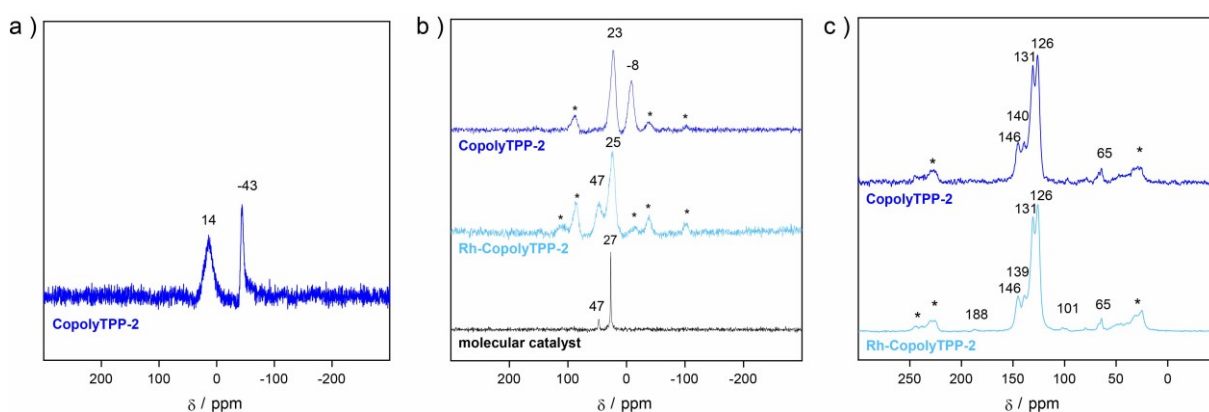


Figure 42: a) ^{11}B MAS NMR spectra of **CopolyTPP-2**, b) ^{31}P MAS NMR spectra of molecular catalyst, **Rh-CopolyTPP-2** and **CopolyTPP-2**, c) ^{13}C CPMAS NMR spectrum of **Rh-polyTPP-2** and **CopolyTPP-2**.

Furthermore, ^{13}C CPMAS NMR spectra were measured showing signals in the aromatic region at 146, 140, 131 and 126 ppm deriving from phenyl rings of both comonomers (Figure 42, c). The chemical resonance peak at 65 ppm, detected in the spectra of **CopolyTPP-2** and **Rh-CopolyTPP-2**, is characteristic for the sp^3 carbon of tetraphenylmethane. For **Rh-CopolyTPP-2**, additional signals at 188 and 101 ppm were measured and assigned to the carbonyl ligands and sp^2 carbons of acetylacetonato, respectively.^[192]

The Rh 3d core-level XPS spectrum of **Rh-CopolyTPP-2** proves the presence of Rh(I) and shows a characteristic doublet at 308.8 (3 $\text{d}_{5/2}$) and 313.5 eV (3 $\text{d}_{3/2}$), similar to the doublet of $[\text{Rh}(\text{CO})(\text{acac})(\text{PPh}_3)]$ (Figure 43, a). In comparison to **Rh-polyTPP-2**, the signal maxima of the doublet are shifted to lower energies by 0.6 eV. The data give indications that for **Rh-CopolyTPP-2**, a higher proportion of Rh(I) catalyst was coordinated by a single TPP in

comparison to **Rh-polyTPP-2**, which shows mainly Rh(I) complexes coordinated by multiple TPPs due to exchange of acetylacetonato by TPP, yielding higher overall binding energies.^[194]

The XPS P 2p core-level spectra present peaks with relatively poor resolution, as the percentage of phosphine within the copolymer is comparably low (Figure 43, b). For **CopolyTPP-2**, a single phosphorus species was detected presenting a doublet at 131.8 (2 p_{3/2}) and 132.7 eV (2 p_{1/2}), which is in accordance with signals of borane-protected phosphine units. The spectrum of **Rh-CopolyTPP-2** exhibits a doublet at 132.1 (2 p_{3/2}) and 133.0 eV (2 p_{1/2}), showing oxidized phosphine species P=O. Considering that XPS is a technique mainly detecting the surface of a material, the ratio of oxidized phosphine species, which in many cases appear on the surface, are therefore often overestimated. By taking the poor resolution of the spectrum into account, it has to be noted that the differentiation of oxidized moieties P=O and Rh-coordinated phosphines is rather difficult. However, by comparing the XPS results with ³¹P MAS NMR, it is apparent that NMR spectroscopy gives an overall picture of the phosphorous species, showing successful immobilization of Rh(I) as well as partial oxidation.

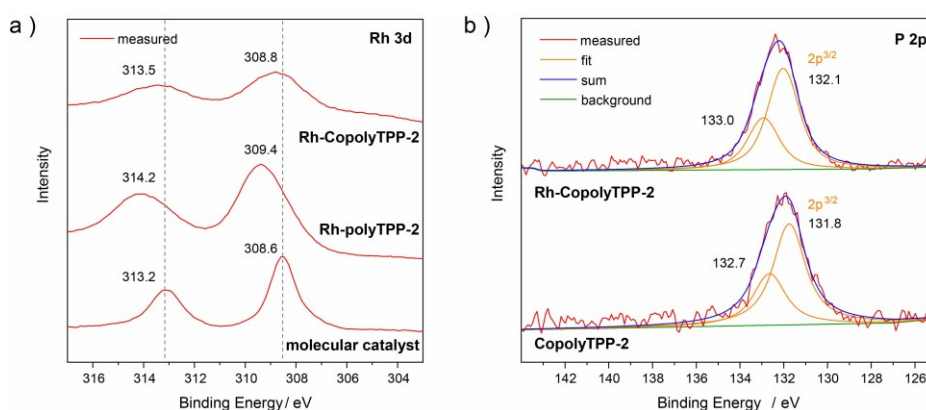


Figure 43: Rh 3d and P 2p XPS spectra. a) Rh 3d XPS spectra of Rh-CopolyTPP-2 in comparison to Rh-polyTPP-2 and molecular catalyst [Rh(CO)(acac)(PPh₃)]. b) P 2p XPS spectra of CopolyTPP-2 and Rh-CopolyTPP-2.

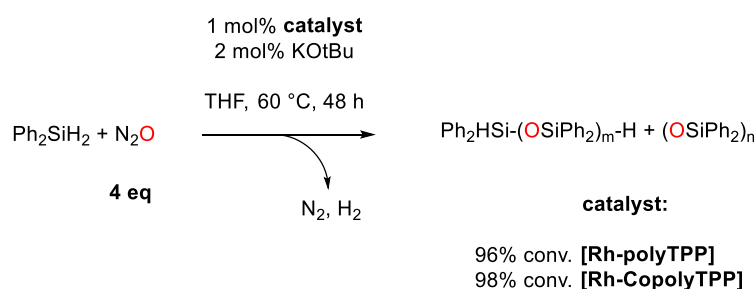
In summary, the dilution of TPP units within **Rh-CopolyTPP-2** led to a reduced metal content as well as an increase in surface area compared to **Rh-polyTPP-2**. Despite partial oxidation of non-coordinated phosphines, XPS data show a similar Rh(I) coordination sphere as it occurs in the molecular catalyst. Hence, it is assumed that the immobilized complexes were successfully separated to obtain more defined catalytic centers in comparison to **Rh-polyTPP-2**.

5.3.2 Applications of Phosphine-based Polymers

5.3.2.1 Hydrosilylation

The catalytic tests for hydrosilylation of nitrous oxide (N_2O) by Rh(I)-immobilized polymers **Rh-polyTPP** and **Rh-CopolyTPP** were performed in Prof. Grützmacher's group at ETH Zürich.

For the catalysis secondary silanes (Ph_2SiH_2) were applied as substrates, which were converted into oligo-siloxanes by oxygen transfer of N_2O to form silicon-oxygen bonds (Scheme 19).^[179] During catalysis, the stable precursors **Rh-polyTPP** and **Rh-CopolyTPP** incorporating $[\text{Rh}(\text{trop}_2\text{NH})](\text{OTf})$ units were transformed into the active amido species $[\text{Rh}(\text{trop}_2\text{N})]$ by addition of the Brønsted base potassium *tert*-butoxide (see 5.1.3).^[179] For the general procedure, silane, 4 equivalents of N_2O , 1 mol% catalyst and 2 mol% base were suspended in tetrahydrofuran and stirred for 48 h at 60 °C.



Scheme 19: Catalytic hydrosilylation of nitrous oxide by Rh(I) immobilized polymers Rh-polyTPP and Rh-CopolyTPP.

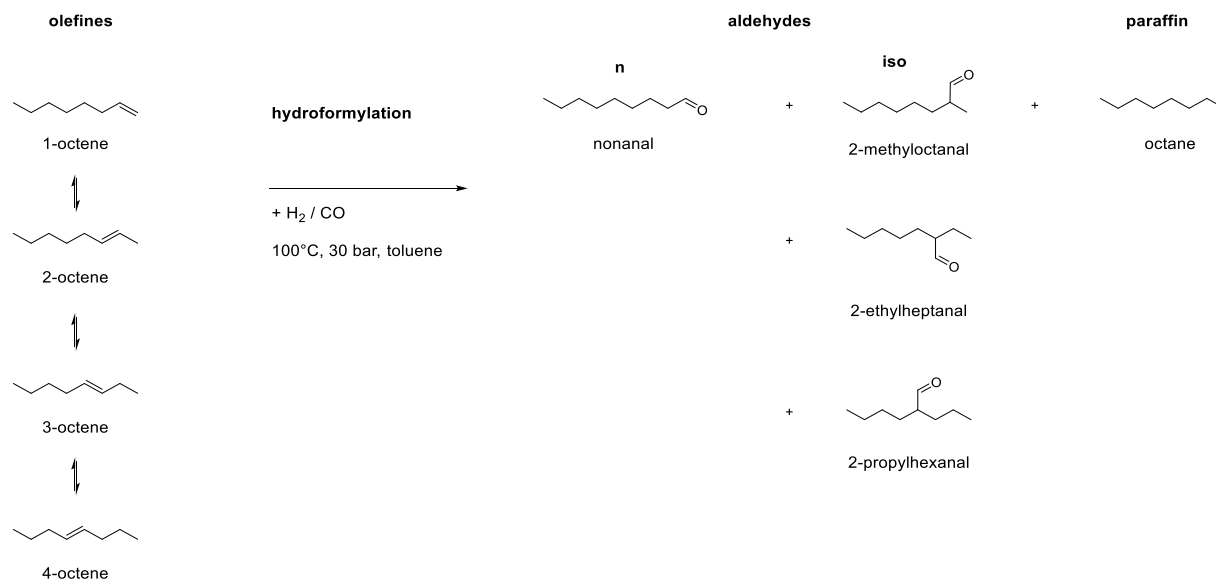
After separation of the solid catalyst, the filtrate was analyzed using NMR spectroscopy to characterize the produced siloxane species. In addition, the gas phase of the reaction was analyzed by GC-TCD and the presence of hydrogen and nitrogen further indicated the successful hydrosilylation. The catalytic studies showed almost quantitative conversion, i.e. for catalysts **Rh-polyTPP** and **Rh-CopolyTPP** conversions of 96 and 98% were achieved, respectively.

5.3.2.2 Hydroformylation

The synthesized Rh-immobilized catalysts were tested for their performance in heterogeneous hydroformylation. The hydroformylation studies were carried out by Carolina Urban, who is working in Prof. Schomäcker's group of Technische Universität Berlin.

If 1-octene is applied as starting material in hydroformylation, in general linear and branched aldehydes are obtained in different ratios depending on the regioselectivity of the catalyst. Typically, *n*-nonanal and iso-aldehydes are produced (Scheme 20). In case

isomerization of 1-octene takes place during the reaction, the formation of iso-aldehydes is likelier. Furthermore, chemoselectivity of the catalyst plays a major role, under CO/H₂ atmosphere hydrogenation reactions can arise and compete with hydroformylation reaction to give octane instead of aldehydes.



Scheme 20: Hydroformylation of 1-octene with Rh(I) immobilized catalyst and all possible reaction products at 30 bar H₂/CO, 100 °C in toluene.

The hydroformylation catalyzed by **Rh-polyTPP-2** was carried at 100 °C and 30 bar of synthesis gas (CO/H₂). The starting materials, 1-octene and **Rh-polyTPP-2** were suspended in toluene. The reaction time was started, when the reaction conditions of 100 °C and 30 bar were reached in the reactor. To follow the reaction progress, samples were taken *via* a syringe to evaluate the composition by gas chromatography (GC). To quantify the products, nonane was added as a calibration standard. The retention times and GC evaluations are listened in the appendix (Table A 1-3).

The gas chromatogram shows besides 1-octene, three species of iso-octenes, thus isomerization took place during the warm-up (Figure 44, a). When the reaction conditions were reached, already 8% of aldehyde was formed, 62% of it was assigned to n-nonanal and the remaining 38% to 2-methyloctanal (Table 5). After 1 h (Figure A 9), 37% of aldehyde were obtained, though the ratio of n- to iso-product reversed, 62% of the gained product was converted into less favored iso-aldehydes. As a consequence, three branched aldehydes were detected and identified as 2-methyloctanal, 2-ethylheptanal and 2-propylhexanal deriving from the corresponding iso-octenes. Within 3 h, 65% conversion was achieved, and the ratio was balanced out at 31:69 (n:iso). After 5 h of reaction time, 70% were converted into aldehydes from which 70% were identified as iso-aldehyde. The chromatogram (Figure 44, b) shows that 2-methyloctanal account for the largest share assumably deriving from isomerized 2-octene. In

the remaining 15 h, the conversion rose up to 91% with a consistent ratio of 29:71 (n:i).

By applying **Rh-polyTPP-2**, conversion rates of 91% were achieved with rather moderate regioselectivity due to isomerization of 1-octene. Nevertheless, high chemoselectivity, thus no hydrogenation product, was observed, which was further validated by gas chromatography-mass spectrometry (GC-MS).

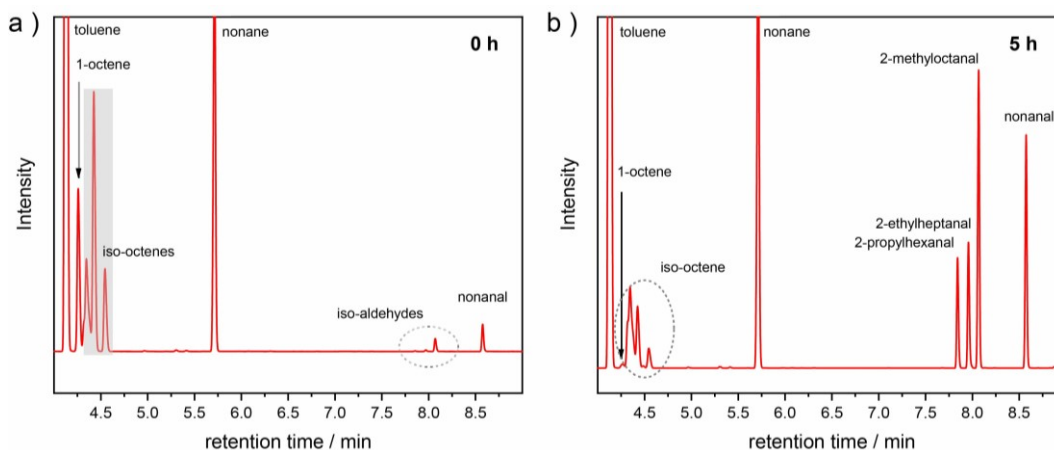


Figure 44: Gas chromatograms of Rh-polyTPP-2 at a) the start of the reaction and b) after 5 h.

Table 5: Hydroformylation of 1-octene catalyzed by Rh-polyTPP-2.

reaction time [h]	conversion to aldehyde [%]	n-aldehyde [%]	i-aldehyde [%]
0	8	62	38
1	37	38	62
3	65	31	69
5	70	30	70
20	91	29	71

Hydroformylation carried out under 30 bar CO/H₂, at 100 °C, 1200 rpm stirring speed, 12 g 1-octene, 12 g toluene, 130 mg Rh-polyTPP-2.

In a second study, copolymer **Rh-CopolyTPP-2** containing less rhodium was tested as hydroformylation catalyst under the same conditions as **Rh-polyTPP-2**. At the starting point, the first sample revealed a conversion of 10% to aldehydes, the ratio amounted to 73:27 for n:iso. In the following hour, the conversion rate reached 65% with a 50:50 ratio. After 3 h, the 88% of octene was converted into aldehydes almost as much as for **Rh-polyTPP-2** after 20 h. The regioselectivity slightly increased towards iso-aldehydes, 56% were detected in GC. Almost full conversion was reached after 5 h, 96% of aldehydes in a ratio of 41:59, were observed. Finally, a 99% conversion with a distribution of 40% n-nonanal and 60% of the three branched aldehydes was obtained after 20 h.

Table 6: Hydroformylation of 1-octene catalyzed by Rh-CopolyTPP-2.

reaction time [h]	conversion to aldehyde [%]	n-aldehyde [%]	i-aldehyde [%]
0	10	73	27
1	65	50	50
3	88	46	54
5	96	41	59
20	99	40	60

Hydroformylation carried out under 30 bar CO/H₂, at 100 °C, 1200 rpm stirring speed, 12 g 1-octene, 12 g toluene, 130 mg Rh-CopolyTPP-2.

In comparison to **Rh-polyTPP-2**, applying **Rh-CopolyTPP-2** as catalyst led to a faster reaction with higher regioselectivity. The turnover frequencies (TOF) after 1 h at 100 °C were calculated to be 698 and 1722 h⁻¹ for **Rh-polyTPP-2** and **Rh-CopolyTPP-2**, respectively, underlining the higher efficiency of **Rh-CopolyTPP-2**. Considering that the conversion of 1-octene to aldehydes already took place during the warm-up, the TOFs including the warm-up might be even higher. The conversion with **Rh-CopolyTPP-2** was almost complete after only 5 h. A detailed look into the data shows that the better results for **Rh-CopolyTPP-2** derived from slower isomerization and thus less generation of branched aldehydes. The evaluation of the gas chromatograms (Table A 3), revealed that n-nonanal was the largest share of hydroformylation product, at any time. It is assumed that for **Rh-CopolyTPP-2**, the active sites are better separated from each other due to the dilution of coordination sites within the polymer. As a result, the coordination environment of **Rh-CopolyTPP-2** is better defined compared to **Rh-polyTPP-2**. Another factor could be the surface area, which is much higher for **Rh-CopolyTPP-2**, thus the active sites should be better accessible.

The result of **Rh-CopolyTPP-2** is comparable with previous reported Rh-P-COF-2, which was applied in hydroformylation of 1-octene at 100 °C for 6 h achieving a conversion of 92% with a molar ratio of 1.1/1 linear/branched aldehydes.^[189] In summary, the hydroformylation using **Rh-polyTPP-2** and **Rh-CopolyTPP-2** showed high chemoselectivity, thus no hydrogenation, and for **Rh-CopolyTPP-2** an almost full conversion within 5 h. Nevertheless, isomerization of 1-octene took place during both reactions, which especially occurred during the warm-up of the reaction. According to Sun *et al.*, the regioselectivity can be further optimized by decreasing the temperature and syn gas pressure of the reaction.^[72,195] Furthermore, the metal loading can be varied by dilution of the phosphine moieties within the copolymer, to decrease the rhodium content of the catalyst. It was reported that a Rh(I) loading of 2 wt% was sufficient for a successful hydroformylation.^[72]

5.4 Conclusion and Outlook

This chapter presents a successful method to synthesize poly(triphenylphosphine) networks preventing oxidation of the phosphine moieties during the polymerization. The protection of phosphine units *via* borane was easily removed by refluxing the material in methanol under inert conditions. The following immobilization of Rh(I) complexes was achieved by addition of the metal precursor during the deprotection, whereby Rh(I) coordinates *in situ* to the polymeric triphenylphosphine. After coordination of the metal complex, the phosphine moieties are protected from oxidation and therefore stable under air. **PolyTPP** possesses a BET surface area of $989 \text{ m}^2 \text{ g}^{-1}$, which was decorated with the molecular hydrosilylation catalyst $[\text{Rh}(\text{trop}2\text{NH})](\text{OTf})$ to yield **Rh-polyTPP** with 8 wt% rhodium. As the porosity decreases significantly after metal coordination, a copolymer synthesized from tetrabromopyrene was designed, called **Rh-CopolyTPP**. The diluted amount of phosphine moieties within the polymer led to reduced amounts of Rh catalyst in the pores. **Rh-CopolyTPP** exhibits a rhodium content of 6.6 wt% and a surface area of $290 \text{ m}^2 \text{ g}^{-1}$. For both materials, almost quantitative yields were reached during hydrosilylation of nitrous oxide to form non-hazardous nitrogen by transferring oxygen into the silane bonds. By applying **Rh-CopolyTPP** as catalyst, 98% conversion was detected, whereas **Rh-polyTPP** usage resulted in a minimally lower value of 96%. It is assumed, that despite a lower rhodium loading, higher surface areas lead to a better accessibility of the catalytic sites in the catalyst and consequently to higher activity of the material.

To design a hydroformylation catalyst, precursor $[\text{Rh}(\text{CO})_2(\text{acac})]$ was selected and immobilized on **polyTPP**. Solving the chemical structure for **Rh-polyTPP-2** was rather complicated as not only $[\text{Rh}(\text{CO})(\text{acac})(\text{PPh}_3)]$ complexes were formed, but also coordination to multiple phosphine moieties of the polymer network occurred. Consequently, different coordination environments depending on the spatial arrangement of phosphine coordination sites within the pore, led to a mixture of various Rh(I) complexes immobilized in the material. As the coordination process was not fully controllable, it was observed that after exposing the material to air non-complexed TPP moieties oxidized over time. **Rh-polyTPP-2** contains 21.5 wt% of Rh and exhibits a calculated BET surface area of $421 \text{ m}^2 \text{ g}^{-1}$. First hydroformylation tests with 1-octene showed high chemoselectivity and no hydrogenation product, 91% conversion to desired aldehydes was obtained after 20 h. However, high rates of 1-octene isomerization were observed leading to formation of iso-aldehydes and not preferential n-nonanal. The ratio between n-nonanal and iso-aldehyde amounted to 29:71 after 20 h reaction time. To gain more insights into the factors influencing the regioselectivity of the

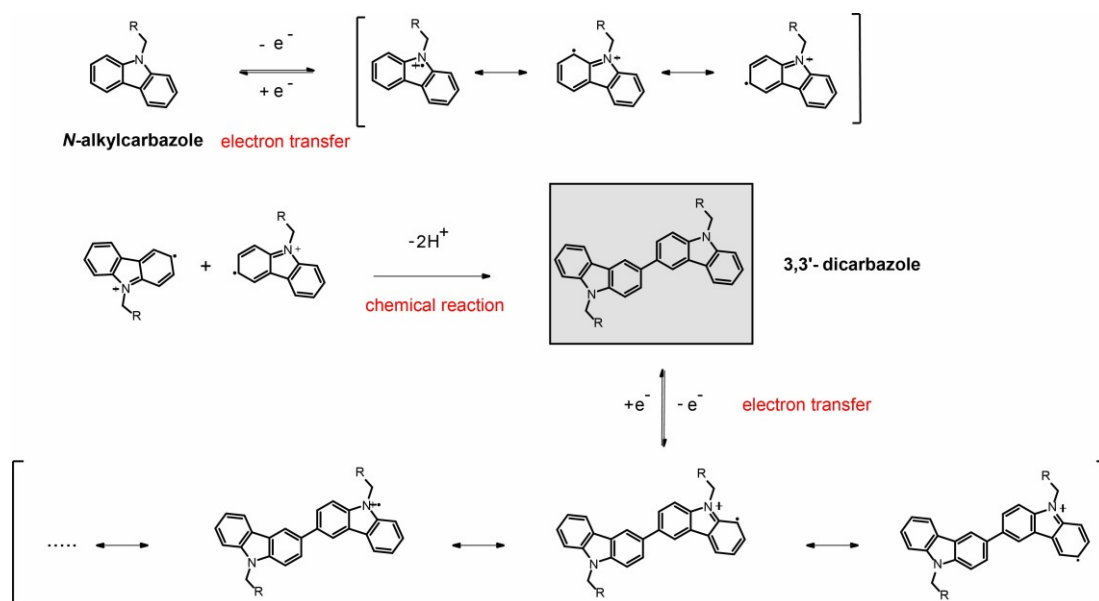
catalyst, a second material was prepared, copolymerized from tetrabromophenylmethane and the phosphine-containing monomer. The resulting rhodium-coordinating copolymer, **Rh-CopolyTPP-2**, was loaded with 8 wt% rhodium and possesses a BET surface area of $1363 \text{ m}^2 \text{ g}^{-1}$. By dilution of the TPP moieties within the network, the possibility of single TPP coordination highly increased and mainly $[\text{Rh}(\text{CO})(\text{acac})(\text{PPh}_3)]$ complexes were formed in the pores. In hydroformylation tests under similar conditions as for **Rh-polyTPP-2**, a conversion of 99% after 20 h was obtained in a ratio of 40:60 n-nonanal to iso-aldehyde. Within 5 h, almost full conversion of 96% was achieved. The calculated TOF after 1 h, was determined to be 1722 h^{-1} pointing out the efficiency of **Rh-CopolyTPP-2** in comparison to **Rh-polyTPP-2** possessing a TOF of 698 h^{-1} . It is assumed that more tailored coordination sites lead to higher regioselectivity. Additionally, catalysts with higher surface areas supposedly require less metal loading and lead to higher conversion rates within less time. For future studies, the regioselectivity must be further improved by testing different copolymers with various percentages of TPP units. Beside this, the choice of reaction temperature, pressure and time can also enhance the catalysts performance. Furthermore, recycling studies must be conducted to confirm on the reusability of the material.

6 Microporous Polymer Films

6.1 Theoretical Background

6.1.1 Electrochemical Oxidation of Carbazole

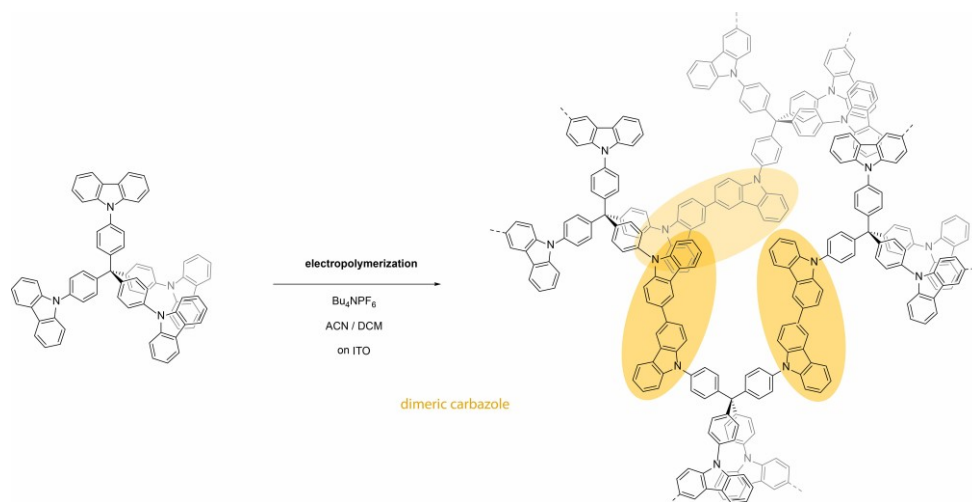
Besides chemical oxidation studies of carbazole, Ambrose *et al.* introduced anodic oxidations of carbazole and *N*-substituted derivatives in 1968.^[196] It was shown that *N*-alkyl carbazoles form *N,N'*-dialkyl-3,3'-dicarbazole in an irreversible, quantitative manner by going through a two-electron oxidation process. The so-called surface electron-chemical reaction-electron transfer (ECE) mechanism describes two separate electron transfer steps: 1) electron transfer, 2) chemical reaction, 3) electron transfer. In the first step, an electron transfer takes place, forming a carbazole radical cation which possesses low stability and reacts immediately with another carbazole radical cation to give a 3,3'-dicarbazole after deprotonation. *N*-substituted dicarbazoles possess a lower oxidation potential compared to *N*-substituted carbazoles thus the next electron-transfer leads to formation of the dimer cation radical. However, this process is reversible due to the high stability of the dimer cation radical as the radical is delocalized over two carbazoles leading to many resonance forms. As a consequence, *N,N'*-dialkyl-3,3'-dicarbazole are formed predominantly.^[82,196]



Scheme 21: Mechanism of electrochemical oxidation of *N*-substituted carbazoles.

6.1.2 Carbazole-based Films

In 2013, Gu and coworkers introduced microporous carbazole-based polymer films by electropolymerization.^[142,197,198] The first polymer film was fabricated from tetrakis(4-(carbazolyl)phenyl)methane and was deposited on an indium tin oxide (ITO) electrode by multicycle cyclic voltammetry (CV).^[142] The first cycle of anodic sweep presents the oxidation of carbazole to form carbazole radical cations. In the second scan, an additional peak at a lower potential is observed, originating from oxidized dimeric carbazoles. With the number of scans, the current of each cycle increases continuously, indicating the growth of the films. Nevertheless, it was stated that only dimeric carbazole units are formed during the electropolymerization, but no higher degree of cross-linkage can be achieved under normal conditions (Scheme 22). In contrast to other MPNs, which are usually obtained as powders, carbazole-based polymer films have the advantage of being synthesized in a controlled fashion in different thicknesses from nano- to micrometers.^[142,199] The thickness of the polymer films is changing linearly with the number of scan cycles during the CV and grows till the point when the films start peeling off the electrode to give a free-standing film. After doping the film with perchlorate to improve the conductivity and work function, they were applied as anode interlayer in solar cells.^[142,198]



Scheme 22: Carbazole-based polymer film on ITO synthesized from tetrakis(4-(carbazolyl)phenyl)methane *via* multicycle CV.^[142]

Following up, another microporous carbazole-based film was published by Gu and coworkers, produced from 1,3,5-tris(4-(9-carbazolyl)phenyl)benzene *via* multicycle CV.^[197] Since the determination of porosity by nitrogen sorption isotherms requires material in the milligram range, up to this point it was impossible to calculate the BET surface area of such electropolymerized films. However, by applying krypton, which possesses a much lower saturation pressure as sorption gas, less material is needed to obtain valid gas sorption

measurements. Consequently, only 120 μg could be applied for the krypton sorption isotherms to calculate the SA_{BET} of 1450 $\text{m}^2 \text{g}^{-1}$.^[197] Since these carbazole-based films combine physical properties such as high porosity, extended π -conjugation and high rate electron transfer these materials were used as chemo- and biosensors.

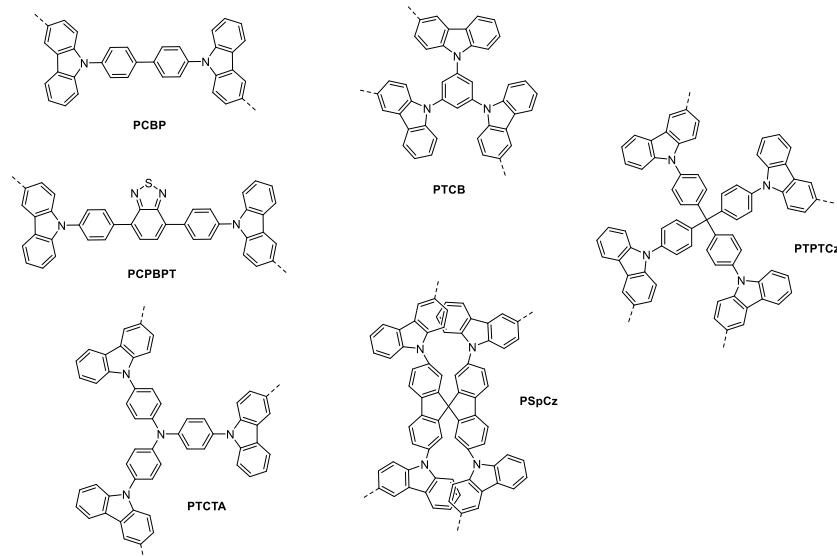


Figure 45: Carbazole-based polymer films synthesized by Palma-Cando and coworkers.^[199]

In 2015, Palma-Cando *et al.* published an electrochemical study of films polymerized from different monomers equipped with 2, 3 or 4 carbazole functionalities (Figure 45).^[199] It was observed that oxidation of carbazole moieties takes place at potentials ranging from 0.93 to 1.05 V *vs.* Ag^0/AgCl on a Pt disc electrode. In addition, the influence of the number of carbazole groups per monomer on the surface area was investigated. The higher substituted monomers, especially films from tetra-functional monomers, showed significantly higher surface areas than polymers from 2- or 3-substituted building units. With increasing numbers of carbazole units, the monomers become more rigid and the cross-linkage density rises. As a reference the equivalent bulk polymers were synthesized *via* oxidative polymerization with iron(III) chloride. For the films the level of cross-linkage is lower in comparison to bulk polymers, which is assumed to occur due to the preferable formation of carbazole dimers whereas in bulk polymers further polymerization in 6,6'-position of the dimers occur.^[199,200] The various porous films were applied as electrochemical detectors of nitroaromatic compounds.^[199]

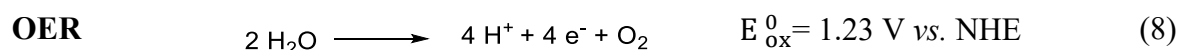
6.1.3 Water Splitting

In case hydrogen production is generated from renewable resources, hydrogen presents a promising emission-free alternative to fossil fuels. In low scale, green hydrogen production is already realized in industry by water electrolysis *via* electrocatalytic process of decomposing water into hydrogen and oxygen.^[201] For this technique an electric current is applied to force the endothermic redox process of water ($\Delta G_0 = 237 \text{ kJ mol}^{-1}$)^[202], thus hydrogen evolution reduction (HER) at the cathode and oxygen evolution reaction (OER) at the anode take place. This overall process is called water splitting:^[201]

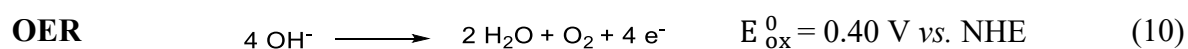


This process is divided into two half-cell reactions, HER and OER, depending on the pH:^[203]

Acidic conditions:



Alkaline conditions:



Water splitting is not only implemented electrocatalytically but also photocatalysis and photoelectrocatalysis are used to achieve overall water splitting or one of the half reactions, OER or HER.^[201,204] To run reactions by solar energy, semiconductors are applied as photocatalysts inducing electron-hole-separation under irradiation of certain light wavelengths according to the band gap. The remaining holes in the valence band as well as the excited electrons in the conduction band contribute to OER and HER.^[202] The combination of photoactive electrodes with water electrolysis results in photoelectrocatalytic water splitting driven by photogenerated electron-hole pairs at one or both electrodes.^[204]

6.1.4 Photoelectrochemical Water Splitting

In 1972, Honda and Fujishima first accomplished direct photoelectrochemical (PEC) water splitting by applying a semiconducting *n*-type titanium oxide (TiO_2) electrode and a platinum counter electrode.^[205] Photoelectrochemical water splitting attracted attention as a promising approach for carbon-free hydrogen production powered by solar energy. In general, PEC cells are composed of a light-harvesting semiconductor as working electrode, which is connected to a metal counter electrode and immersed in a suitable aqueous electrolyte.^[206] Figure 46 depicts

two possible setups for PEC cells. In the first case, a *n*-type semiconductor is applied as photoanode in combination with a common cathode. Under irradiation, electrons get excited, and the generated holes in the valence band (VB) migrate to the surface of the electrode where water oxidation takes place. Meanwhile, excited electrons are transferred *via* the external circuit to the corresponding cathode, where the electrons enable the hydrogen evolution reaction (HER). For the second setup, electrons and holes are photogenerated in the semiconductive *p*-type cathode. The excited electrons in the conduction band (CB) contribute to the hydrogen reduction on the interface of photocathode and electrolyte, as the holes in the valence band drive the external circuit, whereby oxygen evolution (OER) is performed at the connected anode.^[207] Apart from these described systems, even more complex PEC cells have been developed. Ideally, a suitable photocathode as well as photoanode are combined and applied in one cell for PEC water splitting.^[206,207]

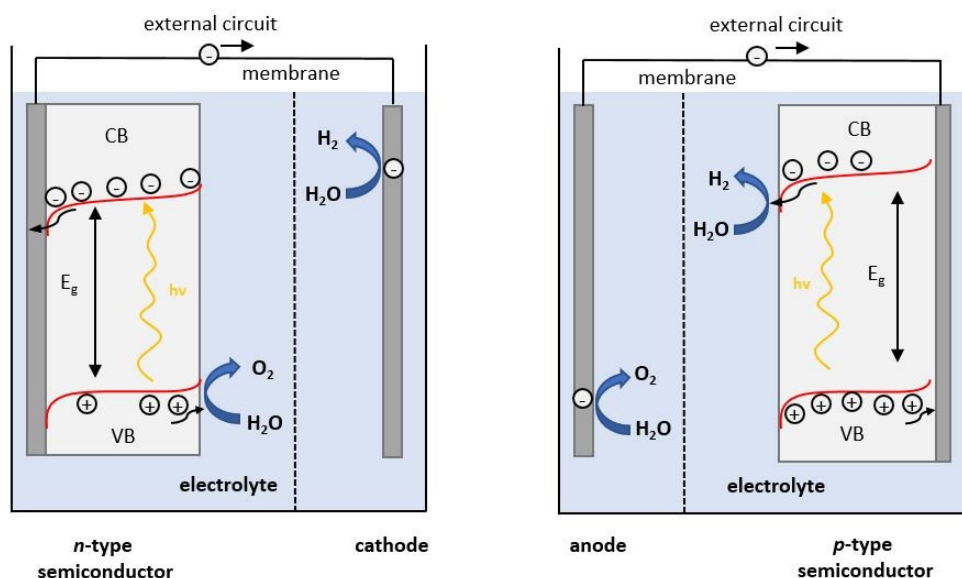


Figure 46: Schematic setup of PEC cell consisting of *n*-type or *p*-type semiconductor.^[207]

Semiconductors play a key role in operating PEC cells as solar energy is converted into an electrical current, which drives the catalytic water splitting. An ideal material for photoelectrodes should provide certain requirements such as efficient light-harvesting properties as well as facile electron-hole separation and efficient charge transfer.^[208] The conductivity of a semiconductor is enhanced by introducing dopants with electron donating or accepting properties, to change the electronic properties. For *n*-type semiconductors the better conductivity is based on an excess of electrons due to doping with donor groups within the materials, whereas *p*-type semiconductor are doped with extra electron acceptor groups leading to a surplus of holes in the valence band.^[209] Besides conductivity, the band gap (E_g) and the positions of valence and conduction band need to be suitable in respect to the oxidation and

reduction potential of water. At best, the redox potential of water is positioned between the edges of conductive and valence band: $E_{CB} > E_{red, water}$ and $E_{VB} < E_{ox, water}$.^[204,210] The size of the band gap determines the range of wavelengths, which is required to overcome the energetic step between valence and conduction band. In case the band gap is too large, efficient light-harvesting becomes more difficult as the required intensity of light cannot be absorbed.^[211] Although the theoretical band gap that is necessary to achieve water splitting is 1.23 eV, the perfect size of the band gap is considered to be between 1.6 and 2.2 eV for efficient water splitting experimentally.^[207] To further optimize the catalytic system, the introduction of suitable co-catalysts is a possible way to enhance surface reaction kinetics as well as a decline in overpotential.^[206,212]

6.2 Objective

For many industrial applications such as energy storage devices, optical coatings or membranes and sensors, thin layers of material are more favorable than powdery materials.^[213] In this respect, polymer films are favored to broaden the usability of microporous polymers. Especially, carbazole-based materials offer this possibility as carbazole is not only polymerizable *via* oxidative reactions, but also by applying electropolymerization. The advantage of an electrochemically deposited material is that a homogeneous and transparent film is formed within minutes without any metal catalyst applied.^[200] Besides, film thickness is easily controlled and therefore it can be precisely tailored for the desired application.

The electropolymerization of carbazole-equipped molecules opens the possibility to design a variety of monomers for embedding organic functionalities into polymer films, which can be applied in catalysis. This offers an option to process films containing phosphine and bipyridine functionalities homogeneously on conductive substrates enhancing the applicability of the material for electrocatalysis.

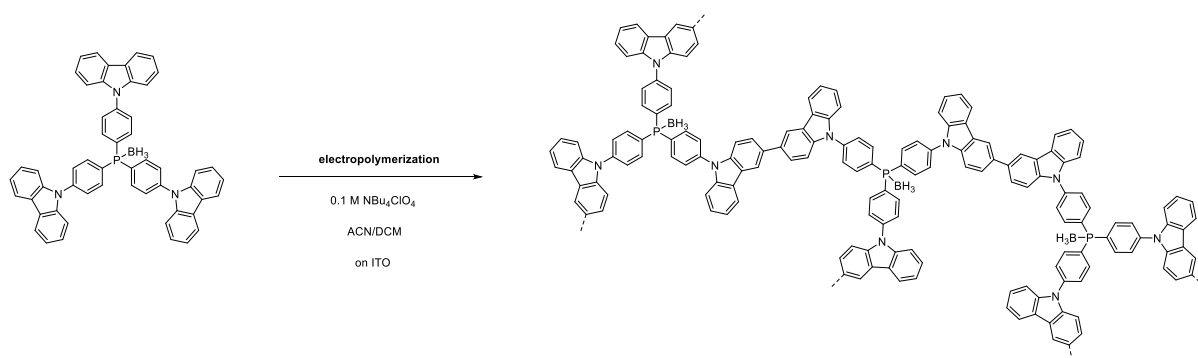
Carbazole films can be polymerized on various substrates, entailing a simple approach of modifying electrodes for electro- or photoelectro-catalysis. This paves the way for applying carbazole films in electrocatalysis as well as using them as photoelectrodes for water reduction. By incorporation of chelating ligands within the polymer films even coordination of co-catalyst *via* post-synthetic modification is possible to tailor the material properties. For that purpose, bipyridine-containing carbazole monomers are electropolymerized on FTO and semiconductors to study their applicability in electrocatalytic OER and as photocathode in PEC cells.

6.3 Results and Discussion

6.3.1 Phosphine-containing Films

As discussed in chapter 5.3, phosphine-containing polymers turned out to be promising candidates as supporting material for different molecular catalysts. This chapter presents a first attempt to synthesize microporous films incorporating phosphine moieties on conductive substrate. For that purpose, triphenylphosphine (TPP) moieties attached to carbazole functionalities were designed and polymerized electrochemically to yield a thin microporous polymer film.

Tris((4-carbazolyl)phenyl)phosphine borane (CzTPP) was synthesized by lithiation of 9-(4-bromophenyl)carbazole and addition of phosphorous trichloride, the subsequent protection with borane was carried out to avoid oxidation during the polymerization (see chapter 5.3.1).^[181]



Scheme 23: Electropolymerization of polyCzTPP via CV on ITO, carried out in a solution of CzTPP.

The polymer film **polyCzTPP** was prepared *via* cyclic voltammetry (CV) from a 1.0 mM solution of CzTPP in acetonitrile and dichloromethane (1:4) by using 0.1 M tetrabutylammonium perchlorate as electrolyte (Scheme 23). The reaction was carried out in a three-electrode cell for which indium tin oxide (ITO) was applied as working electrode, platinum wire as counter electrode and Ag⁰/AgCl as reference electrode. **PolyCzTPP** was deposited *via* 8 cycles of CV and further 15 min of chronoamperometry (CA) at 1.5 V *vs.* Ag⁰/AgCl to create a film on top of ITO (Figure 47). The first scan of CV shows an oxidation peak at 1.51 V *vs.* Ag⁰/AgCl deriving from the formation of carbazolyl cation radicals. For the further scans a new peak appears at 1.18 V *vs.* Ag⁰/AgCl, which progressively increases and shifts towards higher potential, which is assigned to dimerization of carbazoles and thus representing the continuous growth of the polymer film.^[199]

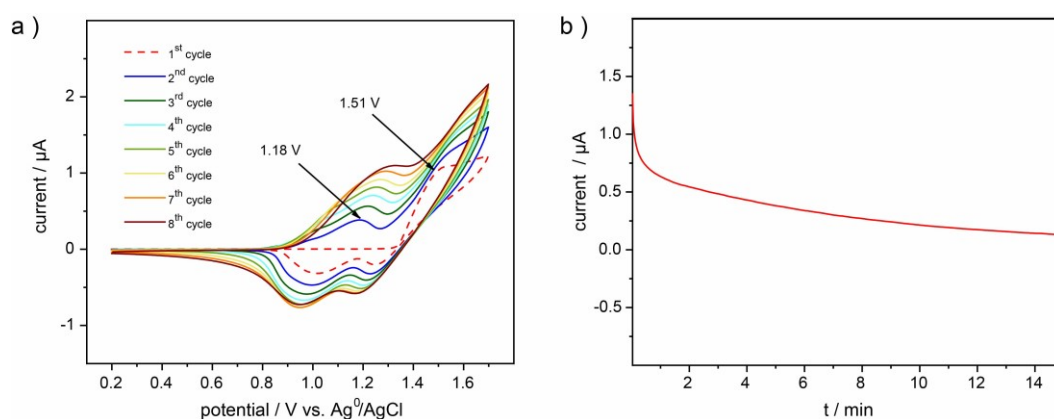


Figure 47: a) Cyclic voltammogram and b) chronoamperometry at ITO electrode, carried out for 1.0 mM solution of CzTPP in ACN/DCM (1:4) by using 0.1 M NBu_4ClO_4 as electrolyte. CV was recorded from 0.2-1.7 V (scan rate of 50 mV/s). CA was recorded at 1.5 V over 15 min.

The phosphine-containing film **polyCzTPP** was characterized by FTIR. The comparison of the fingerprint of monomer and polymer proves the presence of dimerized carbazole species within the film. The prominent C-H vibration band of CzTPP at 723 cm^{-1} , corresponding to disubstituted phenyl rings, disappeared for **polyCzTPP** and a new C-H vibration band at 806 cm^{-1} was detected, according with trisubstituted phenyl rings of the carbazole dimers.^[197] Both spectra show vibration bands for C-H bonds of the phenyl rings of TPP at 746 and 748 cm^{-1} , respectively.

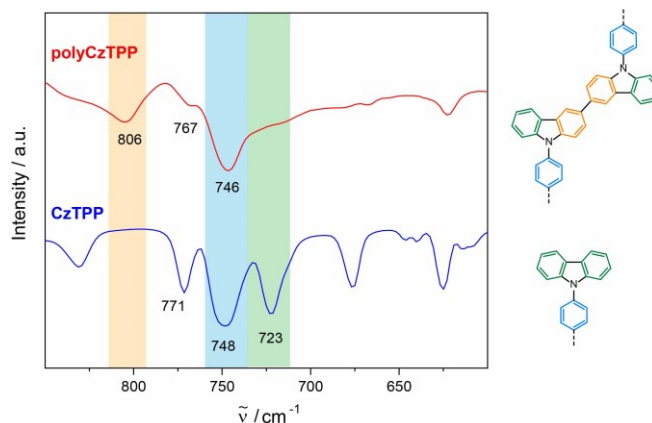


Figure 48: Fingerprint region of FTIR spectra of CzTPP (blue) and polyCzTPP (red).

The chemical structure of **polyCzbiPy** was further analyzed by XPS spectroscopy. The high-resolution N 1s core-level spectrum of **polyCzbiPy** (Figure 49, a) shows one significant species at 400.4 eV deriving from dimerized carbazole units, and a second less intense signal at 402.1 eV originating from incomplete discharged nitrogen atoms, which appear if the deposited film was not sufficiently discharged after applying a potential of 1.5 V.^[142,143] In the P 2p core-level spectrum one doublet was detected at 132.4 (2 $p_{3/2}$) and 133.2 eV (2 $p_{1/2}$), which is assigned to oxidized phosphorus $\text{P}=\text{O}$ species (Figure 49, b). Nevertheless, a clear B 1s signal at 190.8 eV was detected and assigned to $\text{P}-\text{BH}_3$ species, pointing towards partial oxidation of

the phosphine moieties during the electropolymerization. This assumption was confirmed by ^{31}P and ^{11}B MAS NMR spectroscopy showing oxidized as well as intact phosphine units protected by borane (Figure A 10).

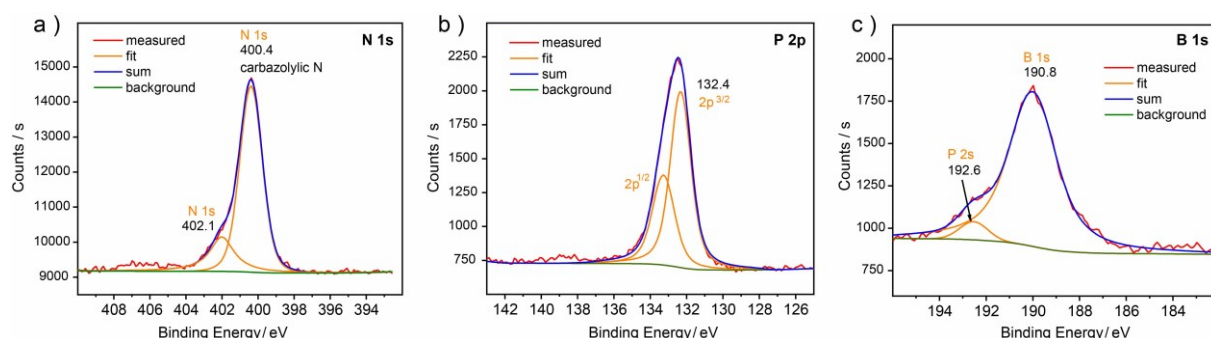


Figure 49: a) N 1s, b) P 2p and c) B 1s XPS spectra of polyCzTPP.

The porosity of **polyCzTPP** was investigated by krypton gas sorption measurements showing that the material possesses a BET surface area of $355 \text{ m}^2 \text{ g}^{-1}$ (Figure A 11).

Scanning electron microscopy (SEM) analysis shows a homogeneously grown film on top of ITO (Figure 50). The thickness of **polyCzTPP** was determined on the intersection between ITO and film and was measured to be around $1.6 \mu\text{m}$ for the films prepared *via* CV as well as CA. The SEM images show that the growth of thicker films could lead to cracks and peeling of the film, assuming the thickness must be carefully controlled to obtain a stable material.

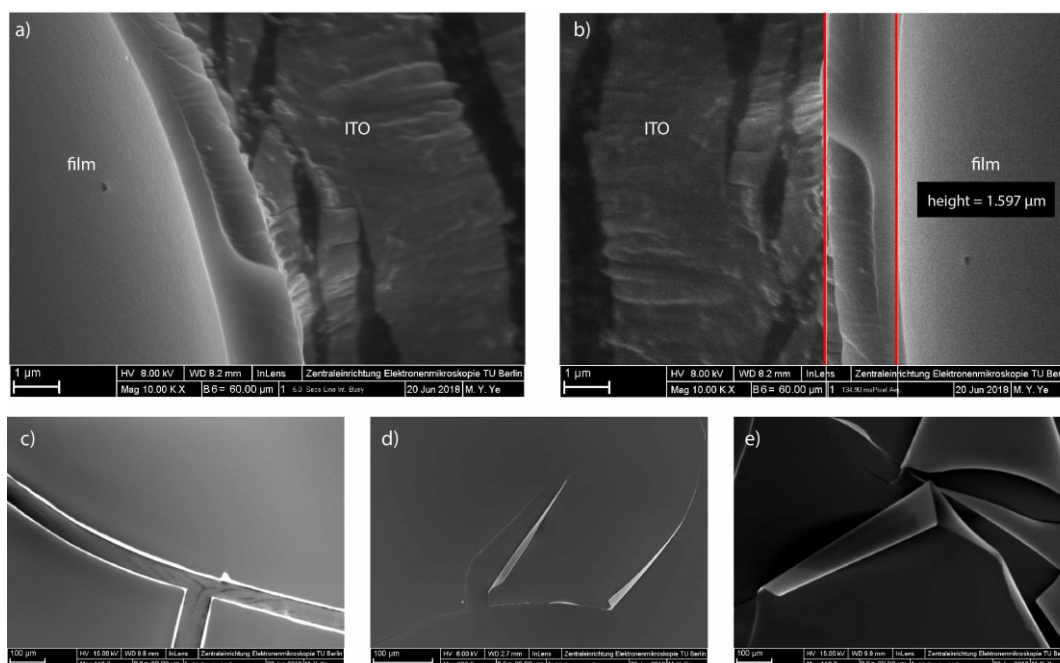


Figure 50: Scanning electron microscopy images of polyCzTPP on ITO: a)-b) show the edge between ITO and polyCzTPP, a film thickness of around $1.6 \mu\text{m}$ was determined. c)-d) shows the top view of film.

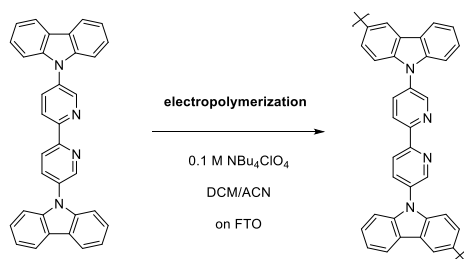
One of the most well-known reactions using triphenylphosphine (TPP) is the Wittig reaction. Recent research shows progress in developing an electrocatalytic route to reduce triphenylphosphine oxide (TPPO) to recycle the by-products of the Wittig reaction and create a catalytic cycle (see 5.1.1).^[165,214,215] Considering the high BET surface area ($355 \text{ m}^2 \text{ g}^{-1}$), homogenous distribution on the substrate, and tunable thickness, the film **polyCzTPP** presented here, could be conceivably applied as a recyclable ‘Wittig electrode’. Instead of reducing the phosphine oxides dissolved in the electrolyte, it would be more beneficial to perform the Wittig reaction on a phosphine-coated electrode, which can be immediately recovered after catalysis and applied in further reaction cycles.

As partial oxidation of the phosphine moieties within **polyCzTPP** occurred, the protection by boranes is assumed to be sensitive towards the conditions applied in the electropolymerization process. For further studies, it is even conceivable that instead of phosphines, directly the phosphine oxide analogue is applied as monomer for depositing an electropolymerized film on FTO. In a following step, the resulting electrode coated with phosphine oxides could then be reduced electrocatalytically and the *in situ* formed triphenylphosphines could enable the catalytic Wittig reaction.

6.3.2 Bipyridine-containing Films

In chapter 4.3.1.1, it was demonstrated that bulk homopolymer CPOP-30^[3] synthesized from 5,5'-di(9*H*-carbazol-9-yl)-2,2'-bipyridine (Czbipy) could be applied as support for a rhenium(I)-based photocatalyst. Since the utilization of powders in devices is less attractive, the goal was to synthesize polymer films from Czbipy, which can then be used as a chelating material for co-catalysts for electrochemical and photoelectrochemical applications.

The polymer film **polyCzbipy** was prepared in accordance with **polyCzTPP** *via* CV from a 1.0 mM solution of Czbipy in acetonitrile and dichloromethane (1:4) by using 0.1 M tetrabutylammonium perchlorate as electrolyte (Scheme 24). The reaction was carried out in a three-electrode cell for which fluorine-doped tin oxide (FTO) was applied as working electrode, platinum wire as counter electrode and Ag^0/AgCl as reference electrode.



Scheme 24: Electropolymerization of polyCzbipy on FTO *via* CV from a solution of Czbipy.

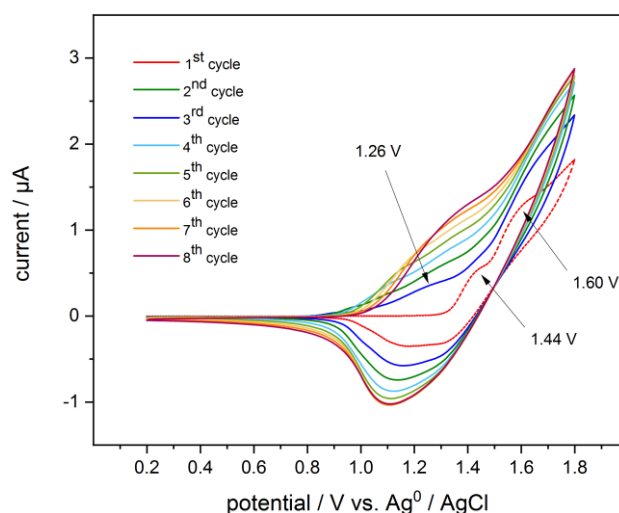


Figure 51: CV at FTO electrode, carried out for 1.0 mM solution of Czbipy in ACN/DCM (1:4) by using 0.1 M NBu₄ClO₄ as electrolyte. CV was recorded from 0.2-1.8 V (scan rate of 50 mV/s).

The carbazole-based films were deposited on FTO *via* eight cycles in CV. In the first oxidation scan of the cyclic voltammogram (Figure 51) two peaks are monitored at 1.44 and 1.60 V vs. Ag⁰/AgCl deriving from oxidation of the carbazole moieties. In the following cycles a further peak appears at 1.26 V vs. Ag⁰/AgCl resulting from polymerization of carbazole functionalities. With increasing cycle numbers, the peak shifts to higher potentials, which points to gradual growth of the polymer film.^[200]

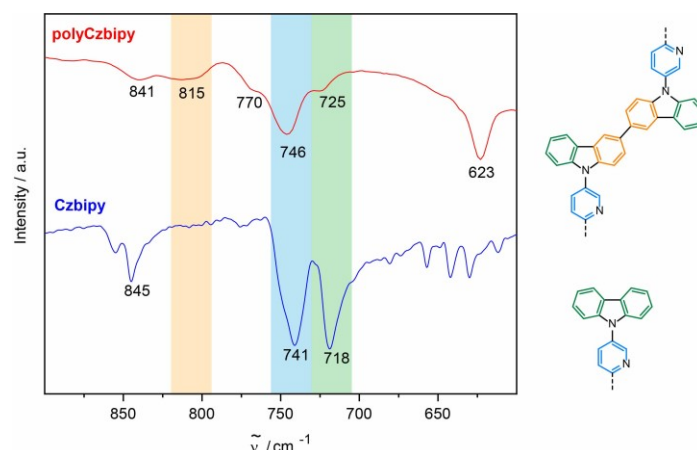


Figure 52: Fingerprint region of FTIR spectra of Czbipy (blue) and polyCzbipy (red).

The FTIR spectra of **polyCzbipy** and Czbipy (Figure 52) show evidence that Czbipy was dimerized during cyclic voltammetry. The fingerprint analysis of the spectrum for **polyCzbipy** shows a new band at 815 cm⁻¹ that was assigned to C-H vibrations of trisubstituted phenyl rings of the carbazole dimers.^[197] In contrast the spectrum for Czbipy only monitors signals at 718 cm⁻¹ for C-H vibrational bands of disubstituted phenyl rings. Disubstituted phenyl species are also detected for **polyCzbipy** at 725 cm⁻¹ but with less intensity, as the carbazole only dimerizes and does not show full cross-linkage. For both spectra, vibration bands

for C-H bonds of bipyridine units are shown at 746 and 741 cm^{-1} , respectively.^[142,197]

SEM analysis (Figure 53) shows the homogeneously distributed polyCzbipy films on the FTO substrate. Images of the cross-section of FTO and film as well as images taken from top view display an even surface of the film. The film thickness was determined to be around 620 to 680 nm by images taken in right angle position to the edge of the film and FTO.

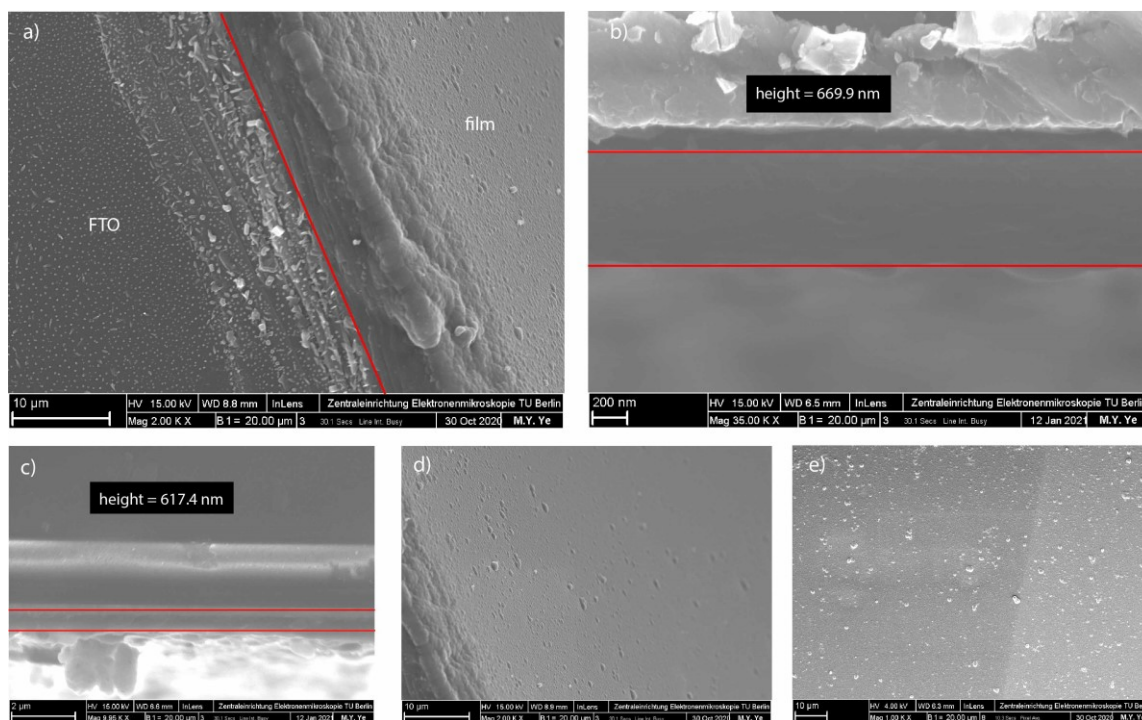
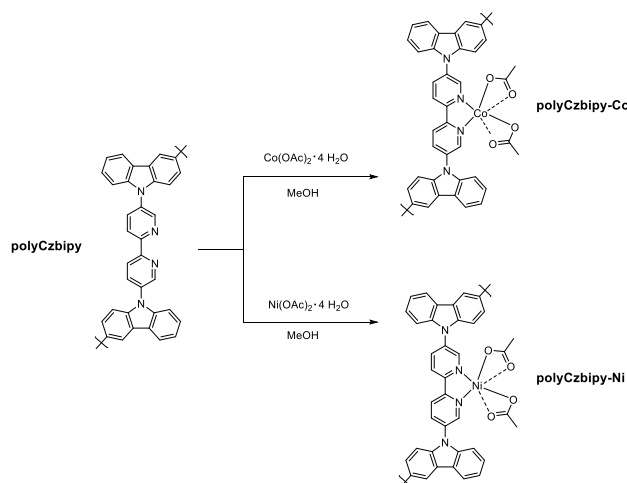


Figure 53: Scanning electron microscopy images of polyCzbipy on FTO: a)-c) show the edge between FTO and polyCzbipy, d) side view and e) top view of film. b) and c) show the film/ITO edge in right angle to measure the film thickness of around 620-680 nm.

The krypton gas sorption measurement (Figure A 12) of **polyCzbipy** revealed that the film is nearly non-porous, the BET surface area was calculated to be 3 $\text{m}^2 \text{g}^{-1}$. As the monomer Czbipy is a linear molecule with only two carbazole moieties, the surface area was expected to be low due to formation of solely dimers, although similar films polymerized from di(carbazolyl)biphenyl were reported possessing a BET surface area of 100 $\text{m}^2 \text{g}^{-1}$.^[199,200] The Czbipy moieties presumably allow to be densely packed due to little distortion within the molecular unit and high flexibility leading to a minimal surface area. Nevertheless, by applying the films in solution the polymer can probably swell so that the bipyridine moieties would become partially accessible.

To immobilize a co-catalyst on the polymer film **polyCzbipy**, nickel and cobalt were coordinated to the free bipyridine moieties to give **polyCzbipy-Ni** and **polyCzbipy-Co**, using nickel acetate and cobalt acetate precursors, respectively (Scheme 25). The metal coordinated films were prepared by soaking the **polyCzbipy** film deposited on FTO in a 0.01 M methanolic solution of the corresponding metal precursor for 3 h.



Scheme 25: Coordination of cobalt(II) acetate and nickel(II) acetate on polymer film polyCzbipy.

The metal-containing as well as the metal-free films on FTO were analyzed by XPS (Figure 54). The high-resolution N 1s core-level spectrum of **polyCzbipy** reveals that the metal-free film contains three species of nitrogen: an intense peak at 400.4 eV corresponding to dimerized carbazole moieties, a second signal at 399.2 eV, which is assigned to pyridinic nitrogen species and a less intense peak at 400.9 eV deriving from incomplete discharged nitrogens, which is often observed for electrochemically deposited films.^[142,143]

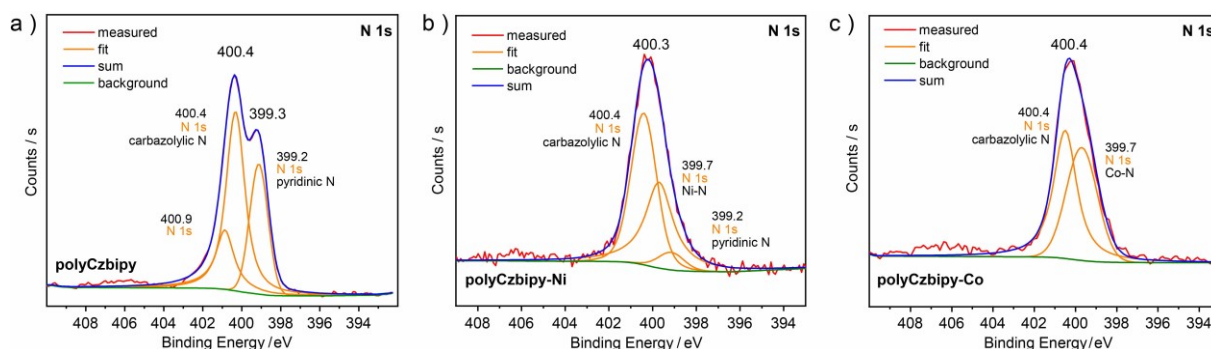


Figure 54: N 1s XPS spectra of a) polyCzbipy, b) polyCzbipy-Ni and c) polyCzbipy-Co.

In comparison, metal-coordinated films **polyCzbipy-Ni** and **polyCzbipy-Co** exhibit a signal at 399.7 eV due to coordination of bipyridine with nickel and cobalt centers in accordance with the reference complexes $\text{Ni}(\text{bipy})(\text{OAc})_2$ and $\text{Co}(\text{bipy})(\text{OAc})_2$ (Figure A 13), respectively. For **polyCzbipy-Co**, the signals at 400.4 eV and 399.7 eV are in the same ratio, consequently, the proportion of carbazolylic nitrogen and coordinated metal is 1:1 and hints towards the complete occupation of bipyridine moieties with Co(II) co-catalyst. This is further confirmed by the XPS survey presenting an atomic% ratio of 1:4 for Co to N, which fits with the theoretical proportion for one repeating unit of **polyCzbipy-Co**. The N 1s core-level spectrum of **polyCzbipy-Ni** shows a third nitrogen species at 399.2 eV deriving from non-coordinated bipyridine. The integrated nitrogen peaks indicate that 80% of the bipyridines were

immobilized with Ni(II) co-catalyst proving that the bipyridine units are accessible even though **polyCzbipy** shows low porosity. The XPS survey supports this calculation as an atomic% ratio of 1:5 for Ni to Co was detected and thus around 80% metal loading of possible coordination sites was achieved.

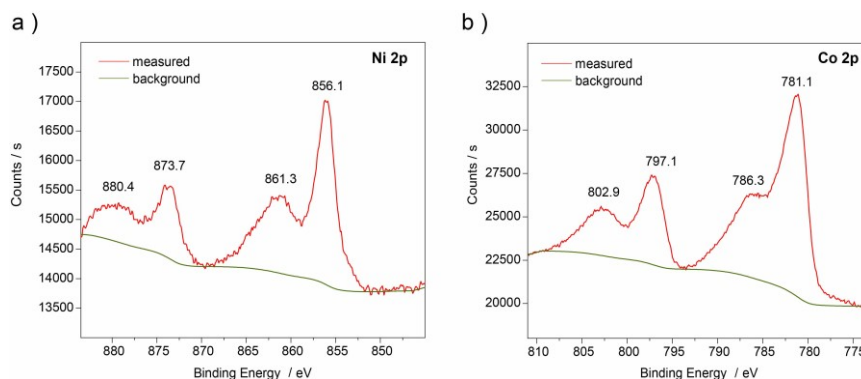


Figure 55: XPS spectra a) Ni 2p of **polyCzbipy-Ni** and b) Co 2p of **polyCzbipy-Co**.

The elemental composition was further investigated by Ni 2p and Co 2p core-level measurements, respectively (Figure 55). The Ni 2p spectrum of **polyCzbipy-Ni** shows a doublet with peaks at 856.1 eV and 873.7 eV, which are assigned to $2p_{3/2}$ and $2p_{1/2}$ signals for Ni(II) species (Figure 55, a), and the corresponding satellites at 861.3 and 880.4 eV.^[144] The Co 2p spectrum of **polyCzbipy-Co** proves the existence of coordinated Co(II) salt. According to literature, the signals detected at 781.1 eV and 797.1 eV were assigned to $2p_{3/2}$ and $2p_{1/2}$ doublet peaks including the characteristic satellites.^[143] The measured binding energies of the metal doublets of **polyCzbipy-Ni** and **polyCzbipy-Co** correspond with the synthesized references Ni(bipy)(OAc)₂ and Co(bipy)(OAc)₂ (Figure A 13).

6.3.2.1 Electrochemical Behaviour

Both metal-coordinated materials, **polyCzbipy-Ni** and **polyCzbipy-Co** were tested as heterogeneous catalysts for oxygen evolution reaction (OER). The metal coordinated films on FTO were applied as electrode in an alkaline aqueous electrolyte (1 M KOH) by using a typical three-electrode system.

The polarization curves of **polyCzbipy-Co** and **polyCzbipy-Ni** (Figure 56) show a clear OER current starting from 1.6 V vs. RHE. As expected, **polyCzbipy-Co** exhibits much higher OER current than **polyCzbipy-Ni**. The **polyCzbipy-Co** catalyst reaches the current of 10 mA, while **polyCzbipy-Ni** only shows a current ~2 mA at the potential of 2.0 V vs. RHE. This trend is consistent with previous reports about the high activity of cobalt(II) species for OER.^[143,216] Nevertheless, the activity is comparably low in contrast to other systems, for example macro/microporous bipyridine-containing COF designed by Zhao and coworkers.^[143] This

paper reveals good activity due to the high accessibility of the co-catalyst within the pores. One factor why metal-containing **polyCzbipys** show relatively low activity is presumably because of the thin coating of **polyCzbipy** and therefore a low amount of co-catalyst.

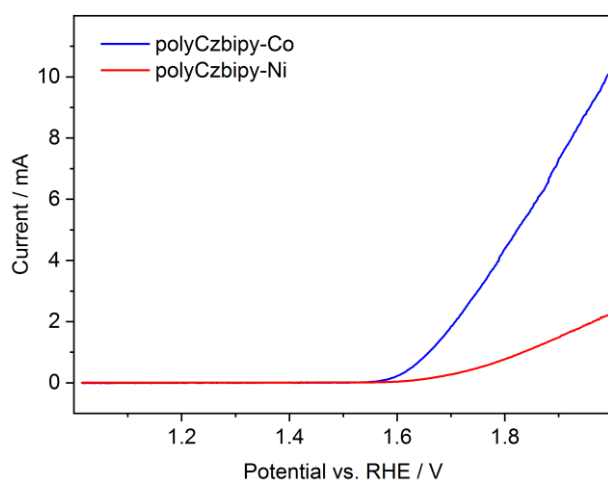


Figure 56: OER performance of polyCzbipy-Ni (red) and polyCzbipy-Co (blue).

Consequently, 20 instead of 8 cycles of polymer film were deposited *via* CV to obtain a thicker film ($\sim 2.5\text{-}3\text{ }\mu\text{m}$) on the electrode and therefore increasing the amount of catalyst. As thicker films of **polyCzbipy-Co** were by five times less active in OER as compared to their thinner counterparts (Figure 57), it is suspected that the densely packed, almost non-porous nature of **polyCzbipy**, apparently makes the active sites less accessible. Moreover, the increase of film thickness seems to decrease the conductivity of the film and therefore diminishes the performance.

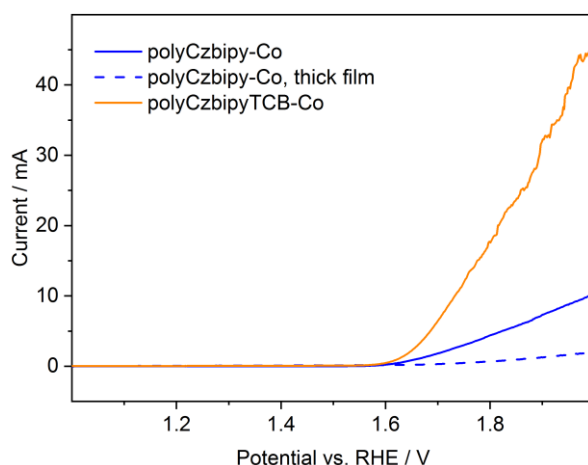


Figure 57: OER performance of polyCzbipyTCB-Co (orange) and thin and thick films of polyCzbipy-Co (blue).

Due to the linear geometry of the monomer, the porosity of **polyCzbipy** is relatively low compared to polymer films with trigonal or tetrahedral carbazole molecules.^[199] It was assumed that by simple addition of a low percentage of trigonal 1,3,5-tri(*N*-carbazolyl)benzene (TCB) as comonomer the porosity would increase and better accessibility should be achieved.

In the following experiment, 20 mol% of TCB were incorporated into a statistical copolymer film synthesized *via* electropolymerization of 8 cycles in CV. So-called **polyCzbipyTCB** was produced according to the procedure developed for **polyCzbipy**. The material **polyCzbipyTCB** was characterized by XPS (Figure A 14) and compared with pure Czbipy films, which showed proportionally more carbazolylic nitrogens in relation to pyridinic nitrogens, suggesting successful incorporation of TCB in the film. After immobilization of cobalt on the polymer film, **polyCzbipyTCB-Co** was analyzed by XPS (Figure A 15) and then also tested as a catalyst for OER. The thin film **polyCzbipyTCB-Co** showed significantly higher activity than **polyCzbipy-Co**. At 2.0 V, the current of **polyCzbipyTCB-Co** was elevated by four times compared to films without TCB (Figure 57).

The Tafel plots (Figure 58) were extracted from the OER polarization curves, and show that **polyCzbipy-Co** and **polyCzbipyTCB-Co** possess low slopes of 72.0 and 85.0 mV/dec, respectively, indicating a significantly faster reaction kinetics comparing to **polyCzbipy-Ni** (Tafel slope 129.8 mV/dec) and thicker film containing Co(II) catalyst (Tafel slope 333.7 mV/dec).

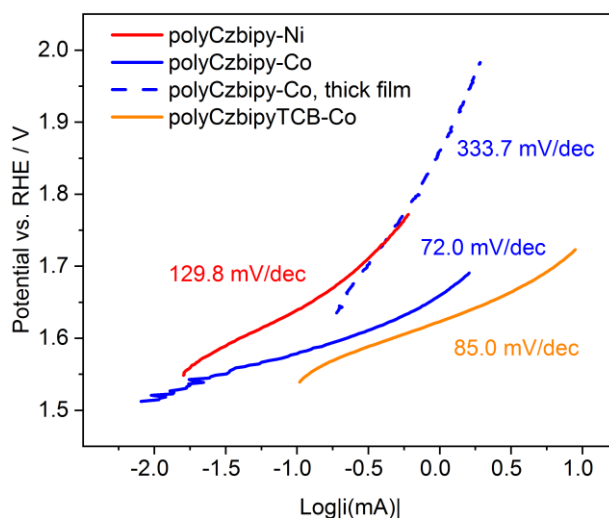


Figure 58: Tafel plots for **polyCzbipy-Ni**, **polyCzbipy-Co** (thin and thick film) and **polyCzbipyTCB-Co**.

6.3.2.2 Photochemical Behaviour

The photoactivity of the corresponding bulk polymer **CPOP-30**^[3] was already shown in the previous chapter (4.3.1.1). Using the powdered **CPOP-30**, the direct band gap was determined to be 2.97 eV by the Tauc plot method (Figure 8). To confirm the applicability of the film **polyCzbipy** for photocatalysis, an UV-Vis spectrum of **polyCzbipy** synthesized *via* 8 cycles in CV, was conducted. The adsorption edge of **polyCzbipy** was detected at 400 nm, which corresponds to an optical band gap energy of 3.03 eV calculated from the Tauc plot, thus in accordance with the band gap of bulk polymer **CPOP-30**.

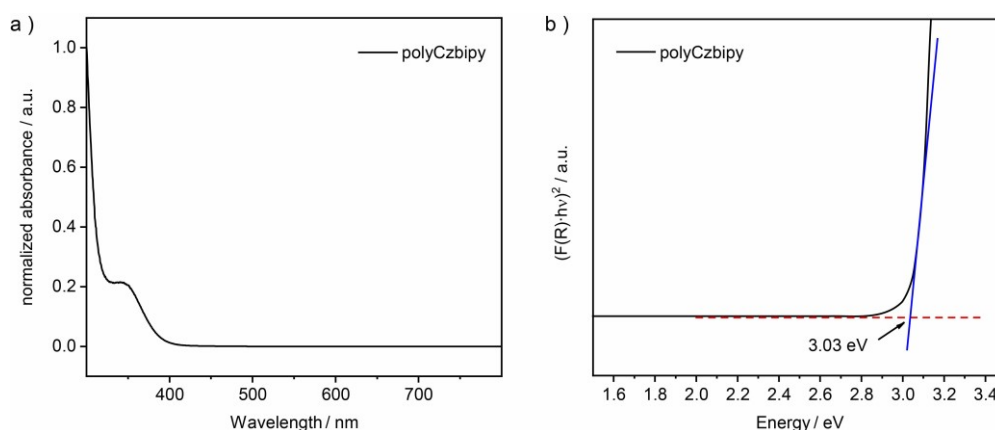


Figure 59: a) UV-Vis spectrum of polyCzbipy and b) Tauc plot for determination of direct band gap.

Besides the band gap, the absolute positions of valence band maximum as well as the conduction band edge regarding the vacuum level are necessary to identify good candidates for photocatalysis. The band positions were calculated from ultraviolet photoelectron spectroscopy (UPS) measurements (Figure 60).

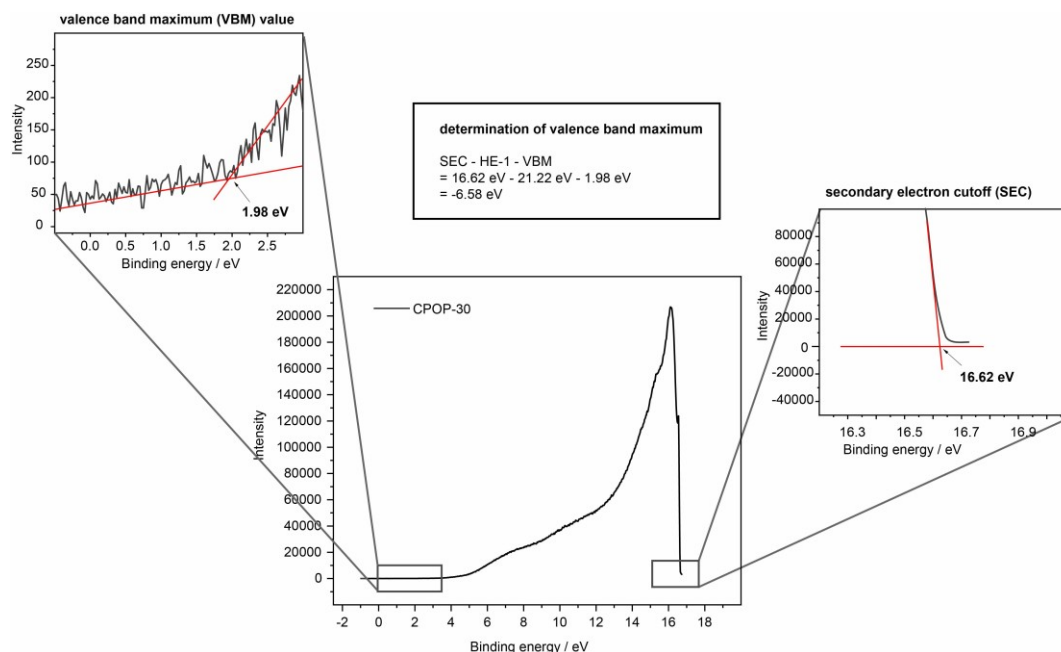


Figure 60: UPS measurement of CPOP-30 to determine the valence band maximum position of -6.58 eV.

The valence band maximum (VBM) value was identified by extrapolation of the starting point of photoexcitation, which showed a value of 1.98 eV. The secondary electron cutoff (SEC) was determined to be 16.62 eV. The valence band energy was calculated by subtraction of VBM value and energy of photon source (He-1, 21.22 eV) from SEC, which leads to a valence band maximum position in respect to vacuum level of -6.58 eV.

If the band gap defined by the Tauc plot is taken in consideration, a schematic band diagram (Figure 61) can be presented to depict the determined edges of valence and conduction

band. The standard redox energy of hydrogen evolution reaction (HER) $\text{H}_2\text{O}/\text{H}_2$ and oxygen evolution reaction (OER) $\text{H}_2\text{O}/\text{O}_2$ are set at -4.44 eV and -5.67 eV vs. vacuum, respectively.^[210] As the valence band maximum is located below and the conduction band minimum above the water oxidation and reduction potential, the material should in theory be qualified for overall water splitting.

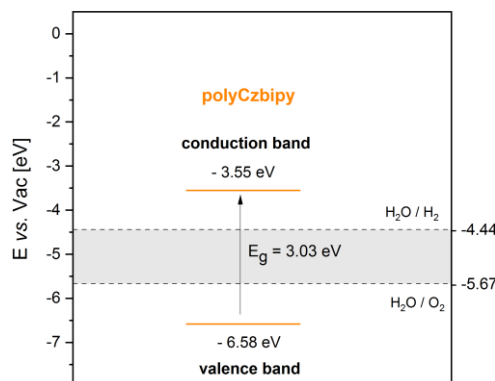


Figure 61: Schematic band diagram of polyCzbipy.

6.3.2.3 Photoelectrochemical Behaviour

The polymer films polyCzbipy proved to be chemically stable in an aqueous solution, as observed for OER in alkaline KOH solution. Furthermore, nickel(II) and cobalt(II) coordinated **polyCzbipy** films show considerable OER activity (6.3.2.1). In addition, the absorption in visible-light range as well as suitable band positions motivated to further investigate the films for photoelectrochemical applications. The photoelectrocatalytic tests, which are presented in this chapter were carried out by Tianyi Wang from Helmholtz Zentrum Berlin (HZB).

The photoelectrochemical performance was studied in a photoelectrochemical (PEC) cell. For this purpose, pristine **polyCzbipy** as well as the Ni(II) and Co(II) coordinated films deposited on FTO were tested in linear sweep voltammetry (LSV) under AM 1.5 chopped illumination in a potential range from -0.4 V to 0.4 V vs. Ag^0/AgCl applying a 0.1M KPi electrolyte solution with a pH of 7.8 (Figure 62, a-c)). In the PEC cell, the samples were alternately irradiated for 2 s and kept in dark for 2 s with increasing potential.

Notably, it was observed that pristine **polyCzbipy** film shows the highest photocurrent intensities as well as a sharp response to irradiation. The photocurrent increases immediately with opening of the shutter of the solar simulator indicating fast charge transfer kinetics. The metal-loaded electrodes provide reduced photocurrents (Figure 62, b-c)), especially **polyCzbipy-Co** shows a strong decline in photo-response as well as a degraded photocurrent, which is clearly visible from the lowered scan rate and differed periodicity. Degradation of performance from metal coordinated films may derive from the overloading of molecular

catalyst which can influence the amount of light passing through the material, thus inhibit efficient catalysis.^[212] In contrast, the performance of **polyCzbipy-Ni** remains in the same range as pure **polyCzbipy**. The Ni-coordinated material reached a maximum current density of $2.5 \mu\text{A cm}^{-1}$ and clear photo-response under irradiation.

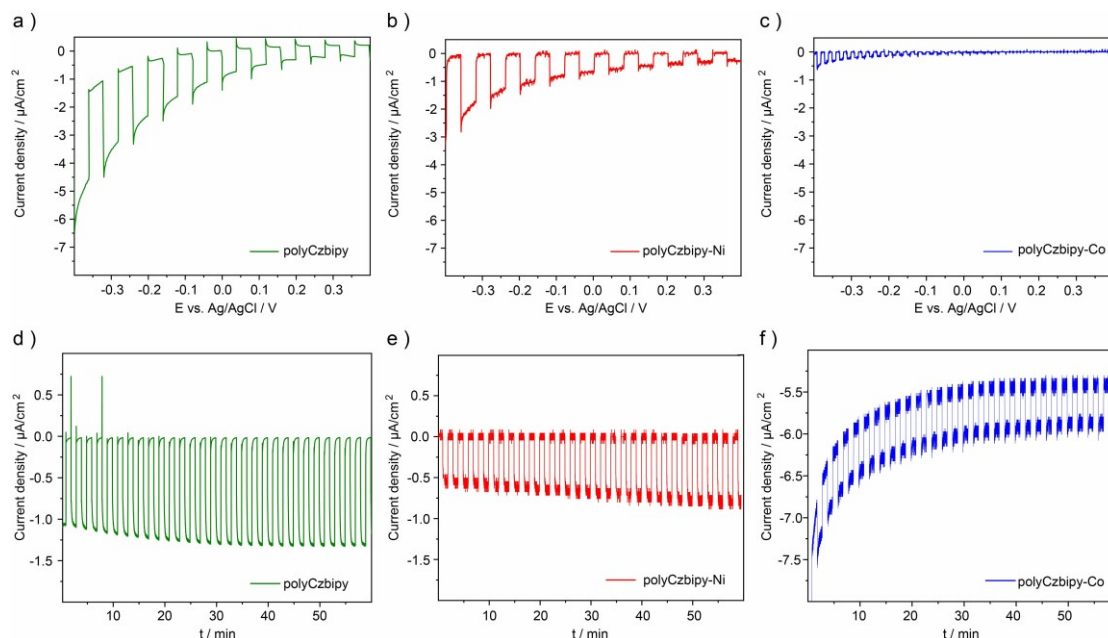


Figure 62: Linear sweep voltammetry under chopped illumination (of 2s) from -0.4 V to 0.4 V vs. Ag⁰/AgCl of a) polyCzbipy, b) polyCzbipy-Ni and c) polyCzbipy-Co. Photocurrent stability test under chopped irradiation (of 60 s) for 1h of d) polyCzbipy, e) polyCzbipy-Ni and f) polyCzbipy-Co.

Under chopped illumination of 60 s, photoelectrochemical stability was studied for 1 h at 0.4 V vs. Ag⁰/AgCl for **polyCzbipy** and **polyCzbipy-Ni**, and at -0.4 V vs. Ag⁰/AgCl for **polyCzbipy-Co** (Figure 62, d-f)). The photocurrents slightly increased over time and maximal currents of $1.3 \mu\text{A cm}^{-1}$ and approximately $0.9 \mu\text{A cm}^{-1}$ were observed for metal-free and metal coordinated films, respectively. After around 30 min, the amplitude of the curves remained stable and degradation due to irradiation was not detected suggesting that the polymer films are stable under chopped illumination and applied voltages and therefore applicable for photoelectrochemical purposes. The photocurrents are relatively low in contrast to typical semiconductive photoelectrodes such as CuO and CuBi₂O₄, but by comparing with purely organic materials on FTO, similar values of $0.9 \mu\text{A cm}^{-1}$ were reported for BDT-ETTA COF film prepared by Sick and coworkers.^[217]

For open-circuit potential (OCP) measurements, the samples were set-up in a solar simulator and the potentials were measured for 8 min (Figure 63). When the potential was stabilized in the dark, the shutter was opened manually until the potential leveled off, then the shutter was closed again. Under light illumination, all films showed an almost vertical increase in potential, where the upwards shift pointed towards *p*-type character of the materials implying

the presence of excess electron holes in the valence band. This can be expected as the network contains acceptor groups within the material such as bipyridine, which leads to a *p*-type material.^[218] The differences between open circuit potentials in dark and under irradiation (ΔOCP) were determined to be 0.24 V, 0.28 V and 0.51 V for **polyCzbipy-Ni**, **polyCzbipy** and **polyCzbipy-Co**, respectively.

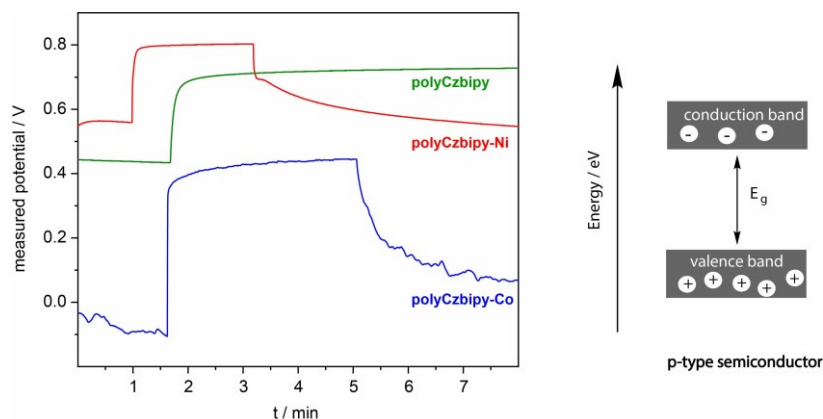


Figure 63: Open circuit potential measurement of **polyCzbipy** (green), **polyCzbipy-Ni** (red) and **polyCzbipy-Co** (blue) which reveal *p*-type character.

6.3.2.4 Bipyridine-containing Films on Semiconductors

One attempt to enhance the charge-carrier lifetimes of electrodes is the coating of polymer layers on the semiconductor photoelectrode. The coupling of both materials should help to create an intermediate charge storage layer by formation of redox pairs whereby recombination is prevented through spatial separation of charges. Due to the extended lifetime of redox states, an increase in photocatalytic efficiency should be achieved. The following chapter focuses on the combination of photocathodes with polymer films.

Copper oxide (CuO) and Copper Bismuth oxide (CuBi₂O₄) photoelectrodes prepared by pulsed laser deposition on FTO were provided by Helmholtz Zentrum Berlin (HZB).^[219] These *p*-type electrodes were coated with **polyCzbipy** in accordance with the previously reported procedure for plain FTO (see 6.3.2). The polymer film **polyCzbipy** was deposited on top of the electrodes *via* cyclic voltammetry from a 2.0 mM solution of Czbipy.

The first oxidation scans of cyclic voltammograms at CuO/FTO as well as CuBi₂O₄/FTO clearly show the formation of oxidized carbazoles at 1.58 V vs. Ag⁰/AgCl, which are necessary to form the desired carbazole dimers and thus to cross-link the monomers (Figure 64). In the following cycle, a peak at 1.35 or 1.33 V vs. Ag⁰/AgCl was observed, respectively. This peak indicated the formation of polymer, hence validating the successful polymerization on the significantly less conductive semiconductor CuO/FTO and CuBi₂O₄/FTO.

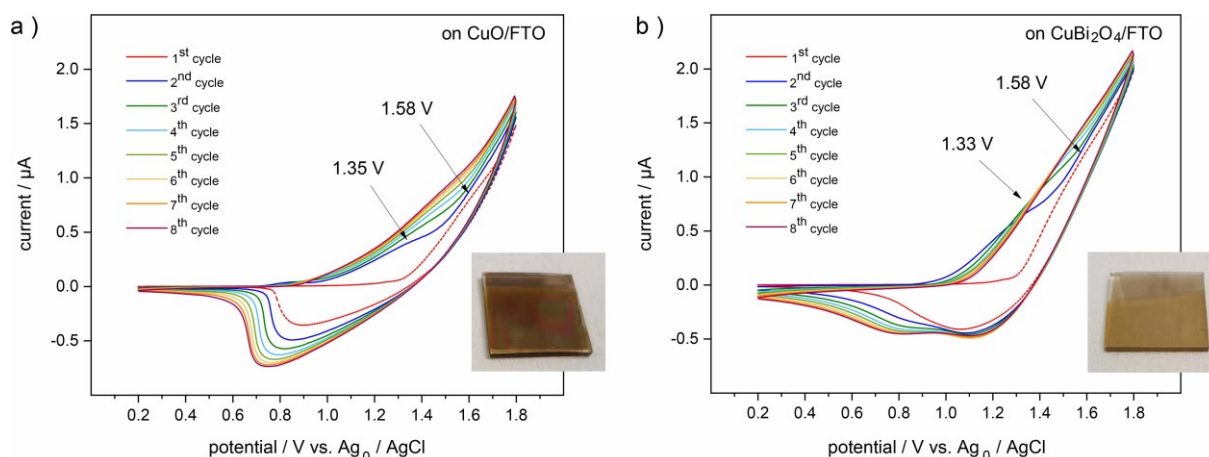


Figure 64: Cyclic voltammogram at a) CuO/FTO and b) CuBi₂O₄/FTO electrode, carried out for 2.0 mM solution of Czbipy in ACN/DCM (1:4) by using 0.1 M NBu₄ClO₄ as electrolyte. CV was recorded from 0.2-1.8 V (scan rate of 50 mV/s).

For photoelectrochemical tests, polymer films **polyCzbipy** deposited on CuO and CuBi₂O₄ were post-synthetically modified with nickel acetate. By immersing the cathodes in a Ni(II) solution, the co-catalyst coordinated to the bipyridine coordination site to yield **polyCzbipy-Ni** on CuO/FTO and CuBi₂O₄/FTO, respectively.

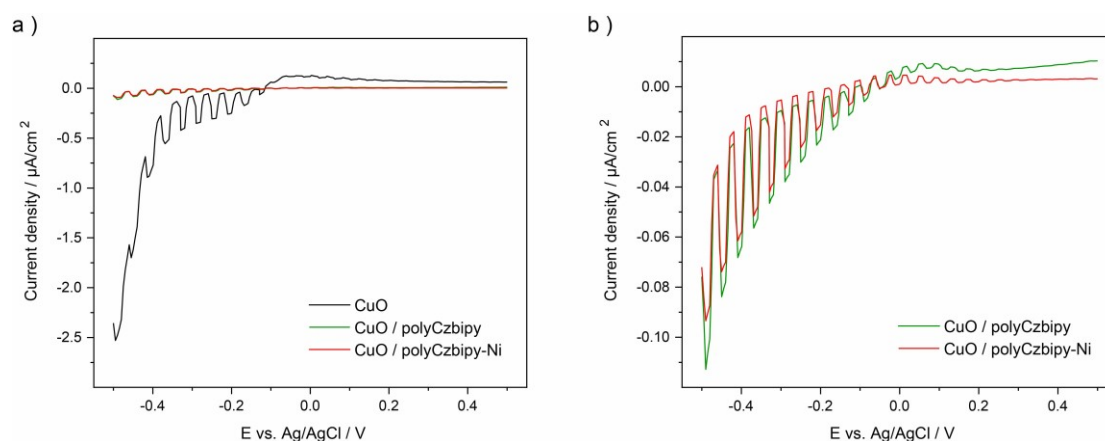


Figure 65: a) Linear sweep voltammetry under chopped illumination (of 2s) from -0.5 V to 0.5 V vs. Ag⁰/AgCl of CuO (black), CuO/polyCzbipy (green) and CuO/polyCzbipy-Ni (red). b) Enlarged section of voltammogram of CuO/polyCzbipy (green) and CuO/polyCzbipy-Ni (red).

First, the photoelectrochemical performances of the modified photocathodes were studied in a PEC cell. For this purpose, pure CuO/FTO and CuBi₂O₄/FTO substrates, pristine **polyCzbipy** as well as **polyCzbipy-Ni** on the photoelectrodes were tested in linear sweep voltammetry (LSV) under AM 1.5 chopped illumination in a potential range from -0.5 V to 0.5 V vs. Ag⁰/AgCl. The linear sweep voltammetry measurements of CuO/FTO as substrate (Figure 65) depict significant differences in current density between bare CuO and **polyCzbipy** coated CuO photocathodes. **CuO/polyCzbipy** as well as the Ni(II) coordinated equivalent possess a photocurrent density around 0.04 μA cm⁻², which is much lower in comparison to **FTO/polyCzbipy**. The additional carbazole film probably creates an energetic barrier for

charge injection. As a result, a drastic drop in photocurrent density for **CuO/polyCzbipy** was detected. Considering the band gap of CuO, which is determined to be <1.5 eV, the band positions of CuO and **polyCzbipy** with a significantly higher band gap, do not align with each other.^[210]

The OCP measurements (Figure 66) show the expected vertical increase in potential under irradiation, which points out that all materials exhibit *p*-type character.^[220] The differences between open circuit potentials in dark and under irradiation (Δ OCP) were determined to be 0.3 V, 0.2 V and 0.35 V for CuO, **CuO/polyCzbipy**, and **CuO/polyCzbipy-Ni**, respectively. The coordination of co-catalyst Ni(II) with bipyridine shows an enhancement in photovoltage in comparison to **CuO/polyCzbipy**.

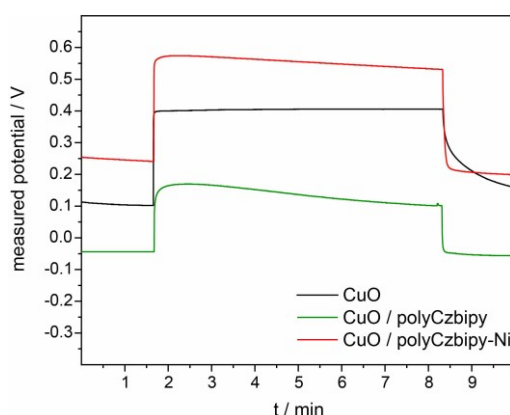


Figure 66: Open circuit potential measurement of CuO (black), CuO/polyCzbipy (green) and CuO/polyCzbipy-Ni (red) which reveal *p*-type character.

The linear sweep voltammogram under chopped illumination displays that bare CuBi₂O₄ exhibits a current density up to 90 $\mu\text{A cm}^{-2}$, whereas **CuBi₂O₄/polyCzbipy-Ni** and **CuBi₂O₄/polyCzbipy** have reduced current densities of 60 and 47 $\mu\text{A cm}^{-2}$, respectively (Figure 67, a). Notably, the coordination of the Ni(II) complex led to an enhancement in performance compared to pristine **polyCzbipy** on CuBi₂O₄. In addition, several scans of **CuBi₂O₄/polyCzbipy** in LSV were monitored showing that with each scan an enhancement of current density was observed (Figure 67, b). In comparison to CuO substrates, it is notable that the combination of CuBi₂O₄ photocathodes with **polyCzbipy** results in higher-performing semiconductors, which is assumably due to better matching band positions (Figure 68). CuBi₂O₄ prepared by pulsed layer deposition possesses a band gap of 1.90 ± 0.05 eV and its conduction band is located on a similar level as **polyCzbipy**.^[219,221,222] In contrast, the valence band edge of CuBi₂O₄ is situated higher relatively to **polyCzbipy**, therefore photogenerated holes can sufficiently travel from one to the other semiconductor.^[222] The lower photocurrent density values for coated CuBi₂O₄ probably derive from the amorphous structure of **polyCzbipy** that disturbs fast transport of photo-induced charges.

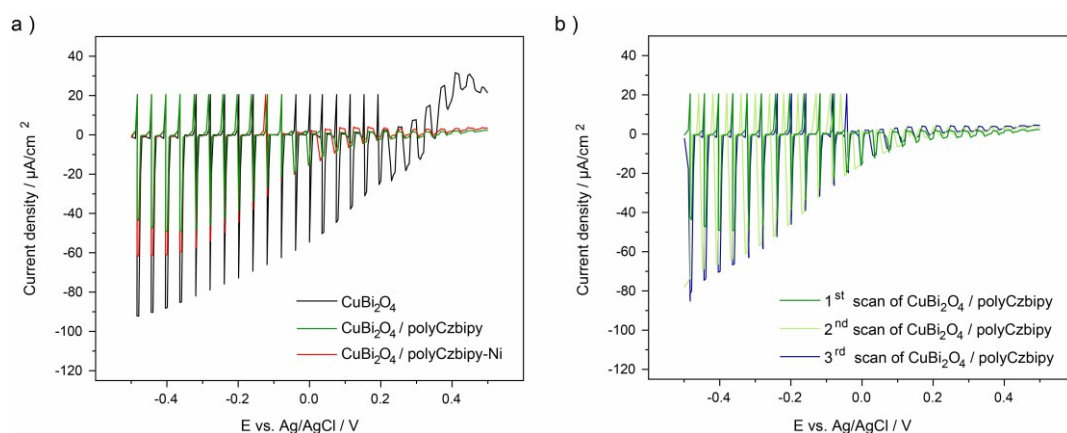


Figure 67: a) Linear sweep voltammetry under chopped illumination (of 2s) from -0.5 V to 0.5 V vs. Ag⁰/AgCl of CuBi₂O₄ (black), CuBi₂O₄/polyCzbipy (green) and CuBi₂O₄/polyCzbipy-Ni (red). b) LSV for different scans of CuBi₂O₄/polyCzbipy.

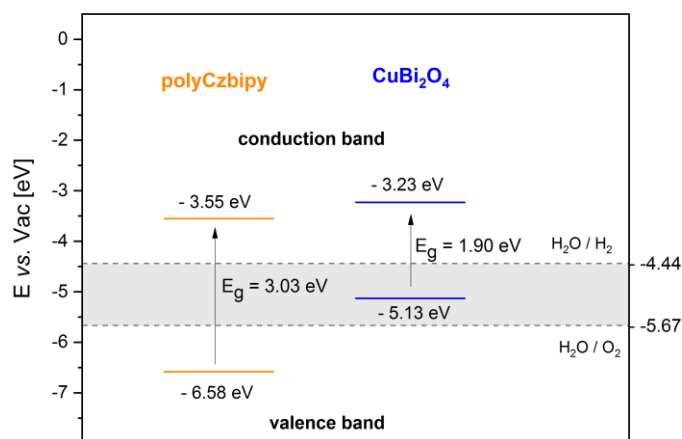


Figure 68: Schematic band diagram of polyCzbipy and CuBi₂O₄. ^[222]

It can be speculated that the amorphous structure of **polyCzbipy** might be advantageous for charge storage, as charge trapping at defect states is more probable in non-crystalline materials. Though, the disordered nature of **polyCzbipy** might limit the transport of charge carriers and inhibit fast transport to the interface where the charges participate in the photoelectrocatalytic reaction.

Open-circuit potential measurements underline the *p*-type character of the measured materials as a stepwise increase in potential was detected under illumination (Figure 69). ΔOCP for bare CuBi₂O₄ and **CuBi₂O₄/polyCzbipy-Ni** were determined to be 0.3 V, whereas the material without co-catalyst, **CuBi₂O₄/polyCzbipy** shows a significantly higher ΔOCP of 0.65 V. ΔOCP displays the shift in Fermi level and thus the photovoltage at the junction between CuBi₂O₄ and **polyCzbipy**, strongly indicating the charge injection from metal oxide into the polymer layer.^[223] The high ΔOCP value emphasizes the usability of **CuBi₂O₄/polyCzbipy** as photocathode material for photoelectrocatalytic hydrogen evolution reaction.

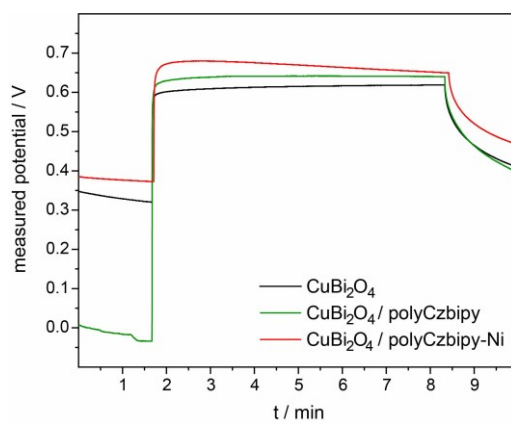


Figure 69: Open circuit potential measurement of CuBi_2O_4 (black), $\text{CuBi}_2\text{O}_4/\text{polyCzbipy}$ (green) and $\text{CuBi}_2\text{O}_4/\text{polyCzbipy-Ni}$ (red) which reveal *p*-type character.

6.4 Conclusion and Outlook

In summary, a phosphine-containing **polyCzTPP** film was successfully polymerized on ITO *via* cyclic voltammetry (CV) from a solution of CzTPP. The thickness of the film was determined to be $\sim 1.6 \mu\text{m}$ possessing a BET surface area of $355 \text{ m}^2 \text{ g}^{-1}$, as calculated from SEM analyses and the Kr adsorption isotherm, respectively. SEM images also showed a homogeneous distribution of the polymer on the substrate. With increasing film thickness, the carbazole-films tend to peel off. In these circumstances, the thickness of **polyCzTPP** film has to be carefully controlled by the number of scans in CV to form a stable coating. XPS and solid-state NMR spectroscopy point towards partial oxidation of the phosphines during the electropolymerization. One conceivable field of applications for **polyCzTPP** is the use of phosphine-coated films as a potential ‘Wittig electrode’. The partial oxidation of the material should not be an obstacle; it is even considered to start from a triphenylphosphine oxide containing film and reduce the phosphine oxide electrochemically before starting the Wittig reaction.^[214,215]

Bipyridine-containing **polyCzbipy** films were successfully produced on various conductive substrates such as FTO, FTO/CuO and FTO/CuBi₂O₄. The homogeneously deposited films were stable under the applied conditions and their thickness was controlled by different number of scans in CV. **PolyCzbipy** coated substrates were simply modified with co-catalysts by immersing the material in nickel or cobalt solutions. The applicability of Ni(II) and Co(II) coordinated **polyCzbipy** films was tested in electrocatalytic OER showing moderate activity. By increasing the film thickness, a drop of activity was observed. If, however the porosity of the films was slightly increased, by adding low ratios of the comonomer TCB, the activity of **polyCzbipyTCB-Co** was significantly enhanced. The Tafel plots showed that **polyCzbipy-Co** and **polyCzbipyTCB-Co** possess faster reaction kinetics compared to the Ni-coordinated equivalents.

Furthermore, the photoelectrocatalytic behavior of metal-free and modified **polyCzbipy** was tested. Open circuit potential measurements show that **polyCzbipy** exhibits *p*-type character due to the incorporated acceptor groups bipyridine and is therefore applicable as photocathode. The chopped LSV studies performed for testing the photoelectrochemical behavior of **polyCzbipy**/FTO displayed sharp photo-responses under irradiation without any degradation. Even though the maximum current density of $3.0 \mu\text{A cm}^{-1}$ is rather moderate in comparison to inorganic semiconductors, these values are comparable to other pure organic semiconductors.^[217,224] The coordination of Co(II) and Ni(II) salts led to a decrease in photo-response, which could derive from formation of metal nanoparticles under illumination. Nickel

coordinated films seem to be suitable for photocatalytic applications and should therefore be targeted in future studies. Furthermore, combinations of two *p*-type materials as photocathodes were synthesized. For this purpose, semiconductive CuO and CuBi₂O₄ were coated with **polyCzbipy**. In a solar simulator, **CuO/polyCzbipy** displayed a significant decrease in photocurrent density, which is assumed to be the case due to mismatching band alignments and therefore inhibition of efficient charge transfer through the electrode. In contrast, **CuBi₂O₄/polyCzbipy-Ni** and **CuBi₂O₄/polyCzbipy** give photocurrent densities of 60 and 47 $\mu\text{A cm}^{-2}$, respectively. ΔOCP for **CuBi₂O₄/polyCzbipy** was calculated to be 0.65 V probably deriving from the charge injection from metal oxide underlining the potential of carbazole film coated CuBi₂O₄ as photocathode. Nevertheless, bare CuBi₂O₄ exhibits the highest photocurrent density indicating that the amorphous nature of **polyCzbipy** might be on one hand advantageous for electron storage due to defect formation, but on the other hand the conductivity is rather low and fast electron-hole transport is limited. Moreover, porosity is playing a role in enhancing the efficiency of photoelectrocatalysis. Preliminary tests were already undertaken to create a less condensed polymer network by introducing some percentages of trigonal comonomer TCB to achieve higher porosity. In further investigations these kinds of copolymers should be applied as coating material for combined photocathodes with CuBi₂O₄.

7 Summary

This thesis presents different synthesis methods to produce and fine-tune microporous polymer networks for catalytic application as well as gas storage. The synthesis strategies range from oxidative polymerizations and cross-couplings reactions, such as Yamamoto coupling reaction, to electropolymerization, helping to tailor the properties of the materials. Especially, functional groups serving as ligands for metal-organic complexes were incorporated into the microporous structures functioning as macroligands. These defined coordination sites were used for immobilization of catalysts to bridge the gap between homogeneous and heterogeneous catalysis. Bipyridine-containing monomers equipped with carbazole moieties were incorporated into the networks *via* oxidative polymerization as well as electropolymerization to yield polymer films. The chelating ligands were used to coordinate rhenium(I) or nickel(II) catalysts onto the powdery polymers for photocatalytic CO₂ reduction or nickel-catalyzed cross-coupling under visible-light irradiation. Due to the extended π -system and light-harvesting properties of the metal-free carbazole polymer network, the materials proved to be excellent supports of photocatalysts. For electro- and photoelectrocatalytic applications, polymer films electropolymerized from bipyridine-containing carbazole monomers were decorated with cobalt(II) and nickel(II) co-catalysts. Due to the controllability of the film thickness and choice of co-catalyst, the films could be applied in electrocatalytic OER. In addition, the electropolymerized films provide an approach to coat any conductive substrate, such as semiconductors, to design new photoelectrodes. Besides bipyridine, phosphine-containing films were also prepared, which could be conceivable applied in electrocatalytic Wittig reactions. Additionally, phosphine-containing bulk polymers were synthesized *via* Yamamoto cross-coupling reaction, for heterogenization of Rh(I) hydrosilylation and hydroformylation catalysts. It is advantageous that the amount of metal, the coordination spheres of immobilized complexes and surface area of the material are optimized by incorporation of an additional comonomer. Therefore, copolymers with diluted amounts of phosphine units were synthesized. It turned out that the addition of a comonomer helped to increase the activity of the phosphine-containing polymer networks in hydrosilylation and hydroformylation reactions.

A second topic besides catalysis, was the design of solid-state hydrogen storage materials. For that purpose, the hydrogen affine molecule *N*-ethylcarbazole (NECz), which is

known for its capacity to bind hydrogen chemically for reversible hydrogen storage, was applied as comonomer for materials synthesized *via* oxidative polymerization. At first, physisorption of hydrogen on NECz-containing microporous materials was tested, presenting relatively high uptakes and isosteric heats of adsorption in comparison to other microporous polymers. In a second step, the polymeric backbone of the NECz-containing copolymers was successfully hydrogenated by means of platinum nanoparticles and elevated hydrogen pressure. Depending on the amount and size of nanoparticles, different hydrogenation levels were achieved. Primary tests show that thermal dehydrogenation of the solid-state hydrogen carriers is possible, although the reversibility is only accomplished, if a balance between stability of the scaffold as well as enough hydrogenated NECz units are maintained. This new concept shows that carbazole-based microporous polymer networks are promising candidates for chemical hydrogen storage materials besides physisorption at uneconomically, low temperatures.

8 Experimental Section

In this chapter all used materials and analysis methods for the characterization of monomers and polymers are listed. Furthermore, the synthesis routes and sample preparations are presented.

8.1 Materials

All used chemicals are enumerated here which were used without further purifications (Table 7).

Table 7: Applied Chemicals.

compound	acronym	supplier	specification
[1,1'-bis(diphenylphosphino)ferrocene]dichloropalladium(II)	Pd(dppf)Cl ₂	Apollo	
1,3-dimethyl-3,4,5,6-tetrahydro-2(1 <i>H</i>)-pyrimidinone	DMPU	Acros	97%
1,3,5-tris(4,4,5,5-tetramethyl-1,3,2-dioxaborolan-2-yl)benzene		AK scientific	98%
1,3,5-tris(<i>N</i> -carbazolyl)benzene	TCB	Sigma-Aldrich	98%
1,3,6,8-tetrabromopyrene		TCI	>98%
1,4-dibromobenzene		Sigma-Aldrich	98%
1,5-cyclooctadiene	COD	Sigma-Aldrich	>99%
2,2'-bipyridine	bipy	Alfa Aesar	99%
5,5'-dibromo-2,2'-bipyridine		abcr	95%
9-(4-bromophenyl)carbazole		Alfa Aesar	98%
18-crown-6		Acros	99%
acetone		Sigma-Aldrich	98%
acetonitrile	ACN	Roth	
anhydrous chloroform	CHCl ₃	Sigma-Aldrich	
anhydrous diethyl ether	Et ₂ O	Sigma-Aldrich	99+%, contains BHT
anhydrous <i>N,N</i> -	DMF	Alfa Aesar	99.8%

dimethylformamide			
anhydrous tetrahydrofuran	THF	Sigma-Aldrich	anhydrous, 99.9%
bis(1,5-cyclooctadiene)nickel(0)	Ni(COD) ₂	abcr	98%
borane dimethyl sulfide complex	BH ₃ μSMe ₂	Sigma-Aldrich	
bromine	Br ₂	Alfa Aesar	99.5%
carbazole		Sigma-Aldrich	98%
cesium carbonate	Cs ₂ CO ₃	Sigma-Aldrich	99%
chloroplatinic acid solution	H ₂ PtCl ₆	Sigma-Aldrich	8 wt% in H ₂ O
cobalt(II) acetate tetrahydrate	Co(OAc) ₂	Alfa Aesar	98%
copper(I) iodide	CuI	Sigma-Aldrich	>99.5%
cyclohexane		Roth	>99.5%
deuterated acetone	acetone-d ₆	Sigma-Aldrich	water <0.01%
deuterated chloroform	CDCl ₃	euriso-top	water <0.01%
deuterated dimethyl sulfoxide	DMSO-d ₆	euriso-top	water <0.01%
dichloromethane	DCM	Roth	>99.5% for synthesis
diethyl ether	Et ₂ O	Sigma-Aldrich	>99.8%, contains BHT
ethanol	EtOH	Honeywell	>99.8%
hydrochloric acid	HCl	Roth	10% in water
iron(III) chloride	FeCl ₃	Sigma	reagent grade, 97%
methanol	MeOH	Roth	>99 , for synthesis
n-buthyllithium	nBuLi	Sigma-Aldrich	2.5 M in hexane
N-ethylcarbazole	NECz	Sigma-Aldrich	97%
n-hexane	cHex	Carl Roth	>99%
nickel(II) acetate tetrahydrate	Ni(OAc) ₂	Aldrich	
pentacarbonylchlororhenium(I)	Re(CO) ₅ Cl		>99%
phosphorus trichloride	PCl ₃	Sigma-Aldrich	99%
potassium bromide	KBr	Sigma-Aldrich	>99%
potassium carbonate	K ₂ CO ₃	abcr	99%
rhodium(I)dicarbonyl acetylacetonate	Rh(CO) ₂ (acac)	Acros	99%
tetrabutylammonium perchlorate	NBu ₄ ClO ₄	Sigma-Aldrich	for electrochemical analysis, >99%

tetrahydrofuran	THF	Sigma-Aldrich	>99%
tetrakis(triphenylphosphine) palladium(0)	Pd(PPh ₃) ₄	Sigma-Aldrich	>99.99%
tetraphenylmethane	TPM	abcr	96%
triethylamine	TEA	Sigma-Aldrich	>99%
triethanolamine	TEOA	Sigma-Aldrich	>99%
triphenylphosphine	PPh ₃	Sigma-Aldrich	99%

8.2 Characterization Methods and Sample Preparation

8.2.1 Nuclear Magnetic Resonance Spectroscopy (NMR)

The NMR spectra were measured on a Bruker Avance II 200 MHz or 400 MHz or on a Bruker Avance III 500 MHz spectrometer in the given solvent. The chemical shifts δ were obtained in ppm whereby tetramethylsilane was applied as standard measurements for ^1H and ^{13}C . The splitting is recorded as s (singlet), d (doublet), q (quartet) and m (multiplet). The coupling constant J is measured in Hertz (Hz).

For solid-state NMRs a Bruker Avance 400 MHz employing cross-polarization magic angle spinning spectrometer (CPMAS) was used. ^{13}C CPMAS spectra were operated at 100 MHz at a spinning rate between 7 and 12 kHz. ^{31}P MAS and ^{11}B MAS spectra were operated at 168 and 162 MHz, respectively.

8.2.2 Gas Sorption Measurements

For the determination of surface areas nitrogen sorption isotherms at 77 K were measured by an Autosorb-iQ-MP from Quantachrome and a Quadrasorb SI device. The recorded data were analyzed by means of the BET theory. Before the samples were transferred into the glass measuring cell, they were activated at 80 °C under high vacuum for 12 h.

Hydrogen sorption isotherms were carried out on a Quantachrome Autosorb-iQ-MP instrument at 1 bar and 77 and 87 K, respectively. The isosteric heat of adsorption Q_{is} was calculated from the temperature-dependent isotherms at 77 and 87 K employing the Clausius-Clapeyron equation.

Krypton sorption adsorption isotherms were conducted on a on a Quantachrome Autosorb-iQ-MP instrument at 87 K. The obtained data was analyzed by BET theory to calculate the surface area.

8.2.3 Fourier Transform Infrared Spectroscopy (FTIR)

Infrared spectra were measured by means of potassium bromide pellets carried out on a Thermo Nicolet Magna-IR 750 spectrometer. Potassium bromide was dried at 120 °C overnight before the pellets were pressed. The data were recorded in transmission mode in the range of 4000 to 400 cm^{-1} . The peaks are listed in wavenumbers $\tilde{\nu}$.

8.2.4 Ultraviolet-Visible Spectroscopy (UV-Vis)

The diffuse reflectance ultraviolet–visible spectra were collected on Varian Cary 300 UV-Vis Spectrophotometer. The solids were evenly distributed on the sample holder to detect the solid-state UV-Vis spectra.

8.2.5 Thermogravimetric Analysis (TGA)

For thermogravimetric analysis a TGA 1 Star System from Mettler Toledo was used. A heating rate of 10 K min⁻¹ from 25 °C up to 1000 °C was applied. The measurements were carried out under nitrogen and air flow.

8.2.6 Thermal Gravimetric Mass Spectroscopy (TG-MS)

Thermal gravimetric mass spectroscopy was carried out by a Netzsch TG 209F1 Libra. The samples were heated up to 300 °C with a rate of 2 K min⁻¹, then the temperature was kept for 1 h at 300 °C. The evolved gases were detected and determined by MS.

8.2.7 Flash Chromatography

Flash chromatography was used for purification and carried out on a Biotage Isolera™ One column chromatography using Biotage SNAP™ KP-Sil Cartridges with silica gel 60 and UV-Vis detectors set to 254 nm and 366 nm.

8.2.8 Inductively Coupled Plasma Optical Emission Spectrometry (ICP-OES)

ICP measurements were carried out on a Varian ICP-OES 715 ES spectrometer. The polymers were dissolved in a mixture of sulfuric acid, nitric acid and hydrochloric acid in a ratio of 2:2:1. The polymers were microwaved in the acidic mixture to accomplish the sample digestion before they were diluted with distilled water.

8.2.9 Ultraviolet Photoelectron Spectroscopy (UPS)

The UPS measurements were carried out by a hemispherical analyzer (Specs Phoibos 100). To determine the valence band maximum edge and work function of the material, a He-I source ($E_{\text{He-I}}=21.21$ eV) was applied for ultraviolet photoelectron spectroscopy.

8.2.10 Scanning Electron Microscopy (SEM)

Scanning electron microscopy (SEM) images were taken by ZEISS GeminiSEM 500 NanoVP. The polymer films were sputtered with gold (5 or 25 nm) in an argon atmosphere.

8.2.11 Transmission Electron Microscopy (TEM)

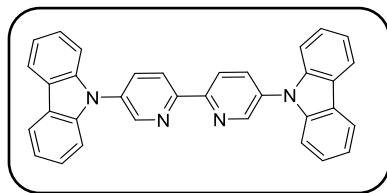
Transmission electron microscopy was carried out on a FEI Tecnai G2 20 S-TWIN transmission electron microscope (FEI Company, Eindhoven, Netherlands) equipped with a LaB6 source at 200 kV acceleration voltage. For the images, a Gatan MS794 P CCD camera was applied.

8.2.12 X-Ray Photoelectron Spectroscopy (XPS)

The x-ray photoelectron spectroscopy was measured on a K-Alpha™ + X-ray Photoelectron Spectrometer System (Thermo Scientific) with a hemispheric 180 ° dual-focus analyzer with a 128-channel detector. The X-ray monochromator used micro-focused Al-K α radiation.

8.3 Synthesis of the Monomers

Synthesis of 5,5'-di(9*H*-carbazol-9-yl)-2,2'-bipyridine (Czbipy)



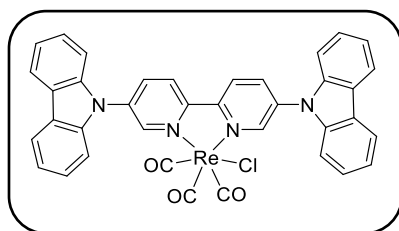
$$M = 486.58 \text{ g mol}^{-1}$$

5,5'-Di(9*H*-carbazol-9-yl)-2,2'-bipyridine was synthesized according to a reported procedure by Shan *et al.*^[225] Under Ar atmosphere, a mixture of 5,5'-dibromo-2,2'-bipyridine (500 mg, 1.59 mmol), carbazole (586 mg, 3.5 mmol), copper(I) iodide (61 mg, 0.32 mmol), 18-crown-6 (84 mg, 0.32 mmol), potassium carbonate (549 mg, 3.98 mmol) and 1,3-dimethyl-3,4,5,6-tetrahydro-2(1*H*)-pyrimidinone (DMPU, 1.67 mL) were placed in a pre-heated 100 mL Schlenk flask. The flask was connected to a reflux condenser before the mixture was stirred for 24 h at 190 °C in an oil bath. At 190 °C the reaction mixture turned into a yellow solution, after 24 h a black viscous oil was obtained which was quenched with 2 M HCl solution (100 mL). The mixture was extracted with dichloromethane and washed with NH₃·H₂O (25%, 60 mL) and water. The combined organic layers were dried over magnesium sulfate and the solvent was removed *in vacuo*. The crude product was purified by column chromatography on amino-functionalized silica gel from cyclohexane and dichloromethane. The obtained yellow solid was further purified by recrystallization from a mixture of cyclohexane and dichloromethane and yielded a light yellow crystalline solid 540 mg (1.11 mmol, 70%).

¹H NMR (200 MHz, CDCl₃, 25 °C): δ = 9.02 (d, *J* = 2.4 Hz, 2H), 7.12 (d, *J* = 8.4 Hz, 2H), 8.19 (d, *J* = 7.5 Hz, 4H), 8.12 (dd, *J* = 8.4 Hz, *J* = 2.5 Hz, 2H), 7.56-7.41 (m, 8H), 7.36 (dt, *J* = 6.7 Hz, *J* = 2.5 Hz, 4H) ppm.

¹³C NMR (50 MHz, CDCl₃, 25 °C): δ = 154.1, 147.8, 140.7, 135.3, 135.0, 126.5, 124.1, 122.3, 120.9, 120.7, 109.6 ppm.

Synthesis of rhenium(dicarbazolylbipyridine)(tricarbonyl) chloride [Re(Czbipy)(CO)₃Cl]



$$M = 792.09 \text{ g mol}^{-1}$$

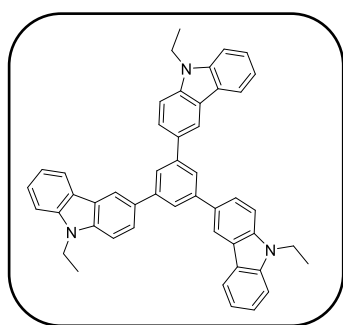
Under inert conditions, 5,5'-di(9*H*-carbazol-9-yl)-2,2'-bipyridine (243 mg, 0.5 mmol) and rhenium pentacarbonyl chloride (181 mg, 0.5 mmol) were dissolved and refluxed in toluene for

20 h. After cooling the reaction to room temperature, the solid was collected by filtration and was washed with hexane and toluene. To purify the compound, it was recrystallized in hexane to yield an orange solid (182 mg, 50%)

¹H NMR (400 MHz, DMSO-d₆, 25 °C): δ = 9.40 (d, J = 1.8 Hz, 2H), 9.17 (d, J = 8.8 Hz, 2H), 8.82 (dd, J = 8.7, 1.9 Hz, 2H), 8.34 (d, J = 7.8 Hz, 4H), 7.65 – 7.55 (m, 8H), 7.42 (t, J = 7.3 Hz, 4H) ppm.

¹³C NMR (100 MHz, DMSO-d₆, 25 °C): δ = 198.0, 153.2, 150.7, 139.9, 138.1, 137.0, 127.3, 126.4, 124.2, 122.0, 121.4, 109.8 ppm.

Synthesis of 1,3,5-tris(9-ethyl-9H-carbazol-3-yl)benzene



C₄₈H₃₉N₃

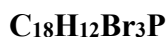
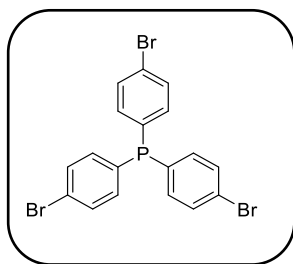
M = 657.861 g mol⁻¹

1,3,5-Tris(9-ethyl-9H-carbazol-3-yl)benzene was synthesized according to procedure reported by Ou and coworkers.^[156] 1,3,5-Tris(4,4,5,5-tetramethyl-1,3,2-dioxaborolan-2-yl)benzene (428 mg, 0.94 mmol), 3-bromo-9-ethylcarbazole (800 mg, 2.92 mmol), [1,1'-bis(diphenylphosphino)ferrocene]dichloropalladium(II) (103 mg, 0.14 mmol), cesium carbonate (3250 mg, 10.0 mmol), 1,4-dioxane (20 mL) and water (4 mL) were placed in a 100 mL Schlenk finger and were degassed by three freeze-pump-thaw cycles. Under Ar atmosphere, the suspension was stirred for 20 h at 90 °C. After cooling to room temperature, the brown suspension was quenched with water (30 mL). The mixture was extracted with dichloromethane and water. The combined organic layers were dried over magnesium sulfate and the solvent removed *in vacuo*. The crude product was purified by column chromatography from a mixture of cyclohexane and dichloromethane. The product was obtained as off-white solid (488 mg, 74%).

¹H NMR (500 MHz, CDCl₃, 25 °C): δ = 8.53 (d, J = 1.6 Hz, 3H), 8.21 (d, J = 7.6 Hz, 3H), 8.04 (s, 3H), 7.94 (dd, J = 8.6 Hz, J = 1.6 Hz, 3H), 7.55 (d, J = 8.6 Hz, 3H), 7.51 (dt, J = 7.6 Hz, J = 1.1 Hz, 3H), 7.46 (d, J = 8.0 Hz, 3H), 7.27 (t, J = 7.3 Hz, 3H), 4.45 (q, J = 7.3 Hz, 6H), 1.50 (t, J = 7.2 Hz, 9H) ppm.

¹³C NMR (100 MHz, CDCl₃, 25 °C): δ = 143.4, 140.6, 139.7, 132.8, 126.0, 125.6, 125.0, 123.7, 123.3, 120.8, 119.4, 119.1, 108.9, 108.7, 37.8, 14.0 ppm.

Synthesis of tris(4-bromophenyl)phosphine



$$M = 498.98 \text{ g mol}^{-1}$$

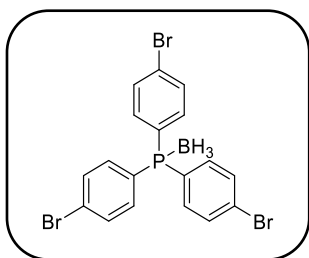
Tris(4-bromophenyl)phosphine was synthesized according to a reported procedure by Fischer *et al.*^[226] In a pre-dried Schlenk flask 1,4-dibromobenzene (4.48 g, 19.00 mmol) was dissolved in diethyl ether (110 mL). At -78 °C *n*-butyllithium (2.5 M in hexane, 7.5 mL, 18.75 mmol) was added slowly over 30 min. After 2 h of stirring at -78 °C, phosphorus trichloride (0.5 mL, 5.73 mmol) was added dropwise to the colorless solution which immediately turned yellow. Then the solution was allowed to slowly warm up to room temperature and stirred overnight. A saturated mixture of sodium bicarbonate (30 mL) and water (30 mL) was added so that the organic layer could be separated. The residual aqueous layer was extracted with dichloromethane (2 x 25 mL). The combined organic layers were dried over magnesium sulfate and the solvent was removed *in vacuo*. The crude product was purified by column chromatography from cyclohexane and 2.29 g (4.59 mmol, 80%) of a white crystalline solid was obtained as a product.

¹H NMR (200 MHz, CDCl₃, 25 °C): δ = 7.48 (dd, ³*J*_{HH} = 8.5 Hz, ⁴*J*_{PH} = 1.2 Hz, 6H, H-3), 7.12 (dd, ³*J*_{HH} = 8.5 Hz, ³*J*_{PH} = 7.2 Hz, 6H, H-2) ppm.

³¹P NMR (81 MHz, CDCl₃, 25 °C): δ = -8.46 ppm.

¹³C NMR (50 MHz, CDCl₃, 25 °C): δ = 135.2 (d, ³*J*_{CP} = 12 Hz), 135.1 (d, ²*J*_{CP} = 20 Hz), 132.0 (d, ¹*J*_{CP} = 7 Hz), 124.0 ppm.

Synthesis of tris(4-bromophenyl)phosphine-borane



$$M = 512.81 \text{ g mol}^{-1}$$

Tris(4-bromophenyl)phosphine-borane was synthesized according to a procedure of Van Overschelde *et al.*^[181] In a pre-dried Schlenk finger tris(4-bromophenyl)phosphine (100 mg, 0.2 mmol) was added and dissolved in anhydrous dichloromethane (0.4 mL). Then borane dimethyl sulfide complex (0.19 mL, 2.0 mmol) was added and after stirring the reaction for

24 h at room temperature, saturated aqueous ammonia chloride solution (1 mL) was added. The reaction mixture was stirred for another 1 h, after that it was poured into water (10 mL). The collected organic phase was washed with saturated aqueous sodium bicarbonate solution (15 mL) before it was dried over magnesium sulfate and filtrated over silica. The crude product was purified by column chromatography from cyclohexane (70%) and dichloromethane (30%) and 297 mg (0.58 mmol, 83%) of a white crystalline solid was obtained as a product.

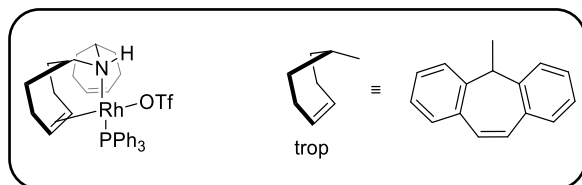
^1H NMR (200 MHz, CDCl_3 , 25 °C): δ = 7.60 (dd, J = 8.5 Hz, J = 2.0 Hz, 6H), 7.40 (dd, J = 10.6 Hz, J = 8.5 Hz, 6H) ppm, 0.2-2.4 (br s).

^{31}P NMR (81 MHz, CDCl_3 , 25 °C): δ = 21 ppm.

^{11}B NMR (160 MHz, CDCl_3 , 25 °C): δ = -38 ppm.

^{13}C NMR (50 MHz, CDCl_3 , 25 °C): δ = 134.6 (d, J = 10.4 Hz), 132.5 (d, J = 10.4 Hz), 127.5 (d, J = 58.47 Hz), 127.2 (d, 3.1 Hz) ppm.

Synthesis of rhodium(I) amido bis(olefin) complex $[\text{Rh}(\text{trop}_2\text{NH})(\text{PPh}_3)](\text{OTf})$



$\text{C}_{52}\text{H}_{64}\text{F}_3\text{NO}_3\text{PRhS}$

$M = 974.01 \text{ g mol}^{-1}$

The complex $[\text{Rh}(\text{trop}_2\text{NH})(\text{PPh}_3)](\text{OTf})$ was provided and developed by Grützmacher and coworkers.^[190] Dimer $[\text{RhCl}(\text{trop}_2\text{NH})(\text{PPh}_3)]_2$ (1.0 eq, 0.63 mmol, 500 mg) (trop_2N = bis(5-H-dibenzo-[a,d]cyclohepten-5-yl)amide) and silver trifluoromethanesulfonate (AgOTf) (1.03 eq, 0.65 mmol, 166 mg) were suspended in dichloromethane (15 mL) and were stirred for 12 h. The suspension was filtered over celite, the product was precipitated from the remaining filtrate. The solid was decanted off and dried under vacuum (542 mg, 0.06 mmol, 95%).

^1H NMR (200 MHz, CDCl_3 , 25 °C): δ = 7.84 (m, 6H), 7.70-7.55 (m, 9H), 7.40-7.15 (m, 8H), 7.00-6.85 (m, 4H), 6.85-6.70 (m, 4H), 5.66 (dd, $^3J_{\text{PH}} = 5.8 \text{ Hz}$, $^2J_{\text{RhH}} = 2.1 \text{ Hz}$, 1H), 5.43 (ddd, $^3J_{\text{HH}} = 9.3 \text{ Hz}$, $^2J_{\text{RhH}} = 3.3 \text{ Hz}$, $^3J_{\text{PH}} = 2.8 \text{ Hz}$, 2H), 4.94 (ddd, $^3J_{\text{HH}} = 9.3 \text{ Hz}$, $^2J_{\text{RhH}} = 1.8 \text{ Hz}$, $^3J_{\text{PH}} = 2.7 \text{ Hz}$, 2H), 4.91 (d, $^4J_{\text{PH}} = 8.4 \text{ Hz}$, 2H) ppm.

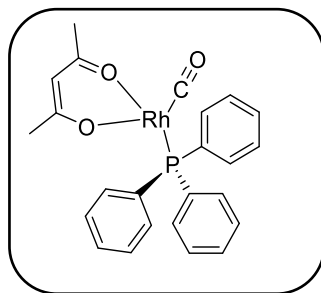
^{31}P NMR (162 MHz, CDCl_3 , 25 °C): δ = 40.6 (d, $^1J_{\text{RhP}} = 137.7 \text{ Hz}$) ppm.

^{13}C NMR (101.6 MHz, CDCl_3 , 25 °C): δ = 136.9, 135.5 (d, $^2J_{\text{RhC}} = 1.8 \text{ Hz}$), 134.6, 134.5 (d, $^2J_{\text{PC}} = 9.6 \text{ Hz}$), 131.0 (d, $^4J_{\text{PC}} = 2.3 \text{ Hz}$), 129.6, 129.5, 129.0 (d, $^1J_{\text{PC}} = 46.4 \text{ Hz}$), 128.7 (d, $^3J_{\text{PC}} = 10.1 \text{ Hz}$), 128.5, 128.2, 127.5, 127.2, 126.4, 126.4, 119.8 (q, $^1J_{\text{FC}} = 321.1 \text{ Hz}$), 74.2 (d, $^1J_{\text{RhC}} = 13.3 \text{ Hz}$), 74.0 (d, $^1J_{\text{RhC}} = 6.9 \text{ Hz}$), 72.7 (d, $^3J_{\text{PC}} = 1.4 \text{ Hz}$) ppm.

^{31}P MAS NMR (168 MHz, 25 °C): δ = 34, 14 ppm.

Synthesis of rhodium(triphenylphosphine)carbonylacetylacetonate

[Rh(PPh₃)(CO)(acac)]



C₂₅H₂₅O₃PRh

M = 507.35 g mol⁻¹

In a round bottom flask triphenylphosphine (71 mg, 0.27 mmol) and rhodium(triphenylphosphine)carbonylacetylacetonate (70 mg, 0.27 mmol) were dissolved in dichloromethane (15 mL). The reaction mixture immediately turned yellow and evolution of gas was observed. After stirring the reaction for 20 h at room temperature, the solvent was removed under vacuum and yellow powder was obtained as product (144 mg, 105%).

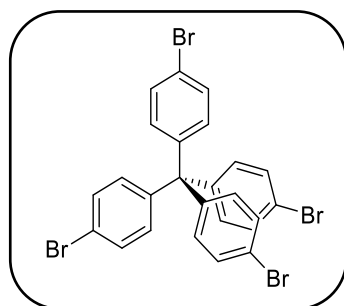
¹H NMR (200 MHz, CDCl₃, 25 °C): δ = 7.74-7.32 (m, 15H), 5.43 (s, 1H, H-C(sp²)), 2.09 (s, 3H, CH₃), 1.61 (s, 3H, CH₃) ppm.

³¹P NMR (81 MHz, CDCl₃, 25 °C): δ = 48.7 (d, ¹J_{RhP} = 176.7 Hz) ppm.

¹³C NMR (50 MHz, CDCl₃, 25 °C): δ = 186.7 (d, ¹J_{RhCO} = 256.0 Hz), 134.7 (d, *J* = 11.3 Hz), 132.9, 132.5 (d, *J* = 14.4 Hz), 132.2 (d, *J* = 18.2 Hz), 130.5, 128.7 (d, *J* = 11.5 Hz), 128.3 (d, *J* = 10.4 Hz), 101.0, 27.8 (d, *J* = 6.0 Hz), 27.0 ppm.

³¹P MAS NMR (168 MHz, 25°C): δ = 47, 27 ppm.

Synthesis of tetrakis(4-bromophenyl)methane



C₂₅H₁₆Br₄

M = 636.02 g mol⁻¹

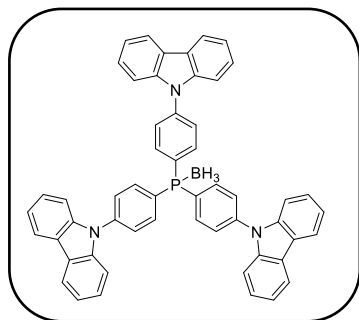
Tetrakis(4-bromophenyl)methane was synthesized according to synthesis of Nguyen *et al.* with slight modifications.^[227] Tetraphenylmethane (4.00 g, 12.5 mmol) was placed in a round flask, neat bromine (8 mL, 156 mmol) was added dropwise and the mixture was stirred for 45 min. At 0 °C ethanol (50 mL) was slowly added. The orange mixture was allowed to come to room temperature, stirred overnight and quenched by addition of bisulfite solution (100 mL). Additionally, the yellow solid was washed with water and ethanol. The crude product was

purified by column chromatography from cyclohexane. 4.93 g (7.75 mmol, 62%) of a white solid were obtained as a product.

^1H NMR (200 MHz, CDCl_3 , 25°C): δ = 7.39 (d, $^3J_{\text{HH}}$ = 8.7 Hz, 8H), 7.01 (d, $^3J_{\text{HH}}$ = 8.7 Hz, 8H) ppm.

^{13}C NMR (50 MHz, CDCl_3 , 25°C): δ = 144.6, 132.5, 131.2, 121.0, 63.8 ppm.

Synthesis of tris(4-(*N*-carbazolyl)phenyl)phosphine-borane



$$M = 771.71 \text{ g mol}^{-1}$$

Tris(4-(*N*-carbazolyl)phenyl)phosphine-borane (CzTPP) was synthesized according to tris(4-bromophenyl)phosphine borane. In a pre-dried Schlenk flask 9-(4-bromophenyl)carbazole (2.00 g, 6.2 mmol) was dissolved in diethyl ether (60 mL). At -78°C *tert*-butyllithium (2.5 M in hexane, 7.3 mL, 12.40 mmol) was added slowly over 15 min. After 2 h of stirring at -78°C , and 1 h at room temperature, the reaction was cooled to -78°C and phosphorus trichloride (0.16 mL, 1.86 mmol) was added dropwise to the colorless solution which immediately turned yellow. Then the solution was allowed to slowly warm up to room temperature and stirred overnight. A saturated mixture of sodium bicarbonate (30 mL) and water (30 mL) was added so that the organic layer could be separated. The residual aqueous layer was extracted with dichloromethane (2 x 25 mL). The combined organic layers were dried over magnesium sulfate and the solvent was removed *in vacuo*. The crude product was purified by column chromatography from cyclohexane and dichloromethane, and 1.058 g (1.396 mmol, 75%) of tris(4-(*N*-carbazolyl)phenyl)phosphine was obtained. In a second step, tris(4-(*N*-carbazolyl)phenyl)phosphine (200 mg, 0.264 mmol) was added and dissolved in anhydrous dichloromethane (18 mL) in a pre-dried Schlenk finger. Then borane dimethyl sulfide complex (0.25 mL, 2.64 mmol) was added and after stirring the reaction for 24 h at room temperature, saturated aqueous ammonia chloride solution (3 mL) was added. The reaction mixture was stirred for another 1 h, after that it was poured into water (15 mL). The collected organic phase was dried over magnesium sulfate and filtrated over silica. The crude product was purified by column chromatography from cyclohexane and dichloromethane and 175 mg (0.227 mmol, 86%) of a white crystalline solid was obtained as a product.

^1H NMR (500 MHz, CDCl_3 , 25 °C): δ = 8.17 (d, J = 7.63 Hz, 6H), 8.05 (t, J = 9.30 Hz, 6H), 7.85 (d, J = 7.93 Hz, 6H), 7.59 (d, J = 8.15 Hz, 6H), 7.46 (t, J = 7.70 Hz, 6H), 7.35 (t, J = 7.45 Hz, 6H), 0.7-2.0 (br s, 3H) ppm.

^{31}P NMR (81 MHz, CDCl_3 , 25 °C): δ = 20.4 ppm.

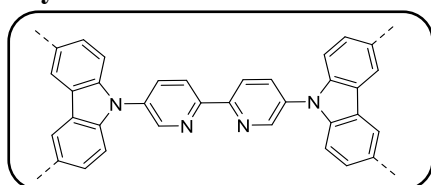
^{11}B NMR (160 MHz, CDCl_3 , 25 °C): δ = -37.6 ppm.

^{13}C NMR (125 MHz, CDCl_3 , 25 °C): δ = 141.2, 140.3, 135.1 (d, J = 10.7 Hz), 127.3 (d, J = 57.2 Hz), 127.2 (d, J = 10.7 Hz), 126.4, 124.0, 120.9, 120.7, 109.9 ppm.

8.4 Synthesis of the Polymers

8.4.1 Carbazole-based Polymers

Synthesis of CPOP-30^[3]

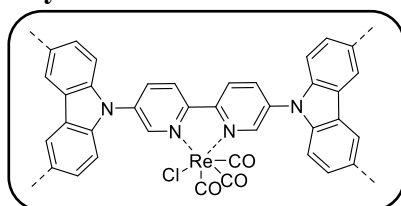


Under Argon atmosphere, 5,5'-di(9*H*-carbazol-9-yl)-2,2'-bipyridine (200 mg, 0.41 mmol) was dissolved in anhydrous chloroform (30 mL) was added dropwise to an iron(III) chloride (1200 mg, 7.40 mmol, 18 eq) suspension in anhydrous chloroform (30 mL). The reaction mixture was stirred for 24 h at room temperature. Methanol (50 mL) was added to quench the reaction. The yellow solid was filtered off and was refluxed in a mixture of hydrochloric acid solution (6 M, 50 mL) and methanol (50 mL) for 24 h. The process was repeated 3 times before the filtration cake was washed with aqueous ammonia solution (10 wt%), water and methanol. The resulting yellow polymer was purified by Soxhlet extraction from methanol overnight and dried in the vacuum oven at 80 °C. The product was obtained as yellow powder (188 mg, 95%).

^{13}C CPMAS NMR (100 MHz, 10 kHz, 25 °C): δ = 152, 137, 130, 121, 106 ppm.

S_{BET} : 880 m² g⁻¹

Synthesis of CPOP-30-Re^[3]



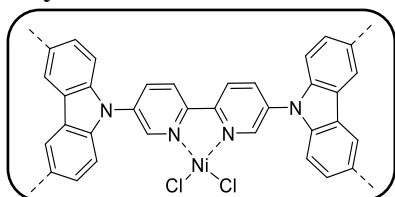
Under Argon atmosphere, CPOP-30 (100 mg, 0.21 mmol) and $\text{Re}(\text{CO})_5\text{Cl}$ (76 mg, 0.21 mmol)

were placed in a Schlenk flask and anhydrous methanol (30 mL) were added. The reaction mixture was refluxed for 24 h. The polymer was filtered off and washed with methanol before it was purified by Soxhlet extraction from chloroform overnight and dried in the vacuum oven at 80 °C. The product was obtained as orange powder (134 mg, 81%).

^{13}C CP MAS NMR (100 MHz, 10 kHz, 25°C): δ = 151, 135, 122, 107 ppm.

S_{BET} : 620 m² g⁻¹

Synthesis of CPOP-30-Ni



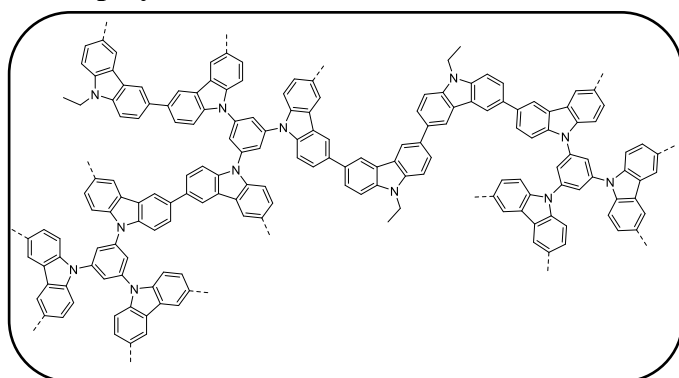
Under Argon atmosphere, **CPOP-30** (100 mg, 0.21 mmol) was dispersed in a methanolic solution of NiCl₂ (42 ml, 5 mM, 0.21 mmol) and was refluxed for 24 h while gently stirring. The polymer was filtered off and washed with methanol and chloroform, and dried in the vacuum oven at 80 °C.

S_{BET} : 470 m² g⁻¹

General procedure for the oxidative copolymerizations

The oxidative polymerization was carried out according to the synthesis of the carbazole-based polymer network CPOP-1^[1]. Per 1 eq of monomer 18 eq of iron(III) chloride were applied.

For copolymer P_{0.2}



Under Argon atmosphere, the monomer mixture of 1,3,5-tris(*N*-carbazolyl)benzene (172.1 mg, 0.30 mmol, 0.8 eq) and *N*-ethylcarbazole (14.65 mg, 0.08 mmol, 0.2 eq) dissolved in anhydrous chloroform (20 mL) was added dropwise to an iron(III) chloride (1095.0 mg, 6.75 mmol, 18 eq) suspension in anhydrous chloroform (30 mL). The reaction mixture was stirred for 24 h at room temperature. Methanol (50 mL) was added to the reaction mixture and was stirred for another 2 h. The filtration cake was suspended in solution of hydrochloric acid (6 M, 50 mL)

and methanol (50 mL) and was stirred overnight. The solid was filtered off and washed with methanol, tetrahydrofuran and dichloromethane. The resulting polymer was purified by Soxhlet extraction from methanol overnight and dried in the vacuum oven at 80 °C.

^{13}C CPMAS NMR (100 MHz, 7 kHz, 25°C): δ = 136, 121, 106, 9 ppm.

^{13}C CPMAS NMR (100 MHz, 12 kHz, 25°C): δ = 136, 121, 106, 32 ppm.

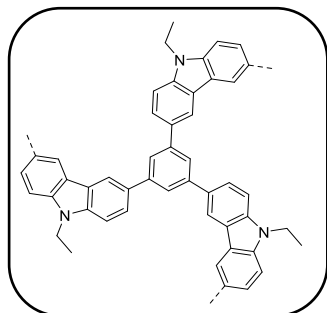
Kinetic study for copolymerization P_{0.5}

Under Argon atmosphere, the monomer mixture of 1,3,5-tris(*N*-carbazolyl)benzene (143 mg, 0.25 mmol, 0.5 eq) and *N*-ethylcarbazole (49 mg, 0.25 mmol, 0.5 eq) was dissolved in anhydrous chloroform (25 mL). A sample of 1 mL was taken for ^1H NMR spectroscopy before the comonomer solution was added quickly to an iron(III) chloride (1460 mg, 9.0 mmol, 18.0 eq) suspension in anhydrous chloroform (40 mL). After 15 s, 30 s, 1 min, 5 min, 10 min, 20 min and 24 h samples of 1-4 mL were taken, diluted with chloroform and poured into a HCl solution (6 M, 10 mL). The organic phase was separated, dried with magnesium sulfate and filtered off. Then the solvent was removed under reduced pressure and the remaining solid was dissolved in deuterated chloroform for ^1H NMR spectroscopy.

General procedure for impregnation with chloroplatinic acid

The chloroplatinic acid solution was prepared depending on the desired concentration of platinum within the polymer. Proportions of 0.5-7 wt% of Pt were applied. For that purpose, the exact volume of chloroplatinic acid (8 wt% in water) was pipetted into a vial and was diluted by 3 mL methanol per 100 mg solid. The carbazole-based material (~100 mg) was mortared and the obtained homogeneous powder was placed in an extra 100 mL round flask. Under sonification, the diluted chloroplatinic acid solution was added dropwise to the powder until the liquid was soaked up. The sonication was stopped when the solid was dried under air. It was further dried for 5 h under vacuum. The final weight percentage of platinum was determined by ICP-OES.

Synthesis of polyTNECzB



Under Argon atmosphere, 1,3,5-tris(9-ethyl-9*H*-carbazol-3-yl)benzene (230 mg, 0.35 mmol) was dissolved in anhydrous chloroform (40 mL) and was added dropwise to an iron(III) chloride (1229 mg, 6.30 mmol, 18 eq) suspension in anhydrous chloroform (20 mL). The reaction mixture was stirred for 24 h at room temperature. Methanol (50 mL) was added to the reaction mixture and was stirred for another 2 h. The yellow solid was filtered off and was washed with methanol, water and dichloromethane. The resulting yellow polymer was purified by Soxhlet extraction from methanol overnight and dried in the vacuum oven at 80 °C. The product was obtained as yellow powder (223 mg, 97%).

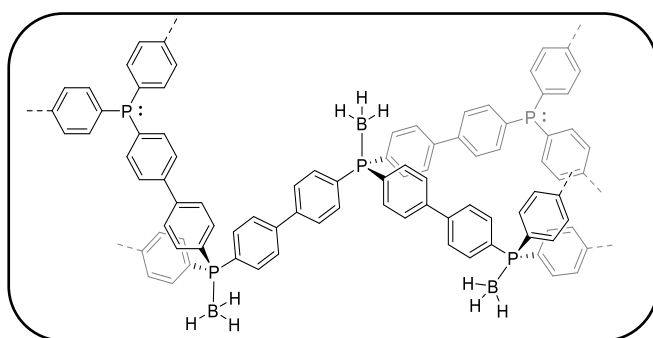
^{13}C CP/MAS NMR (100 MHz, 7 kHz, 25°C): δ = 139, 134, 124, 108, 37, 13 ppm.

^1H MAS NMR (400 MHz, 7 kHz, 25°C): δ = 7.1, 0.8 ppm.

S_{ABET} : 727 m² g⁻¹

8.4.2 Phosphine-based Polymers

Synthesis of polyTPP



PolyTPP was synthesized under PPN-6 Yamamoto conditions.^[68] In a glovebox bis(1,5-cyclooctadiene)nickel(0) (730 mg, 2.65 mmol), 2,2'-bipyridine (414 mg, 2.65 mmol) and 1,5-cyclooctadiene (0.33 mL, 2.67 mmol) were dissolved in dimethylformamide (55 mL) and tetrahydrofuran (55 mL) in a round-bottom flask. After stirring the violet, black solution for 5 min tris(4-bromophenyl)phosphine borane (400 mg, 0.78 mmol) was added. The reaction mixture was stirred for 20 h at room temperature. At 0 °C hydrochloric acid (3M, 100 mL) was

added slowly and the mixture was stirred for 2 h. The off-white solid was filtered and washed with acetone and was dried over vacuum at 80 °C. As product, an off-white powder was obtained. Yield, 194 mg (0.70 mmol, 90%).

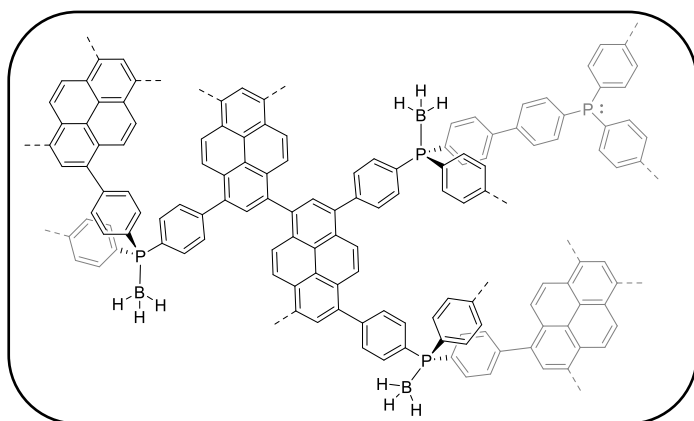
^{13}C CPMAS NMR (100 MHz, 10 kHz, 25°C): δ = 142, 133, 127 ppm.

^{31}P MAS NMR (168 MHz, 10 kHz, 25°C): δ = 22, -8 ppm.

^{11}B MAS NMR (128 MHz, 10 kHz, 25°C): δ = -42 ppm.

S_{BET} : 989 m² g⁻¹

Synthesis of CopolyTPP



CopolyTPP was synthesized under PPN-6 Yamamoto conditions.^[68] In a glovebox bis(1,5-cyclooctadiene)nickel(0) (545 mg, 1.98 mmol), 2,2'-bipyridine (311 mg, 1.98 mmol) and 1,5-cyclooctadiene (0.24 mL, 1.99 mmol) were dissolved in dimethylformamide (35 mL) and tetrahydrofuran (35 mL) in a round-bottom flask. After stirring the violet, black solution for 5 min tris(4-bromophenyl)phosphine borane (150 mg, 0.29 mmol) and 1,3,6,8-tetrabromopyrene (114 mg, 0.22 mmol) were added. The reaction mixture was stirred for 20 h at room temperature. At 0 °C hydrochloric acid (6M, 50 mL) was added slowly and the mixture was stirred for 2 h. The yellow solid was filtered and washed with acetone and was dried over vacuum at 80 °C. As product, a yellow powder was obtained. Yield, 112 mg (0.07 mmol, 90%).

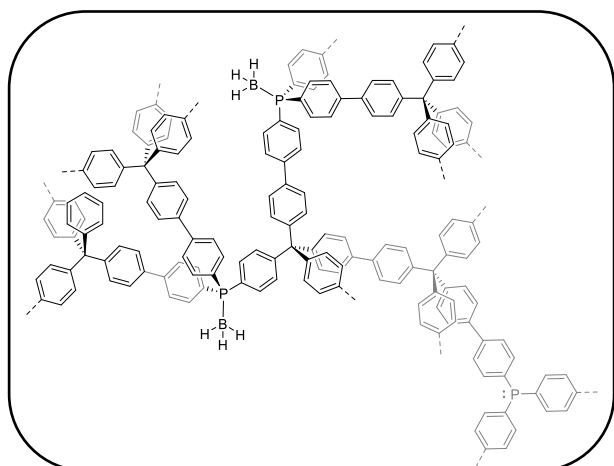
^{13}C CPMAS NMR (100 MHz, 10 kHz, 25°C): δ = 143, 132, 127 ppm.

^{31}P MAS NMR (168 MHz, 10 kHz, 25°C): δ = 22, -8 ppm.

^{11}B MAS NMR (128 MHz, 10 kHz, 25°C): δ = -42 ppm.

S_{BET} : 797 m² g⁻¹

Synthesis of CopolyTPP-2



CopolyTPP-2 was synthesized under PPN-6 Yamamoto conditions.^[68] In a glovebox bis(1,5-cyclooctadiene)nickel(0) (1184 mg, 4.30 mmol), 2,2'-bipyridine (672 mg, 4.30 mmol) and 1,5-cyclooctadiene (0.53 mL, 4.33 mmol) were dissolved in dimethylformamide (70 mL) and tetrahydrofuran (70 mL) in a round-bottom flask. After stirring the violet, black solution for 5 min tris(4-bromophenyl)phosphine borane (103 mg, 0.20 mmol) and tetra(4-bromophenyl)methane (509 mg, 0.80 mmol) were added. The reaction mixture was stirred for 20 h at room temperature. At 0 °C hydrochloric acid (3M, 200 mL) was added slowly and the mixture was stirred for 2 h. The beige solid was filtered and washed with acetone and was dried over vacuum at 80 °C. As product, an off-white powder (349 mg) was obtained.

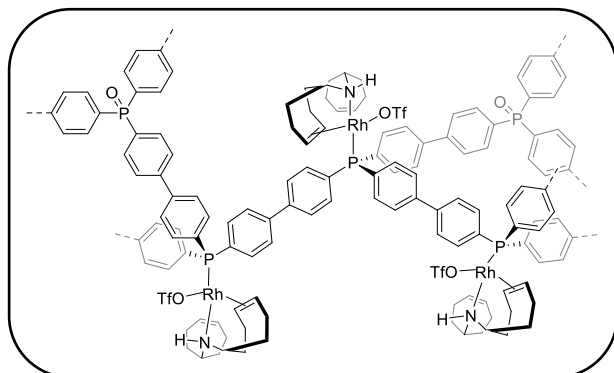
¹³C CPMAS NMR (100 MHz, 10 kHz, 25°C): δ = 146, 140, 131, 126, 65 ppm.

³¹P MAS NMR (168 MHz, 10 kHz, 25°C): δ = 23, -8 ppm.

¹¹B MAS NMR (128 MHz, 10 kHz, 25°C): δ = 14, -43 ppm.

*S*_{BET}: 1430 m² g⁻¹

Synthesis of Rh-polyTPP



Under inert conditions, **polyTPP** (100 mg, 0.366 mmol) and rhodium(I) amido bis(olefin) complex [Rh(trop₂NH)](OTf) (trop₂N = bis(5-H-dibenzo-[a,d]cyclohepten-5-yl)amide)

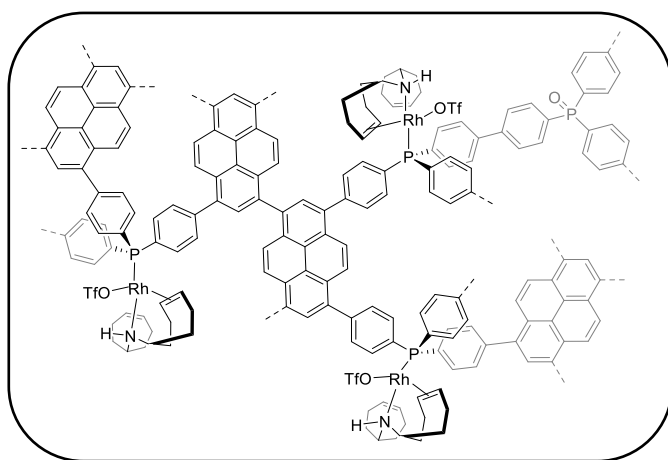
(260 mg, 0.366 mmol) were placed in a pre-dried Schlenk flask and then dispersed in anhydrous methanol (15 mL). The reaction mixture was refluxed overnight. The solid was filtered off and washed with methanol. After drying in the vacuum oven, the polymer was obtained as an orange powder.

^{13}C CP/MAS NMR (100 MHz, 10 kHz, 25°C): δ = 135, 128, 72 ppm.

^{31}P MAS NMR (168 MHz, 10 kHz, 25°C): δ = 40, 26, 12 ppm.

S_{ABET} : 31 m² g⁻¹

Synthesis of Rh-copolyTPP

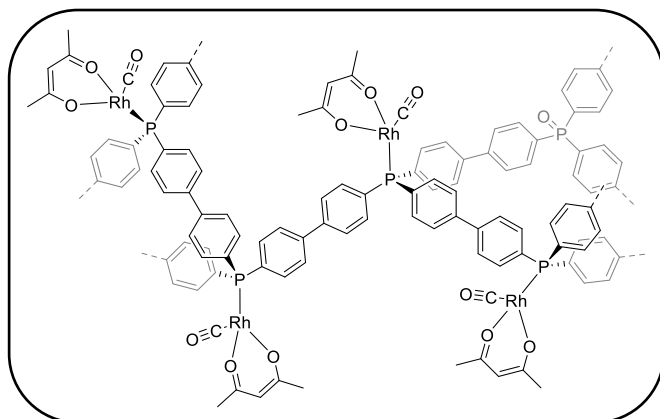


Under inert conditions, **CopolyTPP** (100 mg) and rhodium(I) amido bis(olefin) complex [Rh(trop₂NH)](OTf) (trop₂N = bis(5-H-dibenzo-[a,d]cyclohepten-5-yl)amide) (260 mg, 0.366 mmol) were placed in a pre-dried Schlenk flask and then dispersed in anhydrous methanol (15 mL). The reaction mixture was refluxed overnight. The solid was filtered off and washed with methanol. After drying in the vacuum oven, the polymer was obtained as yellow powder.

^{31}P MAS NMR (168 MHz, 10 kHz, 25°C): δ = 41, 29, -8 ppm.

S_{ABET} : 290 m² g⁻¹

Synthesis of Rh-polyTPP-2



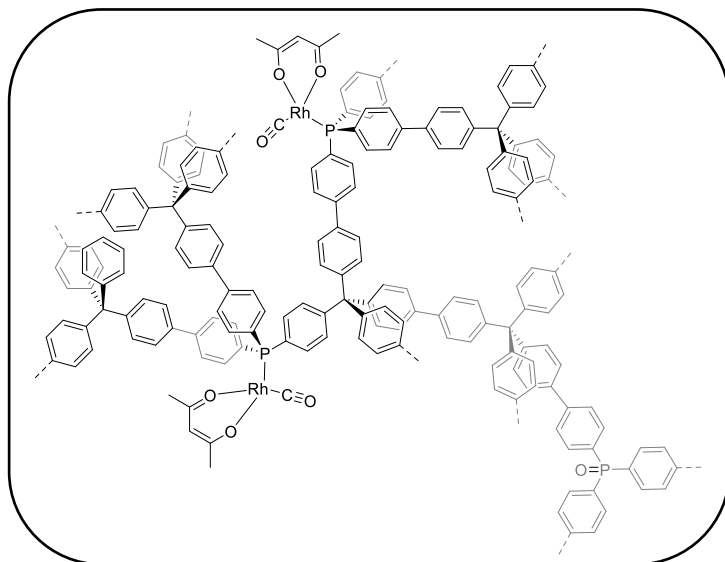
Under inert conditions, **polyTPP** (200 mg, 0.732 mmol) and rhodium(I) dicarbonyl acetylacetonate $[\text{Rh}(\text{CO})_2(\text{acac})]$ (208 mg, 0.806 mmol) were placed in a pre-dried Schlenk flask and then dispersed in anhydrous methanol (25 mL). The reaction mixture was refluxed overnight. The solid was filtered off and washed with methanol. After drying in the vacuum oven, the polymer was obtained as a brown powder.

^{13}C CPMAS NMR (100 MHz, 10 kHz, 25°C): $\delta = 188, 144, 132, 128, 99$ ppm.

^{31}P MAS NMR (168 MHz, 10 kHz, 25°C): $\delta = 47, 31, -8$ ppm.

S_{ABET} : 421 m² g⁻¹

Synthesis of Rh-CopolyTPP-2



Under inert conditions, **CopolyTPP-2** (200 mg) and rhodium(I) dicarbonyl acetylacetonate $[\text{Rh}(\text{CO})_2(\text{acac})]$ (59 mg, 0.277 mmol) were placed in a pre-dried Schlenk flask and then dispersed in anhydrous methanol (25 mL). The reaction mixture was refluxed overnight. The solid was filtered off and washed with methanol. After drying in the vacuum oven, the polymer

was obtained as a beige powder.

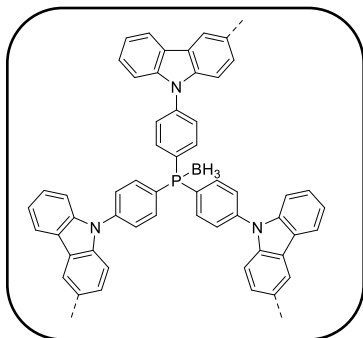
^{13}C CPMAS NMR (100 MHz, 10 kHz, 25°C): δ = 188, 146, 139, 131, 126, 101, 65 ppm.

^{31}P MAS NMR (168 MHz, 10 kHz, 25°C): δ = 47, 25 ppm.

S_{ABET} : 1363 m² g⁻¹

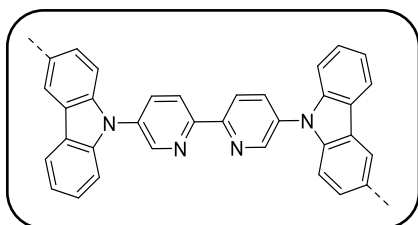
8.4.3 Microporous Polymer Films

Synthesis of polyCzTPP



For the electrochemical polymerization, tris(4-(*N*-carbazolyl)phenyl)phosphine borane (CzTPP) (77 mg, 0.1 mmol, 0.05 mM) and tetrabutylammonium perchlorate (6.84 g, 20 mmol, 0.1 M) were dissolved in dichloromethane (160 mL) and acetonitrile (40 mL). The solution was placed in a three-electrode cell. ITO electrode was applied as working electrode, platinum wire and Ag⁰/AgCl were used as counter and reference electrode, respectively. Eight cycles of cyclic voltammograms were recorded from 0.2 to 1.7 V at a scan rate of 50 mV/s. Further 15 min of chronoamperometry (CA) at 1.5 V vs. Ag⁰/AgCl were performed to deposit a thicker film. After successful deposition of the film, a potential of 0 V was applied for 3 min to discharge the material. The disposed film on FTO was rinsed in ethanol and was dried at room temperature.

Synthesis of polyCzbipy

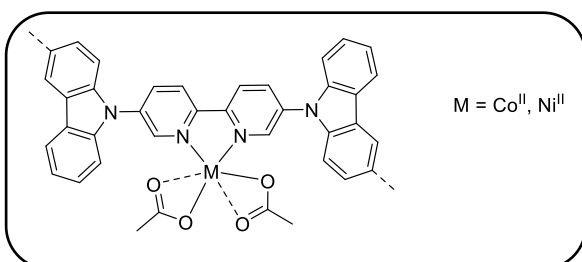


For the electrochemical polymerization, 5,5'-di(9*H*-carbazol-9-yl)-2,2'-bipyridine (24.4 mg, 0.05 mmol, 1.0 mM) and tetrabutylammonium perchlorate (1.70 g, 5.0 mmol, 0.1 M) were dissolved in dichloromethane (40 mL) and acetonitrile (10 mL). The solution was placed in a three-electrode cell. FTO electrode was applied as working electrode, platinum wire and Ag⁰/AgCl were used as counter and reference electrode, respectively. Multiple cycles of cyclic

voltammograms were recorded from 0.2 to 1.8 V at a scan rate of 50 mV/s. After successful deposition of the film, a potential of 0 V was applied for 60 s to discharge the material. The disposed film on FTO was rinsed in ethanol and was dried at room temperature.

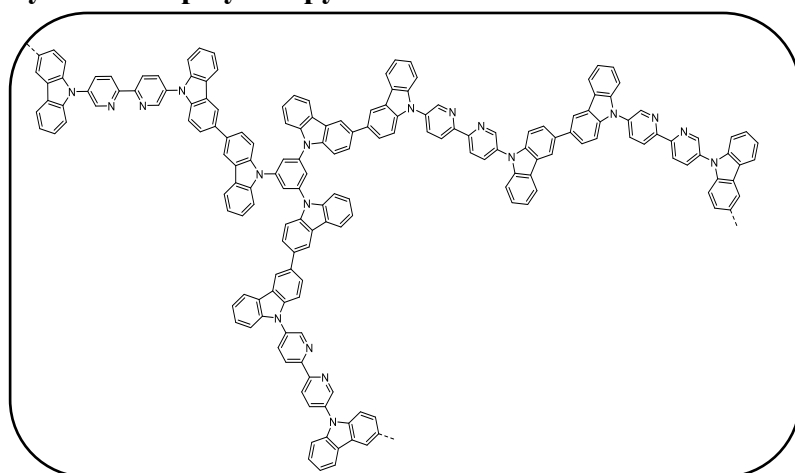
For Kr isotherm measurements: The films were synthesized under the same conditions as mentioned above. To increase the thickness of the films, chronoamperometry was applied at 1.6 V for 1 h. The film was discharged by applying a potential of 0 V for 2 min. After rinsing the film in ethanol, the material was allowed to dry in air, the film started peeling off the electrode. The collected peeled off film was dried at 80 °C for 30 min under vacuum.

Synthesis of polyCzbipy-Co and polyCzbipy-Ni



The electrode coated with polymer film polyCzbipy was immersed into a methanolic (15 mL) solution of nickel acetate tetrahydrate (43 mg, 0.173 mmol), or alternatively cobalt acetate tetrahydrate (43 mg, 0.173 mmol) for 1 h. After that, the electrode was immersed for 15 min in a solution of methanol. The procedure was repeated 3 times, before the electrode was allowed to dry under air.

Synthesis of polyCzbipyTCB



For the electrochemical polymerization, 5,5'-di(9H-carbazol-9-yl)-2,2'-bipyridine (19.5 mg, 0.04 mmol), tris(N-carbazolyl)benzene (5.7 mg, 0.01 mmol) and tetrabutylammonium perchlorate (1.70 g, 5.0 mmol, 0.1 M) were dissolved in dichloromethane (40 mL) and acetonitrile (10 mL). The solution was placed in a three-electrode cell. FTO electrode was

applied as working electrode, platinum wire and Ag^0/AgCl were used as counter and reference electrode, respectively. Multiple cycles of cyclic voltammograms were recorded from 0.2 to 1.8 V at a scan rate of 50 mV/s. After successful deposition of the film, a potential of 0 V was applied for 60 s to discharge the material. The disposed film on FTO was rinsed in ethanol and was dried at room temperature.

The cobalt acetate coordination of **polyCzbipyTCB-Co** was done according to preparation of **polyCzbipy-Co**.

8.5 Catalysis

8.5.1 Photocatalytic CO_2 Reduction

The photocatalytic CO_2 reduction of was performed in a two-necked quartz photoreactor (36 mL). The photocatalyst (10 mg **CPOP-30/CPOP-30-Re** or 7 mg of molecular catalyst $[\text{Re}(\text{Czbipy})(\text{CO})_3\text{Cl}]$) was dispersed in a mixture (in total 10 mL) of solvent (dimethylformamide or acetonitrile) and sacrificial agent (triethanolamine (TEOA), 10–20 V%). The reaction mixture was saturated with CO_2 (>99%) and sealed with rubber septum, then was irradiated using a 300 W Xenon light (L.O.T.-Quantum Design, Germany) equipped with 395 nm filter. In general, the distance between photoreaction and light source was kept at 10 cm. The reaction mixture was stirred with a speed of 500 rpm. During the reaction, the temperature was kept at 20 °C using a thermostat. The gases were sampled from the headspace using a syringe and analyzed by gaseous chromatography equipped with TCD detector.

8.5.2 Visible-light-mediated Nickel Catalysis

A pre-dried vial with stirring bar was charged with $\text{NiCl}_2\cdot\text{glyme}$ (5 μmol), Czbipy or **CPOP-30** (5 μmol , 2.43 mg), 4-iodobenzotrifluoride (100 μmol) and sodium p-toluensulfinate (200 μmol). After adding anhydrous dimethylacetamide (2 mL), the vial was sealed by a septum and Parafilm. The mixture sonicated and degassed by bubbling with argon. Under stirring (800 rpm), the reaction mixture was irradiated with 440 nm LED for 22 h. After stopping the reaction, 1 eq 1,3,5-trimethoxybenzene was added as an internal standard for the ^1H NMR analysis to determine the conversion of reactants.

8.5.3 Hydrogenation

In general, hydrogenation reactions were carried out in an autoclave reactor type. Typically, a desired amount of catalyst was added to a reactor, then it was evacuated and refilled with nitrogen and evacuated again 3 times. After this, nitrogen was replaced by hydrogen, and the reaction started when the conditions reached 40 bar (pressure of hydrogen) and 150 °C. The reactions were run for 72 h.

8.5.4 Hydrosilylation

For the general procedure of hydrosilylation, under anhydrous conditions diphenylsilane (Ph_2SiH_2 , 1 eq) was applied as substrate which was dissolved in tetrahydrofuran. The catalyst **Rh-polyTPP** or **Rh-copolyTPP** (1 mol%) and potassium *tert*-butoxide (2 mol%) were added. The reaction vessel was evacuated and filled with nitrous oxide (4 eq), then it was warmed up to 60 °C and was stirred for 48 h. After the reaction, the gas phase was analyzed by GC-TCD for produced hydrogen and nitrogen. After separation of the catalyst, the filtrate was analyzed by ^1H NMR spectroscopy.

8.5.5 Hydroformylation

The reactor for hydroformylation was loaded with 130 mg of catalyst, 12.0 g toluene and 12.0 g 1-octene and was purged with syngas. The reactor was closed, and the reaction was stirred at 1200 rpm. After reaching the reaction conditions of 100 °C, 30 bar of syngas (H_2/CO), the reaction time was started and the first sample was taken *via* syringe. The samples were analyzed by GC. Before the samples were injected, 14 mg of n-nonane as internal standard were added to the sample of the reaction. More samples were taken after 1, 3, 5 and 20 h. After 20 h the reaction was stopped.

The turnover frequency (TOF) was calculated as following: $\text{TOF} = n(\text{aldehydes})/(n(\text{Rh}) \cdot t(\text{h}))$

8.5.6 Electrocatalytic Oxygen Evolution Reaction (OER)

All the electrochemical measurements were carried out in a conventional three-electrode cell using the Gamry reference 600 potentiostats (Gamry, USA) at room temperature. Ag^0/AgCl electrode and graphite rod were used as reference and counter electrodes, respectively. The IFO/FTO substrates with grown polymer films were used as the working electrodes directly for evaluating the OER activity of various catalysts. The OER experiments were conducted in N_2 saturated 1 M KOH electrolyte. The linear sweep voltammetry (LSV) was conducted with a

sweep rate of 10 mV/s with real-time iR corrected by the potentiostat at the measured electrolyte R_u . The reference electrode was calibrated with RHE by the Nernst equation:

$$E_{\text{RHE}} = E_{\text{Ag/AgCl}} + 0.0591 \cdot \text{pH}$$

The Tafel slop was calculated from the OER polarization curve by setting x axis as Log i (i stands for current) and y axis as overpotential.

8.5.7 Photoelectrochemical (PEC) Measurements

Photoelectrochemical measurements were carried out in a PEC cell. The cell was equipped with Ag/AgCl electrode as a reference electrode, a Pt wire as counter electrode and the synthesized materials on FTO as working electrode. For the electrolyte, a 0.1 M potassium phosphate buffer (KPi) solution was used (pH = 7.8). For chopped measurements, the circular area of 0.28 cm² was irradiated under AM 1.5 illumination (= 100 mW/cm²) which was produced by a solar simulator, and in the dark. To determine the photocurrent density a WACOM Super Solar Simulator (Model WXS-505-5H, AM1.5, Class AAA) was applied.

9 Appendix

9.1 Spectra and Characterization Methods

9.1.1 Carbazole-based Polymers

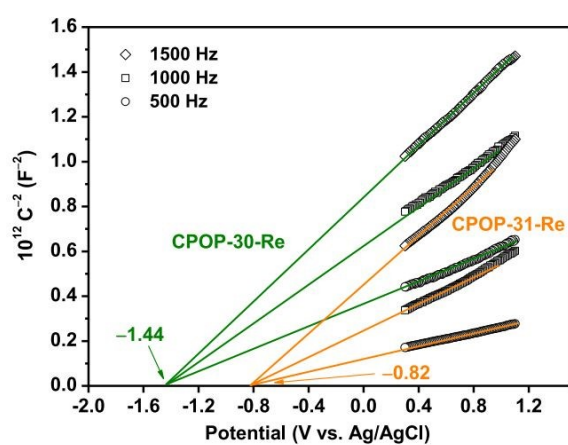


Figure A 1: Mott-Schottky plot for CPOP-30-Re and CPOP-31-Re^[3] (phenanthroline-containing equivalent to CPOP-30-Re).

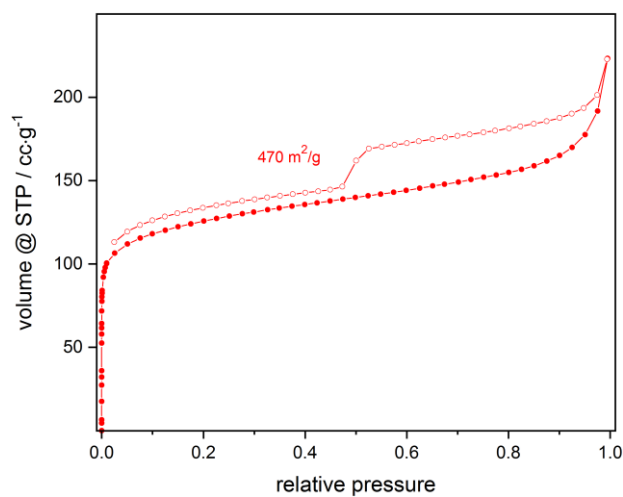


Figure A 2: Nitrogen isotherm of CPOP-30-Ni.

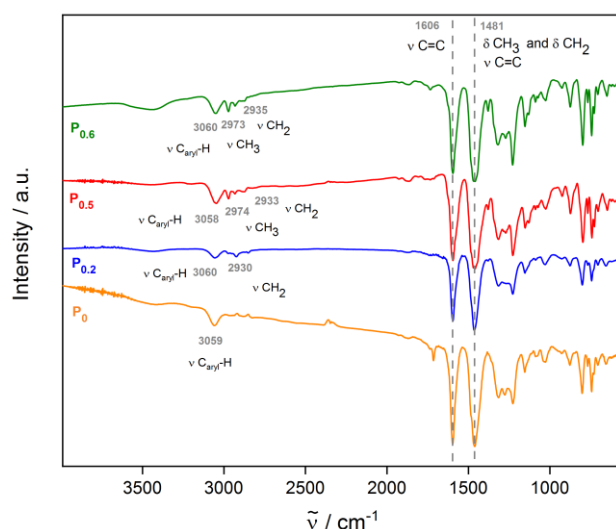


Figure A 3: FTIR of copolymer $P_{0.6}$, $P_{0.5}$ and $P_{0.2}$, as well as P_0 .

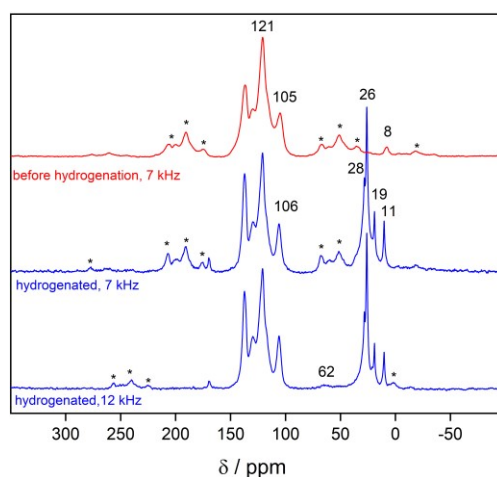


Figure A 4: ^{13}C CPMAS NMR spectra of $P_{0.5}$ (red) and $hP_{0.5}\text{-Pt}_{2.7}$ (blue).

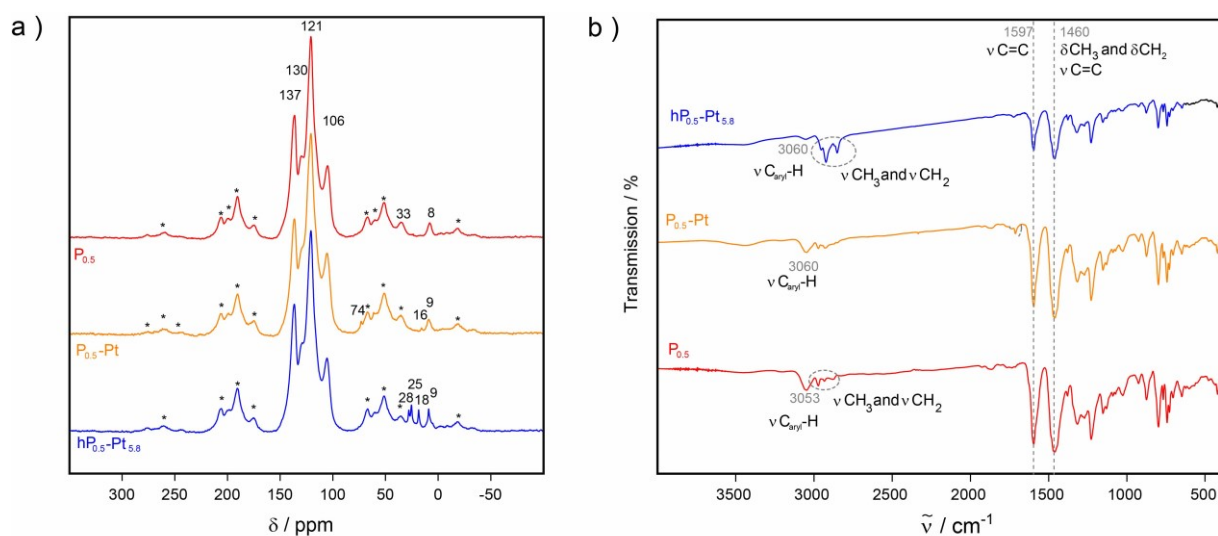


Figure A 5: a) ^{13}C CPMAS NMR spectra of $P_{0.5}$ (red), $P_{0.5}\text{-Pt}$ (orange) and $hP_{0.5}\text{-Pt}_{5.8}$ (blue) measured at 7 kHz. b) FTIR spectra of $P_{0.5}$ (red), $P_{0.5}\text{-Pt}$ (orange) and $hP_{0.5}\text{-Pt}_{5.8}$ (blue).

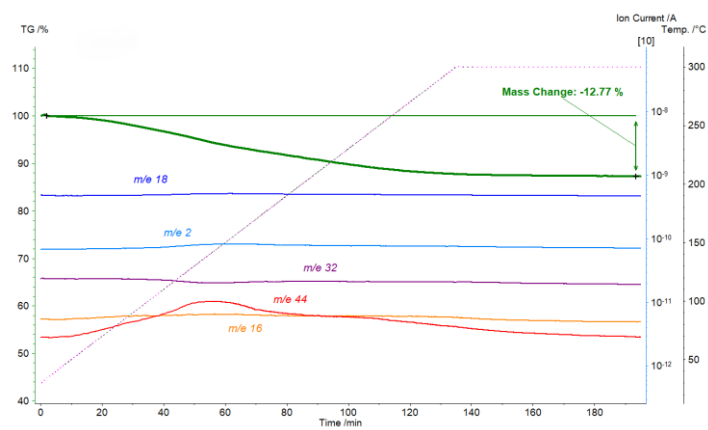


Figure A 6: TG-MS measurement of $P_{0.5}$ -Pt.

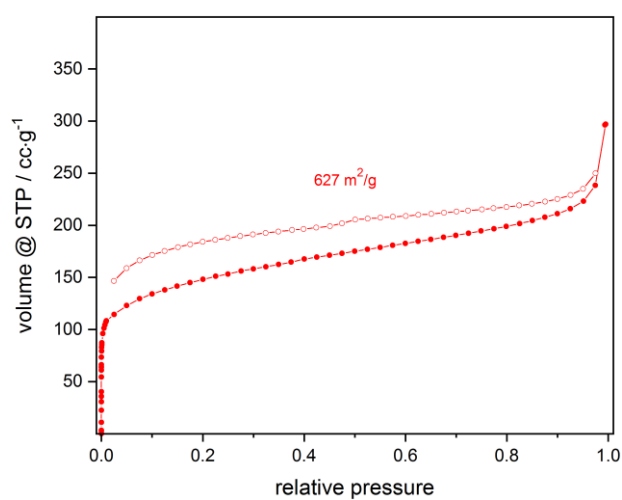


Figure A 7: Nitrogen isotherm of polyTNECzB.

9.1.2 Phosphine-based Polymers

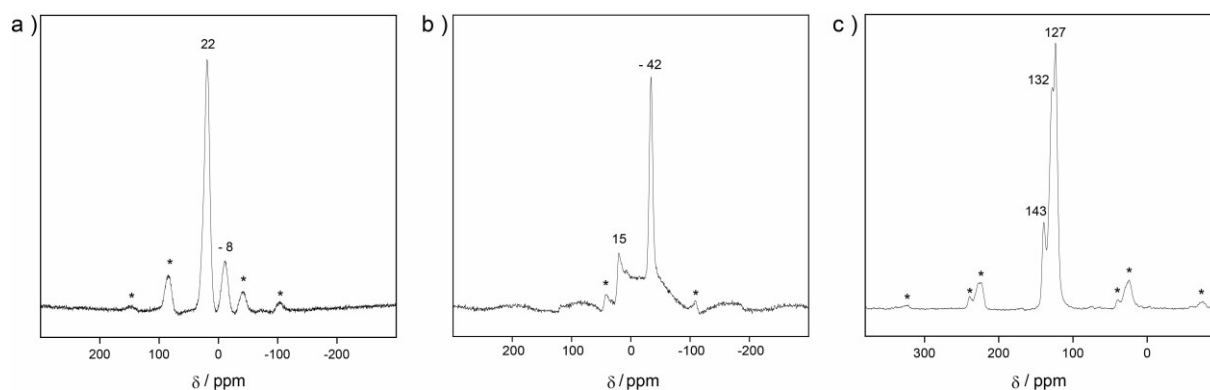


Figure A 8: a) ^{31}P MAS, b) ^{11}B MAS and c) ^{13}C CPMAS NMR spectra of CopolyTPP.

Table A 1: List for retention times of GC.

retention time [min]	compound
4,131	toluene
4,257	n-octene
4,345	i-octene
4,425	i-octene
4,545	i-octene
5,716	nonane
7,846	propylhexanal
7,96	ethylheptanal
8,066	methyloctanal
8,575	nonanal

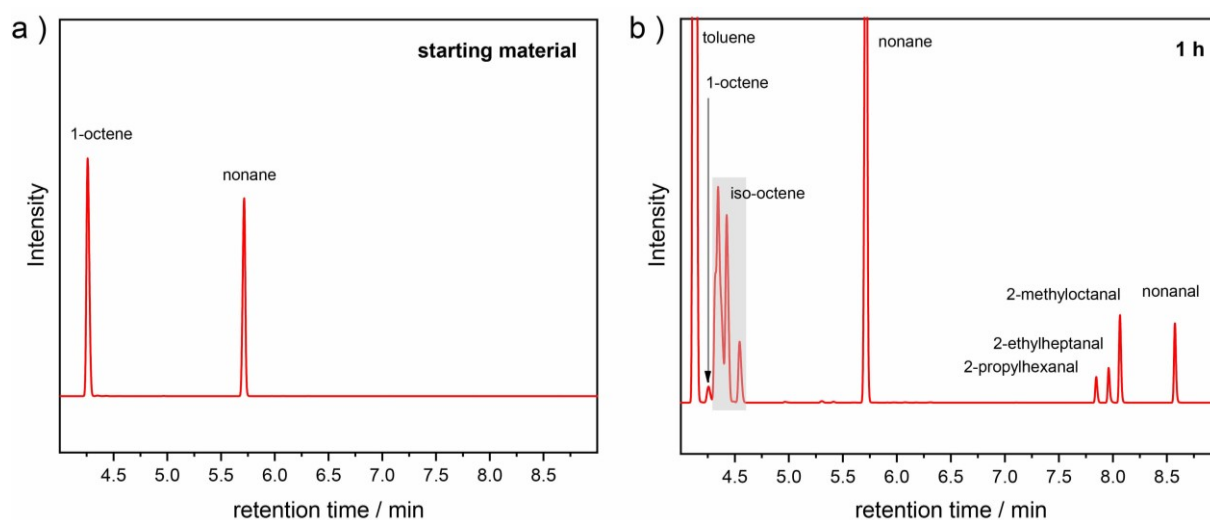


Figure A 9: Gas chromatograms of a) 1-octene and b) hydroformylation reaction with Rh-polyTPP-2 after 1 h with nonane as standard.

Table A 2: Evaluation of chromatograms of Rh-polyTPP-2 in mol%.

reaction time [h]	1- octene	iso- octene	iso- octene	iso- octene	iso- aldehyde	methyl- octanal	n- nonanal
0	50.00	12.60	22.24	7.59	0.35	2.56	4.67
1	2.22	30.40	17.00	5.62	9.91	16.14	18.71
3	0.58	16.90	7.23	2.41	21.50	26.21	25.16
5	0.56	14.14	5.93	2.19	24.23	27.64	25.27
20	0.10	0.90	0.08	0.13	32.01	35.32	31.47

mol% of the compounds detected by GC, calculated by means of nonane as standard.

Table A 3: Evaluation of chromatograms of Rh-CopolyTPP-2 in mol%.

reaction time [h]	1- octene	iso- octene	iso- octene	iso- octene	iso- aldehyde	methyl- octanal	n- nonanal
0	66.00	1.43	16.67	6.04	0	2.64	7.24
1	6.18	13.50	11.81	3.79	10.80	21.73	32.19
3	1.30	6.65	2.89	1.01	15.22	32.18	40.78
5	0.76	2.17	0.72	0	24.94	31.84	39.58
20	0.46	0.73	0	0	26.83	32.82	39.17

mol% of the compounds detected by GC, calculated by means of nonane as standard.

9.1.3 Microporous Polymer Films

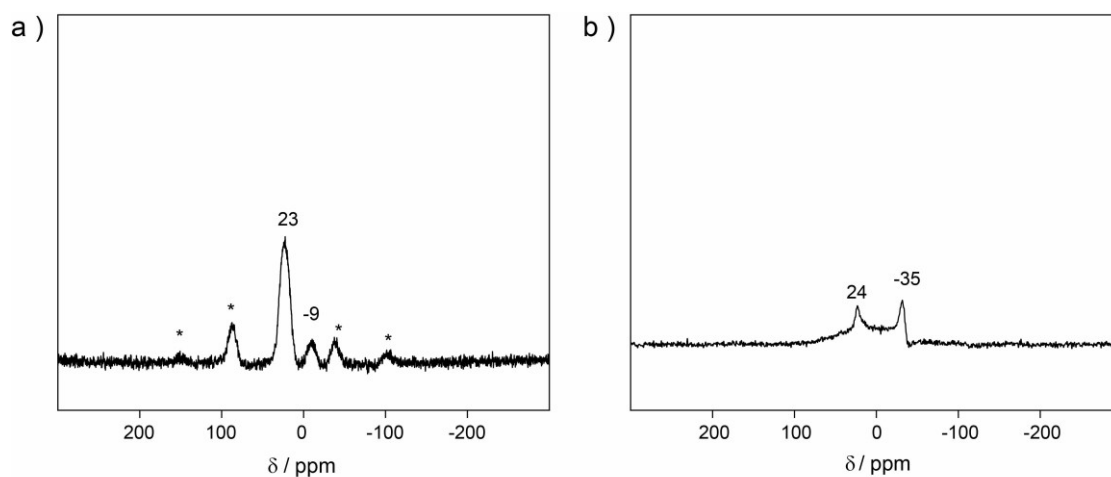


Figure A 10: a) ^{31}P MAS and b) ^{11}B MAS spectra of polyCzTPP.

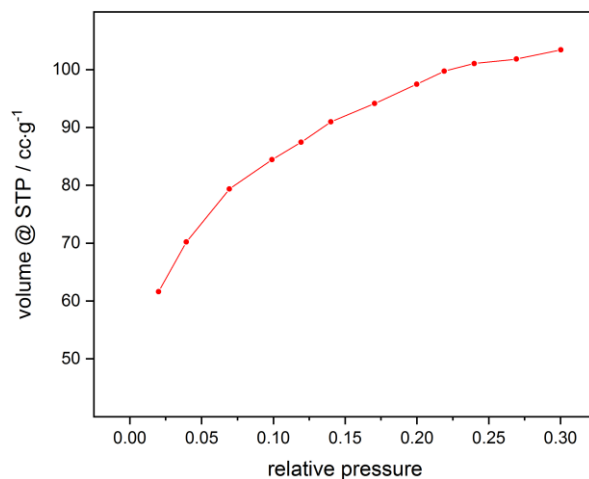


Figure A 11: Krypton adsorption isotherm of polyCzTPP.

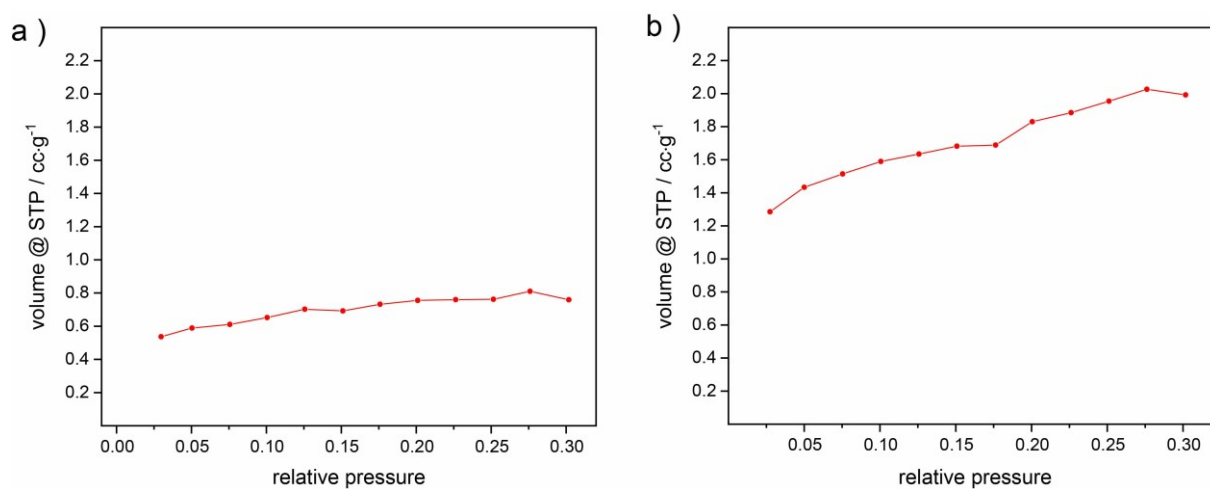


Figure A 12: Krypton adsorption isotherm of a) polyCzbipy b) polyCzbipyTCB.

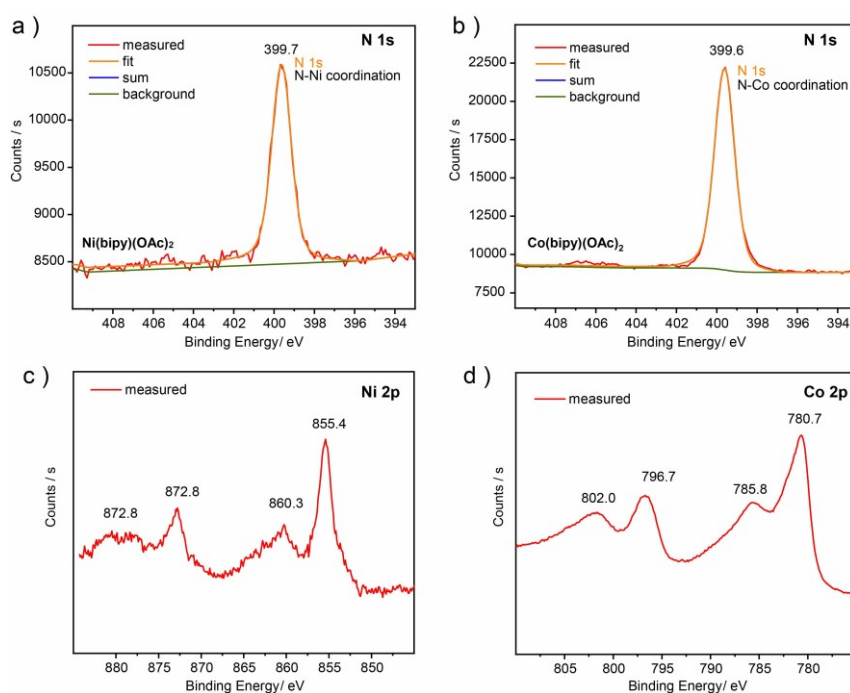


Figure A 13: N 1s XPS spectra as references of a) Ni(bipy)(OAc)₂, b) Co(bipy)(OAc)₂. C) Ni 2p spectrum of Ni(bipy)(OAc)₂, and d) Co 2p spectrum of Co(bipy)(OAc)₂.

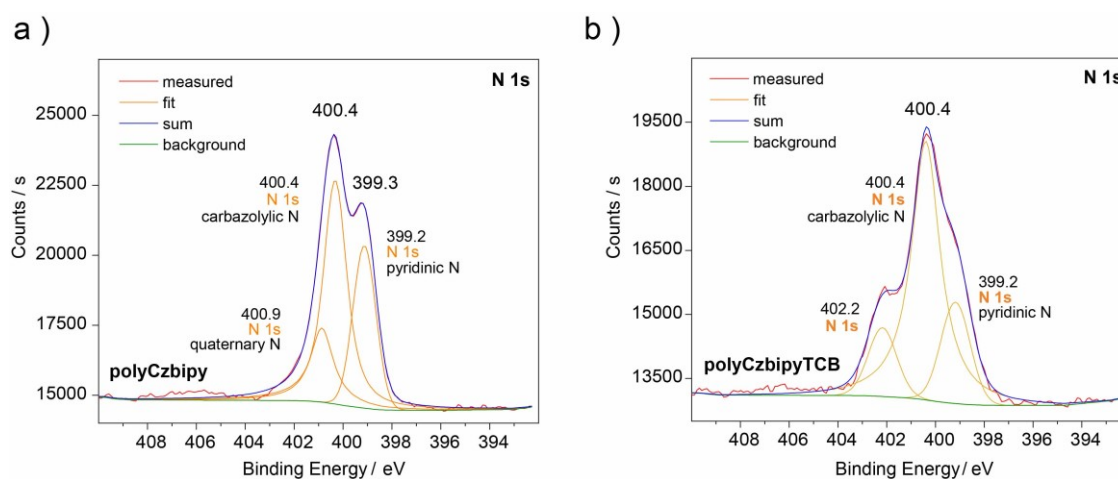


Figure A 14: N 1s XPS spectra of a) polyCzbipy, b) polyCzbipyTCB.

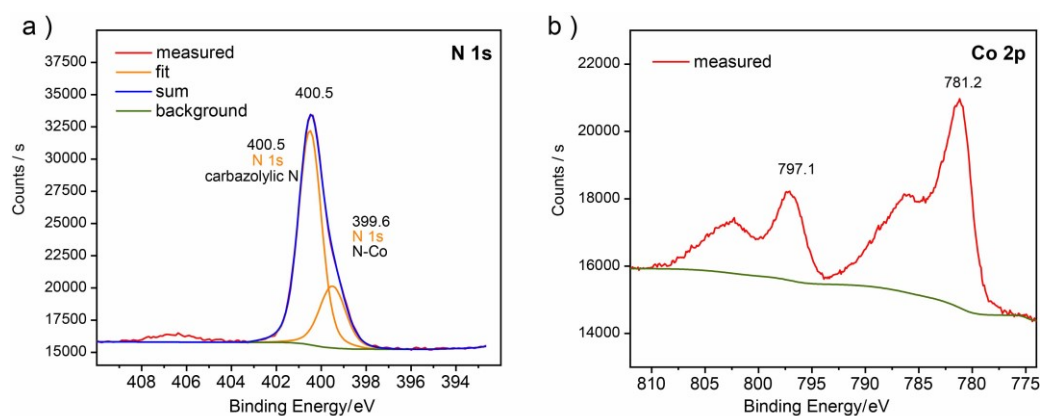


Figure A 15: a) N 1s and b) Co 2p XPS spectra of polyCzbipyTCB-Co.

9.2 References

- [1] Q. Chen, M. Luo, P. Hammershøj, D. Zhou, Y. Han, B. W. Laursen, C.-G. Yan, B.-H. Han, *J. Am. Chem. Soc.* **2012**, *134*, 6084–6087.
- [2] F. M. Wisser, Y. Mohr, E. A. Quadrelli, J. Canivet, *ChemCatChem* **2020**, *12*, 1270–1275.
- [3] H.-P. Liang, A. Acharjya, D. A. Anito, S. Vogl, T.-X. Wang, A. Thomas, B.-H. Han, *ACS Catal.* **2019**, 3959–3968.
- [4] G. P. Pez, A. R. Scott, A. C. Cooper, H. Cheng, L. D. Bagzis, J. B. Appleby, **2004**.
- [5] “World Energy Outlook 2019 – Analysis - IEA,” can be found under <https://www.iea.org/reports/world-energy-outlook-2019>, **n.d.**
- [6] P. Preuster, C. Papp, P. Wasserscheid, *Acc. Chem. Res.* **2017**, *50*, 74–85.
- [7] “Technology Roadmap - Energy and GHG Reductions in the Chemical Industry via Catalytic Processes – Analysis - IEA,” can be found under <https://www.iea.org/reports/technology-roadmap-energy-and-ghg-reductions-in-the-chemical-industry-via-catalytic-processes>, **n.d.**
- [8] C. Copéret, M. Chabanas, R. Petroff Saint-Arroman, J.-M. Basset, *Angew. Chemie Int. Ed.* **2003**, *42*, 156–181.
- [9] M. Rose, *ChemCatChem* **2014**, *6*, 1166 – 1182.
- [10] M. König, M. Rigo, N. Chaoui, T. T. Ngoc, J. D. Epping, J. Schmidt, P. Pachfule, M.-Y. Ye, M. Trunk, J. Teichert, et al., *Angew. Chemie Int. Ed.* **2020**, anie.202004092.
- [11] K. S. W. Sing, *Pure Appl. Chem.* **1985**, *57*, 603–619.
- [12] J. Rouquerol, D. Avnir, C. W. Fairbridge, D. H. Everett, J. M. Haynes, N. Pernicone, J. D. F. Ramsay, K. S. W. Sing, K. K. Unger, *Pure Appl. Chem.* **1994**, *66*, 1739–1758.
- [13] M. Thommes, K. Kaneko, A. V. Neimark, J. P. Olivier, F. Rodriguez-Reinoso, J. Rouquerol, K. S. W. Sing, *Pure Appl. Chem.* **2015**, *87*, 1051–1069.
- [14] S. Sircar, R. Mohr, C. Ristic, M. B. Rao, *J. Phys. Chem. B* **1999**, *103*, 6539–6546.
- [15] W. Kukulka, K. Cendrowski, B. Michalkiewicz, E. Mijowska, *RSC Adv.* **2019**, *9*, 18527–18537.
- [16] K. Sumida, D. L. Rogow, J. A. Mason, T. M. McDonald, E. D. Bloch, Z. R. Herm, T.-H. Bae, J. R. Long, *Chem. Rev* **2012**, *112*, 724–781.
- [17] A. Thomas, *Angew. Chemie Int. Ed.* **2010**, *49*, 8328–8344.
- [18] F. Schüth, *Chem. Mater.* **2001**, *13*, 3184–3195.
- [19] Brian J. Melde, Brian T. Holland, A. Christopher F. Blanford, A. Stein*, **1999**, DOI 10.1021/CM9903935.

-
- [20] F. Schüth, K. S. W. Sing, J. Weitkamp, *Handbook of Porous Solids*, Wiley-VCH Verlag, **2002**.
- [21] K. Nishi, R. W. Thompson, in *Handb. Porous Solids*, Wiley-VCH Verlag GmbH, **2008**, pp. 736–814.
- [22] R. Dawson, A. I. Cooper, D. J. Adams, *Prog. Polym. Sci.* **2012**, *37*, 530–563.
- [23] N. Chaoui, M. Trunk, R. Dawson, J. Schmidt, A. Thomas, *Chem. Soc. Rev.* **2017**, *46*, 3302–3321.
- [24] S. Brunauer, P. H. Emmett, E. Teller, *J. Am. Chem. Soc.* **1938**, *60*, 309–319.
- [25] I. Langmuir, *J. Am. Chem. Soc.* **1918**, *40*, 1361–1403.
- [26] K. Sing, in *Colloids Surfaces A Physicochem. Eng. Asp.*, Elsevier, **2001**, pp. 3–9.
- [27] F. Rouquerol, J. Rouquerol, K. Sing, *Adsorption by Powders and Porous Solids*, Elsevier, **1999**.
- [28] E. P. Barrett, L. G. Joyner, P. P. Halenda, *J. Am. Chem. Soc.* **1951**, *73*, 373.
- [29] L. D. Gelb, K. E. Gubbins, *Langmuir* **1999**, *15*, 305–308.
- [30] A. Cronstedt, *Akad. Handl. (Stockholm)* **1756**, *18*, 120.
- [31] R. M. Barrer, *J. Chem. Soc.* **1948**, 2158.
- [32] D. W. Breck, W. G. Eversole, R. M. Milton, T. B. Reed, T. L. Thomas, *J. Am. Chem. Soc.* **1956**, *78*, 5963–5972.
- [33] J. D. Sherman, *Proc. Natl. Acad. Sci. U. S. A.* **1999**, *96*, 3471–8.
- [34] M. J. Zamzow, B. R. Eichbaum, K. R. Sandgren, D. E. Shanks, *Sep. Sci. Technol.* **1990**, *25*, 1555–1569.
- [35] M. Sevilla, R. Mokaya, in *Energy Environ. Sci.*, Royal Society Of Chemistry, **2014**, pp. 1250–1280.
- [36] V. A. Davankov, S. V. Rogoshin, M. P. Tsyurupa, *J. Polym. Sci. Polym. Symp.* **1974**, *47*, 95–101.
- [37] B. F. Hoskins, R. Robson, *J. Am. Chem. Soc.* **1990**, *112*, 1546–1554.
- [38] M. Fujita, S. Washizu, K. Ogura, Y. J. Kwon, *J. Am. Chem. Soc.* **1994**, *116*, 1151–1152.
- [39] B. F. Abrahams, B. F. Hoskins, D. M. Michail, R. Robson, *Nature* **1994**, *369*, 727–729.
- [40] D. Venkataraman, J. S. Moore, G. B. Gardner, S. Lee, *J. Am. Chem. Soc.* **1995**, *117*, 11600–11601.
- [41] O. M. Yaghi, H. Li, *J. Am. Chem. Soc.* **1995**, *117*, 10401–10402.
- [42] O. M. Yaghi, G. Li, H. Li, *Nature* **1995**, *378*, 703–706.
- [43] P. Kuhn, M. Antonietti, A. Thomas, *Angew. Chemie Int. Ed.* **2008**, *47*, 3450–3453.
- [44] O. M. Yaghi, H. Li, M. Eddaoudi, M. O’Keeffe, *Nature* **1999**, *402*, 276–279.

-
- [45] H. Furukawa, K. E. Cordova, M. O’Keeffe, O. M. Yaghi, *Science* (80-.). **2013**, 341.
- [46] H. Furukawa, N. Ko, Y. B. Go, N. Aratani, S. B. Choi, E. Choi, A. Ö. Yazaydin, R. Q. Snurr, M. O’Keeffe, J. Kim, et al., *Science* (80-.). **2010**, 329.
- [47] L. J. Murray, M. Dincă, J. R. Long, A. W. C. van den Berg, C. O. Areán, R. C. Lochan, M. Head-Gordon, T. Düren, R. Q. Snurr, H. Frost, et al., *Chem. Soc. Rev.* **2009**, 38, 1294.
- [48] P. Horcajada, C. Serre, M. Vallet-Regí, M. Sebban, F. Taulelle, G. Férey, *Angew. Chemie Int. Ed.* **2006**, 45, 5974–5978.
- [49] A. P. Côté, A. I. Benin, N. W. Ockwig, M. O’Keeffe, A. J. Matzger, O. M. Yaghi, *Science* (80-.). **2005**, 310.
- [50] J.-X. Jiang, F. Su, A. Trewin, C. D. Wood, N. L. Campbell, H. Niu, C. Dickinson, A. Y. Ganin, M. J. Rosseinsky, Y. Z. Khimyak, et al., *Angew. Chemie Int. Ed.* **2007**, 46, 8574–8578.
- [51] T. Ben, H. Ren, M. Shengqian, D. Cao, J. Lan, X. Jing, W. Wang, J. Xu, F. Deng, J. M. Simmons, et al., *Angew. Chemie - Int. Ed.* **2009**, 48, 9457–9460.
- [52] P. M. Budd, B. S. Ghanem, S. Makhseed, N. B. McKeown, K. J. Msayib, C. E. Tattershall, *Chem. Commun.* **2004**, 4, 230–231.
- [53] J. Lee, O. K. Farha, J. Roberts, K. A. Scheidt, S. T. Nguyen, J. T. Hupp, *Chem. Soc. Rev.* **2009**, 38, 1450.
- [54] P. M. Budd, K. J. Msayib, C. E. Tattershall, B. S. Ghanem, K. J. Reynolds, N. B. McKeown, D. Fritsch, *J. Memb. Sci.* **2005**, 251, 263–269.
- [55] T. Mitra, R. S. Bhavsar, D. J. Adams, P. M. Budd, A. I. Cooper, *Chem. Commun.* **2016**, 52, 5581–5584.
- [56] F. J. Uribe-Romo, J. R. Hunt, H. Furukawa, C. Klöck, M. O’Keeffe, O. M. Yaghi, *J. Am. Chem. Soc.* **2009**, 131, 4570–4571.
- [57] F. J. Uribe-Romo, C. J. Doonan, H. Furukawa, K. Oisaki, O. M. Yaghi, *J. Am. Chem. Soc.* **2011**, 133, 11478–11481.
- [58] S. Kandambeth, A. Mallick, B. Lukose, M. V. Mane, T. Heine, R. Banerjee, *J. Am. Chem. Soc.* **2012**, 134, 19524–19527.
- [59] B. Wang, X. L. Lv, D. Feng, L. H. Xie, J. Zhang, M. Li, Y. Xie, J. R. Li, H. C. Zhou, *J. Am. Chem. Soc.* **2016**, 138, 6204–6216.
- [60] L. Hao, B. Luo, X. Li, M. Jin, Y. Fang, Z. Tang, Y. Jia, M. Liang, A. Thomas, J. Yang, et al., *Energy Environ. Sci.* **2012**, 5, 9747.
- [61] S. Kuecken, A. Acharjya, L. Zhi, M. Schwarze, R. Schomäcker, A. Thomas, *Chem. Commun.* **2017**, 53, 5854–5857.

-
- [62] N. B. McKeown, P. M. Budd, *Chem. Soc. Rev.* **2006**, 35, 675.
- [63] Y. Xu, S. Jin, H. Xu, A. Nagai, D. Jiang, R. M. Barrer, R. Fricke, H. Kosslick, G. Lischke, M. Richter, et al., *Chem. Soc. Rev.* **2013**, 42, 8012.
- [64] N. Miyaura, A. Suzuki, *J. Chem. Soc. Chem. Commun.* **1979**, 866.
- [65] K. Sonogashira, Y. Tohda, N. Hagihara, *Tetrahedron Lett.* **1975**, 16, 4467–4470.
- [66] J. Schmidt, M. Werner, A. Thomas, *Macromolecules* **2009**, 42, 4426–4429.
- [67] W. Lu, D. Yuan, D. Zhao, C. I. Schilling, O. Plietzsch, T. Muller, S. Bräse, J. Guenther, J. Blümel, R. Krishna, et al., *Chem. Mater.* **2010**, 22, 5964–5972.
- [68] W. Lu, D. Yuan, J. Sculley, D. Zhao, R. Krishna, H. C. Zhou, *J. Am. Chem. Soc.* **2011**, 133, 18126–18129.
- [69] X. Cui, W. Li, P. Ryabchuk, K. Junge, M. Beller, *Nat. Catal.* **2018**, 1, 385–397.
- [70] S. Shylesh, V. Schünemann, W. R. Thiel, *Angew. Chemie - Int. Ed.* **2010**, 49, 3428–3459.
- [71] C. Copéret, F. Allouche, K. W. Chan, M. P. Conley, M. F. Delley, A. Fedorov, I. B. Moroz, V. Mougel, M. Pucino, K. Searles, et al., *Angew. Chemie Int. Ed.* **2018**, 57, 6398–6440.
- [72] Q. Sun, M. Jiang, Z. Shen, Y. Jin, S. Pan, L. Wang, X. Meng, W. Chen, Y. Ding, J. Li, et al., *Chem. Commun.* **2014**, 50, 11844–11847.
- [73] S. Hübner, J. G. de Vries, V. Farina, *Adv. Synth. Catal.* **2016**, 358, 3–25.
- [74] H. Hoegl, in *J. Phys. Chem.*, American Chemical Society, **1965**, pp. 755–766.
- [75] A. Aboukassim, K. Faïd, A. Siove, *Die Makromol. Chemie* **1993**, 194, 29–36.
- [76] J. V. Grazulevicius, P. Stroehriegl, J. Pielichowski, K. Pielichowski, *Prog. Polym. Sci.* **2003**, 28, 1297–1353.
- [77] Z.-B. Zhang, M. Fujiki, H.-Z. Tang, M. Motonaga, K. Torimitsu, *Macromolecules* **2002**, 35, 1988–1990.
- [78] A. Iraqi, I. Wataru, *J. Polym. Sci. Part A Polym. Chem.* **2004**, 42, 6041–6051.
- [79] J.-F. Morin, M. Leclerc, D. Adès, A. Siove, *Macromol. Rapid Commun.* **2005**, 26, 761–778.
- [80] A. Siove, R. David, D. Ades, C. Roux, M. Leclerc, *J. Chim. Phys.* **1995**, 92, 787.
- [81] P.-L. T. Boudreault, S. Beaupré, M. Leclerc, *Polym. Chem.* **2010**, 1, 127–136.
- [82] M. Li, *Chem. - A Eur. J.* **2018**, DOI 10.1002/chem.201803246.
- [83] Q. Chen, D.-P. Liu, M. Luo, L.-J. Feng, Y.-C. Zhao, B.-H. Han, *Small* **2014**, 10, 308–315.
- [84] L.-J. Feng, Q. Chen, J.-H. Zhu, D.-P. Liu, Y.-C. Zhao, B.-H. Han, *Polym. Chem.* **2014**,

- 5, 3081.
- [85] L. Pan, M.-Y. Xu, L.-J. Feng, Q. Chen, Y.-J. He, B.-H. Han, *Polym. Chem.* **2016**, *7*, 2299–2307.
- [86] Q. Chen, B.-H. Han, *Macromol. Rapid Commun.* **2018**, *39*, 1800040.
- [87] H. Wang, Z. Cheng, Y. Liao, J. Li, J. Weber, A. Thomas, C. F. J. Faul, *Chem. Mater.* **2017**, *29*, 4885–4893.
- [88] H.-P. Liang, Q. Chen, B.-H. Han, *ACS Catal.* **2018**, *8*, 5313–5322.
- [89] J. Luo, X. Zhang, J. Lu, J. Zhang, *ACS Catal.* **2017**, *7*, 5062–5070.
- [90] Y. Liao, Z. Cheng, M. Trunk, A. Thomas, *Polym. Chem.* **2017**, *8*, 7240–7247.
- [91] E. A. Rozhkova, K. Ariga, *From Molecules to Materials: Pathways to Artificial Photosynthesis*, Springer International Publishing, **2015**.
- [92] K. Li, X. An, K. H. Park, M. Khraisheh, J. Tang, *Catal. Today* **2014**, *224*, 3–12.
- [93] G. Sahara, O. Ishitani, *Inorg. Chem.* **2015**, *54*, 5096–5104.
- [94] J. Hawecker, J. M. Lehn, R. Ziessel, *J. Chem. Soc. Chem. Commun.* **1983**, 536–538.
- [95] Y. Tamaki, K. Watanabe, K. Koike, H. Inoue, T. Morimoto, O. Ishitani, *Faraday Discuss.* **2012**, *155*, 115–127.
- [96] M. R. Wasielewski, *Chem. Rev.* **1992**, *92*, 435–461.
- [97] A. J. Morris, G. J. Meyer, E. Fujita, *Acc. Chem. Res.* **2009**, *42*, 1983–1994.
- [98] Y. Tamaki, O. Ishitani, *ACS Catal.* **2017**, *7*, 3394–3409.
- [99] P. D. Tran, L. H. Wong, J. Barber, J. S. C. Loo, *Energy Environ. Sci.* **2012**, *5*, 5902–5918.
- [100] B. Gholamkhash, H. Mametsuka, K. Koike, T. Tanabe, M. Furue, O. Ishitani, *Inorg. Chem.* **2005**, *44*, 2326–2336.
- [101] R. M. Navarro Yerga, M. C. Álvarez Galván, F. del Valle, J. A. Villoria de la Mano, J. L. G. Fierro, *ChemSusChem* **2009**, *2*, 471–485.
- [102] V. S. Mothika, P. Sutar, P. Verma, S. Das, S. K. Pati, T. K. Maji, *Chem. – A Eur. J.* **2019**, *25*, 3867–3874.
- [103] B. Bonillo, R. S. Sprick, A. I. Cooper, *Chem. Mater.* **2016**, *28*, 3469–3480.
- [104] J. X. Jiang, A. Trewin, D. J. Adams, A. I. Cooper, *Chem. Sci.* **2011**, *2*, 1777–1781.
- [105] A. Ajayaghosh, *Chem. Soc. Rev.* **2003**, *32*, 181–191.
- [106] M. Waki, K. Yamanaka, S. Shirai, Y. Maegawa, Y. Goto, Y. Yamada, S. Inagaki, *Chem. – A Eur. J.* **2018**, *24*, 3846–3853.
- [107] C. Wang, Z. Xie, K. E. DeKrafft, W. Lin, *J. Am. Chem. Soc.* **2011**, *133*, 13445–13454.
- [108] E. M. Johnson, R. Haiges, S. C. Marinescu, *ACS Appl. Mater. Interfaces* **2018**, *10*,

- 37919–37927.
- [109] W. Liang, T. L. Church, S. Zheng, C. Zhou, B. S. Haynes, D. M. D'Alessandro, *Chem. - A Eur. J.* **2015**, *21*, 18576–18579.
- [110] T. Fenton, S. Gillingham, T. Jin, G. Li, *Dalt. Trans.* **2017**, *46*, 10721–10726.
- [111] C. Cavedon, P. H. Seeberger, B. Pieber, *European J. Org. Chem.* **2020**, *2020*, 1379–1392.
- [112] S. Z. Tasker, E. A. Standley, T. F. Jamison, *Nature* **2014**, *509*, 299–309.
- [113] J. Twilton, C. Le, P. Zhang, M. H. Shaw, R. W. Evans, D. W. C. MacMillan, *Nat. Rev. Chem.* **2017**, *1*, 0052.
- [114] G. Lan, Y. Quan, M. Wang, G. T. Nash, E. You, Y. Song, S. S. Veroneau, X. Jiang, W. Lin, *J. Am. Chem. Soc.* **2019**, *141*, 15767–15772.
- [115] Y.-Y. Zhu, G. Lan, Y. Fan, S. S. Veroneau, Y. Song, D. Micheroni, W. Lin, *Angew. Chemie Int. Ed.* **2018**, *57*, 14090–14094.
- [116] Y. Pan, N. Zhang, C. H. Liu, S. Fan, S. Guo, Z. M. Zhang, Y. Y. Zhu, *ACS Catal.* **2020**, *10*, 11758–11767.
- [117] D. S. Ahmed, G. A. El-Hiti, E. Yousif, A. A. Ali, A. S. Hameed, *J. Polym. Res.* **2018**, *25*, 1–21.
- [118] T. Ben, C. Pei, D. Zhang, J. Xu, F. Deng, X. Jing, S. Qiu, *Energy Environ. Sci.* **2011**, *4*, 3991–3999.
- [119] R. E. Morris, P. S. Wheatley, *Angew. Chemie Int. Ed.* **2008**, *47*, 4966–4981.
- [120] T. He, P. Pachfule, H. Wu, Q. Xu, P. Chen, *Nat. Rev. Mater.* **2016**, *1*, 1–17.
- [121] U. Eberle, M. Felderhoff, F. Schüth, *Angew. Chemie - Int. Ed.* **2009**, *48*, 6608–6630.
- [122] N. B. McKeown, P. M. Budd, D. Book, *Macromol. Rapid Commun.* **2007**, *28*, 995–1002.
- [123] T. He, Q. Pei, P. Chen, *J. Energy Chem.* **2015**, *24*, 587–594.
- [124] D. Dean, B. Davis, P. G. Jessop, *New J. Chem.* **2011**, *35*, 417–422.
- [125] P. Makowski, A. Thomas, P. Kuhn, F. Goettmann, *Energy Environ. Sci.* **2009**, *2*, 480.
- [126] J. O. Abe, A. P. I. Popoola, E. Ajenifuja, O. M. Popoola, *Int. J. Hydrogen Energy* **2019**, *44*, 15072–15086.
- [127] L. Ouyang, K. Chen, J. Jiang, X.-S. Yang, M. Zhu, *J. Alloys Compd.* **2020**, *829*, 154597.
- [128] N. A. A. Rusman, M. Dahari, *Int. J. Hydrogen Energy* **2016**, *41*, 12108–12126.
- [129] B. Sakintuna, F. Lamari-Darkrim, M. Hirscher, *Int. J. Hydrogen Energy* **2007**, *32*, 1121–1140.
- [130] Q.-L. Zhu, Q. Xu, *Energy Environ. Sci.* **2015**, *8*, 478–512.
- [131] N. Brückner, K. Obesser, A. Bösmann, D. Teichmann, W. Arlt, J. Dungs, P.

- Wasserscheid, *ChemSusChem* **2014**, 7, 229–235.
- [132] S.-C. Cui, X.-Z. Sun, J.-G. Liu, *ChemSusChem* **2016**, 9, 1698–1703.
- [133] J. Okal, W. Tylus, L. Kępiński, *J. Catal.* **2004**, 225, 498–509.
- [134] M. T. Greiner, T. C. R. Rocha, B. Johnson, A. Klyushin, A. Knop-Gericke, R. Schlögl, *Zeitschrift für Phys. Chemie* **2014**, 228, 521–541.
- [135] M. Mikkelsen, M. Jørgensen, F. C. Krebs, *Energy Environ. Sci.* **2010**, 3, 43–81.
- [136] Y. Hayashi, S. Kita, B. S. Brunschwig, E. Fujita, *J. Am. Chem. Soc.* **2003**, 125, 11976–11987.
- [137] E. E. Benson, C. P. Kubiak, *Chem. Commun.* **2012**, 48, 7374–7376.
- [138] B. J. Shields, B. Kudisch, G. D. Scholes, A. G. Doyle, *J. Am. Chem. Soc.* **2018**, 140, 3035–3039.
- [139] N. Richter, C. Cavedon, Thesis for Acquiring the Degree of Bachelor of Science in Chemistry with the Topic : A Visible-Light Harvesting Ligand Enables Photocatalyst-Free Nickel- Catalyzed Cross-Coupling Reactions, **2020**.
- [140] C. H. Lim, M. Kudisch, B. Liu, G. M. Miyake, *J. Am. Chem. Soc.* **2018**, 140, 7667–7673.
- [141] L. Yang, H. Lu, C. Lai, G. Li, W. Zhang, R. Cao, F. Liu, C. Wang, J. Xiao, D. Xue, *Angew. Chemie Int. Ed.* **2020**, 59, 12714–12719.
- [142] C. Gu, Y. Chen, Z. Zhang, S. Xue, S. Sun, K. Zhang, C. Zhong, H. Zhang, Y. Pan, Y. Lv, et al., *Adv. Mater.* **2013**, 25, 3443–3448.
- [143] X. Zhao, P. Pachfule, S. Li, T. Langenhahn, M. Ye, C. Schlesiger, S. Praetz, J. Schmidt, A. Thomas, *J. Am. Chem. Soc.* **2019**, 141, 6623–6630.
- [144] M. Cai, S. Ding, B. Gibbons, X. Yang, M. C. Kessinger, A. J. Morris, *Chem. Commun.* **2020**, 56, 14361–14364.
- [145] Q. Chen, A. Dong, D. Wang, L. Qiu, C. Ma, Y. Yuan, Y. Zhao, N. Jia, Z. Guo, N. Wang, *Angew. Chemie Int. Ed.* **2019**, 58, 10671–10676.
- [146] D. Teichmann, W. Arlt, P. Wasserscheid, R. Freymann, *Energy Environ. Sci.* **2011**, 4, 2767.
- [147] M. Sobota, I. Nikiforidis, M. Amende, B. S. Zanón, T. Staudt, O. Höfert, Y. Lykhach, C. Papp, W. Hieringer, M. Laurin, et al., *Chem. - A Eur. J.* **2011**, 17, 11542–11552.
- [148] Y. Kim, Y. Kwon, K. Lee, J. Park, H. Seo, T. Kim, *Mol. Cryst. Liq. Cryst.* **2004**, 424, 153–158.
- [149] M. Li, S. Kang, J. Du, J. Zhang, J. Wang, K. Ariga, *Angew. Chemie Int. Ed.* **2018**, 57, 4936–4939.
- [150] E. Sari, G. Yilmaz, S. Koyuncu, Y. Yagci, *J. Am. Chem. Soc.* **2018**, jacs.8b08668.

-
- [151] L. Bai, X. Wang, Q. Chen, Y. Ye, H. Zheng, J. Guo, Y. Yin, C. Gao, *Angew. Chemie - Int. Ed.* **2016**, *55*, 15656–15661.
- [152] K. Morawa Eblagon, K. Tam, K. M. K. Yu, S. L. Zhao, X. Q. Gong, H. He, L. Ye, L. C. Wang, A. J. Ramirez-Cuesta, S. C. Tsang, *J. Phys. Chem. C* **2010**, *114*, 9720–9730.
- [153] K. M. Eblagon, D. Rentsch, O. Friedrichs, A. Remhof, A. Zuettel, A. J. Ramirez-Cuesta, S. C. Tsang, *Int. J. Hydrogen Energy* **2010**, *35*, 11609–11621.
- [154] K. M. Thomas, *Catal. Today* **2007**, *120*, 389–398.
- [155] F. Sotoodeh, K. J. Smith, *J. Catal.* **2011**, *279*, 36–47.
- [156] A. Ou, A. Guédin, B. W. Skelton, S. Amrane, C. W. Evans, M. Norret, K. S. Iyer, J.-L. Mergny, N. M. Smith, *Chem. Commun.* **2018**, *54*, 9647–9650.
- [157] G. Wittig, G. Geissler, *Justus Liebigs Ann. Chem.* **1953**, *580*, 44–57.
- [158] H. Pommer, P. C. Thieme, in *Wittig Chem.*, Springer-Verlag, **2005**, pp. 165–188.
- [159] H. A. Van Kalker, A. L. Blom, F. P. J. T. Rutjes, M. A. J. Huijbregts, *Green Chem.* **2013**, *15*, 1255–1263.
- [160] B. L. L. Kürti, *Strategic Applications of Named Reactions in Organic Synthesis*, Elsevier Inc., **2005**.
- [161] C. J. O'Brien, J. L. Tellez, Z. S. Nixon, L. J. Kang, A. L. Carter, S. R. Kunkel, K. C. Przeworski, G. A. Chass, *Angew. Chemie Int. Ed.* **2009**, *48*, 6836–6839.
- [162] H. Staudinger, J. Meyer, *Helv. Chim. Acta* **1919**, *2*, 635–646.
- [163] R. Appel, *Angew. Chemie Int. Ed. English* **1975**, *14*, 801–811.
- [164] O. Mitsunobu, M. Yamada, *Bull. Chem. Soc. Jpn.* **1967**, *40*, 2380–2382.
- [165] S. Manabe, C. M. Wong, C. S. Sevov, *J. Am. Chem. Soc.* **2020**, jacs.9b12112.
- [166] A. Voituriez, N. Saleh, *Tetrahedron Lett.* **2016**, *57*, 4443–4451.
- [167] B. Cornils, W. A. Herrmann, M. Rasch, *ChemInform* **2010**, *26*, no-no.
- [168] M. Lenarda, L. Storaro, R. Ganzerla, *J. Mol. Catal. A Chem.* **1996**, *111*, 203–237.
- [169] M. I. Qadir, R. Webber, J. Dupont, in *Adv. Organomet. Chem.*, Academic Press Inc., **2019**, pp. 259–274.
- [170] C. Li, W. Wang, L. Yan, Y. Ding, *Front. Chem. Sci. Eng.* **2018**, *12*, 113–123.
- [171] J. A. Osborn, G. Wilkinson, J. J. Mrowca, in *Inorg. Synth.*, Wiley, **2007**, pp. 67–71.
- [172] D. Evans, J. A. Osborn, G. Wilkinson, *J. Chem. Soc. A Inorganic, Phys. Theor.* **1968**, 3133–3142.
- [173] N. Miyaura, T. Yanagi, A. Suzuki, *Synth. Commun.* **1981**, *11*, 513–519.
- [174] W. Zhou, D. He, *Chem. Commun.* **2008**, 5839–5841.
- [175] W. Zhou, D. He, **2009**, DOI 10.1039/b900591a.

- [176] J. Fritsch, F. Drache, G. Nickerl, W. Böhlmann, S. Kaskel, *Microporous Mesoporous Mater.* **2013**, *172*, 167–173.
- [177] A. R. Ravishankara, J. S. Daniel, R. W. Portmann, *Science (80-.)*. **2009**, *326*, 123–125.
- [178] R. Zeng, M. Feller, Y. Ben-David, D. Milstein, *J. Am. Chem. Soc.* **2017**, *139*, 5720–5723.
- [179] T. L. Gianetti, S. P. Annen, G. Santiso-Quinones, M. Reiher, M. Driess, H. Grützmacher, *Angew. Chemie Int. Ed.* **2016**, *55*, 1854–1858.
- [180] T. Zweifel, J.-V. Naubron, T. Büttner, T. Ott, H. Grützmacher, *Angew. Chemie Int. Ed.* **2008**, *47*, 3245–3249.
- [181] M. Van Overschelde, E. Vervecken, S. G. Modha, S. Cogen, E. Van der Eycken, J. Van der Eycken, *Tetrahedron* **2009**, *65*, 6410–6415.
- [182] M. Ohff, J. Holz, M. Quirnbach, A. Börner, *Synthesis (Stuttg.)*. **1998**, *1998*, 1391–1415.
- [183] E. L. Gamble, P. Gilmont, *J. Am. Chem. Soc.* **1940**, *62*, 717–721.
- [184] J. M. Brunei, B. Faure, M. Maffei, *Coord. Chem. Rev.* **1998**, *178–180*, 665–698.
- [185] Q. Zhang, Y. Yang, S. Zhang, *Chem. - A Eur. J.* **2013**, *19*, 10024–10029.
- [186] Z. Yang, B. Yu, H. Zhang, Y. Zhao, Y. Chen, Z. Ma, G. Ji, X. Gao, B. Han, Z. Liu, *ACS Catal.* **2016**, *6*, 1268–1273.
- [187] M. Trunk, J. F. Teichert, A. Thomas, *J. Am. Chem. Soc.* **2017**, *139*, 3615–3618.
- [188] R. Tao, X. Shen, Y. Hu, K. Kang, Y. Zheng, S. Luo, S. Yang, W. Li, S. Lu, Y. Jin, et al., *Small* **2020**, *16*, 1906005.
- [189] Y. Liu, A. Dikhtiarenko, N. Xu, J. Sun, J. Tang, K. Wang, B. Xu, Q. Tong, H. J. Heeres, S. He, et al., *Chem. – A Eur. J.* **2020**, *26*, 12134–12139.
- [190] M. Trincado, H. Grützmacher, F. Vizza, C. Bianchini, *Chem. - A Eur. J.* **2010**, *16*, 2751–2757.
- [191] J. Schmidt, M. Werner, A. Thomas, *Macromolecules* **2009**, *42*, 4426–4429.
- [192] J. Zakzeski, H. R. Lee, Y. L. Leung, A. T. Bell, *Appl. Catal. A Gen.* **2010**, *374*, 201–212.
- [193] W. Zhou, Y. Li, D. He, *Appl. Catal. A Gen.* **2010**, *377*, 114–120.
- [194] F. Porta, S. Tollari, C. Bianchi, S. Recchia, *Inorganica Chim. Acta* **1996**, *249*, 79–83.
- [195] Q. Sun, Z. Dai, X. Liu, N. Sheng, F. Deng, X. Meng, F.-S. Xiao, *J. Am. Chem. Soc.* **2015**, *137*, 5204–5209.
- [196] J. F. Ambrose, R. F. Nelson, *J. Electrochem. Soc.* **1968**, *115*, 1159.
- [197] C. Gu, N. Huang, J. Gao, F. Xu, Y. Xu, D. Jiang, *Angew. Chemie Int. Ed.* **2014**, *53*, 4850–4855.
- [198] C. Gu, Y. Chen, Z. Zhang, S. Xue, S. Sun, C. Zhong, H. Zhang, Y. Lv, F. Li, F. Huang,

- et al., *Adv. Energy Mater.* **2014**, *4*, DOI 10.1002/aenm.201301771.
- [199] A. Palma-Cando, U. Scherf, *ACS Appl. Mater. Interfaces* **2015**, *7*, 11127–11133.
- [200] A. Palma-Cando, U. Scherf, *Macromol. Chem. Phys.* **2016**, *217*, 827–841.
- [201] I. Dincer, C. Acar, *Int. J. Hydrogen Energy* **2014**, *40*, 11094–11111.
- [202] S. Chen, T. Takata, K. Domen, *Nat. Rev. Mater.* **2017**, *2*, 1–17.
- [203] N. T. Suen, S. F. Hung, Q. Quan, N. Zhang, Y. J. Xu, H. M. Chen, *Chem. Soc. Rev.* **2017**, *46*, 337–365.
- [204] K. Sivula, R. Van De Krol, *Nat. Rev. Mater.* **2016**, *1*, DOI 10.1038/natrevmats.2015.10.
- [205] A. Fujishima, K. Honda, *Nature* **1972**, *238*, 37–38.
- [206] Y. H. Chiu, T. H. Lai, M. Y. Kuo, P. Y. Hsieh, Y. J. Hsu, *APL Mater.* **2019**, *7*, 80901.
- [207] J. Joy, J. Mathew, S. C. George, *Int. J. Hydrogen Energy* **2018**, *43*, 4804–4817.
- [208] Z. Wang, L. Wang, *Sci. China Mater.* **2018**, *61*, 806–821.
- [209] B. I. Shklovskii, A. L. Efros, *Electronic Properties of Doped Semiconductors*, **1984**.
- [210] A. G. Tamirat, J. Rick, A. A. Dubale, W. N. Su, B. J. Hwang, *Nanoscale Horizons* **2016**, *1*, 243–267.
- [211] L. M. Peter, K. G. Upul Wijayantha, *ChemPhysChem* **2014**, *15*, 1983–1995.
- [212] C. Ding, J. Shi, Z. Wang, C. Li, *ACS Catal.* **2017**, *7*, 675–688.
- [213] S. Wuttke, D. D. Medina, J. M. Rotter, S. Begum, T. Stassin, R. Ameloot, M. Oschatz, M. Tsotsalas, *Adv. Funct. Mater.* **2018**, *28*, 1801545.
- [214] B. Chakraborty, P. W. Menezes, M. Driess, *J. Am. Chem. Soc.* **2020**, *142*, 14772–14788.
- [215] B. Chakraborty, A. Kostenko, P. W. Menezes, M. Driess, *Chem. – A Eur. J.* **2020**, *26*, 11829–11834.
- [216] M. Y. Ye, S. Li, X. Zhao, N. V. Tarakina, C. Teutloff, W. Y. Chow, R. Bittl, A. Thomas, *Adv. Mater.* **2020**, *32*, 1903942.
- [217] T. Sick, A. G. Hufnagel, J. Kampmann, I. Kondofersky, M. Calik, J. M. Rotter, A. Evans, M. Döblinger, S. Herbert, K. Peters, et al., *J. Am. Chem. Soc.* **2018**, *140*, 2085–2092.
- [218] L. Li, Z. Cai, Q. Wu, W. Y. Lo, N. Zhang, L. X. Chen, L. Yu, *J. Am. Chem. Soc.* **2016**, *138*, 7681–7686.
- [219] R. Gottesman, A. Song, I. Levine, M. Krause, A. T. M. N. Islam, D. Abou-Ras, T. Dittrich, R. Krol, A. Chemseddine, *Adv. Funct. Mater.* **2020**, *30*, 1910832.
- [220] Y. Wang, S. Lany, J. Ghanbaja, Y. Fagot-Revurat, Y. P. Chen, F. Soldera, D. Horwat, F. Mücklich, J. F. Pierson, *Phys. Rev. B* **2016**, *94*, 245418.
- [221] R. Patil, S. Kelkar, R. Naphade, S. Ogale, *J. Mater. Chem. A* **2014**, *2*, 3661–3668.
- [222] J. K. Cooper, Z. Zhang, S. Roychoudhury, C.-M. Jiang, S. Gul, Y.-S. Liu, R. Dhall, A.

-
- Ceballos, J. Yano, D. Prendergast, et al., *Chem. Mater.* **2021**, *33*, 945.
- [223] M. S. Prévot, X. A. Jeanbourquin, W. S. Boureé, F. Abdi, D. Friedrich, R. Van De Krol, N. N. Guijarro, F. Le Formal, K. Sivula, *Chem. Mater.* **2017**, 4952.
- [224] L. Yao, A. Rahmanudin, N. Guijarro, K. Sivula, *Adv. Energy Mater.* **2018**, *8*, 1802585.
- [225] G.-G. Shan, L.-Y. Zhang, H.-B. Li, S. Wang, D.-X. Zhu, P. Li, C.-G. Wang, Z.-M. Su, Y. Liao, *Dalt. Trans.* **2012**, *41*, 523–530.
- [226] S. Fischer, A. Schimanowitz, R. Dawson, I. Senkowska, S. Kaskel, A. Thomas, *J. Mater. Chem. A* **2014**, *2*, 11825–11829.
- [227] P. Pandey, O. K. Farha, A. M. Spokoyny, C. A. Mirkin, M. G. Kanatzidis, J. T. Hupp, S. T. Nguyen, F. J. Uribe-Romo, J. R. Hunt, H. Furukawa, et al., *J. Mater. Chem.* **2011**, *21*, 1700.